



HAL
open science

Discrete element modeling of concrete structures under impact

Andria Antoniou

► **To cite this version:**

Andria Antoniou. Discrete element modeling of concrete structures under impact. Materials Science [cond-mat.mtrl-sci]. Université Grenoble Alpes, 2018. English. NNT : 2018GREAI077 . tel-01990419

HAL Id: tel-01990419

<https://theses.hal.science/tel-01990419>

Submitted on 23 Jan 2019

HAL is a multi-disciplinary open access archive for the deposit and dissemination of scientific research documents, whether they are published or not. The documents may come from teaching and research institutions in France or abroad, or from public or private research centers.

L'archive ouverte pluridisciplinaire **HAL**, est destinée au dépôt et à la diffusion de documents scientifiques de niveau recherche, publiés ou non, émanant des établissements d'enseignement et de recherche français ou étrangers, des laboratoires publics ou privés.



THÈSE

Pour obtenir le grade de

DOCTEUR DE LA COMMUNAUTÉ UNIVERSITÉ GRENOBLE ALPES

Spécialité : 2MGE : Matériaux, Mécanique, Génie civil, Electrochimie

Arrêté ministériel : 25 mai 2016

Présentée par

Andria ANTONIOU

Thèse dirigée par **Laurent DAUDEVILLE**

et coencadrée par **Philippe MARIN** et **Serguei POTAPOV**

préparée au sein du **Laboratoire Sols, Solides,
Structures et Risques**
dans l'**École Doctorale I-MEP2 - Ingénierie - Matériaux,
Mécanique, Environnement, Energétique, Procédés,
Production**

Modélisation aux éléments discrets des structures en béton sous impact

Discrete element modelling of concrete structures under impact

Thèse soutenue publiquement le **14 décembre 2018**,
devant le jury composé de :

Monsieur Marco DI PRISCO

Professeur, Politecnico di Milano, Président

Madame Federica DAGHIA

Maître de Conférences, ENS Paris Saclay, Rapporteur

Monsieur Ivan IORDANOFF

Professeur, Arts et Métiers ParisTech, Rapporteur

Monsieur Eric BUZAUD

Ingénieur de Recherche, CEA DAM, Examineur

Monsieur Laurent DAUDEVILLE

Professeur, Université Grenoble Alpes, Directeur de thèse

Monsieur Philippe MARIN

Maître de Conférences, Grenoble INP, Co-encadrant

Monsieur Serguei Potapov

Ingénieur de Recherche, EDF Paris Saclay, Co-encadrant

Acknowledgments

I have to admit that writing this part of my PhD dissertation might be the most satisfying moment of these very last months. Not only because it makes me feel even closer to the end but also because it gives me the opportunity to express my appreciation to numerous precious people that helped me with their unconditional support during this valuable journey in the world of research.

First of all, I would like to express my special gratitude to my supervisors Laurent DAUDEVILLE, Philippe MARIN and Serguei POTAPOV for having accompanied me during these years devoting their valuable time, guidance and enlighten me with their advice. Without them, I would not have been able to accomplish this work.

Thank you, Laurent, for giving me the opportunity to work on a topic specific to my interests and to help broaden my knowledge keeping my future prospects in mind. Thank you, Philippe, for always finding an innovative solution and for your patience and attention in re-reviewing my manuscript. Thank you, Serguei, for introducing me to the work of EUROPLEXUS and for your constant availability to assist me with constructive inputs.

I wish to thank the members of my dissertation committee: Marco DI PRISCO, Federica DAGHIA, Ivan IORDANOFF and Eric Buzaud for accepting to offer their time generously and to provide their valuable feedback. Thank you for giving me the honour to participate in this process.

I take the opportunity to acknowledge the significant contribution of Pascal FORQUIN, Yann MALÉCOT and Christophe PONTIROLI providing me with their experimental data.

I want to offer my special thanks to Rémi Cailletaud, the informatician of the laboratory 3-SR, without him I would have been in big troubles.

I will always keep my PhD period as a sweet experience thanks to all of you that helped me to replace bitter moments with unforgettable memories. I will start from the first friends I met in Grenoble, Corinne and Ester, even if their staying here was quite short, thank you, for keeping in contact and for trying always to meet somewhere around. Andrea, Dionysse, Nill and Valentin, thank you for filling my depressive rainy Sundays, with a cup of coffee or pizzas and endless conversations. I am very happy to have met Vincent who helped me not to lose motivation during the second year, thank you, Vincent.

The third year probably is the most demandable, full of pressure and limited time. I feel lucky that a new friend entered my life, Giovanna, thank you for sharing endless hours working together, thank you for always being ready to listen to my "problems" and for helping me to look on the bright side. I could not have omitted, Matteo, thank you for being a real friend, thank you for criticising all my wrong decisions, thank you for letting me share my troubles with you. Joyee, my sweet flatmate,

thank you for all your support during the endless nights I spent writing my dissertation, thank you for making our apartment joyful. Augustin, thank you for the beautiful conversations, thank you for helping me to improve French with so much patience and thank you for translating my abstract in French. Florian, thank you for sharing your funny and interesting stories with me and making me laugh.

Myriam, Thomas, Katya, Adrien, Eris, Baptiste, Arnaud, Jérémy, thank you for making Grenoble feel like home. Alejandro, Ioanna, Stavroula, Katerina, Christiana, Maria, Despo, Marie, Artemi, thank you for letting me feel all your love from far away.

Parents are given to us. We cannot choose them. I feel very blessed that Panayiota and Kyriakos are not only my parents but also my friends in life. I am grateful to be your daughter and thankful for supporting all my decision and standing by me. Thank you for educating me with ethical principles. I would not have been capable of reaching here without them. Thank you for everything. Ευχαριστω για ολα!

You left too early,

I know you are always around!

To my grandpa

Abstract

The objective of this work is the development of a numerical tool capable of modelling sensitive concrete or reinforced concrete infrastructures subjected to severe dynamic loadings due to natural or manmade hazards, such as aircraft impacts. This study proposes a 3D discrete element method able to predict advance damage states and to obtain realistic macro-cracks and materials fragments thanks to its discrete nature.

We thoroughly evaluated the influence of mesh creation parameters on the discretisation characteristics and on the macroscopic concrete behaviour. We implemented a compaction constitutive law to describe the behaviour of concrete correctly under high confinement. We improved the constitutive model for dynamic loading with the use of a more realistic modelling of the dynamic fracture energy.

The identification procedure of the constitutive model parameters is based on simulation of laboratory tests: quasi-static compression and tension, high confinement triaxial compression and dynamic spalling. Finally, the reliability of our approach is verified with three different types of hard impact tests on structures: 1) perforation and penetration of confined concrete cylindrical targets with ogive-nosed steel projectiles; 2) edge-on impact tests of concrete targets with aluminium projectiles of a particular geometry; 3) drop-weight impact on a reinforced concrete beam.

L'objectif de ce travail de recherche est le développement d'un outil numérique capable de simuler le comportement d'infrastructures sensibles en béton soumises à des charges dynamiques extrêmes d'origine naturelle ou anthropique tel que l'impact d'un avion sur une centrale nucléaire. Pour ce faire, il est proposé une modélisation 3D par éléments discrets, capable de décrire des états de dommages avancés en obtenant des macro-fissures et des fragments réalistes grâce à la nature discrète du modèle.

Dans un premier temps, nous avons étudié de manière exhaustive l'influence des paramètres de création du maillage sur les caractéristiques de la discrétisation et sur le comportement macroscopique du béton. Nous avons mis en œuvre une loi de comportement de compaction, pour décrire correctement le comportement du béton sous confinement élevé. Ensuite, nous avons amélioré le modèle de comportement dynamique en modélisant de façon plus réaliste l'énergie de rupture dynamique.

La procédure d'identification des paramètres du modèle est réalisée via des simulations numériques d'essais de laboratoire: Compression et traction quasi-statiques, essai de compression triaxiaux à fort confinement, écaillage dynamique. Enfin, l'approche est validée par la simulation de trois essais différents d'impact sur structures en béton : 1) Perforation et pénétration de cibles cylindriques confinées par des projectiles en acier de type ogive; 2) Essais d'impact sur la tranche avec des projectiles à géométrie particulière; 3) Impact par masse tombante sur une poutre de béton armé.

Résumé (Longue)

Aujourd'hui la conception des infrastructures sensibles en béton requiert la prise en compte d'évènements extrêmes tels que les attaques terroristes ou des accidents industriels. Les explosions ou les impacts induisent des charges extrêmes (taux de déformation et contraintes moyennes élevés) avec une faible probabilité d'occurrence mais avec des conséquences potentiellement dévastatrices. Par conséquent, la conception de structures en béton sous impact nécessite d'une part, d'être en mesure de bien comprendre les mécanismes d'endommagement du béton sous impact et, d'autre part, de développer des méthodes de calcul avancées capables de prédire les endommagements dans les ouvrages de protection en béton.

La plupart des modèles existants de comportement du béton considèrent le matériau soumis à des contraintes moyennes faibles à modérées et sous chargement quasi statique. Cependant, la modélisation des structures en béton soumises à des impacts nécessite de prendre en compte des taux de déformation allant de conditions quasi-statiques à des centaines de s^{-1} . Par conséquent, les essais dynamiques et la modélisation du comportement du béton sous chargement rapide constituent des défis majeurs. De plus, la modélisation des structures en béton soumis à des impacts durs nécessite de prendre en compte le comportement du matériau en compression triaxiale avec des contraintes de confinement de l'ordre de centaines de MPa.

Les méthodes existantes de conception des systèmes de protection en béton soumis à des impacts reposent principalement sur des expériences grandeur nature et des formules empiriques qui peuvent être non économiques. Généralement, ces méthodes ne tiennent pas compte du comportement non linéaire complexe du béton. La demande sociétale croissante de méthodes d'analyse prédictives motive le développement d'outils numériques avancés.

Trois phases peuvent être observées au sein des structures en béton soumises à des impacts durs, elles sont reliées à différents modes et phénomènes de dégradation. Toutes les phases peuvent apparaître simultanément, tandis que l'impacteur peut être considéré rigide, il ne subit aucun endommagement. La première phase est liée à l'écaillage et à la formation d'un cratère sur la face avant, dus aux fissures coniques liées à de la compression non confinée. Le cratère a une surface plus grande que la section transversale de l'impacteur. Au cours de la deuxième phase, le projectile pénètre dans le noyau de la cible en formant un trou cylindrique de diamètre très proche du diamètre du projectile. Cette phase est appelée phase tunnel, elle crée une zone de fort confinement

par l'inertie du matériau environnant. La troisième phase est liée à la fissuration sur la face arrière en béton qui produit une écaille due à l'état de traction sur la face libre. Cette zone est assez large mais pas aussi profonde que le cratère de la face avant. Enfin, l'augmentation de la vitesse d'impact du projectile entraîne une variation de la profondeur du tunnel et peut conduire à une perforation totale de la cible.

Différentes méthodes numériques ont été utilisées pour tenter d'apporter une réponse à ce type de problèmes: méthode des éléments finis (FEM), méthode des éléments finis étendus (XFEM), «Smooth particle hydrodynamics» (SPH) et méthode des éléments discrets (DEM). La FEM est fondée sur l'hypothèse d'un milieu continu, elle atteint donc ses limites pour la prédiction des endommagements sévères (fissuration, fragmentation, perforation,...) dus à des impacts. Néanmoins, il est nécessaire de choisir une méthode numérique capable de reproduire ces phénomènes d'endommagement. Par ailleurs, la XFEM n'est pas encore en mesure de modéliser de nombreuses discontinuités dus à des impacts à grande vitesse. La méthode des éléments discrets (DEM) est une alternative puissante à la FEM lorsque des états avancés d'endommagement et de rupture doivent être recherchés. En effet, la DEM permet d'obtenir facilement des faciès de macro-fissures et des fragments de matière réalistes du fait de sa nature discrète.

La DEM a été développé à l'origine par Cundall et Strack pour les matériaux granulaires. Notre approche DEM est une extension pour les matériaux cohésifs tels que le béton. Elle a été largement développée au laboratoire 3S-R (université de Grenoble Alpes) en collaboration avec le centre de recherche et développement d'Électricité de France (EDF R&D Paris-Saclay). Cette méthode a démontré sa capacité à modéliser des phénomènes complexes tels que la pénétration, l'écaillage et la cratérisation. Il convient de souligner que, dans notre approche, les éléments discrets ne représentent pas les constituants du béton (granulats). Le modèle proposé a pour objectif de reproduire un comportement isotrope et homogène à l'échelle macroscopique. Par conséquent, le comportement constitutif local (microscopique) des liens entre les éléments discrets repose sur un modèle phénoménologique, c'est-à-dire construit à partir d'observations à l'échelle macroscopique. L'échelle micro (des éléments discrets) n'a donc aucun sens physique, elle est définie pour des raisons de commodité de calcul.

Le modèle de comportement du béton dans le cadre de la DEM est pris en compte via des interactions de type ressort entre les éléments discrets au sein desquels la masse est concentrée. Les raideurs normale KN et tangentielle KS sont définies à l'échelle microscopique. Des relations micro-macro inspirées d'une formule d'homogénéisation permettent d'identifier les raideurs locales à partir des grandeurs macroscopiques que sont le module de Young E et le coefficient de Poisson ν . En

outre, une troisième interaction semblable à un ressort de roulement, avec K_R comme rigidité de roulement, contrôle la résistance au roulement du modèle et évite les ruptures fragiles. La loi normale force/déplacement du modèle est élastique avec endommagement. Un critère de Mohr-Coulomb modifié est utilisé pour décrire le comportement non linéaire en cisaillement. Le comportement non linéaire en compression est plastique avec écrouissage, il vise à modéliser le phénomène de compaction (fermeture de porosité). De plus, la dépendance à la vitesse de déformation est prise en compte en tension via la résistance dynamique du lien entre éléments discrets.

Après avoir calibré l'ensemble des paramètres du modèle de comportement d'un béton de référence ayant fait l'objet de nombreuses analyses expérimentales au laboratoire 3SR, des tests d'impact dur menés sur des cibles réalisées avec le béton de référence ont été simulés « en aveugle » afin de valider la fiabilité de l'approche proposée aux éléments discrets. Trois campagnes expérimentales différentes ont été utilisées. Tout d'abord, une série d'essais réalisés par le CEA-Gramat, avec des éprouvettes de béton cylindrique confinées, soumises à des impacts de projectiles rigides en forme d'ogive. Un test de perforation et deux tests de pénétration associés à trois vitesses d'impact différentes ont été simulés. Ensuite, deux tests d'impact sur la tranche conduits par Erzar à l'Université de Metz avec différentes tailles de projectiles et différentes vitesses d'impact ont été simulés pour évaluer la capacité du modèle à représenter les modes d'endommagement fragile. Enfin, la simulation d'un essai d'impact sur poutre en béton armé, réalisé à l'Université de Toronto, a permis d'analyser la capacité du modèle couplé FEM / DEM de Masurel pour la prise en compte des armatures en acier dans des éléments structuraux en béton.

Les résultats numériques des simulations d'impact sont en bon accord avec les résultats expérimentaux. Pour le test de perforation, les résultats sont parfaitement concordants. Cependant, une légère différence est observée sur les deux courbes déplacements en fonction du temps des tests de pénétration. Les endommagements des cibles en béton sont bien prédits par le modèle aux éléments discrets pour toutes les expériences. Les phénomènes observés expérimentalement, tels que la cratérisation sur la face avant avec éjection de fragments et la phase tunnel, ont été reproduits avec succès lors de toutes les simulations. De plus, une croûte avec fissure inclinée est prévue sur la face arrière de l'éprouvette de perforation. Des dommages dus à la formation de cratères ont été observés dans les simulations de pénétration, avec une profondeur de pénétration plus grande avec l'impact à grande vitesse qu'avec l'impact à faible vitesse. En outre, le mode de défaillance de cratérisation a également été reproduit avec succès dans les simulations d'impact de bord. Enfin, la simulation de chute de poids a permis de démontrer la capacité du modèle à éléments discrets à générer les macro-fissures obliques en bon accord avec l'expérience.

Tous ces résultats de simulation valident le modèle d'éléments discrets et démontrent que l'outil développé est maintenant capable de simuler des applications industrielles.

Table of contents

Abstract	3
Résumé.....	9
Résumé (Longue).....	11
Introduction.....	19
1 Literature Review	23
1.1 Concrete	24
1.1.1 Quasi-Static Compressive Strength	24
1.1.2 Quasi-Static Tensile Test.....	25
1.1.3 Triaxial tests.....	26
1.1.4 Dynamic compression	29
1.1.5 Dynamic tension	30
1.1.6 Strain Rate Dependency	31
1.2 Impacts on concrete.....	34
1.2.1 Reference impact tests.....	34
1.2.2 Classification of impacts	37
1.2.3 Impact effects on concrete.....	41
1.3 Simplified design methods	44
1.3.1 Soft impacts.....	44
1.3.2 Hard impacts	45
1.4 Numerical methods.....	48
1.4.1 Finite element method (FEM)	48
1.4.2 Extended finite element method (XFEM).....	51
1.4.3 Smoothed-Particle Hydrodynamics (SPH) method	51
1.4.4 Discrete Element Method	52

1.4.5	Lattice Discrete Particles Method (LDPM)	53
1.4.6	Finite-Discrete Element Method	54
1.5	Conclusion	55
2	The Discrete Element Method	57
2.1	Mesh generation method.....	58
2.2	Principles of the algorithm	60
2.2.1	Calculation loop.....	61
2.2.2	Calculation of the discrete element mass	62
2.2.3	Determination of the integration critical time step	62
2.3	Definition of interactions	63
2.3.1	Interaction range coefficient	63
2.3.2	Search of neighbours method	65
2.3.3	Calculation of interactions.....	66
2.4	Moment transfer law	69
2.4.1	Description of the moment transfer law.....	69
2.5	Constitutive behaviour of discrete element concrete model	72
2.5.1	Linear elastic behaviour.....	73
2.5.2	Non-linear elastic with damage behaviour	74
2.5.3	Compaction law.....	76
2.5.4	Mohr-coulomb modified criterion	78
2.5.5	Strain rate dependency	79
2.6	Steel-Concrete bond model	82
2.6.2	Significant sliding.....	84
2.6.3	Steel-concrete interaction zone	86
2.7	Conclusion	87
3	Identification procedure of the parameters for the discrete element mesh and the concrete constitutive model.....	89

3.1	Identification of the parameters for the mesh generation	90
3.1.1	Influence of boundary conditions	90
3.1.2	Mesh generation parameters.....	96
3.2	Identification of the parameters for the concrete constitutive model.....	108
3.2.1	Mesh for quasi-static uniaxial tests.....	108
3.2.2	Mesh for high-confinement tests.....	122
3.2.3	Mesh for dynamic spalling test	128
3.3	Conclusion	130
4	Numerical simulations of impact experiments	133
4.1	CEA impact experiments	133
4.1.1	Modelling of CEA impact experiments	137
4.1.2	Numerical results.....	141
4.2	Edge-on-impact test	152
4.2.1	Edge-on-impact modelling	153
4.2.2	Numerical results.....	156
4.3	Drop-weight impact on a reinforced concrete beam.....	160
4.3.1	Modelling.....	162
4.3.2	Calibration of parameters	164
4.3.3	Numerical results for SS0b test	165
	Conclusions and perspectives	169
	Conclusions.....	169
	Perspectives.....	171
	Bibliography.....	173

Introduction

Concrete is the most commonly used artificial material in the world (more than one cubic meter per inhabitant annually). Presently, sensitive infrastructures are necessarily protected by reinforced concrete (RC) shielding barriers due to the growing demand for security. Natural accidental conditions or manmade hazards such as earthquakes and missile impacts require designing under severe loadings. The mechanical response of RC structures under impact conditions is characterised by complex phenomenon amplified by concrete heterogeneity and able to produce intense fragmentation. Therefore, it is essential to comprehend the mechanisms of concrete behaviour under impact loadings and develop adequate designing methods.

Existing design methods for concrete protection structures under impacts are mainly based on full-size experiments and empirical formulae that are not economical. The use of experimentation on structures being very expensive and empirical formulae are insufficient including the complex non-linear behaviour of concrete. The existing demand for realistic predictions leads to the development of numerical tools. However, the relevance of numerical predictions is significantly dependent on the accuracy of the constitutive model employed to describe the behaviour of concrete.

Most of the constitutive models for concrete focus on the material behaviour under low and moderate mean stresses under quasi-static loading conditions. However, the modelling of concrete structures submitted to impacts requires accounting strain rates ranging from quasi-static conditions to hundreds of s^{-1} . Furthermore modelling structures under hard impacts requires accounting the material behaviour under triaxial compression with confinement stresses in the order of hundreds of MPa.

The objective of this project is to develop a numerical model able to predict the response of reinforced concrete structures subjected to severe impacts and to describe associated damages. Finite element approaches are widely spread for non-linear analysis, though they reach their limits when trying to describe precisely macro-cracking which is essential for modelling impact problems. On the contrary, discrete element methods are suitable to simulate advance damage states due to their capability to handle discontinues functions.

The current study is a collaboration between the laboratory 3S-R (University of Grenoble Alpes) and the research centre of EDF R&D (Paris-Saclay). This PhD thesis is subsequent of previous studies that chose to develop the discrete element approach in EUROPLEXUS fast dynamics software. The

discrete element was selected due to its ability to model strong discontinuities. Although, this approach initialised by Hentz in 2003 in SDEC software, with the introduction of the cohesive interactions as an extension of the original method of Cundall and Strack. After, Frangin in 2006 developed FE/DE coupling for 3D elements. Then, Rousseau in 2009 set up the framework of a coupling FE/DE method with shell FE able to simulate industrial-scale structures, in EUROPLEXUS. After, Masurel in 2015 developed a steel-concrete bond with a combined finite/discrete element approach. Additionally, Omar in 2015 implemented the constitutive model of concrete with strain rate dependency under dynamic loadings. The purpose of the present PhD study is to assimilate the previous developments and introduce some new features in EUROPLEXUS, for a reliable prediction of damage on impacted reinforced concrete structures. The primary target is the implementation of the compaction constitutive law, to adequately describe the behaviour of concrete under high confinement.

Moreover, we modified the constitutive model for dynamic loading. The proposed modification offers a more realistic modelling of the dynamic fracture energy by controlling the increase of the maximum distance limit at the interaction scale. We thoroughly studied the influence of both mesh creation and constitutive model parameters on the macroscopic behaviour of concrete. Additionally, the main objective of the current PhD study is the simulation of hard impacts, where we modelled concrete using discrete elements and projectiles or other steel parts with finite elements. Hence, we defined a condition for the size discretisation of finite and discrete elements in contact to properly manage the force transfer from the one object to the other.

This dissertation contains seven parts: introduction, four main chapters, a conclusion with perspectives and bibliography.

The first chapter is the literature review with a brief overview of the main characteristics of concrete and its mechanical properties. It introduces the problem of impact loading by explaining its effects and damage modes of reinforced concrete structure, referring to experimental campaigns. The last section is devoted to design and numerical methods commonly used to analyse severe loadings and fracturing problems.

Chapter two is dedicated to the description of the main concepts of the discrete element method. Main principles of the algorithm, calculation of forces, definition of interactions and the constitutive law for concrete are presented. It is worth to highlight that the discrete elements of this approach do not represent the constituents of concrete, but to reproduce an isotropic and homogeneous behaviour at the macroscopic scale. Consequently, the use of macroscopic phenomenological constitutive laws relies on the local microscopic behaviour of the discrete elements.

Chapter three is dedicated to the identification procedure of the discrete element method for concrete. It presents the influences of the mesh creation parameters on the mesh characteristics and the macroscopic behaviour of concrete. The second part shows the calibration of the constitutive model thanks to laboratory experiments. Furthermore, it introduces the need to create a condition for the ratio between the size of finite and discrete element sizes in contact.

The fourth chapter presents the application of the mixed finite/discrete element method, to model three series of hard impact tests. Comparison between experimental data and numerical results is given to show the capability of our model to predict the effects and damage modes of impacted concrete. First, we comment simulations of perforation and penetration test on confined concrete specimens impacted by ogive-nosed steel projectiles by CEA-Gramat. These simulations verify the ability of our model to produce the effects of hard impacts into concrete. The second set of simulations is the edge-on impact tests performed by Erzar on concrete tiles with projectiles of particular homothetic geometry to visualise the evolution of damages in a two-dimensional configuration. Finally, the simulation of the drop-weight impact on a reinforced concrete beam from the University of Toronto is discussed for the validation of the steel-concrete bond to model the response of reinforced concrete.

The dissertation ends with the section of conclusions and perspectives.

Chapter 1

Literature Review

This chapter presents a brief literature review on the behaviour of concrete and its main characteristics. The problem of impulsive loading is introduced by explaining its effects and damage modes on reinforced concrete structures, concerning experimental campaigns. Then, simplified design and numerical methods commonly used to analyse severe loadings and fracturing problems are discussed.

Most of the constitutive models for concrete focus on the material behaviour under low and moderate confining pressures and are limited under static loading conditions. However, the modelling of concrete structures submitted to impacts requires accounting strain rate effects on a broad range. Figure 1.1 shows the strain rates involved in concrete material when subjected to various quasi-static and dynamic loads. Consequently, the dynamic testing and modelling of material constitute a significant issue in material science and civil engineering.

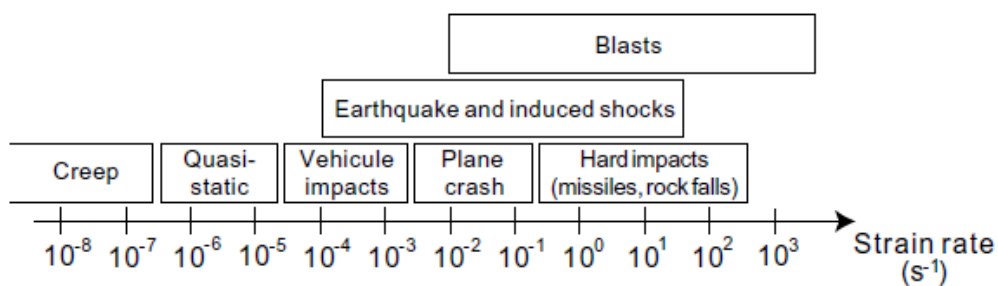


Figure 1.1: Strain rates involved in concrete structures submitted to various loads (Bischoff and Perry [9]).

Furthermore modelling structures under hard impacts requires accounting both strain rates ranging from quasi-static conditions to values up to hundreds of s⁻¹ and triaxial compression stresses with confinement stresses in the order of hundreds of MPa.

1.1 Concrete

Concrete is an artificial sedimentary rock composed mainly of water, aggregates and cement. Often additives and reinforcement are included in the mixture to improve its properties. Concrete is the most widely used construction, structural material in the world. The United States Geological Survey estimated in 2006 that about 7.5 billion cubic meters of concrete are made each year, which is more than one cubic meter for every person on Earth [94]. The predominance of this material is due to its workability. Once, its ingredients are mixed a fluid mass is created that is easily moulded into any form. Another important feature is the durability of this composite material after hardening and the cost of its components.

Therefore its composition can be varied dramatically from one concrete to another: type of aggregates and cement, type of reinforcement, but also regarding the quantity of these materials. The microstructure of concrete is described as heterogeneous porous material due to the complex arrangement of several constituents. However, on a sufficiently large scale (greater than about ten times the size of the largest aggregate), concrete can be considered homogeneous and continuous (Mazars [92]). Its mechanical properties have been studied several years ago through experiments. It can be regarded as a quasi-brittle material with high compressive strength but always lower tensile strength. For this reason, it is usually reinforced with steel rebars; thus it can also withstand a good amount of tensile stress.

In addition, severe loadings such as impacts generate complex multi-phase phenomena resulting by high strain rates and extreme triaxial stress states. Concrete is a highly sensitive strain-rates material; hence strain rate dependency is of great importance for the modelling of concrete under dynamic loadings. Besides, it is essential to analyse the behaviour of concrete under triaxial stress and high confining pressures. Although this study focuses on the dynamic response of the concrete, it is necessary to identify its behaviour under quasi-static compression and tension, to be able to build constitutive models and simulate complex phenomena.

1.1.1 Quasi-Static Compressive Strength

The main property of concrete is to absorb compressive loads, which corresponds to the unconfined axial compressive strength. The compressive strength of concrete is measured directly through quasi-static direct compression test. This test performs on cylindrical specimens aged at least 28 days, with a specific saturation level. These samples typically have a ratio between height and diameter equals two.

The specimen is placed between the rigid steel plates of a compression machine, then a loading of standard speed is applied. After the failure of the sample, the compressive strength is defined from the stress-strain curve.

Then ultimate strength is determined by the individual strength of the cement paste, of the aggregates and their interaction. The strength of the cement paste depends on the type of cement and the cement water ratio. Important to point out is that the interface zone between the cement paste and the aggregates induce cracking since cracks exist in this zone even before the application of any load.

Figure 1.2 gives the stress-strain curve of concrete under direct quasi-static compression is given Figure 1.2. One can see at point 1 that cracks are already present in the interface zone, before the application of loading. At point 2 the load increases up to nearly 30–40 % of the compressive strength. These cracks are quite constant; thus the material behaves linearly. After the stress-strain curve becomes non-linear and cracks are initialised in the loading direction. These cracks propagate into the cement matrix while the curve reaches the point 3. Then, the non-linear response becomes more prominent. Finally, concrete failure occurs at point 4 where macroscopic cracks procedure and it is followed by a strain softening behaviour.

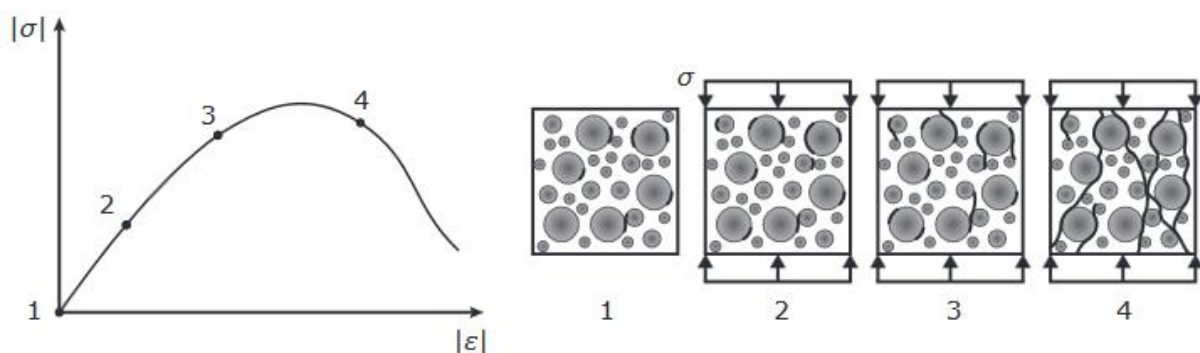


Figure 1.2: Failure mechanism of concrete under quasi-static compression (Mang et al. [90])

1.1.2 Quasi-Static Tensile Test

The tensile strength of concrete is usually only 10 per cent of its compressive strength. Figure 1.3 illustrates the stress-strain curve of concrete under direct quasi-static tension. The response is linear until almost 75 per cent of the tensile strength (point 2). At this phase, the initial microcracks remain stable. Thereafter, new microcracks appear reducing the macroscopic stiffness and the stress-strain curve becomes non-linear. These cracks propagate throughout the specimen and a softening branch follows after the peak stress is reached (point 3). Some of the cracks create a localised deformed zone which forms a macrocrack that eventually splits the sample into two parts (point 4).

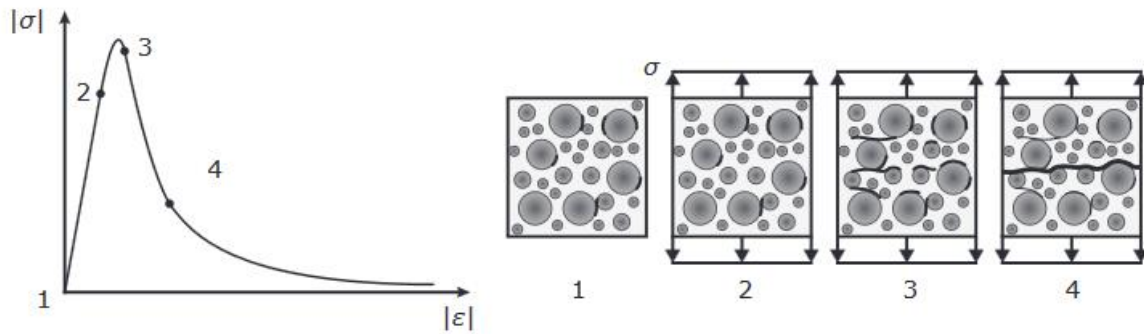


Figure 1.3: Failure mechanism of concrete under quasi-static tension (Mang et al. [90])

The measurement of the tensile strength through the direct tensile test is complicated because it requires the use of particular shapes of specimens, to avoid inaccurate secondary effects. The quasi-static characterisation of concrete in tension is usually done by indirect splitting tensile test (Brazilian test). A cylindrical concrete specimen is subjected to uniformly distributed compressive forces at two opposing sides on its lateral surface Figure 1.4 (a). These compressive forces develop evenly distributed tensile stresses at the perpendicular axes of the specimen.

Another indirect method is the bending test with prismatic specimens. These specimens are supported like a simple beam with a specific load on the middle of the top surface Figure 1.4 (b). The maximum tensile stress develops only in a thin surface layer on the opposite side of the loading the edge.

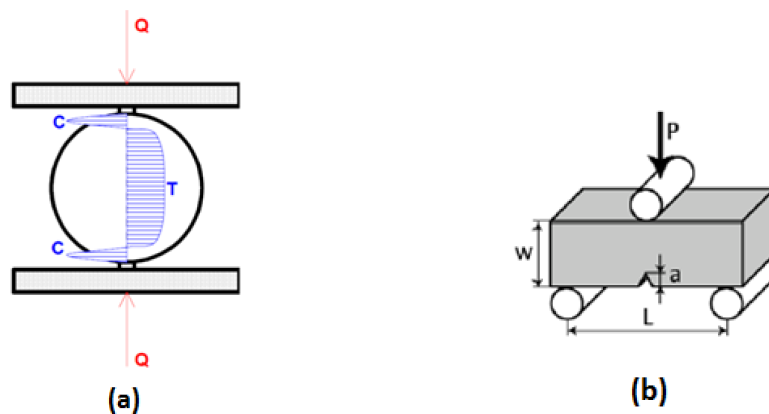


Figure 1.4: (a) Brazilian test and (b) bending test

1.1.3 Triaxial tests

Impact loadings create high stresses leading to different damage modes, strongly dependent on the loading path and stress state; inducing compaction with irreversible strain due to the structure inertial confining pressure. Two phenomena appear simultaneous during compaction: (1) the

cohesive bond of concrete disappears and powder takes its place, (2) the structure of the material is damaged with the closure of the porosity (Gabet et al. [52]). Triaxial tests are used to study the behaviour of concrete subjected to confining pressure. Many authors (Schmidt et al. [117], Sfer et al. [119] and Warren et al. [141]) observed higher concrete resistance and transition from brittle to ductile behaviour with confinement. Under very high confinement the response becomes elasto-plastic with hardening because of the closure of porosity.

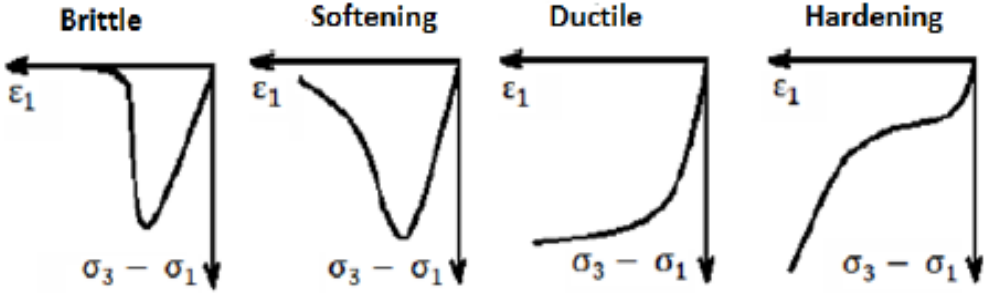


Figure 1.5: Transition of concrete behaviour from brittle to ductile (Omar [103])

Triaxial tests are conducted in two steps: initially, isotropic pressure is applied in all directions with a fluid and then deviatoric stress is added vertical by a piston with a constant velocity. Deviatoric stress is defined as the difference between the axial stress and the radial pressure. Several combinations of loadings exist for the triaxial test as shown in Figure 1.6.

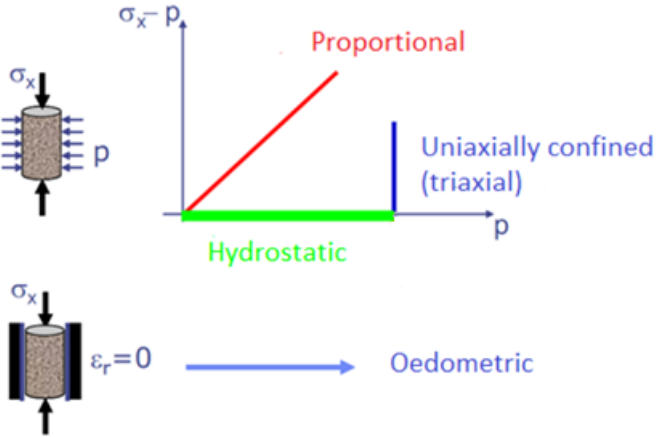


Figure 1.6: Different loading paths (Gabet et al. [52])

- The hydrostatic test consists the application of an isotropic pressure around the entire specimen that increases linearly with time.
- The oedometric test restricts of all the radial deformations and the specimen is axially compressed
- The triaxial test is separated in two phases; first hydrostatic pressure is applied around the whole specimen until a specific value chosen by the user. Then this pressure is kept constant radially while the axial loading is increasing with stable velocity.
- Proportional test imposes the specimen to axial loading while keeping the lateral pressure proportional to the axial stress.

Triaxial tests with very high confinement in the order of Giga Pascal were performed, by Gabet [51] thanks to the GIGA press of the laboratory 3S-R (University of Grenoble Alpes) to study the mechanical behaviour of concrete subjected to severe loadings such as explosions. Gabet obtained results from triaxial test with different confining pressures. Figure 1.7 illustrates his experimental data for with confining pressures 50, 100, 200, 500 and 650 MPa, where every curve is noted by an acronym TRX which stands for triaxial test and a number which specifies the conducted confining pressure.

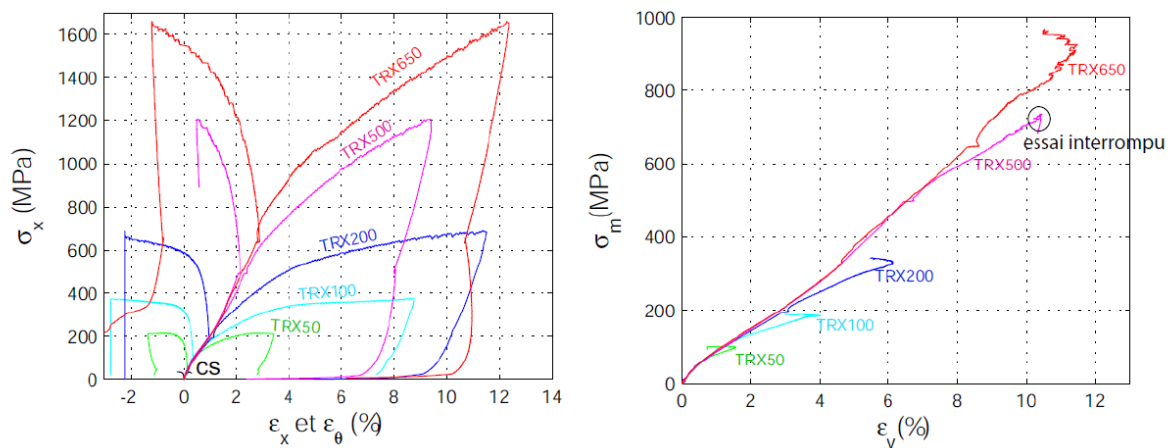


Figure 1.7: Triaxial tests: stress-strain curve (left), volumetric behaviour (right) (Gabet [51])

Furthermore, Vu [136] used also the GIGA press of the 3S-R to study the influence of the saturation level on the triaxial behaviour of concrete (Figure 1.8).

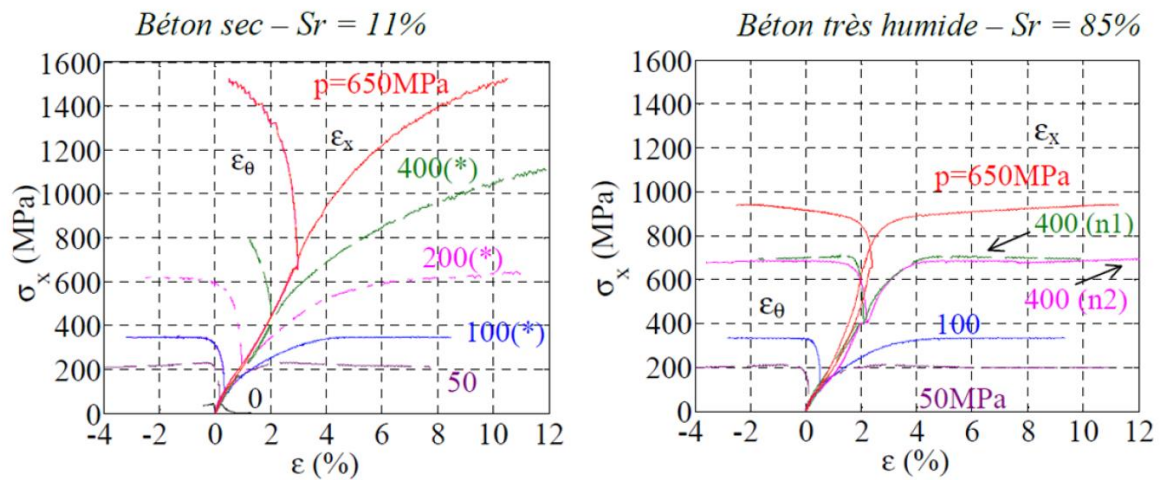


Figure 1.8: Triaxial tests with different saturation level: dry concrete $S_r = 11\%$ (left), very saturated $S_r = 85\%$ (right)

The presented results of Gabet [51] and Vu [136] performed on an ordinary reference concrete with compressive strength ($f_c = 34\text{MPa}$). These experimental data will consider as a reference concrete to identify the material parameters for our discrete element model.

1.1.4 Dynamic compression

Bischoff and Perry [9] in 1991 collected information about different experimental devices available in the literature to explore a wide range of strain rates of concrete in compression. Direct compression tests with the help of hydraulic machines were used for static loading 10^{-5} s^{-1} up to strain rates of 10^{-1} s^{-1} [14]. Takeda [132] employed a pneumatic-hydraulic system to reach higher strain rates up to 1^{-1} s^{-1} . However, these techniques experience difficulties to obtain constant strain rates due to the short duration of the experiments. Thus, the strain rate comes to be dependent on the stiffness of the machine and the stiffness of the specimen. Charpy or V-notch bar test was used to achieve strain rates 1 s^{-1} [55].

Higher strain rates in the order of 10 s^{-1} may be induced with a drop weight impact test [142]. Kolsky bar or Split Hopkinson Pressure Bar (SHPB) [80] allows reaching strain rates up to 10^2 s^{-1} . SHPB is a modification of the Hopkinson bar setup [65] with the addition of another bar in contact with the rear face of the specimen Figure 1.9. It consists of a projectile, an incident bar and a transition bar with the specimen being sandwiched between the two bars. An incident compressive pulse is generated and propagates along the incident bar until it reaches the sample. Then, a part of the initial pulse is reflected back into the incident bar and the remaining is transmitted throughout the specimen into the transmission bar. Particle velocities and forces at the front and rear face of the

sample are measured through strain-gauges, glued on the bars. Even higher strain rates ($>10^3 \text{ s}^{-1}$) may be reached with the use of explosive charges.

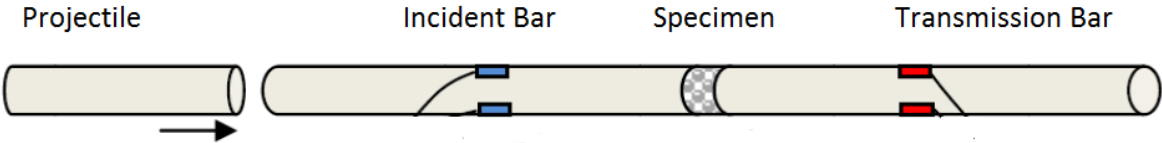


Figure 1.9: Split Hopkinson Pressure Bar experimental setup (Erzar [40])

The relative increase in compressive strength (Figure 1.10) starts at unity for static testing and reaches a value of about 1.7 for low-grade concrete, and about 1.3 for high-grade concrete when loaded more rapidly at $\dot{\sigma}=1 \text{ MPa/s}$. Beyond this stress rate, the increase is much higher, reaching values of 4 and higher.

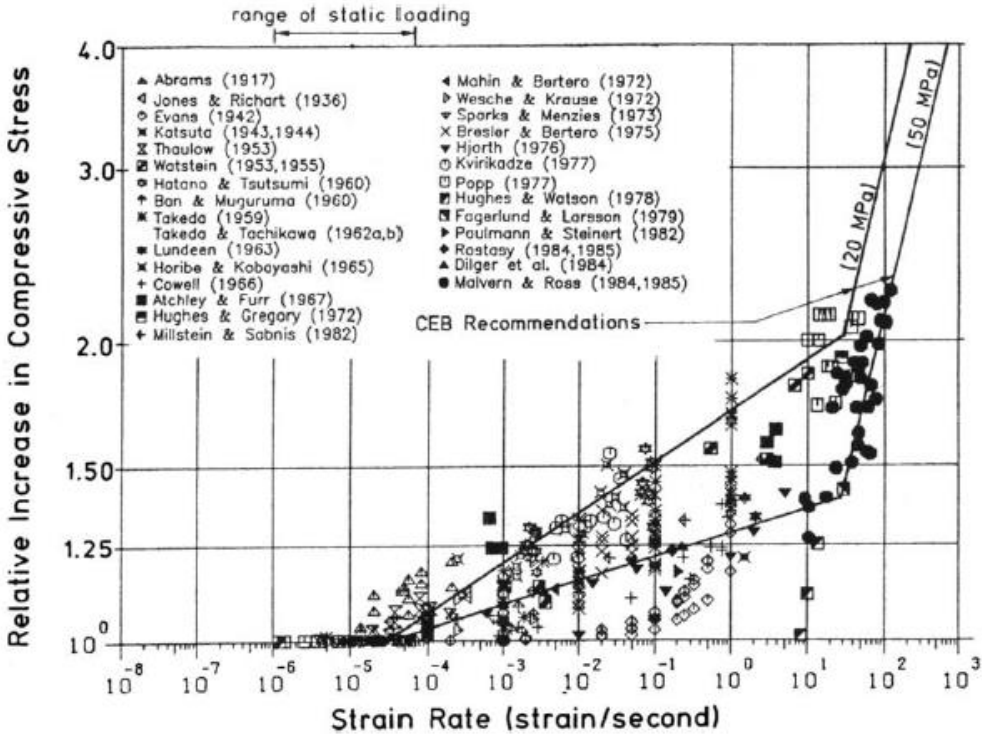


Figure 1.10: Strain rate dependency of the compressive strength (Bischoff and Perry [9])

1.1.5 Dynamic tension

Toutlemonde [134] conducted direct tensile tests with a hydraulic device to study the tensile strength of concrete for static loading 10^{-6} s^{-1} up to strain rates of 1 s^{-1} . Zielinski [148] used the

principle of Split Hopkinson Pressure Bar [80] for strain rates up to 1.5 s^{-1} . Higher strain rates were reached with another experimental device by using the spalling technique. Brara and Klepaczko [13] performed spalling tests using a Hopkinson bar made of aluminium alloy.

Hopkinson pressure bar was introduced by Hopkinson [65] in 1914 which measured stress pulse propagation in an elastic metal bar. He estimated the duration and amplitude of a pressure pulse generated by an impact at the end of a cylindrical steel bar [65]. Spalling is defined as the material failure in tension due to partial reflection of pressure wave at the material transition to a material with lower acoustic impedance. Commonly, spalling is related to the fracture in a plate of the material which occurs near the free surface remote from the impulsive loaded area [143].

Therefore, the principle of this technique is the generation of a dynamic tensile loading pulse due to the reflection of a short compressive pulse on the free surface of the tested concrete sample. This technique allows reaching high strain-rates in order of 20 to 200 s^{-1} and short damage duration about 10 microseconds.

During a spalling Hopkinson bar test, a projectile impacts on the surface of the Hopkinson bar, with a concrete specimen glued at the rear surface of the bar Figure 1.12. After, the impact generates a compressive wave inside the bar. The compressive pulse propagates along the bar until it reaches the bar specimen interface. Then a part of the incident pulse is transmitted on the specimen and the other part is reflected back on the Hopkinson bar. The transmitted compressive pulse is travelling inside the concrete specimen until the free end. At the free end of the sample is reflected back as a tensile wave. When the reflected tensile pulse exceeds the transmitted compressive pulse, the specimen is leading to a possible damage that may results fragmentation.

Figure 1.11 shows a strain-rate sensitivity which observed experimentally by different authors. Malvar and Crawford [89] collected the numerical data.

1.1.6 Strain Rate Dependency

Concrete's behaviour under dynamic loading is of great importance to this study. Experimentally has been observed that both the tensile [89] and compressive [9] strengths of concrete increase with strain-rate, especially when the strain-rate is greater than a transition strain-rate, which is around 10^0 - 10^1 s^{-1} for uniaxial tension and 10^2 s^{-1} for uniaxial compression. The strain rate dependency in both tension and compression for moderate rates and influenced by the moisture content. At high strain rates, this dependency becomes very important in tension whereas it remains negligible in compression.

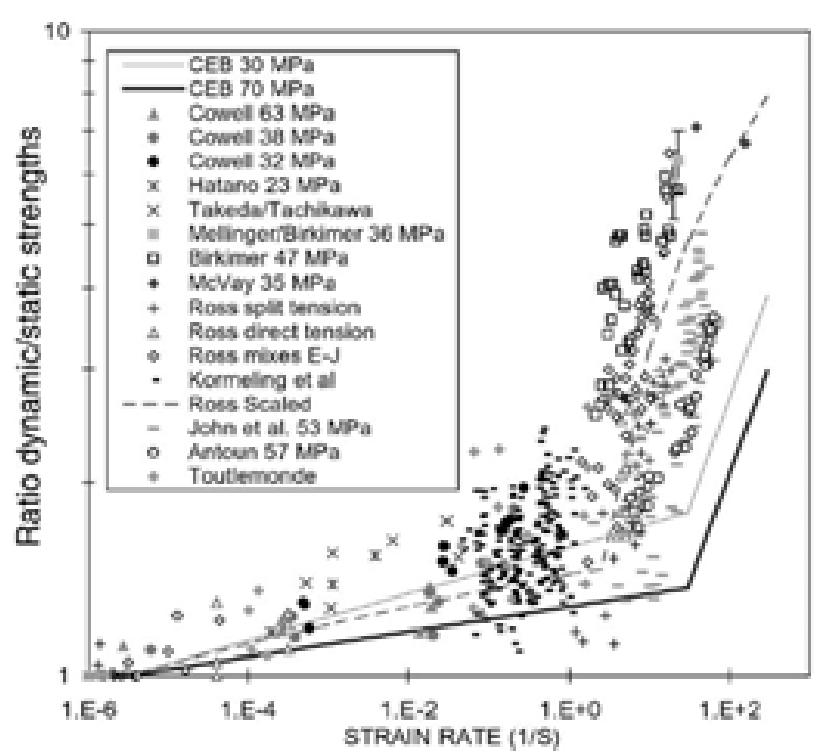


Figure 1.11: Strain rate dependency of the tensile strength (Malvar and Crawford [89])

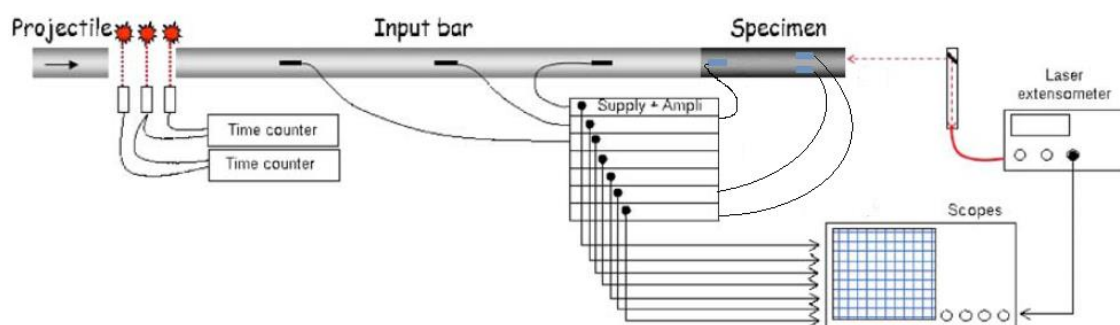


Figure 1.12: Spalling Hopkinson bar experimental setup (Forquin et al. [47])

However, it has been found that the strain-rate enhancement of the compressive strength of concrete-like materials [9] is caused mainly by the introduction of radial confinement in split Hopkinson pressure bar (SHPB) tests [81],[82],[146],[147] which cannot be interpreted merely as material behaviour. Brace and Jones [12] first explained that the compressive strength increase can be due to the change of stress state from uniaxial stress to uniaxial strain under increasing radial confinement.

Furthermore, in a very interesting paper by G. Cusatis [32], the author demonstrates that for strain rates higher than 10^{-1} s^{-1} the inertia forces cannot be neglected and provide a significant contribution to the strength enhancement recorded during experiments. He also shows that taking into account inertia forces thanks to a 3D transient dynamics model allows describing most of the strain rate effect observed in uniaxial compression, whereas it is necessary to include a strain-rate dependency in the micro-level model to describe correctly the observed strain rate effect in uniaxial tension.

For this reason, the spalling experiments focused on the rate effect in tension. Recently, the spalling technique by mean of Hopkinson bar has been used from many researchers to study the behaviour of concrete in tension at very high strain rates (up to 120 s^{-1}) [13],[120]. The strain rate dependency of the tensile strength is reported as a dynamic increase factor (DIF: the ratio of dynamic strength to quasi-static strength) by the European Committee for Concrete (CEB) [20]. The concrete rate dependency is bilinear and it can be divided into two regimes. The first regime corresponds to moderate rate effects and the second regime which appears beyond $\dot{\epsilon} \approx 10^0 \text{ s}^{-1}$ with extensive rate effects. At the second regime, the rate effects are more evident than the first.

The physical interpretation of the rate dependency for concrete in tension is attributed in several parameters. To begin with, rate dependency occurs at low loading rates because of the heterogeneity of the material. After, in each regime dominates a different parameter.

On the one hand, the moisture content of the specimens influences the moderate strain rate regime. It is assumed that the free water present inside the nanopores of the material exhibit a phenomenon similar to the Stefan effect [41]. Stefan effect is the phenomenon that occurs when a viscous liquid is trapped between two plates that are separated rapidly, causing a force on the plates that is proportional to the velocity of separation.

On the other hand, the micro-inertia effects in the fracture zone are responsible for the extensive strain rate regime. According to Zielinski [148], the increase in strength at high loading rates induces due to short time to explore the weakest links in the material and the cracks are forced to develop along a shorter path of higher resistance, which results in a higher strength.

Fracture energy is another significant property of concrete; Zhang et al. [146] reported its sensitivity to loading rate by conducting three-point bending tests on notched beams over a wide loading range from 10^{-4} to 10^3 mm/s . They showed that under low strain rates there is a slight effect whereas under high rates the increase of fracture energy is even more pronounced than the peak load. Brara and Klepaczko [13] demonstrated also a strong dependency of fracture energy on loading rates beyond 1000 GPa/s . Weerheijm et al. [142] obtained a slight influence of loading rates under 1000 GPa/s on

fracture energy and a rate-dependent softening curve which becomes more brittle with the rate increase.

1.2 Impacts on concrete

Impacts are defined as extreme severity loadings with a low probability of occurrence, and very short duration. Natural hazards: avalanches, rock falls or manmade hazards vehicles in a collision with structures, aircraft impacts on nuclear shielding barriers and military missile impacts may induce devastating consequences. Therefore, it is necessary to thoroughly comprehend the mechanisms of concrete behaviour under impact to develop sufficient design methods.

The study of impacts on structures started from the mid-17th century. For the purpose of safety regulations, national nuclear safety agencies and nuclear energy companies conducted several experimental campaigns to increase the knowledge about the local phenomena and damage modes of concrete structures subjected to impacts considering real-scale experiments and small-scale laboratory tests. Kœchlin and Potapov [78] separated these tests into two limited cases based on the velocity of the impactor and the strength of both impactor and structure.

1.2.1 Reference impact tests

The French Alternative Energies and Atomic Energy Commission (CEA) and the Electricity of France (EDF) performed a series of test (Figure 1.13) presented by Sokolovsky et al. [126], Fiquet et al. [45], Gueraud et al. [54]. They studied the perforation of reinforced concrete slabs by rigid missiles. Parameters such as the form and the diameter of the missile nose, the weight of the missile, the reinforcement and the thickness of the slab were varied to predict the ballistic limit (the velocity limit required for the missile to penetrate the target) of reinforced concrete slabs.

EDF launched a research program on the non-linear behaviour of reinforced concrete slabs subjected to soft impact tests that are described by Dulac et al. [37]. They tried to gather some guidelines for plastic design by observing the overall response of the slabs.

The German army research centre (Wehrtechnische Dienststelle für Waffen und Munition) conducted at Meppen site, a collection of 21 reinforced concrete slabs impact of soft/deformable projectiles. It was reported that the main failure mode of the impacted slabs was a shear failure (Figure 1.14). Their aim was the improvement/validation of existing methods for the treatment of aircraft impact loads on concrete slabs by observing their ultimate bearing capacity. Several authors used these tests to validate numerical methods on the prediction of damage in reinforced concrete

slabs under soft impacts. These studies are detailed in in Jonas et al. [72], [74], Nachtsheim and Stangenberg [97], [98], Rüdiger and Riech [113].

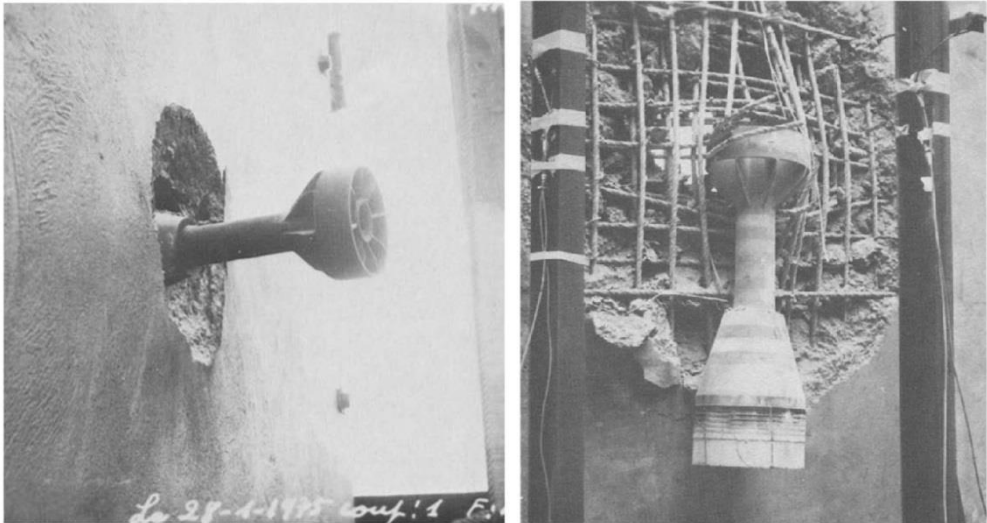


Figure 1.13: EDF – CEA perforation test, Front face shot 1 (left), Backface shot 6 (right) (Fiquet et al. [45])

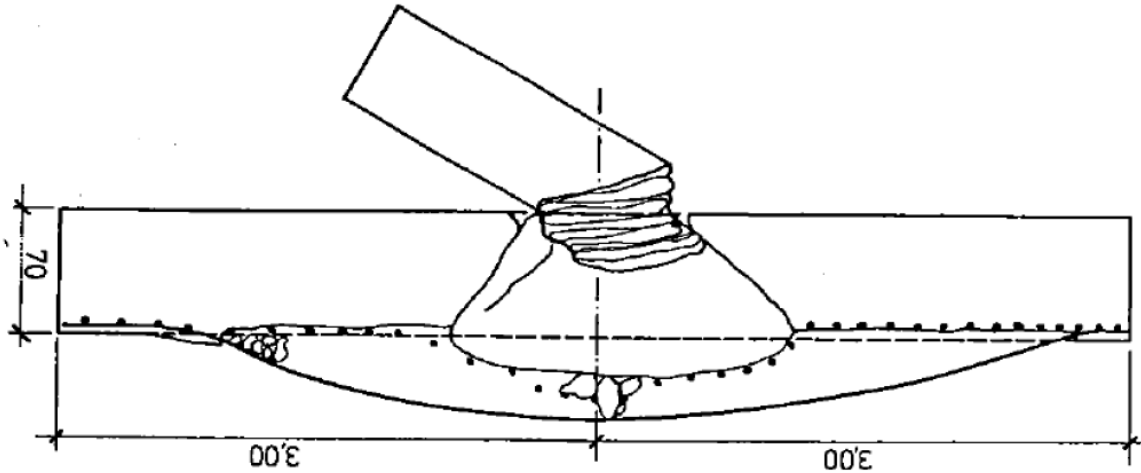


Figure 1.14: Meppen test, damage mode of a reinforced concrete slab subjected to soft impact by a deformable projectile (Jonas et al. 178[74])

Kojima [79] describes a series of 12 missile impact tests on reinforced concrete slabs varying the velocity, the hardness (soft-nosed/deformable) and (hard-nosed/non-deformable) of the striker and the thickness of the target with the presence or absence of rear face reinforcement and a single/double layer of reinforcement. The author investigated the local effects on the impacted slabs

concluding that the degree of damage from a hard-nosed missile is more significant than from a soft-nosed missile. The degree of damage is higher with the increase of the missile velocity and the decrease of the slab thickness. Steel lining, the rear face of the reinforced concrete slab effectively prevents perforation or scabbing.



Figure 1.15: Kojima test missiles with different hardness (Kojima [79])

Ohno et al. [101] selected five different types of projectiles with different nose (flat, hemispherical, conical) and different material (steel, stainless, aluminium and vinyl chloride) with varying magnitudes of axial strength. He evaluated the transition between soft and hard impacts on reinforced concrete slabs. The velocity of the projectiles kept the same for all the tests, but the target thickness was varied. The authors observed that the axial deformation increases as the axial strength of projectile decreases. The perforation thickness is constant regardless of the difference of the nose shape.

Sugano et al. [129]-[131] executed different campaigns of tests in collaboration with the Sandia National Laboratories. Three scales of experiments were performed: 1) small scale with 48 deformable and 25 rigid missiles of different sizes; 2) intermediate scale with 1 deformable missile and 4 impacts of aircraft engines; 3) a full-scale crash with an F4-Phantom military jet of 19 tons weight impacted a rigid RC wall at a velocity of 774 km/h (Figure 1.16). Sugano concluded that: 1) small-scale tests give similar results to intermediate scale test and that aircraft engines can be considered as deformable; 2) no effect on local damage by the reinforcement ratio; 3) existing

empirical formulas for predicting rigid missiles impact local damage are suitable; and 4) nonlinear response analysis can sufficiently predict the results of tests.



Figure 1.16: Full-scale aircraft impact test (Sugano et al. 182[129])

1.2.2 Classification of impacts

The classification of soft and hard impacts was introduced by Eibl [38] and it was adopted by the Euro-International Concrete Comity [18]. A simple system of two colliding bodies, m_1 the projectile with initial striking speed, m_2 the structure which is motionless before the impact, a contact spring with stiffness k_1 , in between the two masses to represent the force of the deforming bodies after contact, and another spring with a stiffness k_2 to simulate the resisting capacity of the structure is used to describe the impact. This model separates the two types of impacts by accounting only the deformability of the two bodies. Nonlinear force-deformation relationships define the two springs.

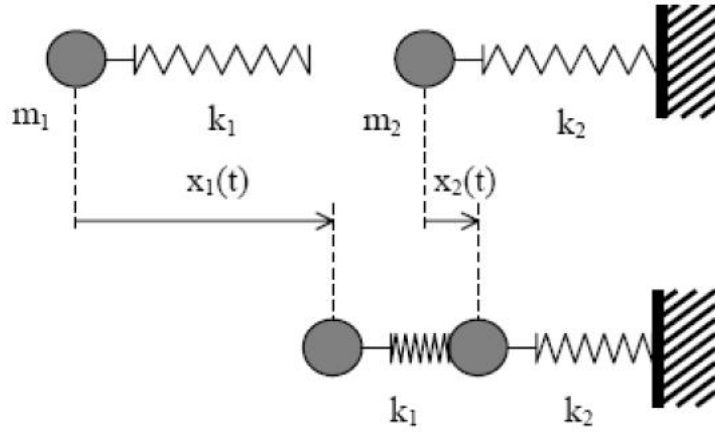


Figure 1.17: Simple model of an impact using a two-mass system (Daudeville and Malécot [33])

The following differential equations of motion describe the system:

$$m_1 \ddot{x}_1(t) + k_1[x_1(t) - x_2(t)] = 0 \quad (a) \tag{1.1}$$

$$m_2 \ddot{x}_2(t) - k_1[x_1(t) - x_2(t)] + k_2 x_2(t) = 0 \quad (b)$$

If the structure displacement is negligible compared to the projectile $x_1(t) \gg x_2(t)$ then:

$$F(t) = k_1 x_1(t) \tag{1.2}$$

Thus, the equations of motion (1.1) are uncoupled as showed by the equation (1.3). It is possible to find x_1 by solving equation (1.3). Then, the impact force $F(t)$ is computed from the equation (1.2) and finally, equation (1.3) gives the response of the structure from:

$$m_1 \ddot{x}_1(t) + k_1 x_1(t) = 0 \quad (a) \tag{1.3}$$

$$m_2 \ddot{x}_2(t) + k_2 x_2(t) = F(t) \quad (b)$$

A soft impact defines as the case where the target resists with no deformations; hence the kinetic energy of the projectile is wholly transferred to its deformation Figure 1.18.

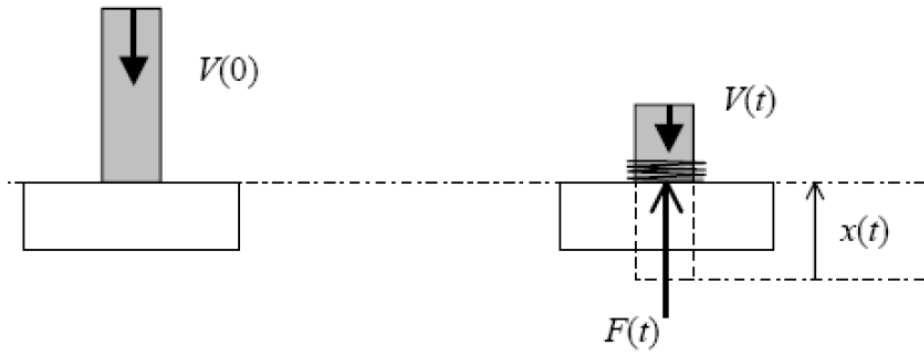


Figure 1.18: Soft impact (Daudeville and Malécot [33])

Conversely, when $x_1(t) \ll x_2(t)$ the two equations of motion cannot be uncoupled and the impact is called hard, whereas the kinetic energy of the rigid projectile is fully or partially absorbed by deformation of the target Figure 1.19.

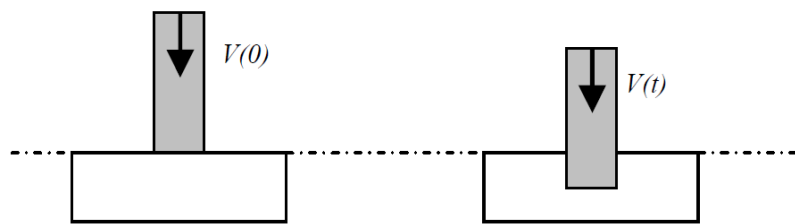


Figure 1.19: Hard impact (Daudeville and Malécot [33])

However, Kœchlin and Potapov [78] presented a more precise classification of impacts based not only on the deformability of the two colliding masses but considering also the velocity of the impactor and the material characteristics. They separate the two types of impacts based on the bearing capacity of the structure by comparing the strength threshold of the target σ_t with the stress applied by the projectile σ . Then, when the projectile is crashed and the target is not damaged is determined as a soft impact, whereas the penetration of the projectile in the target gives a hard impact.

Kœchlin, in his PhD dissertation [77] proposed a criterion (1.4) for impact classification based on Riera formula [109]. This criterion accounts for the structure and the projectile parameters where: σ_p is the limit strength of the projectile, ρ_p the density of the projectile, V_0 the velocity of the projectile and σ_c the compressive strength of the target considering confinement and strain rate effects.

$$\frac{\sigma_p}{\sigma_c} + \frac{\rho_p V_0^2}{\sigma_c} = 1 \quad (1.4)$$

Figure 1.20 plots this criterion by using the two non-dimensional parameters $\frac{\sigma_p}{\sigma_c}$ on the y-axis and $\frac{\rho_p V_0^2}{\sigma_c}$ on the x-axis. As can be seen in Figure 1.20, when the projectile is rigid $\sigma_p \gg \sigma_c$ or/and very fast $\rho_p V_0^2 \gg \sigma_c$ then the equation (1.4) becomes bigger than 1 and hard impact occurs. Otherwise, the equation remains lower than 1 and the projectile deforms a lot by inducing a soft impact.

This classification is applied for aircraft crash analysis, which is usually considered as a soft impact (Sugano et al. [129]). Although, aircraft engine crash is treated using perforation and scabbing formulas for hard impacts (Figure 1.21).

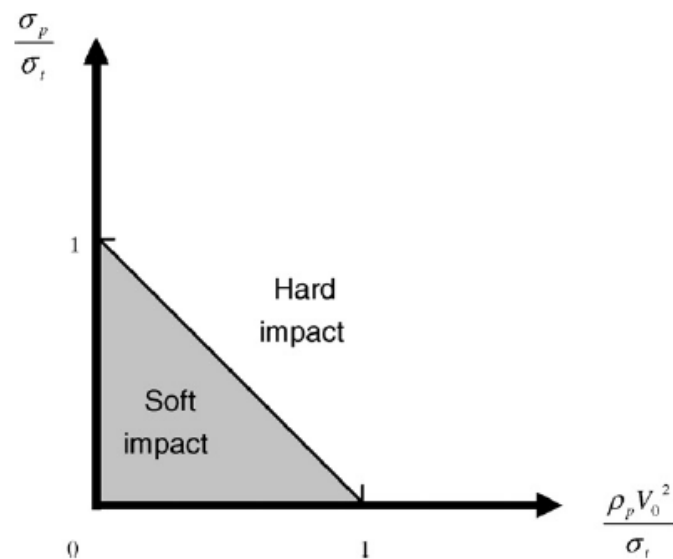


Figure 1.20: Impact classification (Kœchlin and Potapov [78])

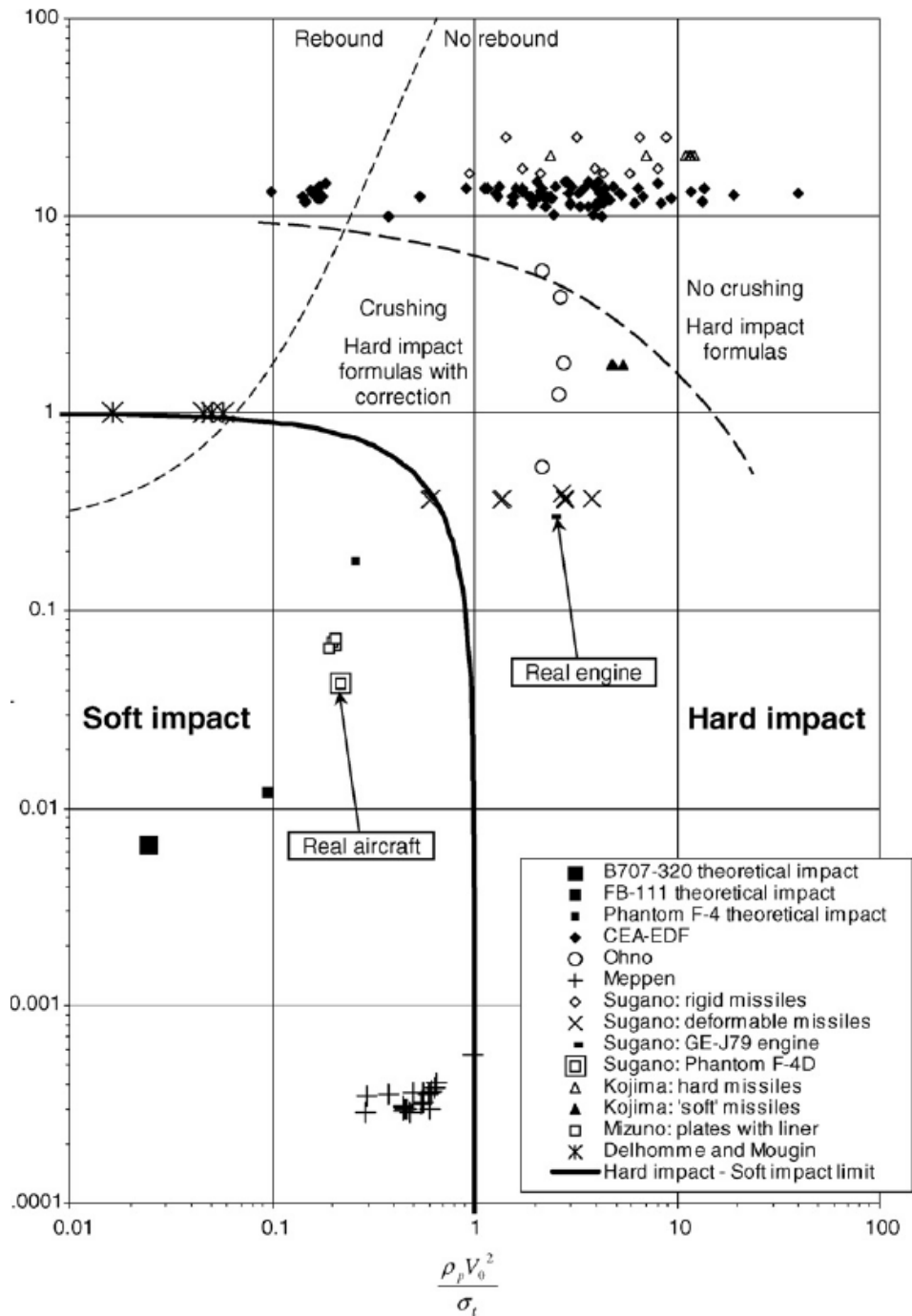


Figure 1.21: Classification of impacts experiments (Kœchlin and Potapov [78])

1.2.3 Impact effects on concrete

Three phases can be observed on concrete structures under hard impacts which are related to different damage modes and phenomena. All the phases may appear together (Zienkiewicz et al. [149]), while the striker is rigid with no damages. Kennedy [76] introduced the terminology of these

phenomena in 1976. He defined seven phenomena during a hard impact as can be seen in Figure 1.22 and are listed below:

- a. Penetration: Tunnelling into the target by the projectile (the length of the tunnel is called the penetration depth).
- b. Cone cracking and plugging: Formation of a cone-like crack under the projectile and the possible subsequent punching-shear plug.
- c. Spalling: Ejection of target material from the proximal face of the target
- d. Radial cracking: Global cracks radiating from the impact point and appearing on either the proximal or distal face of the concrete slab
- e. Scabbing: Ejection of fragments from the distal face of the target
- f. Perforation: Complete passage of the projectile through the target
- g. Overall structural responses and failures: Global bending, shear and membrane responses as well as their induced failures throughout the target.

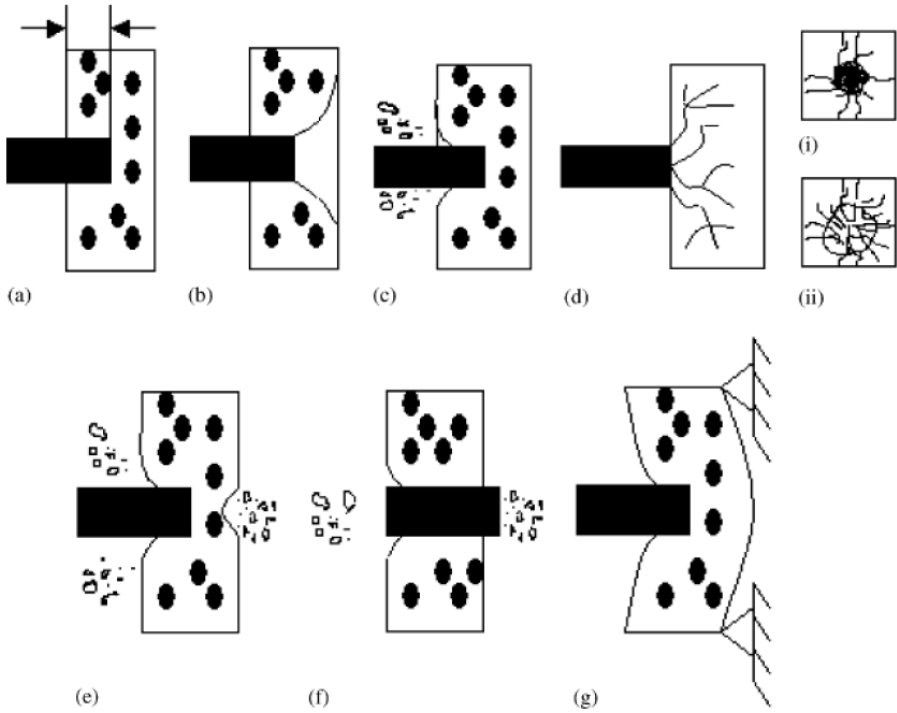


Figure 1.22: Hard impact effects on concrete target (a) Penetration, (b) Cone cracking, (c) Spalling, (d) Cracks on (i) proximal face and (ii) distal face, (e) Perforation and (g) overall target response (Li et al. [83]).

The first phase is related to spalling and cratering on the front face formed by conical cracks due to unconfined compression as explained by Forquin et al. [47]. The crater appears with a noticeable

bigger area than the cross-section of the striking body. During the second phase, the projectile penetrates in the core of the target forming a cylindrical hole with diameter very close to the projectile diameter. This phase is called tunnelling; it creates a zone of high confine pressure by the inertia of the surrounding material. The third phase initialises cracking on the concrete rear face that produces scabbing and it is related to tensile loading [83]. This zone is quite wider than the front face crater but not as deep. Finally, the increase of the impact velocity of the projectile gives rise to tunnelling depth and may lead to full perforation of the target.

On the other hand, the duration of a soft impact is more prolonged, whereas the deformation of the projectile generates waves propagating throughout the structure reflecting on the edges and superimposing on the existing stresses under the impacted area. The response of an impacted concrete structure is a combination of local damage due to a shear mode and global bending. Jonas et al. [74] presented a soft impact perforation scenario on a reinforced concrete slab. Figure 1.23 illustrates the possible damages produced by this scenario.

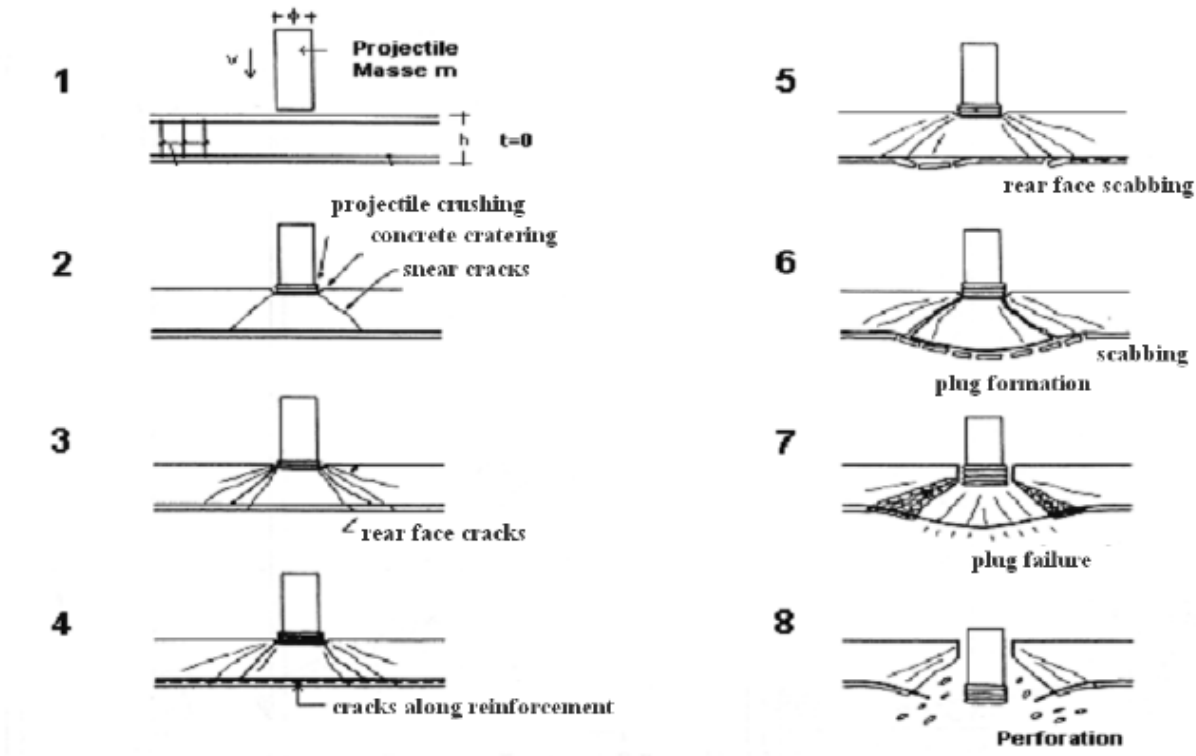


Figure 1.23: Soft impact effects on a reinforced concrete slab (Jonas et al. [74])

As illustrated in Figure 1.23 the projectile crashes on the proximal face of the reinforced concrete slab by creating a conical cratering with shear cracks. A crack zone propagates with diagonal cracking

in various inclinations. Some of them reach the distal face. After, cracking propagates along the interface between the rear face concrete and longitudinal reinforcement. Scabbing of the rear face leads to a cone plug damage mode. If the projectile is able to prolong its penetration, reinforcements fail and the shear plug separates from the slab whereas the projectile perforates.

To conclude with the main problem for soft impacts is the characterisation of the loading at the interface between structure and the impactor. The structure is mainly loaded under bending, existing models for reinforced concrete can deal efficiently with this problem. Contrarily, the modelling of hard impacts requires accounting for complex dissipative phenomena such as high strain rates, high triaxial stresses, penetration and fragmentation. Therefore, it is necessary to develop reliable approaches capable to predict the response of reinforced structures under hard impacts.

1.3 Simplified design methods

The fundamental principle of structural design is to guarantee safety for the community with an economical solution. Thus structures would be capable to preserve their form until ultimate resistance capacity. Concrete is widely used in protection systems of sensitive infrastructures such as nuclear power plants. Nowadays, the increasing risk of accidental conditions (aircraft impact) or military conditions (missile impact) requires assessing the vulnerability and durability of concrete structures under impulsive loadings. Existing design methods for protection systems under impacts are mainly based on full-size experiments and empirical formulae that are not economical.

1.3.1 Soft impacts

Riera [109] studied the reaction force $P(t)$ of a collapsing aircraft on a rigid surface. He considered the impacted structure to be stiff with negligible deformations in comparison with those of the collapsing aircraft. Equation (1.5) gives the contact force at the interface between the two colliding (1.5)

$$P(t) = P_b(x(t)) + \mu(x(t)) V^2(t) \quad (1.5)$$

In which $x(t)$ length of the aircraft, $P_b(x)$ is the necessary buckling force to crush or deform the fuselage of the aircraft, $\mu(x)$ is the mass of the aircraft per unit length and $V(t)$ is the velocity of uncrashed aircraft. The elastoplastic buckling force $P_b(x)$ can be considered as independent of $x(t)$.

1.3.2 Hard impacts

Petry formula (1.6) [116] was originally developed in 1910 to account the penetration depth x (inches) of a rigid missile into a massive target; with K_p the concrete penetrability coefficient, A_p (lb/ft²) is the missile section pressure and V_0 (ft/s) the impact velocity of the projectile. In Petry I formula for massive plain concrete $K_p = 0.00799$ and for normal reinforced concrete $K_p = 0.00426$ [76].

$$x = 12K_p A_p \log_{10} \left(1 + \frac{V_0^2}{215} \right) \quad (1.6)$$

Different authors modified this formula; Amirikian [2] reformed the coefficient K_p to account for the effect of the compressive strength of concrete target f_c Figure 1.24. He also proposed the perforation thickness e (1.7) and scabbing thickness h_s (1.8).

$$e = 2x \quad (1.7)$$

$$h_s = 2.2x \quad (1.8)$$

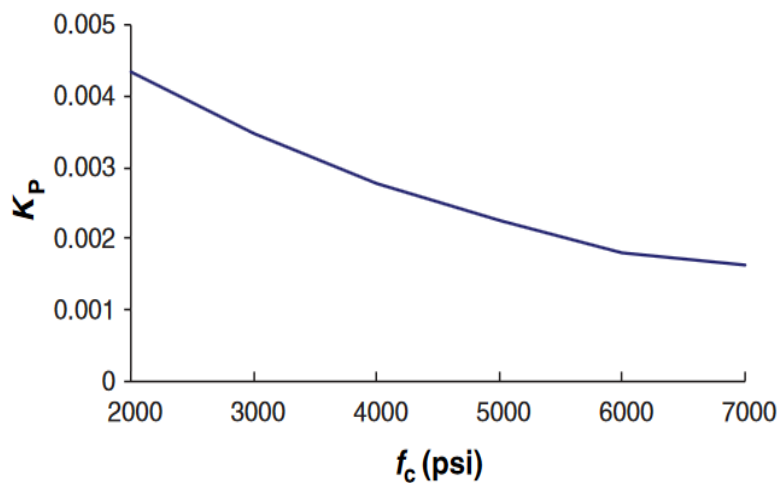


Figure 1.24: Variation of concrete penetrability K_p with unconfined compressive strength of concrete f_c (Li et al. [83])

Later, Walter and Wolde-Tinsae [139] presented the coefficient K_p with the equation (1.9).

$$K_p = 6.34 \times 10^{-3} \exp(-0.2973 \times 10^{-7} f_c) \quad (1.9)$$

The Ballistic Research Laboratory (BRL) formula (1.10) [10] was created in 1941 as an improvement of Petry formula to compute the penetration depth of a rigid projectile in concrete targets, with d (inches) the diameter of the projectile and M (lb) the mass of the projectile.

$$\frac{x}{d} = \frac{427}{\sqrt{f_c}} \left(\frac{M}{d^3} \right) d^{0.2} \left(\frac{V_0}{1000} \right)^{1.33} \quad (1.10)$$

Chelapati et al. [22] in 1972 gave the perforation e and scabbing h_s limits based on BLS formula as:

$$e = 1.3 x \quad (1.11)$$

$$h_s = 2 x \quad (1.12)$$

The Army Corps of Engineers formula (1.13) was developed in 1946 [1] based on statistical fitting of experimental results from the Ordnance Department of the US Army and the BLS to predict the penetration depth.

$$\frac{x}{d} = \frac{282.6}{\sqrt{f_c}} \left(\frac{M}{d^3} \right) d^{0.2} \left(\frac{V_0}{1000} \right)^{1.5} + 0.5 \quad (1.13)$$

Perforation e and scabbing h_s limits are based on ballistic tests with 37, 75, 76.2 and 155 mm steel projectiles.

$$\frac{e}{d} = 1.32 + 1.24 \frac{x}{d} \text{ for } 3 < \frac{e}{d} < 18 \quad (1.14)$$

$$\frac{h_s}{d} = 2.12 + 1.36 \frac{x}{d} \text{ for } 3 < \frac{e}{d} < 18 \quad (1.15)$$

The CEA-EDF perforation limit formula was proposed in 1978 [6], is based on a series of drop-weight and air gun experiments on symmetrical bending reinforcement concrete slabs conducted by CEA and EDF, with V_p (m/s) the ballistic limit, d (m): diameter of the projectile, M (kg) the mass of the projectile; e (m) the thickness of the concrete wall, ρ (kg/m^3) the density of concrete and f_c (Pa) the unconfined compressive strength of concrete.

$$\frac{e}{d} = 0.82 \frac{M^{0.5} V_p^{0.75}}{\rho^{0.125} f_c^{0.375} d^{1.5}} \quad (1.16)$$

CEA-EDF formula can also express as ballistic limit or perforation velocity (1.17)

$$V_p = 1.3\rho^{1/6}f_c^{1/2}\left(\frac{d e^2}{M}\right) \quad (1.17)$$

Then, Fullard [50] improved the formula to take into account the reinforcement quantity with r the percentage of reinforcement described by the percentage each way in each face.

$$V_p = 1.3\rho^{1/6}f_c^{1/2}\left(\frac{d e^2}{M}\right)(r + 0.3)^{2/3} \quad (1.18)$$

Berriaud et al. [7] extended the formula considering the concrete strength, the reinforcement ratio and the projectile nose (1.19), with $M_{a0} = 200 \text{ kg/m}^3$ reference steel reinforcement density, $f_{c0} = 36 \text{ MPa}$ reference compressive strength of concrete, γ a function of the number of steel layers ($\gamma = 0.7$ for 2 steel layers and $\gamma = 0.1$ for 4 steel layers) and N a function of the nose geometry ($N = 1$ for a flat nose, $N = 1.18$ for a hemispherical nose).

$$V_p = 1.9 f_c \rho^{1/3} \left(\frac{d e^2}{M}\right)^{4/3} N^2 \left[0.35 \left(\frac{M_a}{M_{a0}}\right)^\gamma + 0.65\right] \left(\frac{f_c}{f_{c0}}\right)^{-1/2} \quad (1.19)$$

Kennedy [76] in 1976, proposed a formula for the penetration of hard projectiles as a function of effective projectile calibre density which is the ratio of the projectile weight and the effective concrete slab weight.

Forrestal et al. [48] in 1994 suggested an analytical model to measure the penetration of ogive-nose projectiles into concrete slabs depending on the unconfined compressive strength of concrete f_c .

Jones and Rule [75] in 2000 developed a model for normal impact penetration accounting the effects of pressure-dependent friction to calibrate the optimal nose geometry. They reported that lower velocities need a sharper nose to reach maximum depth and for higher impact velocities the sharpening of nose produces excessive friction. The optimal nose geometry for modest friction and frictionless cases are very similar.

A non-dimensional formula based on the dynamic cavity-expansion model for the prediction of penetration from non-deformable projectile was introduced by Chen and Li [23] in 2002. They used different geometrical characteristics into several mediums (metal, concrete, soil) subjected to normal impacts.

Guirgis et al. [57] in 2009 proposed a semi-analytical dimensionless formula based on the volumetric crushing energy density to determine the penetration depth for a rigid projectile into a concrete slab.

Zaidi et al. [145] in 2010 developed an empirical prediction formula for the penetration of ogive nose hard projectiles into concrete targets based on critical impact energies with different CRH ratios of projectiles, by using curve fitting dimensional analysis.

1.4 Numerical methods

The analysis of impacts with empirical formulae based on experimental data is not economical and often is insufficient including the complex non-linear behaviour of concrete. The existing demand for accurate analytical methods motivates the development of numerical tools. Nowadays, thanks to the rapid expansion of computational mechanics; numerical methods based on material constitutive models allow the prediction of the effects of impacted concretes to become more economical and reliable.

1.4.1 Finite element method (FEM)

The finite element method (FEM) is a numerical method to solve partial differential equations based on the variational formulations of the problem and the choice of a specific space for the functions that approximate the unknowns. The method subdivides the space between a collection of smaller and simple parts (Finite element) and simple trial functions approximate the solution of each element.

Simple trial functions give t

he numerical solution to the problem; usually, polynomials, to approximate the complex partial differential equations (PDE) at the element level. Then, these equations are assembled into the global system equation whose solution solves the entire problem. This method is originated from the development of mesh discretisation methods due to the necessity to solve complex elasticity and structural analysis problems in aeronautical and civil engineering in early 1940 by Courant [24] and Hrennikoff [67]. Zienkiewicz and Cheung [149] published the first book on FEM in 1967.

A Boeing 747-400 impact on a nuclear building was analysed by Arros & Doumbalski [4] in 2007 using LS-DYNA software by representing the loading with the Riera method and the FEM Figure 1.25.

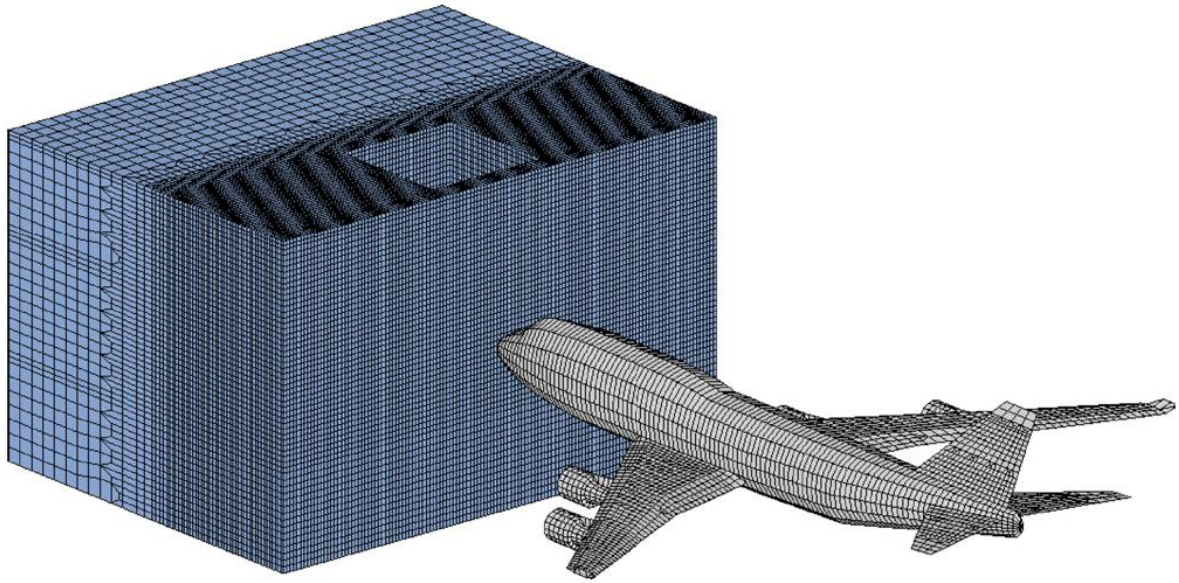


Figure 1.25: FEM model of the nuclear building and the 747-400 airline (Arros & Doumbalski [4])

They obtained similar results with the two methods for the force-time history Figure 1.26 with a relative error of area under the two curves within 2%.

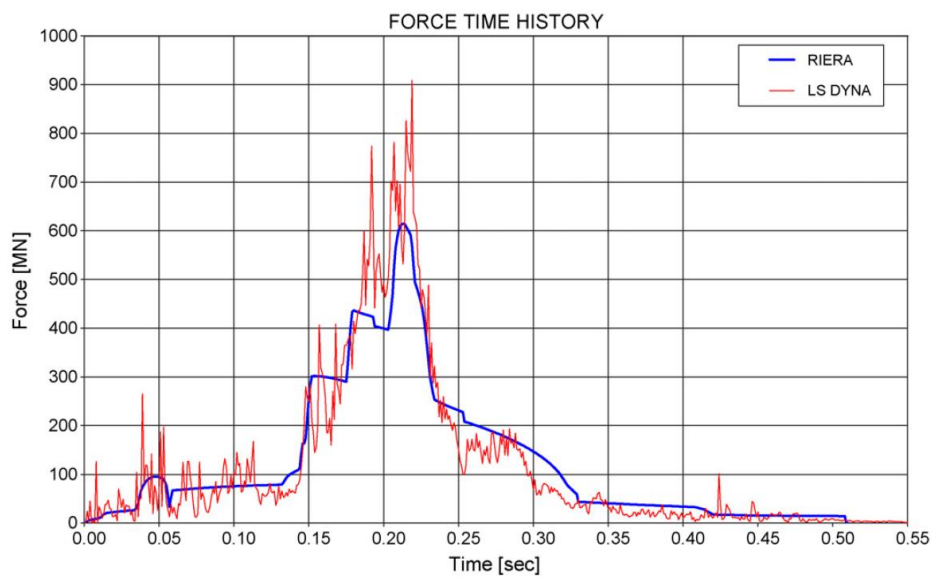


Figure 1.26: The target Riera force history and the reaction history at a rigid target from LS-DYNA run.

FEM is a continuous method; thus it reaches its limits to simulate damages due to hard impacts, but it might be suitable for soft impacts such as aircraft. Nevertheless, it is necessary to select a numerical method capable of reproducing the damage patterns of macro-cracks. For this reason,

erosion techniques are necessary to be used in order to describe complex phenomena on reinforced structures under impacts.

Erosion techniques consist of a damage criterion of eliminating the elements once they reach a threshold of plastic deformation. The use of an appropriate erosion criterion, which is calibrated on experimental data similar to the concerned problem, could give good results of an impact simulation.

Polanco-Loria et al. [105] in 2008 simulated perforation of rigid projectiles on concrete targets for the numerical prediction of ballistic limits using elements with erosion criterion. The numerical prediction of the residual velocity was well matched with the experimental data and all the damage modes (spalling, scabbing and tunnelling) were well described from the simulation Figure 1.27.

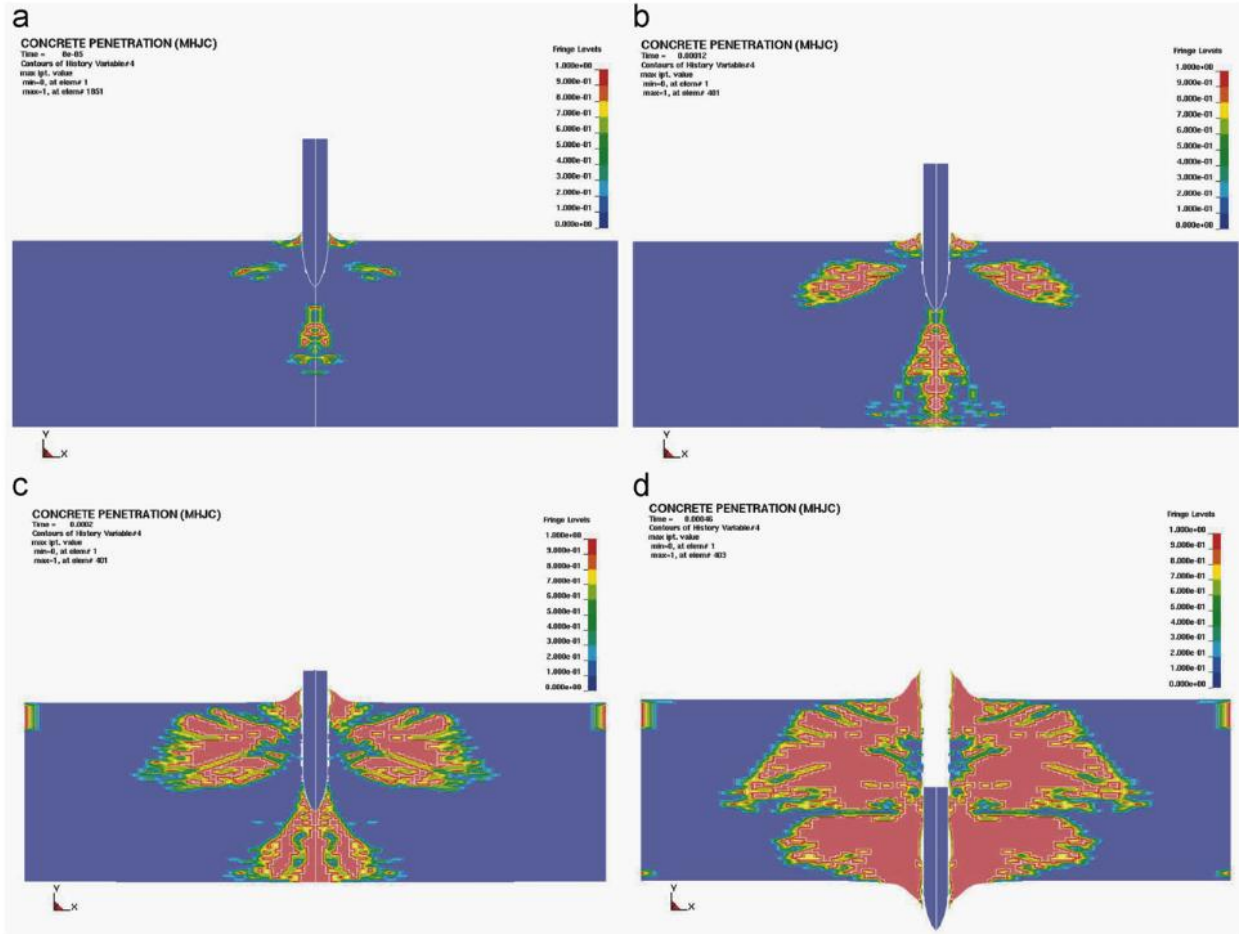


Figure 1.27: Damage modes during perforation throughout the simulation (Polanco-Loria et al. [105])

However, finite elements with erosion techniques it is not convenient because they are mesh dependent and once elements are eroded there is no conservation of mass and energy.

1.4.2 Extended finite element method (XFEM)

The extended finite element method (XFEM) is based on the classical FEM approach that allows finite element discontinuities; by enriching the solution space to a differential equation with discontinuous functions (Moës et al., 1999 [95]).

Xu et al., 2010 [144] simulate a low-speed impact on windshield cracking of a pedestrian-vehicle accident by using XFEM to characterise the cracks propagation. Their simulation seems to be qualitatively correlated with the real accident Figure 1.28. However, XFEM requires developments to such as crack initiation, opening and closing of many cracks and fragmentation in order to be applied in higher velocity impacts.



Figure 1.28: Cracks on windshield in real-world pedestrian-vehicle accident (left), simulation (right)

1.4.3 Smoothed-Particle Hydrodynamics (SPH) method

Smoothed-Particle Hydrodynamics (SPH) was developed by Gingold and Monagh [54] and Lucy [85] in 1977. It is a meshfree Lagrangian method suitable in problems with complex boundaries, like large displacements. The nodes of the elements in the SPH approach are not linked to the structure; thus it has the advantage of solving continuum mechanics equations adjusting easily to the appearance of

discontinuities without mesh adaptations. However, it requires dense assemblies of elements to obtain accurate results with high computational cost.

Huang et al. [69] applied an SPH method to simulate the penetration of an ogive-nosed projectile into a cylindrical concrete target with 315m/s impact velocity, where they obtained adequate results with a thorough description of crack propagation Figure 1.29.

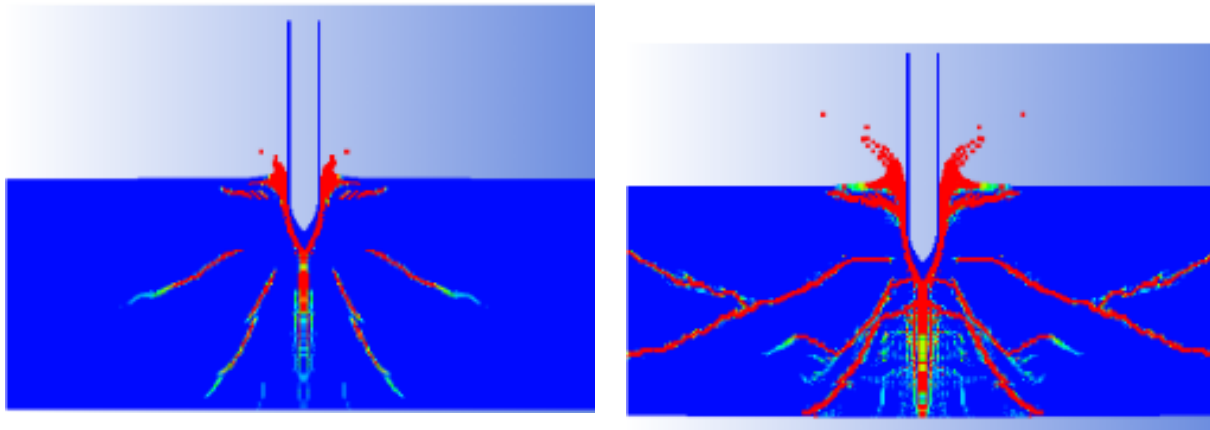


Figure 1.29: The typical calculated damage in concrete impacted by a projectile (Huang et al. [69])

1.4.4 Discrete Element Method

The discrete element method (DEM) is a powerful alternative to FEM when advanced damage states and failure of concrete have to be studied. Indeed, DEM allows easily obtaining realistic macro-crack patterns and material fragments due to its discontinuous nature.

Continuous methods require significant improvements to overcome their difficulties on describing macro-cracking propagation up to failure which requires mesh adaption with damageable criteria which are time consuming. For this reason, new methods have been created where the medium is assembled by discrete particles of simple geometries (spheres, polyhedral). Discrete Element Method (DEM) was originated from the Distinct Element Method which it was initially developed to model rock movements in large scale with 2D rigid assemblies by Cundall [26],[28] and with 3D post – developments by Cundall [27][26] and Hart et al.[61]. Cundall and Strack [29] established a simplified version for granular materials, such as sands with the use of rigid elements, this method is detailed in their previous publications [30],[127].

Discrete elements interact by contact and friction laws and their equation of motion follows the fundamental principle of dynamic which derives from Newton's second law. Cohesive interaction

introduced by Hentz et al. [63], to model cohesive materials such as concrete. The microscopic interactions at the element scale influence the overall macroscopic behaviour of the assembly. Therefore, it is necessary to control the properties of the medium in the micro scale, in order to obtain the correct macroscopic behaviour.

Magnier and Donzé [87] in 1998 simulated an impact of a rigid spherical nose shape missile on plain concrete beams with a DEM. Figure 1.30 shows the damage of the concrete beam after the simulation with spalling on the front face and scabbing on the rear face. One can see the strong potential of the discrete element method to represent multi-cracking.

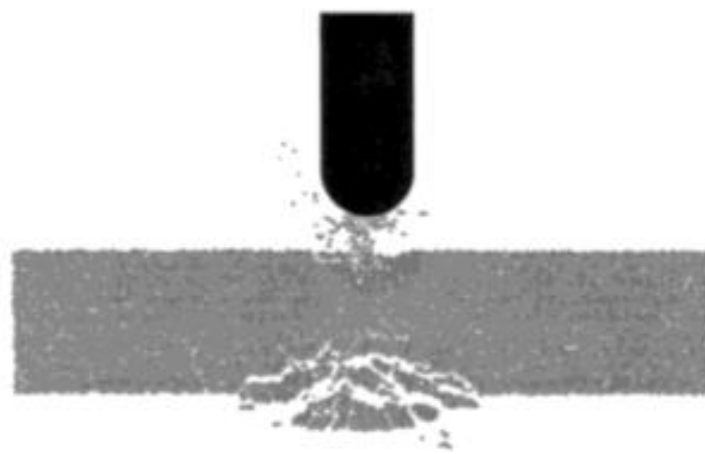


Figure 1.30: Simulation of rigid spherical nose missile on plain concrete (Magnier and Donzé [87])

1.4.5 Lattice Discrete Particles Method (LDPM)

Cusatis et al. [33] recently developed the Lattice Discrete Particles [32]Method (LDPM). He created a mesoscale model for concrete that simulates the mesostructure of concrete using a system of interacting aggregate particles connected by a lattice system. Concrete properties and their size distribution describe the position of each concrete aggregate. A set of polyhedral cells; each including one aggregate particle consist the lattice geometry which represents the cement matrix. Normal and shear stress characterise the interactions between the particles. According to Cusatis, mesoscale models reduce the size of numerical problems and they can capture the fundamental aspects of materials heterogeneity.

Cusatis et al. [31] performed simulations of perforation into a reinforced concrete slab; where LDPM was used to model concrete, elastic-plastic beam elements for the reinforcement and hexahedral finite elements for the projectile. Figure 1.31 illustrates the perforation test model, the numerical prediction of the cratering after perforation and the comparison between the computational results

with the experimental data. As can be seen, the numerical prediction of the ballistic limits is in good accordance with the experiments.

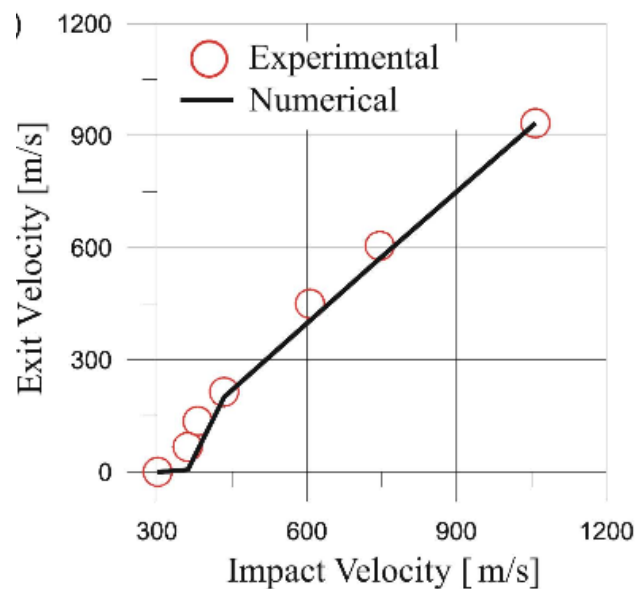
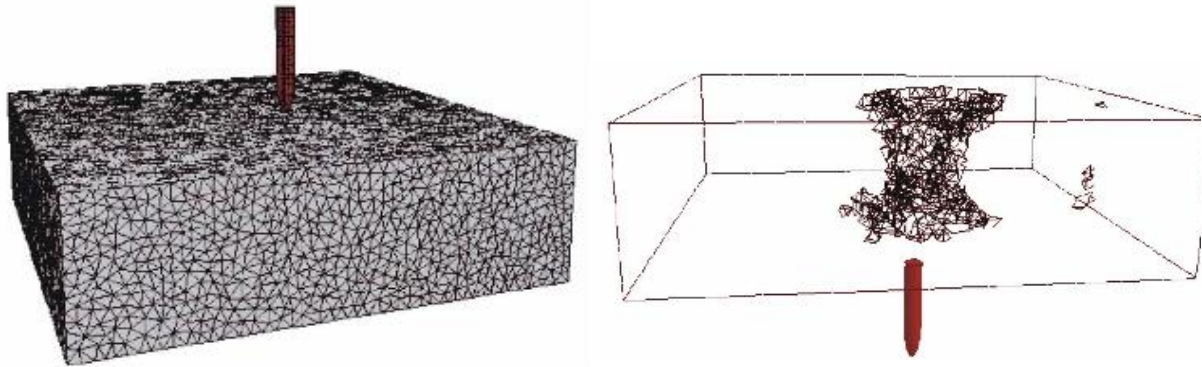


Figure 1.31: perforation test model (up left), obtained a cracking pattern after perforation (upright), exit velocity plot (down) (Cusatis et al. [31])

Nevertheless, it should be noted that for cohesive material LDPM and our DEM are the same approaches. The advantage of our DEM is that the use of simple spherical elements allows handling the contact conditions easily.

1.4.6 Finite-Discrete Element Method

The Finite-Discrete Element Method suggested by Munjiza [96] in 1995 as a synthesis of finite element and discrete element methods aiming to simulate large-scale industrial problems efficiently.

Initially, this method describes the problem with a continuum media by finite elements. Then progressive fracturing is allowed based on a fracturing criterion. Once the finite elements reach the threshold limit; discrete elements are forming able to describe the discontinuity of the fracturing propagation.

Smoljanovic et al. [125] used the FEM/DEM coupling method for the seismic analysis of dry stone masonry structures. Figure 1.32 presents the FEM/DEM model of the masonry structure and its collapse after the seismic numerical analysis.

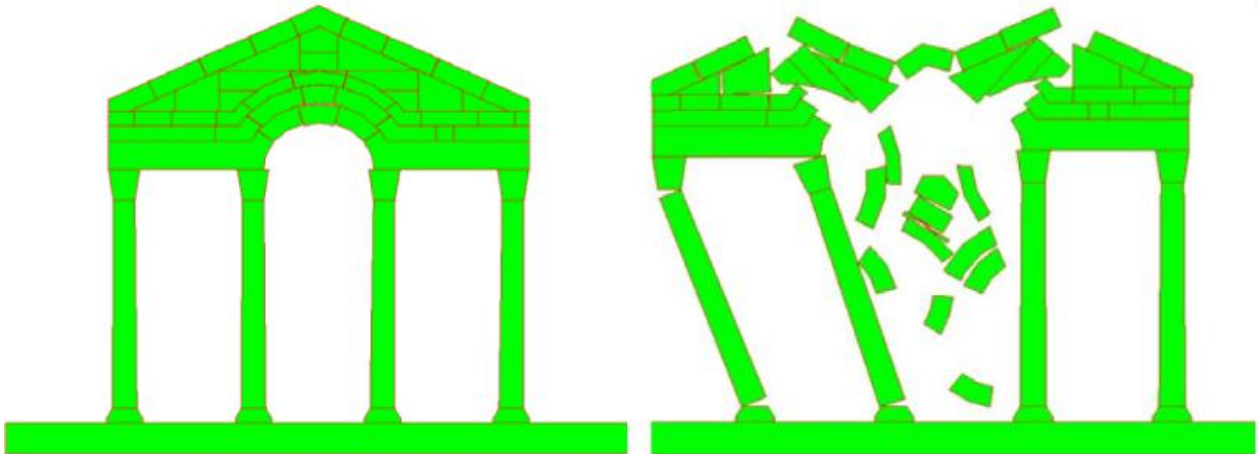


Figure 1.32: FEM/DEM model of the structure (left), Collapse simulation of the structure due to the seismic effect using FEM/DEM (right) (Smoljanovic et al. [125])

1.5 Conclusion

Nowadays, the design of sensitive concrete infrastructures requires accounting extreme hazards such as terrorist attacks or industrial accidents. Explosions or impacts induce extreme loadings (high strain rates and high mean stresses) with a low probability of occurrence but with possibly devastating consequences. Therefore, the design of concrete structures under impact requires both thoroughly comprehending the damage mechanisms of concrete under impact and the development of advanced calculation methods able to predict damage into reinforced concrete barriers.

The modelling of concrete structures submitted to impacts requires accounting strain rates ranging from quasi-static conditions to hundreds of s^{-1} . Furthermore modelling structures under hard impacts requires accounting the material behaviour under triaxial compression with confinement stresses in the order of hundreds of MPa.

Existing design methods for concrete protection systems under impacts are mainly based on full-size experiments and empirical formulae that are possibly not economical. Generally, these methods do not account the complex non-linear behaviour of concrete. The growing society demand for predictive analytical methods motivates the development of advanced numerical tools.

Chapter 2

The Discrete Element Method

This unit describes the main concepts of our discrete element method. Main principles of the algorithm, calculation of forces, definition of interactions and the constitutive law of concrete are presented. It is worth to highlight that the discrete elements of this approach do not represent the constituents of concrete, but the aim the model is to reproduce an isotropic and homogeneous behaviour at the macroscopic scale. Macroscopic phenomenological constitutive laws depend on the local microscopic behaviour of the discrete elements. Furthermore, in this section, the modification of the constitutive model for dynamic loading is proposed. The new law aims to offer a more realistic modelling of the dynamic fracture energy.

Discrete Element Method (DEM) was originally developed by Cundall [25],[27] to model large-scale rock movements of 2D rigid assemblies. Later, Cundall [26] and Hart et al. [61] extended the method with 3D post – developments. Cundall and Strack [29] established a simplified version for granular materials, such as sands with the use of rigid elements. This method is detailed in their previous publications [30],[127]. Afterwards, Hentz et al. [63] implemented the classical method by taking into account the cohesive interaction over the contact interaction, to model cohesive materials such as concrete. In addition, (DEM) is convenient for dynamic problems with complicated phenomena, like fragmentation and multi-cracking due to impacts on reinforced concrete structures due to its ability to model discontinuities. This approach does not depend on any damage mechanics since the medium is naturally discontinuous.

A disordered assembly of rigid non-overlapping spherical elements of different sizes and masses composes our discrete element mesh. These spheres do not represent the concrete constituents, such as the granular or cement matrix. For this reason, it is essential to validate that the model can produce the isotropic and homogeneous behaviour of concrete at the macroscopic scale. Consequently, the use of macroscopic phenomenological constitutive laws relies on the local microscopic behaviour of the discrete elements.

In order to produce a well predictive model, several parameters need to be calibrated by means of linear and nonlinear constitutive laws between two spheres. The local stiffnesses among discrete elements are modelled by spring-like interactions based on displacements [63]. These interactions are controlled by normal and tangential forces applied at an “equivalent contact point” between two discrete elements. Furthermore, a bilinear, elasto-plastic Moment Transfer Law (MTL) was introduced by Plasssiard [104] and it was implemented in this model by Omar et al. [102] to create a rolling resistance between two discrete elements in order to prevent brittle failure. A simple identification of the loading rate dependency is introduced to compute the dynamic strength of the interaction using a Dynamic Increase Factor (DIF) inspired by the CEB formula [20].

The present discrete element model was developed in EUROPLEXUS [40] and it is based in 3D computations. An explicit time marching scheme of central-difference method is used for the discretisation in time. The equation of motion of every particle is given from the fundamental principle of dynamics. To ensure the stability of the integration scheme the critical time step needs to be computed.

2.1 Mesh generation method

The packing method that is currently used is an optimisation of a geometric algorithm proposed by Jerier et al. [71]. The algorithm is based on tetrahedral finite element mesh and it is originated from the technique developed by Cui and O’Sullivan [25] to generate porous sphere packing. It is using a special disordering procedure to fill the geometry with polydisperse non-overlapping spheres. This algorithm is implemented in SherePadder++ free software [122], which is introduced in the open-source SALOME platform [115].

This algorithm generates a mesh with discrete elements of different sizes and masses with sufficient constituents, such as the granular or cement matrix. The aim is to produce an isotropic and homogeneous concrete behaviour at the macroscopic scale.

Initially, a DE packing requires the generation of the geometry which is defined by its characteristics and boundary conditions. Delaunay approach [34] is used to mesh the selected shape with tetrahedral. After, every tetrahedron is filled with polydisperse spheres using an inversion function [5] which is a geometrical procedure. The size distribution of the spheres is calculated from the size of the tetrahedral mesh which can be adjusted by the finite element generator, Netgen [119] and the

parameters given by the user (ratio of maximum over minimum radii $k_1 = \frac{R_{max}}{R_{min}}$ and FE tetrahedron edge length over the mean diameter of the DE assembly $k_2 = \frac{FE_{edge}}{DE_{mean}}$).

The polydisperse sphere packing method initiates once the tetrahedral node coordinates are available. The next two steps are the direct placement of spheres at the middle of each edge and after on every vertex. They are called type 1 and type 2 spheres. The radius for type 1 spheres depends on the FE edge length and the ratio k_2 ($R_{T1} = \frac{FE_{edge}}{2 \cdot k_2}$). Then, type 3 spheres are created in an intermediate position on every face of the tetrahedron being in contact with three non-aligned spheres (type 1 and type 2) on the same face. At the next step, a sphere (type 4) is put in the centre of the tetrahedron. Four new spheres of type 5 are placed close to the vertices and in contact with a sphere of type 2 and three neighbouring spheres. Delaunay triangulation [34],[30] is applied in the centre of fixed spheres to detect the empty volumes and create a tetrahedron network which is filled with spheres of type 6. The next step is the densification phase; it is optional and it creates a more compact mesh by filling the last empty spaces respecting R_{min} . The steps for the mesh generation procedure are illustrated in Figure 2.1.

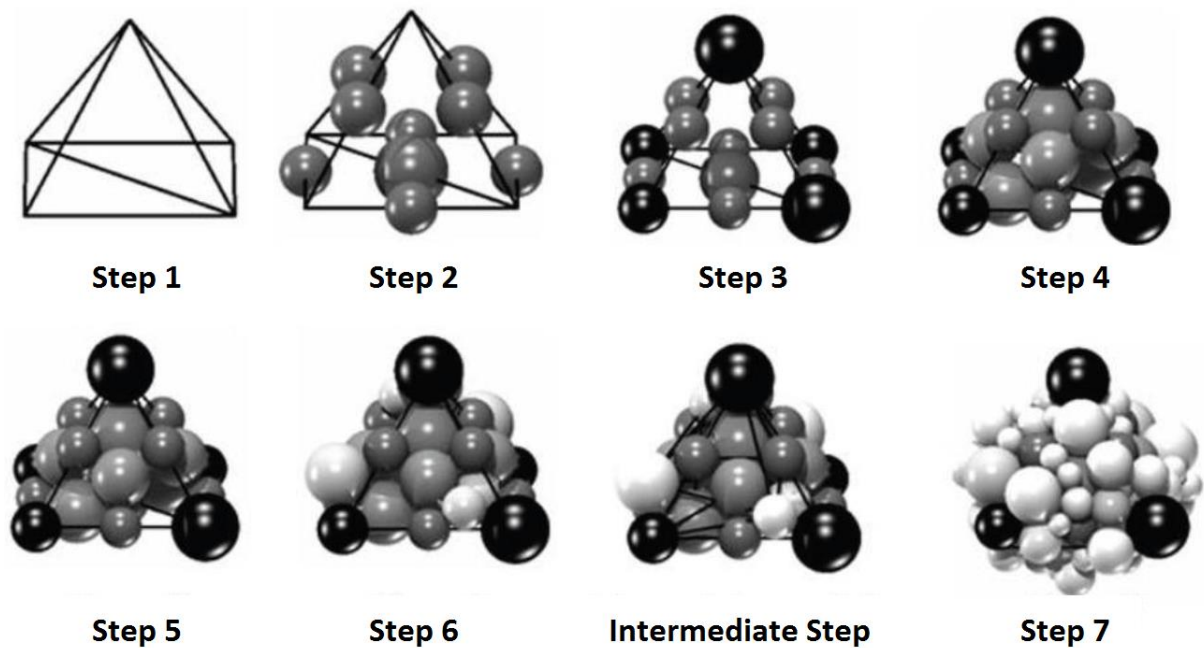


Figure 2.1: Procedure for the mesh generation (Jerrie et al. 178[71])

2.2 Principles of the algorithm

The present numerical model of discrete element method was developed in EUROPLEXUS [40]. EUROPLEXUS is a computer code being jointly developed since 1999 by CEA (CEN Saclay, DMT) and EC (JRC Ispra, IPSC) under a collaboration contract. The DEM algorithm is based in 3D computations and it is composed by spherical point-like rigid particles of individual mass and radius. Each discrete element has one node (sphere's centre) with six degrees of freedom corresponding to three translations and three rotations.

An explicit scheme of central-difference method is used for the discretisation in time which is well adapted to rapid dynamic phenomena such as impacts. Explicit time integration methods calculate the approximate solution of a system at a later time t_{n+1} using the results at the current state t_n as initial conditions. Central difference method defines the approximate velocity (\vec{u}) and acceleration (\vec{u}) at a time interval (Δt) of known values of displacements (u). Velocities are calculated in halfway time-step $\vec{u}\left(t + \frac{\Delta t}{2}\right)$ as the rate of displacement change between the step back $u(t)$ and the step ahead $\vec{u}(t + \Delta t)$. Likewise, accelerations $\vec{u}(t)$ are determined, after defining the velocities in halfway time step back $\vec{u}\left(t - \frac{\Delta t}{2}\right)$ and ahead $\vec{u}\left(t + \frac{\Delta t}{2}\right)$.

$$\vec{u}\left(t + \frac{\Delta t}{2}\right) = \frac{(\vec{u}(t + \Delta t) - \vec{u}(t))}{\Delta t} \tag{2.1}$$
$$\vec{u}(t) = \frac{\left(\vec{u}\left(t + \frac{\Delta t}{2}\right) - \vec{u}\left(t - \frac{\Delta t}{2}\right)\right)}{\Delta t}$$

A discrete element i at the moment t is characterised by its central coordinates, radius (R_i), mass (m_i), translational $\vec{u}_i(t)$ and rotational $\vec{\omega}_i(t)$ accelerations and it is connected with its nearest neighbours. The relative displacement between a particle i and its neighbour j is defined as δ_{ij} , where interaction laws govern forces and moments between the two particles. The equation of motion for every particle is given from the fundamental principle of dynamics, which derives from Newton's second law. According to this, the acceleration $\vec{u}_i(t)$ of a body is equal to the sum of the forces $\vec{F}_i^{tot}(t)$ on that body divided by its mass m_i . Similarly, the rotational equation gives the

rotational acceleration $\vec{\omega}_i(t)$ of a body by replacing forces $\vec{F}_i^{tot}(t)$ with moments $\vec{M}_i^{tot}(t)$ and mass m_i with the moment of inertial I_i .

$$\vec{u}_i(t) = \frac{\sum_{j=1}^n \vec{F}_{j \rightarrow i}(\delta_{ij})}{m_i} = \frac{\vec{F}_i^{tot}(t)}{m_i} \quad (2.2)$$

$$\vec{\omega}_i(t) = \frac{\sum_{j=1}^n \vec{M}_{j \rightarrow i}(\delta_{ij})}{I_i} = \frac{\vec{M}_i^{tot}(t)}{I_i}$$

As a result, the new position of the element can be expressed as:

$$\vec{u}(t + \Delta t) = \vec{u}(t) + \vec{u}\left(t + \frac{\Delta t}{2}\right) \Delta t \quad (2.3)$$

2.2.1 Calculation loop

The principle steps of the current discrete element method after the creation of the mesh are described as follows and they are detailed later:

1. The algorithm looks for interactions and the neighbours' list is updated for every time step.
2. The local interaction forces of each element opposed by its neighbours are calculated as the resultant of the normal and the tangential component.
3. The total force applied to each element is calculated as the sum of the local interaction forces applied to the element.
4. Application of the external forces.
5. Calculation of the acceleration of each element for the next time step by using the fundamental principle of dynamics and knowing the external forces and the mass of the element.
6. Velocities and displacements of the element are computed using the explicit time discretisation scheme of the central difference method.

2.2.2 Calculation of the discrete element mass

The density of concrete (ρ) is an input parameter for the discrete element method. The mass of each particle is equal to the product of the density and its spherical volume. Nevertheless, the sum of the masses of all the discrete elements is smaller than the real mass of the specimen because of the porosity of the assembly. Consequently, to avoid miscalculations due to wrong inertial forces, the mass of each sphere should be corrected accounting for the compactness (c) of the mesh obtaining the actual mass of each discrete element:

$$m = \frac{4\rho}{3c}\pi r^3 \quad (2.4)$$

2.2.3 Determination of the integration critical time step

Explicit integration schemes may lead to instabilities for big-time steps; thus it is important to choose a time step small enough to guarantee the stability of the scheme. In this discrete element method, the interaction is modelled as mass-spring systems with six degrees of freedom and the equation of motion for each element is based on the fundamental principle of dynamics. Then, every particle has a natural frequency $\omega = \sqrt{\frac{K}{m}}$, where K is the stiffness and m is the mass. The stability condition of the integration scheme of the central-difference method is given by Courant et al. [21] and it is written as:

$$\Delta t \leq \frac{2}{\omega} \quad (2.5)$$

To respect this condition, one should calculate the natural frequencies of the system and choose the highest. This solution would have been very time consuming due to a large number of discrete elements where each one is subjected to several interactions. An alternative solution it is to calculate for each discrete element an equivalent stiffness K_{eq} , from all its interactions. For each interaction, by projecting on the three principal axes of the global coordinate system, are determined six equivalent stiffnesses: 3 translations and three rotations for each element. Then, the critical time step is calculated in each direction for every element. Finally, the lowest value is chosen to be the time step. A safety factor p is introduced to take into account the nonlinearities of this calculation ($0 < p < 1$):

$$\Delta t = \frac{p}{\omega} = p \sqrt{\frac{m}{K_{eq}}} \quad (2.6)$$

2.3 Definition of interactions

Rigid, spherical particles were selected for this discrete element method because it is easier and less time consuming to manage contacts between such elements. As has been already described the mesh is generated with a polydisperse spatial arrangement. Moreover, they are randomly distributed into the geometry in order to obtain a homogeneous mesh. Every element has a different amount of neighbouring elements due to its position and size.

Since, the size of the discrete elements do not represent concrete constituents, such as cement paste or aggregates, it is necessary to create a geometry that allows producing concrete behaviour in the macroscopic scale. For this reason, two types of interactions (contact and cohesive) are composing this model. The cohesive interaction is a simple modification (by Hentz et al. [63]) of the original discrete element approach to model the cohesive nature of certain geomaterials such as concrete.

2.3.1 Interaction range coefficient

An interaction range coefficient is defined to increase the number of interactions, even if the discrete elements are not in contact. A cohesive interaction is defined between two spheres a and b of radii R_a and R_b respectively inside an interaction range, which is determined by an interaction coefficient λ Figure 2.2. The cohesive interaction treated by equation (2.7), where $D_{a,b}$ is the distance between the centroids of the elements a and b with $\lambda \geq 1$.

$$\lambda (R_a + R_b) \geq D_{a,b} \quad (2.7)$$

A cohesive link also receives tensile forces and allows taking into account the effects of the cement matrix in concrete; contrariwise a contact link is acting only in compression. The cohesive interactions are initialised at the beginning of the simulation and they exist as long as are not broken whereas the new contact interactions are created. A contact interaction is possible only when the distance between two particles is less than or equal to the sum of their radii, thus $\lambda=1$.

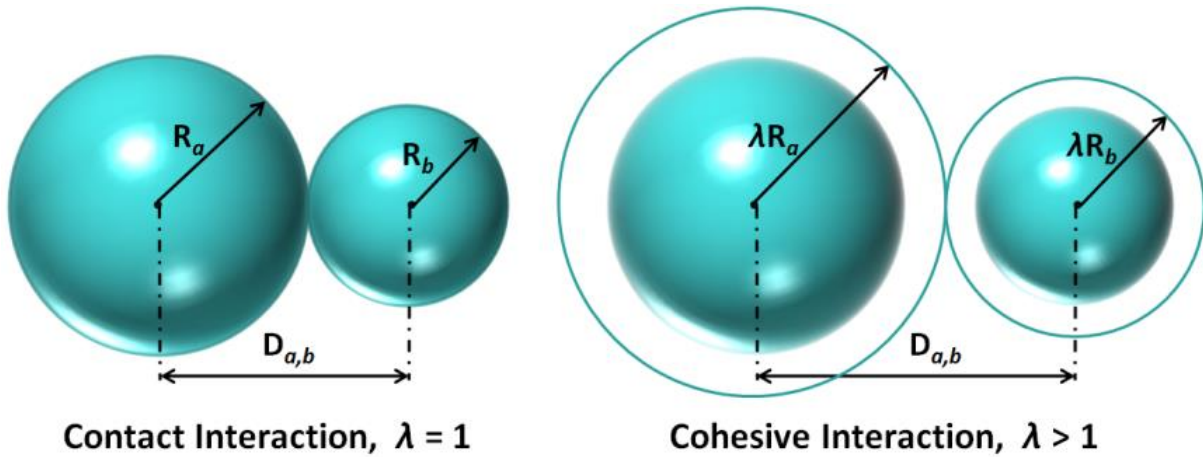


Figure 2.2: Contact Interaction and Cohesive Interaction

The number of links per element with its neighbours varies with the value of λ Figure 2.3. The desired number of interactions can be set by adjusting the interaction range coefficient. Then, the average number of interactions per discrete element is calculated as the number of links over the number of discrete elements equation (2.8). An arbitrary average of twelve links per discrete element was selected by Rousseau [102], a smaller value could lead in privileged directions of interactions and a higher value would encumber the computation time. The average of twelve interactions per particle is also in good accordance for the creation of isotropic specimens.

$$\text{average number of interactions per DE} = \frac{\text{number of links}}{\text{number of DE}} \tag{2.8}$$

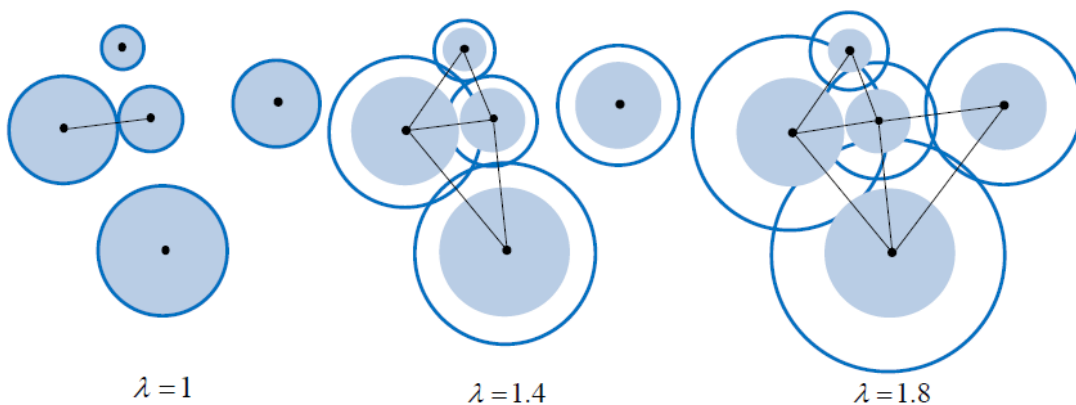


Figure 2.3: Influence of interaction range coefficient on neighbours and the number of interactions (Masurel, [91])

2.3.2 Search of neighbours method

After the creation of the specimen and the selection of the interaction range coefficient λ , it is essential to identify the links between the neighbouring discrete elements. Moreover, the search of neighbours is necessary to perform correctly throughout all the simulation since the specimen deforms under loading and the particles change positions. Jerrie's geometric algorithm produces a dense disorder assembly of discrete elements; thus the search for neighbour method should be sufficient to optimise the computational cost. Spatial sorting algorithms capable of reducing the number of pairwise checks are listed in the PhD thesis of O'Connor [99]. The mesh is structured in such a way that only particles in a bounded region will be controlled for interactions.

Therefore, the current study uses the grid subdivision method, which discretises the geometry in uniform cubic linear cells superimposed on the discrete elements. Then, the particles are associated with the cells that overlap. The algorithm searches for interaction between the discrete elements that a cell contains and the cells in contact and it creates a list of links. The size of the cells is essential because the computational time could be sufficient for not too large cells, although small cells may risk missing possible interactions of discrete elements located outside the cells. For this reason, the cell size should be directly dependent on the discrete element maximum radius.

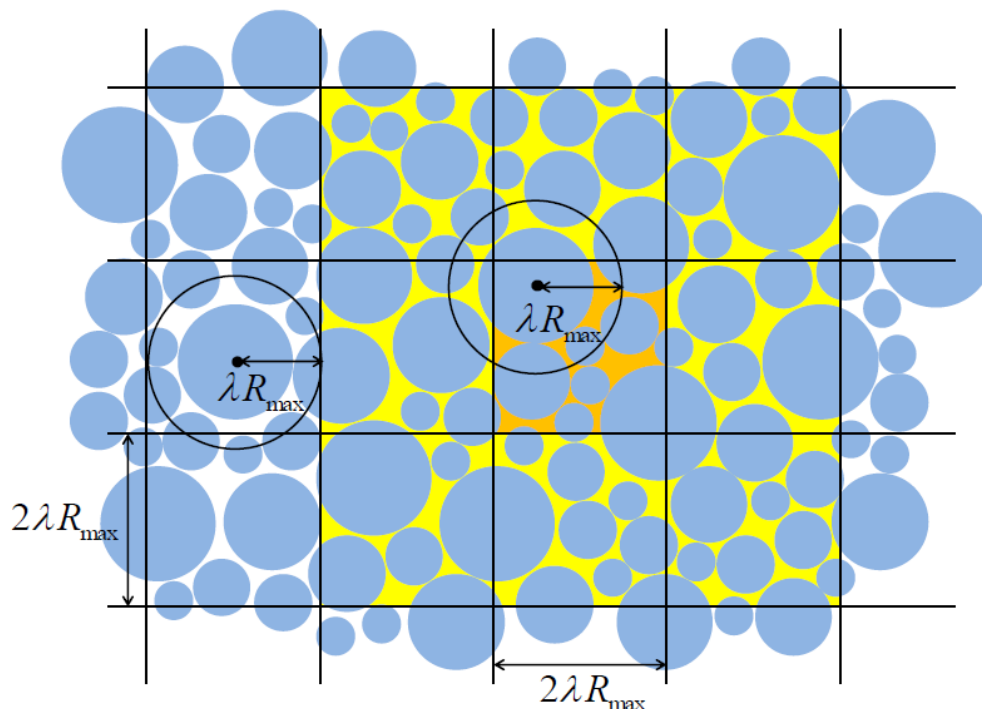


Figure 2.4: Example of the grid method subdivision on a discrete element mesh (Masurel, [91])

Figure 2.4 illustrates an example in two dimensions of the grid subdivision method on a polydisperse spherical disordered assembly of $R_{max}/R_{min} = 3$ and dense compactness. The black lines show the cells' grid superimposed on the discrete element mesh. The selected cell under interaction search is coloured in orange and its neighbour cells are in yellow. The method checks for links only between the particles with their centres in the orange cell and the particles with their centres in the yellow area. Once a cell is controlled it does not consider in the link's search for a neighbouring cell since those interactions have been already listed. The side size of each cell is selected to be $2\lambda R_{max}$ to ensure the efficiency of this method.

2.3.3 Calculation of interactions

The physical interpretation of a link between two discrete elements is the interaction to each other transmitting normal, tangential and rotational efforts, which are computed from their relative movements. These efforts are translated as the resistance of each object to change its position towards the other one and they are imposed at an imaginary contact plane (P) (Figure 2.6) located in an equidistant from the surface of the two particles. The principle for the discrete element method of this study is simplicity; thence spring-like constitutive laws are employed to model these interactions Figure 2.5.

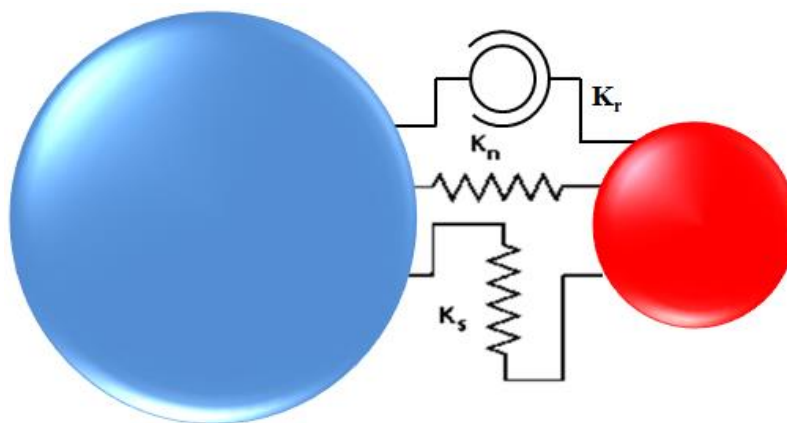


Figure 2.5: Spring-like interaction model

Considering two discrete elements I and J in a cohesive interaction, of radii R_I and R_J and centres G_I and G_J , their link is presented geometrically by the line $\overline{G_I G_J}$ passing through their centres (Figure

2.6). The direction of this line is noted with a unit vector \vec{n} , which is normal to the plane P . The plane P intersects the link at the point C , which is located in the middle from the surfaces of the two spheres.

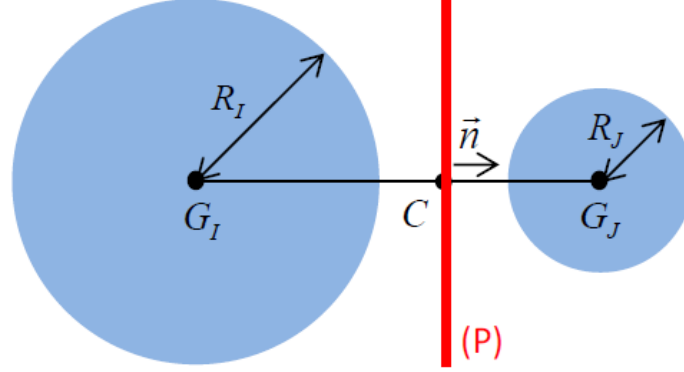


Figure 2.6: Diagram of the intersection point of a cohesive link between two discrete elements I and J

The distance from the centre of the sphere I and the point C is given from the equation (2.9).

$$\overline{G_I C} = \left(R_I + \frac{1}{2} \left(\|\overline{G_I G_J}\| - (R_I + R_J) \right) \right) \vec{n}^t \quad (2.9)$$

The normal component at the plane (P) of the force at the time step $t + 1$ is calculated as the product of the normal spring stiffness and the relative displacement of the link, where D_{IJ}^0 is the initial distance of the two centres and D_{IJ}^{t+1} is their distance at the current moment (2.10).

$$\vec{F}_N^{t+1} = K_N (D_{IJ}^{t+1} - D_{IJ}^0) \vec{n}^{t+1} \quad (2.10)$$

The tangential component of the force on the plane (P) at the time step $t + 1$ is computed in an incremental way using the relative tangential velocity (2.12) of the link at the point C .

$$\vec{V}_N(C \in J/I) = (\vec{V}(C \in J/I) \cdot \vec{n}^{t+1}) \vec{n}^{t+1} \quad (2.11)$$

$$\vec{V}_S(C \in J/I) = \vec{V}(C \in J/I) - \vec{V}_N(C \in J/I) \quad (2.12)$$

Then, the incremental tangential relative displacement is given by multiplying this velocity $\vec{V}_S(C \in J/I)$ with the current time step interval.

$$\Delta \vec{U}_S = \vec{V}_S(C \in J/I) \Delta t \quad (2.13)$$

After, the incremental tangential force (2.14) is taken from the spring as the product of tangential stiffness and the incremental tangential relative displacement.

$$\Delta \vec{F}_S = -K_S \Delta \vec{U}_S \quad (2.14)$$

The movements of the discrete elements in the arrangement are not homogeneous; thus the orientation of the link might change. For this reason, it is necessary to perform two rotations (Hart et al. [61]) on the cumulative tangential. The first rotation is accounting the change of direction (2.15).

$$\vec{F}_S^{rot1,t} = \vec{F}_S^t - \vec{F}_S^t \wedge (\vec{n}^t \wedge \vec{n}^{t+1}) \quad (2.15)$$

The second rotation (2.17) is related to the average velocity according to the new normal unit vector (2.16).

$$\vec{\Omega}_p = \left(\frac{1}{2} (\vec{\Omega}(I/0) + \vec{\Omega}(J/0)) \cdot \vec{n}^{t+1} \right) \vec{n}^{t+1} \quad (2.16)$$

$$\vec{F}_S^{rot2,t} = \vec{F}_S^{rot1,t} - \vec{F}_S^{rot1,t} \times \vec{\Omega}_p \Delta t \quad (2.17)$$

Finally, the tangential force at the time step $t + 1$ is given by adding the incremental tangential force on the transposed cumulative tangential component (2.18).

$$\vec{F}_S^{t+1} = \vec{F}_S^{rot2,t} + \Delta \vec{F}_S \quad (2.18)$$

The three equations (2.19) give the vectors of the internal force of the link at the point C and the moments can be applied directly to the centre of each discrete element since the elements are rigid.

$$\vec{F}_{tot}^{t+1} = \vec{F}_N^{t+1} + \vec{F}_S^{t+1}$$

$$\vec{M}_I(\vec{F}_{tot}^{t+1}) = -\vec{IC} \times +\vec{F}_{tot}^{t+1} \quad (2.19)$$

$$\vec{M}_J(\vec{F}_{tot}^{t+1}) = -\vec{JC} \times +\vec{F}_{tot}^{t+1}$$

2.4 Moment transfer law

Initially, the discrete element method was designed to model granular material. The overall strength of the assembly depends on the particles surface and shape. Frictional contacts offer shear resistance to cohesionless granular assemblies. However, Chareyre [20] showed that the shear capacity of the medium was underestimated when rolling between the particles was allowed without restriction.

In this study, spherical discrete elements are selected and they are treated as point-like rigid particles; hence it is simple to detect contact between them. For this reason, a unique interaction is created between each pair of discrete elements. Consequently, the rotational velocity of the elements is only dependent on the tangential force at the intersection point of the interaction. In reality, the constituents of the concrete (ex. cement paste, granular) interact between them not necessarily only at one point. Therefore, the actual shear resistance of the material is higher due to the complexity of its constituents shape and surface.

Since the principle of this discrete element method is the simplicity the shape of the particles is kept spherical and an alternative solution was selected to increase the shear capacity of the assembly, the Moment Transfer Law (MTL). It is modelled as a moment-rotational spring-like interaction by adding certain rolling resistance between two particles. Iwashita and Oda developed the original idea [70] to model two dimensional circular elements and to simulate the shear band zone of biaxial tests. The three-dimensional version was introduced by Plasssiard [104] and it was implemented in this study by Omar [102].

2.4.1 Description of the moment transfer law

The rolling phenomenon is due to the relative rotation between two discrete elements. Contact evolution of two spherical elements A and B with radius r_A and r_B respectively is considered between two moments with time step dt in the global reference configuration G (Figure 2.7).

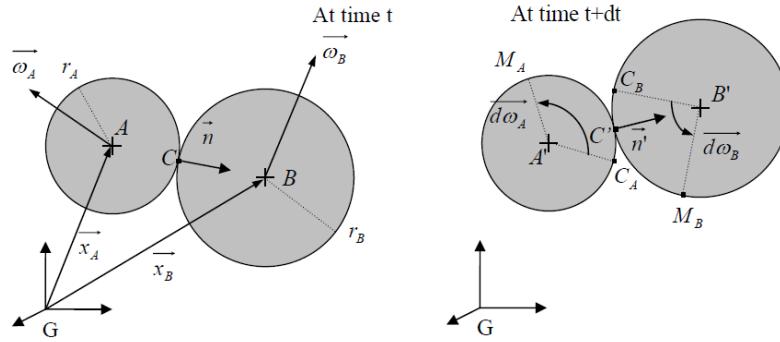


Figure 2.7: Contact evolution between two DE for two time steps t and $t+dt$ (Plassiard [104])

Then, several vectors are created such as the material positions, the incremental displacement $\overrightarrow{dU_r}$, and the incremental rolling $\overrightarrow{d\theta_r}$, in order to describe the resistant moment. The analytical description is given by Omar [103].

$$\overrightarrow{\theta}_r = \sum \overrightarrow{d\theta}_r \quad (2.20)$$

Afterwards, a constitutive law associated with the moment transfer law is defined to reproduce the elastic and plastic behaviour of concrete. Figure 2.8 shows the elasto-plastic model for the rolling resistant. The elastic part is linear and is described by the rolling stiffness K_r . The plastic limit M_{pl} defines the plastic plateau. In the plastic domain, an elastic recovery happens under unloading along a linear part with the same initial rolling stiffness K_r .

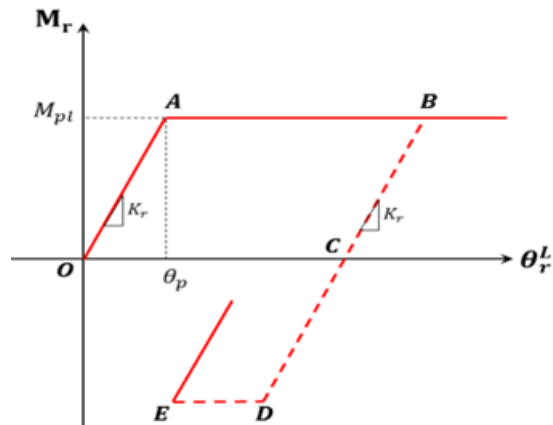


Figure 2.8: Elasto-plastic model for rolling resistant (Omar [103])

A cohesive interaction of two elements A and B with distance D_{ab} between their centroids is considered equivalent to a beam with circular section of a radius $r = \min(r_A, r_B)$. The contact point is

defined at the middle of the net distance between the two spheres (Figure 2.9) and their radius changes as:

$$\begin{aligned} r'_A &= r_A + \frac{1}{2} (D_{ab} - (r_A + r_B)) \\ r'_B &= r_B + \frac{1}{2} (D_{ab} - (r_A + r_B)) \end{aligned} \quad (2.21)$$

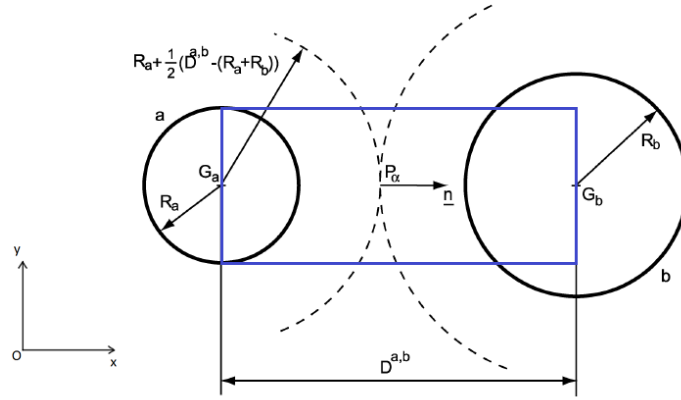


Figure 2.9: Beam model for cohesive link rolling resistant

The beam model in plastic behaviour is used, in order to account the influence of the distance D_{ab} and the radius of the discrete elements on the rolling stiffness K_r .

The fundamental of the strength of materials is used to provide the bending moment around the z -axis:

$$M_f = E I_{ZZ} y'' = E I_{ZZ} \frac{dy'}{dx} = E I_{ZZ} \frac{y'_A - y'_B}{x_A - x_B} \quad (2.22)$$

Where, I_{ZZ} is the quadratic inertia corresponding to the z -axis, and E is Young's modulus.

$$I_{ZZ} = \frac{\pi R^4}{4} \quad (2.23)$$

As have been described by Omar [103], $x_A - x_B$ can be replaced merely by D_{ab} and $y'_A - y'_B$ by the relative rolling between the two spheres as $d\vartheta = \vartheta_A - \vartheta_B$. Thus, the bending moment can be expressed as:

$$M_f = E I_{ZZ} \frac{d\theta}{D_{ab}} \quad (2.24)$$

Therefore, the rolling stiffness K_r is proportional to the term $E I_{zz}/D_{ab}$. A factor βr is introduced to control the rolling resistance. Equation (2.25) expresses the rolling stiffness:

$$K_r = \beta_r \frac{E I_{zz}}{D_{ab}} \quad (2.25)$$

As well the plastic limit of the rolling moment is proportional to the factor $\frac{\sigma I_{zz}}{v}$ where σ can be replaced by the local tensile strength T and v by the radius r of the section. Therefore a factor η is added to control the plastic limit and it is defined as:

$$M_{\text{plas}} = \eta \frac{T I_{zz}}{D_{ab}} \quad (2.26)$$

The moment transfer law is then governed by the pair of parameters $(\beta r, \eta)$. Those two parameters influence the macroscopic behaviour of the model. Thus, we decided that these two parameters need to be identified before any other parameter calibration, to simplify the process.

2.5 Constitutive behaviour of discrete element concrete model

The discrete element model of concrete is given by means of spring-like interactions, defined by normal K_N and tangential K_S stiffnesses [61] at the microscale. These interactions are inspired by the phenomenological behaviour observed at the macroscale. Furthermore, a third rolling spring-like interaction, K_R as rolling stiffness, introduced by Iwashita and Oda [70]. In order to offer rolling resistance to the model, Omar [102] has implemented the rolling spring-like interaction (Moment Transfer Law). The normal force of the discrete element model is described with an elasto-plastic-damage constitutive behaviour law Figure 2.10. The elastic behaviour of concrete is described by macro-micro relations proposed by Donzé et al. [36], while a modified Mohr-Coulomb criterion with a rupture criterion is used to describe the damage in tension and it was proposed by Sawamoto et al. [117]. A Mohr-Coulomb sliding criterion limits the tangential force of the model. Compressive non-linear regime behaviour is governed by the compaction phenomenon, which leads to a plastic-hardening behaviour [124],[135]. Furthermore, strain rate dependency will be introduced in tension allowing the identification of the dynamic strength of the link.

2.5.1 Linear elastic behaviour

Undamaged concrete is considered to be isotropic, homogeneous and linear elastic at the macroscale. The elastic behaviour of concrete is characterised by micro-macro phenomenological spring-like relations defined by Donzé et al. [36]. Those relations were created to deduce the local microscopic parameters K_N (normal stiffness) and K_S (tangential stiffness) from the global macroscopic elasticity coefficients, Young's modulus E , and Poisson's ratio ν . The model of concrete in elasticity is originated from Voigt's hypothesis [39] and the best fit hypothesis of Liao [84] used for regular assemblies. However, those approximations were modified by Donzé [36] to account the polydispersity of disordered assemblies. V denotes the total volume of the representative unit with particles of radius r and N is the total number of inter-particle contacts.

Voigt's hypothesis:

$$E = \frac{4Nr^2}{3V} K_N \frac{2 + 3 \frac{K_S}{K_N}}{4 + \frac{K_S}{K_N}} \quad (2.27)$$

$$\nu = \frac{1 - \frac{K_S}{K_N}}{4 + \frac{K_S}{K_N}} \quad \nu \in \left[0, \frac{1}{4}\right]$$

Liao's model:

$$E = \frac{20Nr^2}{3V} K_N \frac{\frac{K_S}{K_N}}{2 + 3 \frac{K_S}{K_N}} \quad (2.28)$$

$$\nu = \frac{1 - \frac{K_S}{K_N}}{2 + 3 \frac{K_S}{K_N}} \quad \nu \in \left[0, \frac{1}{4}\right]$$

Equations (2.29) shows the micro-macro relations between two elements a and b . $D_{init}^{a,b}$ represents the initial distance between two elements, with radius R_a and R_b and S_{int} is the interaction surface of the link. Young's modulus E and Poisson's ratio ν are considered the input values of the model whereas α, β and γ parameters need to be identified by means of linear quasi-static compression and traction tests.

$$E = \frac{D_{init}^{a,b}}{S_{int}} K_N \frac{\beta + \gamma \frac{K_S}{K_N}}{\alpha + \frac{K_S}{K_N}} \quad S_{int} = \pi \min(R_a, R_b)^2 \quad (2.29)$$

$$v = \frac{1 - \frac{K_S}{K_N}}{\alpha + \frac{K_S}{K_N}} \quad v \in \left[0, \frac{1}{\alpha}\right]$$

Later, a study by Huang [68] proved the dependence of the elastic macroscopic parameters (Young's Modulus E and Poisson's ratio v) on the ratio of shear stiffness over normal stiffness $\frac{K_S}{K_N}$. The expression of Young's Modulus given by Donz 's model [36] could be presented dimensionless (2.30) and vanish its dependence on normal stiffness K_N . That could be pursued by adjusting a value E_0 which derives from the ratio $\frac{K_S}{K_N} = 1$.

$$E_0 = \frac{D_{init}^{a,b}}{S_{int}} K_N \frac{\beta + \gamma}{\alpha + 1} \quad (a)$$

$$\frac{E}{E_0} = \frac{\frac{\beta}{\gamma} + \frac{K_S}{K_N}}{\frac{\beta}{\gamma} + 1} \frac{\alpha + 1}{\alpha + \frac{K_S}{K_N}} \quad (b) \quad (2.30)$$

Equation (2.31) expresses the elastic properties of the normal and tangential stiffness of the link.

$$K_N = E \frac{S_{int}}{D_{init}^{a,b}} \frac{1 + \alpha}{\beta(1 + v) + \gamma(1 - \alpha v)} \quad (a)$$

$$K_S = K_N \frac{1 - \alpha v}{1 + v} \quad (b) \quad (2.31)$$

2.5.2 Non-linear elastic with damage behaviour

The non-linear elastic with damage behaviour of concrete in tension is defined by a local criterion of rupture (2.32) between two elements a and b which was introduced by Sawamoto et al. [117]. This model can be found in several studies [11][64][91][103][112], it is presented in Figure 2.10 (left side) and as can be seen, it is brittle with a local tensile cut off stress T and a softening factor ξ and without plastic deformations of the link.

$$f_2(F_N, F_S) = -S_{int} T - F_N \quad (2.32)$$

Tensile damage function

The damage criterion (2.32) is activated if the normal displacement between two elements a and b is greater than the displacement (D_{damage}) associated with the local tensile strength (F_{tmax}).

$$F_{tmax} = -S_{int} T \quad (2.33)$$

$$D_{damage} = \frac{F_{tmax}}{K_N} \quad (2.34)$$

Beyond this displacement, the link passes into its softening regime where the normal stiffness is defined as $-\frac{K_N}{\xi}$ and it is limited to a maximum distance D_{max} .

$$D_{max} = \frac{F_{tmax}}{K_N} (1 + \xi) \quad (2.35)$$

When the distance of the two elements D_{ab} is bigger than the limit D_{max} , the cohesive link is broken and it cannot receive efforts anymore. Thus the two forces components become equal to zero $F_N = 0$ and $F_S = 0$.

Moreover, as can be seen in Figure 2.10 both the unloading-reloading stiffness ($K_{N,2}$) and the maximum tensile strength (F_{tmax}) of the softening branch are varying and they related with the distance D_{ab} between the two spheres a and b , which becomes the new D_{damage} .

$$D_{damage}^{t+1} = D_{ab} \quad (2.36)$$

$$F_{tmax}^{t+1} = F_{tmax}^t - \frac{K_N}{\xi} (D_{ab} - D_{damage}^t) \quad (2.37)$$

$$K_{N,2} = \frac{F_{tmax}^{t+1}}{D_{damage}^{t+1}} \quad (2.38)$$

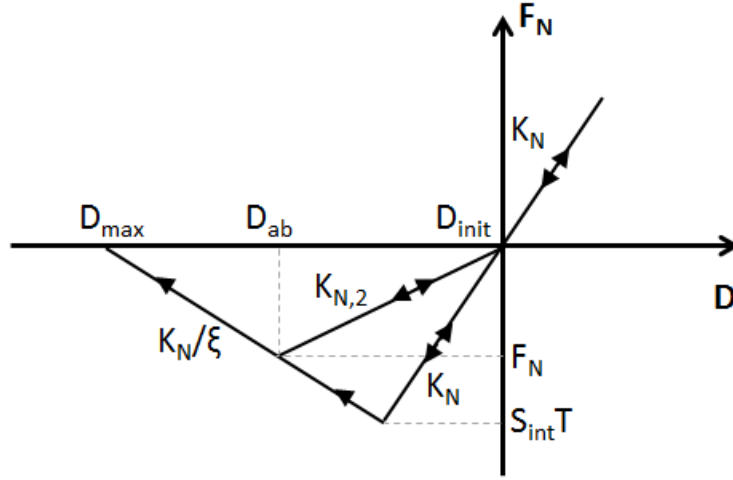


Figure 2.10: Non-linear tensile constitutive model, (Normal force – Displacement)

2.5.3 Compaction law

Figure 2.11(right side) illustrated the compressive non-linear constitutive behaviour of the link. We updated the constitutive model in compression to account for high confining pressures. As can be seen, the model is trilinear with an elasto-plastic-hardening behaviour and it can be described with the parameters: elastic compressive stress limit C_{cel} , plastic compressive stress limit C_{cpl} , and stiffness ratios ξ_1 and ξ_2 . This model was initially used by Shiu [124] and then by Tran [135]. The new model is based on the macroscopic behaviour of concrete under triaxial test and it describes as the compaction phenomenon which occurs under high confining pressures.

Once the elastic compressive limit (F_{cel}) is exceeded, the pore closure leads to a plastic regime with irreversible distance until the plastic compressive limit (F_{cpl}), where consolidation takes place. After, the collapse of porosity leads to a hardening branch. The stiffness of each branch is defined as the ratio of the initial stiffness of the link K_N over the parameters ξ_1 and ξ_2 respectively.

$$F_{cel} = S_{int} C_{cel} \quad (2.39)$$

$$F_{cpl} = S_{int} C_{cpl} \quad (2.40)$$

The elastic compression is limited at distance (D_{el}) (2.41) between the two spheres which is proportional to the initial normal stiffness (K_N) of the link.

$$D_{el} = \frac{F_{cel}}{K_N} \quad (2.41)$$

The maximum plastic distance limit (D_{pl}) (2.42) corresponds to the plastic branch and it is related to the difference between the plastic strength F_{cpl} and the elastic strength F_{cel} of the link over the stiffness $\frac{K_N}{\xi_1}$.

$$D_{pl} = D_{el} + \frac{F_{cpl} - F_{cel}}{K_N/\xi_1} \quad (2.42)$$

After the interaction distance exceeds the elastic limit (D_{el}), plastic-hardening behaviour takes place; where irreversible deformation appears (D_{eq}).

For a displacement D_{ab} greater than D_{el} and smaller than D_{pl} the interaction is located in the section BC, where:

$$F_N^{t+1} = F_{cel}^t + \frac{K_N}{\xi_1} (D_{ab} - D_{el}^t) \quad (2.43)$$

$$F_{cel}^{t+1} = F_N^{t+1} \quad (2.44)$$

$$D_{el}^{t+1} = \frac{F_N^{t+1}}{K_N} \quad (2.45)$$

$$D_{eq} = D_{ab} - D_{el}^{t+1} \quad (2.46)$$

When the displacement D_{ab} is greater than D_{pl} the interaction is considered in the section CD, where:

$$F_N^{t+1} = F_{cpl}^t + \frac{K_N}{\xi_2} (D_{ab} - D_{pl}^t) \quad (2.47)$$

$$F_{cel}^{t+1} = F_{cpl} \quad (2.48)$$

$$D_{eq} = D_{ab} - \frac{F_N^{t+1}}{K_N/\xi_1} \quad (2.49)$$

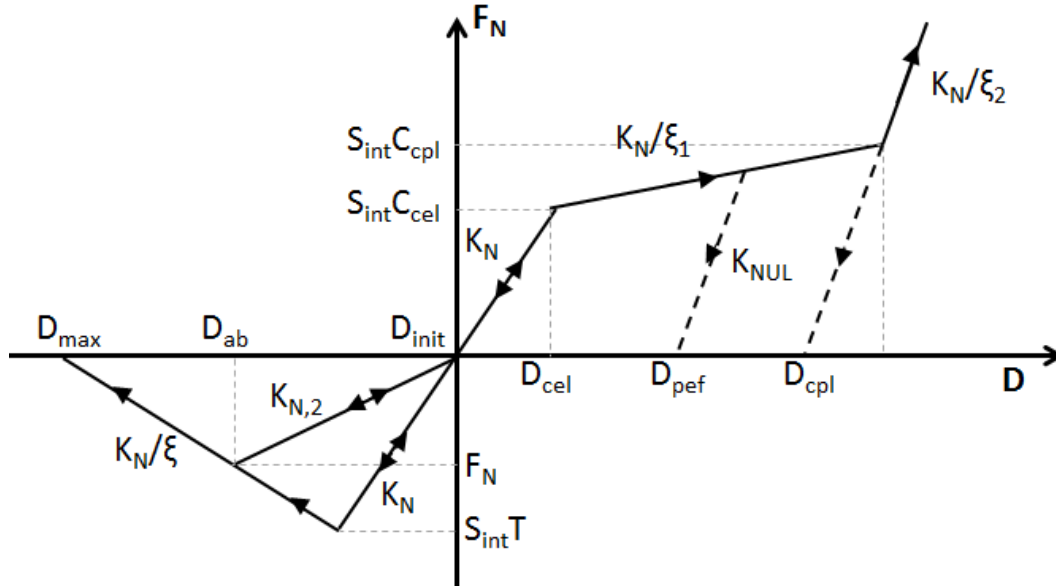


Figure 2.11: Non-linear tensile and compressive constitutive model, (Normal force – Displacement)

2.5.4 Mohr-coulomb modified criterion

Initially, a modified Mohr-Coulomb criterion with sliding function f_1 and a tensile damage function f_2 is used for cohesive links (2.50). When the tangential force (F_S) transcends the sliding function the tangential force is fallen onto the sliding criterion. The modified Mohr-Coulomb criterion of cohesive interactions consists from friction angle Φ_i , a cohesion stress C_o , a local tensile cut off stress T and a softening factor ξ . The softening factor ξ adjusts the tensile stiffness after damage in tension Figure 2.12. Once, the distance of the link is greater become greater than the maximum limit distance (D_{max}) the rupture criterion in tension is exceeded and the cohesive interaction is broken.

$$f_1(F_N, F_S) = |F_S| - \tan(\Phi_i) F_N - S_{int} C_o \quad (a. \text{Shear sliding function}) \quad (2.50)$$

$$f_2(F_N, F_S) = -S_{int} T - F_N \quad (b. \text{Tensile damage function})$$

Once two spheres come in contact, a new contact interaction is created, which follows a standard Mohr-Coulomb criterion with a contact angle Φ_c (2.51). The contact interaction cannot receive any tensile forces and is acting only in compression.

$$f_1(F_N, F_S) = |F_S| - \tan(\Phi_c) F_N \quad (2.51)$$

The criterion of contact interactions is expressed as:

$$f_1 \leq 0, \text{ the contact link is opposed to interpenetration}$$

$$f_1 = 0, \text{ the shear force follows the sliding function}$$

The microscopic parameters, contact Φ_c and frictional Φ_i angles, cohesion C_0 , local tensile strength T , and softening factor ξ , of the model described above need to be identified in order to result in macroscopic parameters, such as compressive σ_c and tensile σ_T strengths and fracture energy G_f . The macroscopic parameters are obtained from the quasi-static test in tension and compression. The compaction law parameters elastic compressive stress limit C_{cel} , plastic compressive stress limit C_{cpl} and stiffness ratios ξ_1 and ξ_2 are identified through inverse modelling of oedometric compression and hydrostatic compression tests.

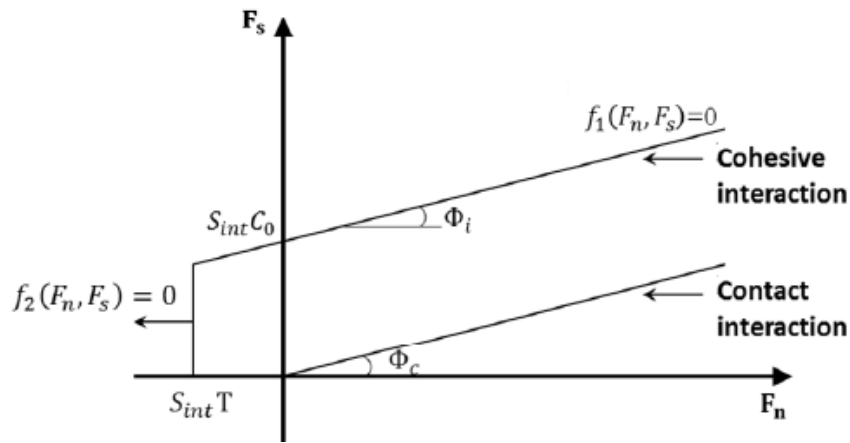


Figure 2.12: Modified Mohr-Coulomb criterion, Tangential force – Normal force.

2.5.5 Strain rate dependency

Experimentally has been observed that both the tensile [12] and compressive [9] strengths of concrete increase with strain-rate, especially when the strain-rate is greater than a transition strain-rate, which is around 10^0 - 10^1 s^{-1} for uniaxial tension and 10^2 s^{-1} for uniaxial compression. However, the increase of compressive strength is a structural effect. The inertia generates radial constrains acting like confining pressure, which increases the concrete compressive strength [12].

Hence the strain rate dependency is implemented in the phenomenological DEM model only in tension. This pragmatic choice allows a simple identification of the dynamic increase factor (DIF) through an inverse analysis based on the dynamic numerical simulation of spalling Hopkinson bar tests.

Omar [103] implemented first the strain rate dependency, in our DEM inspired by the CEB formula [20] to calculate the macroscopic dynamic tensile strength as a function of strain rate, equation (2.52). DIF is defined as the ratio of the dynamic tensile strength over the static tensile strength T_{dyn}/T_{st} . The initial model of Omar increases the maximum distance limit D_{max} using the same DIF ratio. Figure 2.13 shows the Initial constitutive model under dynamic loading.

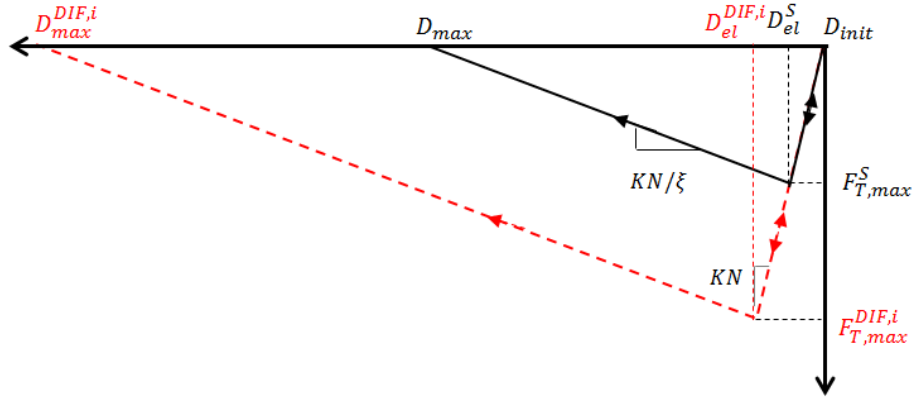


Figure 2.13: Initial constitutive model for dynamic loading

The use of DIF on the maximum distance limit D_{max} results in an increase of fracture energy under dynamic loading (Gf_D) equal to DIF^2 , which is not realistic. The present study introduces a ratio, of the dynamic over the static maximum distance limits D_{max} , which follows the equation (2.55) to correctly preserve the fracture energy (Gf_D) under dynamic conditions equation (2.56). Thus the ratio of static over the dynamic fracture energy is proportional to the product of DIF and the maximum distance limit ratio. Hence the softening branch becomes more brittle with the increase of DIF. The stiffness of the softening branch is controlling by the equation (2.53). Figure 2.14 illustrates the modified constitutive model under dynamic loading. The local parameters: static strain rate ($\dot{\epsilon}_{st}$), moderate strain rate ($\dot{\epsilon}_m$), δ_1 and δ_2 are calibrated with the help of a spalling Hopkinson bar test [3]. Figure 2.14 displays the tensile constitutive model under static and dynamic loadings.

$$DIF = \frac{T_{dyn}}{T_{st}} = \begin{cases} 1 & \text{if } \dot{\epsilon} \leq \dot{\epsilon}_{st} \\ \left(\frac{\dot{\epsilon}}{\dot{\epsilon}_{st}}\right)^{\delta_1} & \text{if } \dot{\epsilon}_{st} < \dot{\epsilon} \leq \dot{\epsilon}_m \\ \theta \left(\frac{\dot{\epsilon}}{\dot{\epsilon}_{st}}\right)^{\delta_2}, \theta = \left(\frac{\dot{\epsilon}_m}{\dot{\epsilon}_{st}}\right)^{(\delta_1 - \delta_2)} & \text{if } \dot{\epsilon} > \dot{\epsilon}_m \end{cases} \quad (2.52)$$

$$KN_{DIF,i} = KN_{DIF,1} + (KN_{DIF,max} - KN_{DIF,1}) \left(\frac{DIF - 1}{DIF_{MAX} - 1} \right) \quad (2.53)$$

$$\frac{1}{\xi_{DIF,i}} = \frac{1}{\xi} + \left(\frac{1}{\xi_{MAX}} - \frac{1}{\xi} \right) \left(\frac{DIF - 1}{DIF_{MAX} - 1} \right) \quad (2.54)$$

$$\frac{D_{max}^{DIF,i}}{D_{max}} = \frac{DIF (1 + \xi_{DIF,i})}{1 + \xi} \quad (2.55)$$

$$\frac{Gf_D}{Gf_S} = \frac{DIF^2 (1 + \xi_{DIF})}{1 + \xi} \quad (2.56)$$

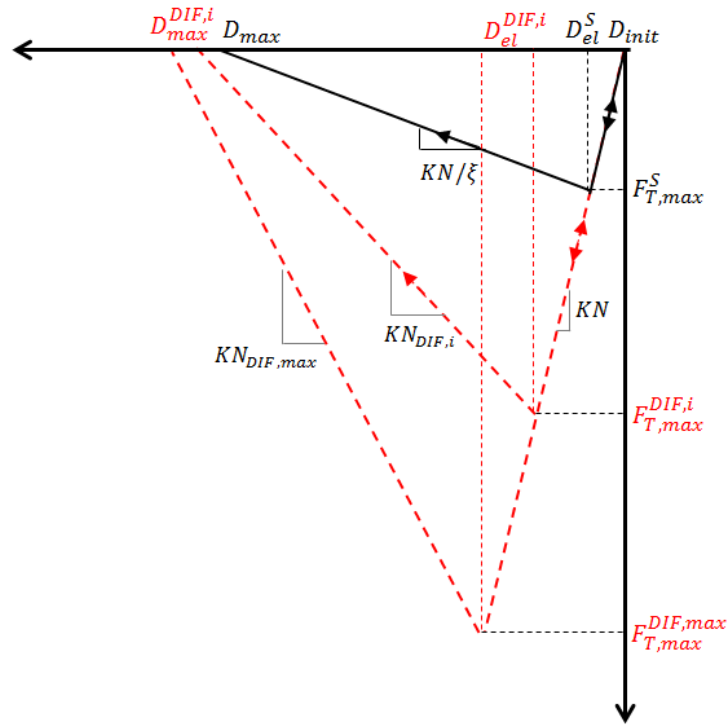


Figure 2.14: Modified constitutive model for dynamic loading

Furthermore, Erzar and Forquin [42] in 2014 showed that the shear response of concrete is also strain rate dependent. The dependency in shear is significantly lower in shear than in tension. However, it is necessary to account for the loading influence on the constitutive law of tangential interactions. For this reason, we limited the value of the dynamic increase factor (DIF) in shear to 2 with the dynamic cohesion to be $C_{0DYN} \leq 2$. The Mohr-Coulomb criterion

under dynamic loading is presented in Figure 2.15 with red colour. Thus, the limit of dynamic tensile stress T_{MAX} is described as the ratio of C_{0DYN} over the tangent of φ_i and the DIF_{max} is given from the equation (2.57).

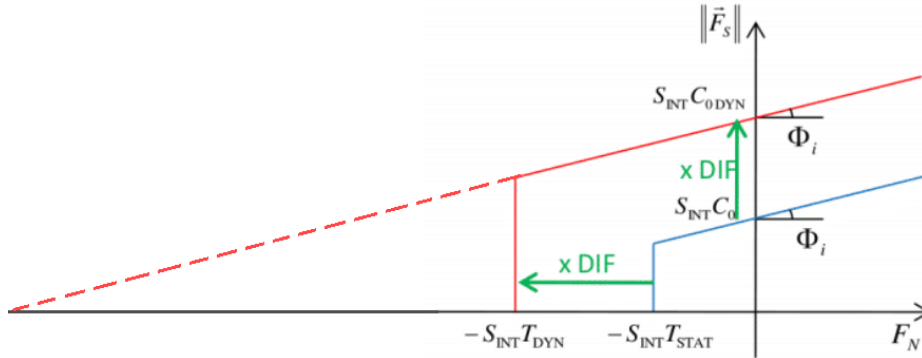


Figure 2.15: Mohr-Coulomb criterion for dynamic loading

$$DIF_{max} = \frac{2.0 C_0}{\tan(\varphi_i) T} \quad (2.57)$$

2.6 Steel-Concrete bond model

There is the need for a constitutive law to represent the steel reinforcement and its interaction with concrete to model reinforced concrete structures. Rousseau [112] used aligned discrete elements to model steel rebars and beam-like interactions between them and the concrete discrete element. Although, complex grids of reinforcement in real structures induce incontinence with complicates mesh.

For this reason, Masurel [91] developed a new model with finite beam-like elements for the steel rebar. In addition, he implemented a special concrete-steel bond model for the interactions between the concrete spherical DE and the steel FE. This model describes the interaction between a given rebar and a group of neighbouring discrete elements by using two non-linear springs, one normal and one tangential to the direction of the rebar. The behaviour of the normal spring is elasto-plastic in compression and brittle in tension, whereas the tangential one relies on the response of the concrete-steel link observed in pull-out tests. This model decouples the normal and tangential forces of the steel-concrete interface. Potapov et al. [107] calibrated this mixed DEM/FEM approach by simulating the steel-concrete link with pull-out tests.

2.6.1.1 Constitutive model of the normal steel-concrete bond interaction

The constitutive law of the steel-concrete interaction for the normal spring was initially proposed by Rousseau [112]; is presented to be brittle in tension and elasto-plastic in compression (Figure 2.16). The linear elastic regime is described by the normal stiffness K_N which connects the interaction with the normal force F_N to its normal displacement u_N . This interaction is modelled as a beam-like element with circular cross-section (S_{int}) and initial distance (h^0) between the two elements; hence the normal stiffness (K_N) is given from the Equation (2.58):

$$K_N = \frac{E S_{int}}{h^0} \quad (2.58)$$

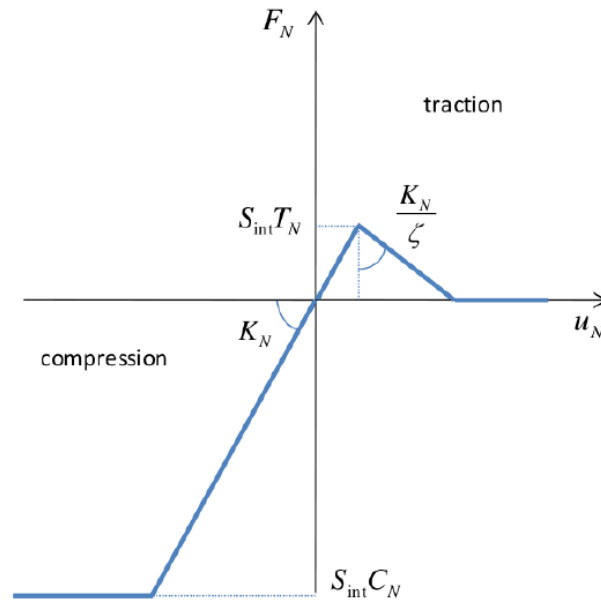


Figure 2.16: Steel-concrete interaction law in normal direction (Masurel [91]).

As has been explained by Rousseau [112]; Young's modulus (E) of the steel-concrete interaction is taken equal to concrete's because the response of the interface zone is associated with the behaviour of the concrete. The interaction cross section is related with the concrete discrete element radius R_j , thus $S_{int} = \pi R_j^2$. The initial distance (h^0) is the distance between the centre of the concrete discrete element j to the reinforcement finite element i .

Steel-concrete tensile constitutive behaviour is similar to concretes behaviour in tension; where after the peak stress (T_N) the interaction is damaged following a softening regime with stiffness $\frac{-K_N}{\zeta}$. Then, it breaks after exceeding the threshold of the maximum allowed distance between the concrete discrete element (j) and the steel finite element (i). After, the interaction becomes a contact link in order to prevent interpenetration of the two elements. In compression, the interaction is subjected to perfect plasticity after the stress limit (C_N).

2.6.1.2 Constitutive model of the tangential steel-concrete bond interaction

The constitutive model of the steel-concrete interaction for the tangential spring is inspired by Torre-Casanova [133] and it is based on the global adhesion stress-sliding response of the bond. Following this idea, Masurel [91] introduced a multipoint law that reproduces the stress-slip curve observed in the pull-out test which differs for high-strength rebar and smooth rebar. One can select the number of points for the discretisation the adhesion law in function of sliding $\tau = f(u_s)$ in order to give the best description for the different rebar types. An example of such a discretisation of the experimental curves of Hamouine et al. [59] (Figure 2.17 left) is shown in Figure 2.17 right, on which 9 points are chosen to represent the curve of the high strength rebar and 6 points for the smooth rebar.

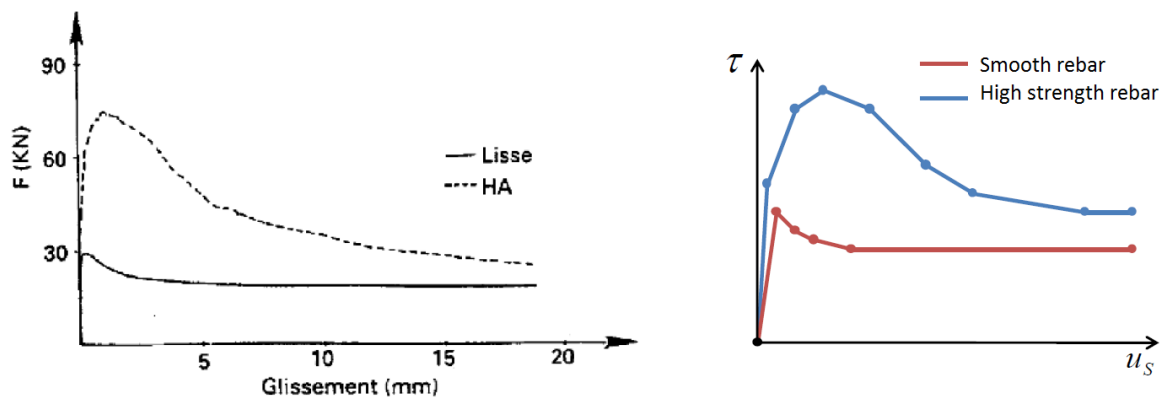


Figure 2.17: Experimental stress-slip curve (left) (Hamouine et al. [59]), multipoint law (Masurel [91])

2.6.2 Significant sliding

Severe loading can impose intense damage on the steel-concrete interface and slip between reinforcement and concrete becomes very important. The steel-concrete interaction is the projection of the concrete discrete element centre on the steel finite element beam, from which distances are drawn to determine the interaction forces. Once, the tangential displacement is very large the

projection may leave the steel finite element beam to which it was connected at the initial step and move on the neighbouring beam element.

It is crucial to maintaining the equilibrium of the steel-concrete interaction in order to avoid instabilities. Its two components (normal and tangential) are decoupled; thus the balance of each component is treated separately.

For the normal component of the bond, when the projection of the discrete element slides on the neighbouring beam element, a normal interaction is created with it. The interaction force of the normal component is given by the equation (2.59) at every time step and it is relating the distance between the centre of the discrete element and its orthogonal projection at the beam element (point P_N).

$$F_N = -K_N(h^n - h^0) \quad (2.59)$$

The normal force computed on the point P_N is then redistributed on the nodes of the given reinforcement beam element. For this reason, even though the interaction slides on the neighbouring beam element; the normal component forces are always in equilibrium for both translation and rotation (Figure 2.18).

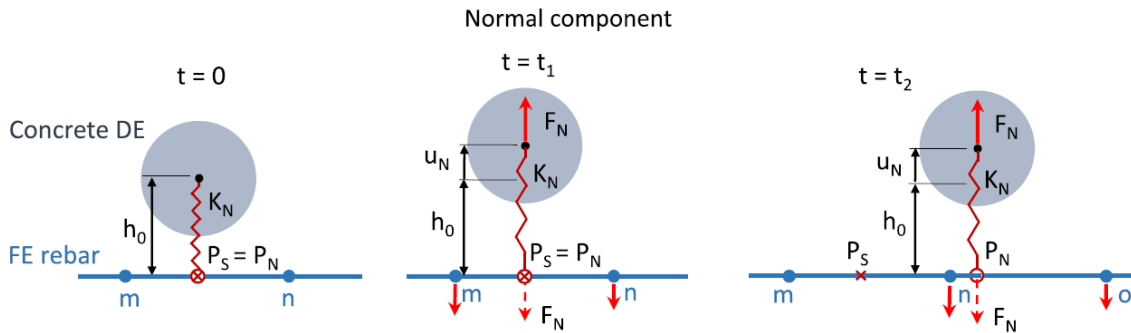


Figure 2.18: Normal behaviour event of significant sliding (Potapov et al. [107])

The tangential component applies resistance to the sliding of the concrete discrete element and it has a different projection on the rebar beam element (point P_S), which it cannot move from its initial position. The tangential force of the steel-concrete interaction is given from the equation (2.60).

$$F_S = -K_S u_S \quad (2.60)$$

Similarly to the normal component, the tangential force is distributed on the nodes of the beam element with the projection of the point P_N . However, the tangential forces are balanced only in

translation but not in rotation, which can lead to instabilities. Two vertical reaction forces R_m and R_n are applied to the same nodes and are computed by using Newton's second law Figure 2.19.

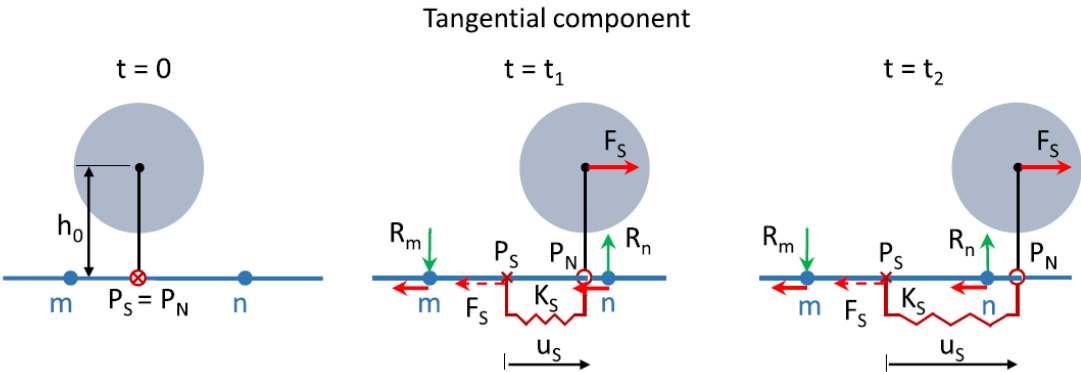


Figure 2.19: Tangential behaviour event of significant sliding (Potapov et al. [107])

2.6.3 Steel-concrete interaction zone

The proposed model for the steel-concrete interface is established by the orthogonal projection of the neighbouring concrete discrete element on a given rebar finite element. Therefore, it is necessary to determine an interaction zone around the reinforcement; where the steel-concrete links will be created. The initial distance of this interaction range D_{int} is dependent on the rebar radius R_s multiplied by a coefficient λ_s , as has been decided by Masurel [91] (2.61).

$$D_{int} = \lambda_s R_s \tag{2.61}$$

Figure 2.20 shows an example for the determination of the steel-concrete interaction zone, which is limited in a zone of D_{int} above and below the centre of the beam finite element. Then, a steel-concrete interaction is created when the distance of discrete element centre orthogonal projection on the beam finite element $D_{s,c}$ is less or equal than the interaction range (2.62).

$$D_{s,c} \geq D_{int} \tag{2.62}$$

A sensitivity study is necessary to study the influence of the mesh parameters on the mesh characteristics and on the macroscopic behaviour of the model. In addition, the effect of each constitutive law parameter should be thoroughly understood; hence a procedure for the calibration of those parameters can be established. Finally, the model parameters need to be identified on simple laboratory experiments such as quasi-static compressive and tensile test, hydrostatic and oedometric test and spalling Hopkinson bar tests.

Chapter 3

Identification procedure of the parameters for the discrete element mesh and the concrete constitutive model

The current discrete element approach derives from the phenomenological behaviour of concrete observed at the macroscale. This model consists of local constitutive laws describing interactions between two particles. However, as has been mentioned the discrete elements do not represent the constituents of the concrete (aggregates, cement paste, voids etc.) and our model does not take into account the effect of free water, but the model aims to reproduce the macroscopic experimental behaviour of concrete. For this reason, several parameters need to be identified through quasi-static and dynamic tests.

Moreover, before calibrating the constitutive model, it is necessary to establish a set of parameters for the mesh creation. This set of parameters is of critical importance because the macroscopic behaviour of the constitutive model depends on the particles assembly. The two basic parameters that affect the packing are the ratio of the radii $k_1 = \frac{R_{max}}{R_{min}}$ and the compactness c , which can be controlled through the geometric algorithm of the packing method (Jerier et al. [71]). Once, the mesh assembly is created the interaction range coefficient λ is defined in order to satisfy the arbitrary choice by Rousseau [112], of twelve links in average per discrete element. In addition, moment transfer law constitutive law introduced to offer shear capacity in the model. The study of Omar [102] showed the influence of the MTL parameters rolling stiffness coefficient β_r and plastic limit coefficient η on the macroscopic behaviour. In particular, the rolling stiffness coefficient β_r has a small influence on Young's modulus and the plastic limit coefficient η affects the non-linear

behaviour. The interdependency of parameters complicates the identification procedure; thus we chose to fix the MTL parameters at the beginning to simplify the calibration process of the other parameters.

Afterwards, the identification procedure of the linear elastic parameters α , β and γ as is based on the results obtained by Huang [68] which demonstrated the reliance of Young's Modulus E and Poisson's ratio ν on the ratio of shear over normal stiffness $\frac{K_S}{K_N}$, for a given particles distribution. Those three parameters are computed on the linear branch of quasi-static compression and tension tests. The macroscopic non-linear branch of the quasi-static compression and tension tests is reproduced by adjusting the microscopic parameters contact Φ_c and frictional Φ_i angles, cohesion C_0 , local tensile strength T , and softening factor ξ . Next is the calculation of compaction law parameters elastic compressive stress limit C_{el} , plastic compressive stress limit C_{pl} and stiffness ratios ξ_1 and ξ_2 using high confinement pressure tests (oedometric and hydrostatic). Finally, concrete's dynamic behaviour is described by the dynamic increase factor where DIF parameters are defined on dynamic spalling Hopkinson bar tests.

3.1 Identification of the parameters for the mesh generation

3.1.1 Influence of boundary conditions

Hentz [64], Rousseau [112], Masurel [91] and Omar [103] used a different configuration for the quasi-static simulation mesh. The loading was applied directly to the discrete elements by blocking the lateral displacements of a layer of particles at the external sides in the normal direction of the long side. Figure 3.1 shows the quasi-static mesh used in previous studies after loading; the blue particles on the edges represent the loading zones.

During this study has been found that the calculation results to a different damage mode than the experimental. The main reason, this behaviour induced was the roughness between the contact surface of the DE loading zones and the DE of the specimen. For this reason, the linear-elastic quasi-static behaviour parameters and the cohesion stress C_0 were not estimated correctly, because this roughness gives additional friction to the model and the deformed specimen tends to a barrel shape due to Poisson's effect.

It should be noted that damage is defined at each time step as a ratio of remaining cohesive links of the considered DE over the initial number of its cohesive links. The damage scale (Figure 3.1) ranges between blue (no damage) and red (all the links are broken).

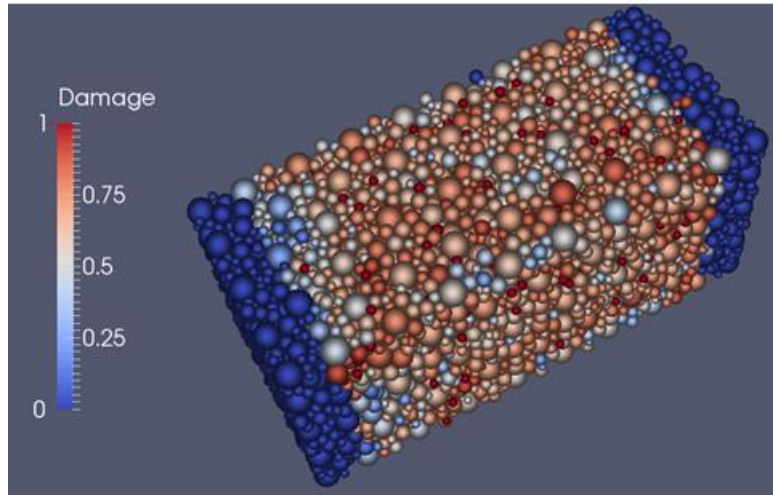


Figure 3.1: Quasi-static discrete element meshes after loading with blocked lateral loading zones

Two solutions have been tried to address this problem and eliminate the undesired friction between specimen and plates.

The first trial was to unblock the lateral displacements of the loading DE zones. This solution did not work, because as can be seen in Figure 3.2, the loading zones are crushed. The crushing of these areas has been observed even before the specimen reach to a failure. The loading plates are weaker than the specimen since the entire specimen is modelled with the same material properties (concrete) and the areas that are imposing the loading are thinner than the specimen. Therefore, the drawback of this trial is the loss of the rigidity of the loading sections.

The second trial was to model the loading zones with rigid elements. Contacts were created between the rigid element and the DE by defining a layer of nodes from the specimen as slave nodes following the kinematic conditions of the loading zones. Those contacts are kept frictionless for calculating the linear-elastic quasi-static parameters since experimentally there are no movements between the specimen and the loading plates during the linear regime. Once these parameters are calibrated, a friction coefficient of 0.5 (found in literature from the study of Burak and Tuncan [15]) is added at the steel-concrete interface to compute the non-linear plastic quasi-static parameter.

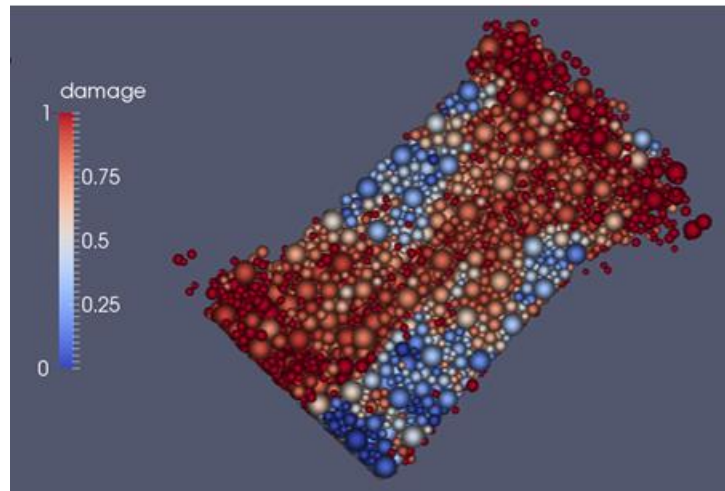


Figure 3.2: Quasi-static discrete element mesh after loading with unblocked lateral loading zones

Figure 3.3 shows the experimental damage mode under uniaxial quasi-static compression (left side) and the mesh after the simulation loaded by rigid elements (right side). It is evident that this solution is better than all the previous since it can well reproduce the cone damage pattern.

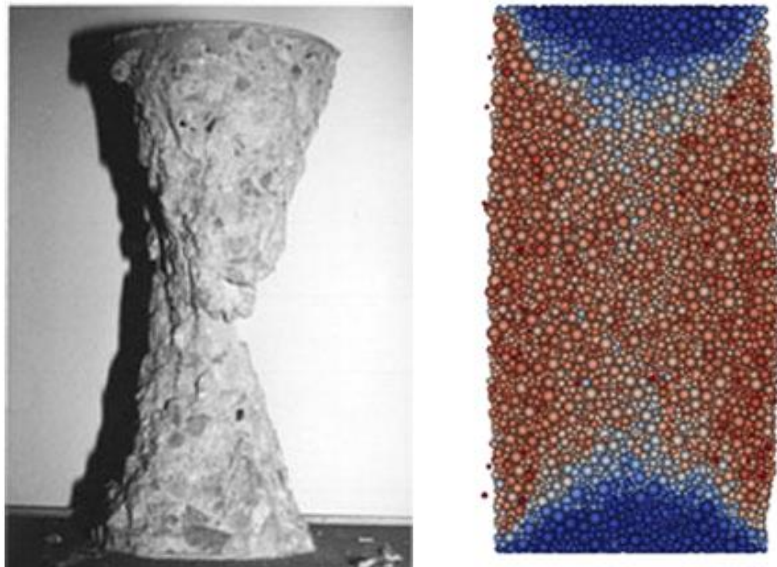


Figure 3.3: Quasi-static experiment damage mode (left) discrete element mesh after loading with rigid elements for the loading zone (right)

In this PhD study we will simulate hard impacts with projectiles of complex geometry and in EUROPLEXUS the shapes of rigid elements are limited to the basic (parallelepiped, cone, and cylinder). Thus, we will use finite elements to model the impactors or other steel parts. Thus, one of the most important parameters is the ratio between finite element sizes and discrete element sizes

in contact. The size of the two types of objects affects the overall behaviour of the specimen. In order, to confirm the proper force transfer from the one type (finite element) of to the other one (discrete element), we performed quasi-static compression simulation by replacing the rigid loading zones to finite elements plates Figure 3.4. The FE plates were discretised with different element types (hexahedral, tetrahedral) and different sizes Figure 3.5. The DE diameters and the size of the FE are listed in Table 3.1 and Table 3.2. Furthermore, the comparison between the finite element size and the maximum, minimum and mean discrete element diameter is given in the three last columns in Table 3.2.

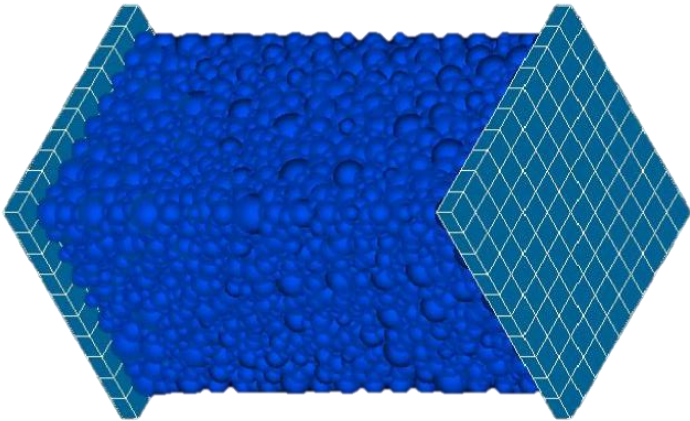


Figure 3.4: Quasi-static compression test mesh with finite element loading plates

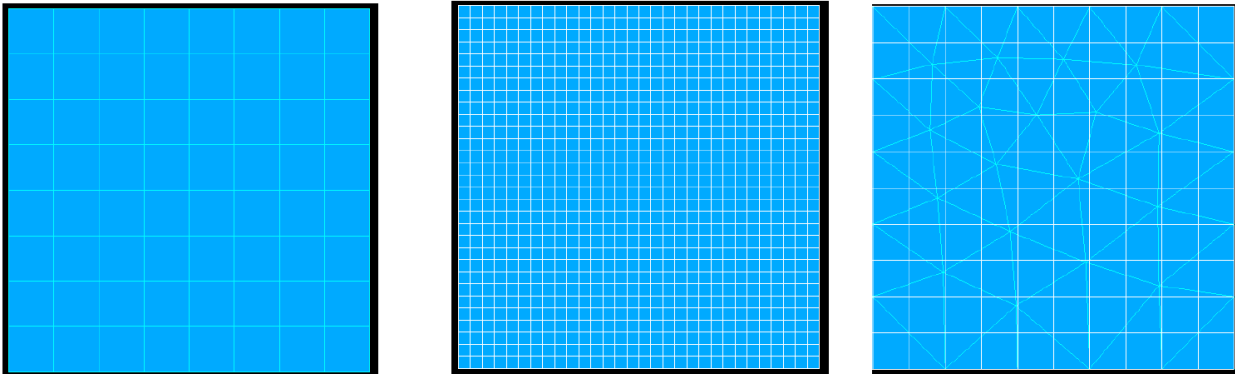


Figure 3.5: FE loading plate discretization 8 hexa (left), 30 hexa (middle), 10 hexa with 5 tetr (right)

Mesh	Dmax (mm)	Dmin (mm)	Dmean (mm)
DE concrete	7.196	2.399	3.741

Table 3.1: DE diameters

FE-TYPE	#FE/side	Size (mm)	Dmax	Dmean	Dmin
HEXA	8	10	bigger	bigger	Bigger
HEXA	10	8	bigger	bigger	Bigger
HEXA	12	6.67	smaller	bigger	Bigger
HEXA	18	4.45	smaller	bigger	Bigger
HEXA	20	4	smaller	bigger	Bigger
HEXA	22	3.64	smaller	smaller	Bigger
HEXA	30	2.67	smaller	smaller	Bigger
HEXA	40	2	smaller	smaller	Smaller
TETR	5	16	bigger	bigger	Bigger
TETR	10	8	bigger	bigger	Bigger

Table 3.2: FE size and type

Figure 3.6 and Figure 3.7 present the results of the simulations of the different finite element plates. It is obvious that when the FE size is smaller than the smallest DE diameter the contact between the two (FE and DE) is not sufficient and the simulation of the compressive test is not reliable. On the contrary, for all the FE discretisation with bigger size than the spheres diameters the results converge. Moreover, the result of a FE size bigger than the mean DE and smaller than the maximum DE can be considered efficient; although the curves 18 and 20 in Figure 3.6 have a small inclination from the curves 8 and 10. Curve 12 seems to adapt well with the curves 8 and 10, even though the FE size is smaller than the maximum DE but with a very small difference in dimensions. Thus, one can conclude that the condition of FE size bigger than the mean DE diameter should be respected, for a proper contact between FE and DE.

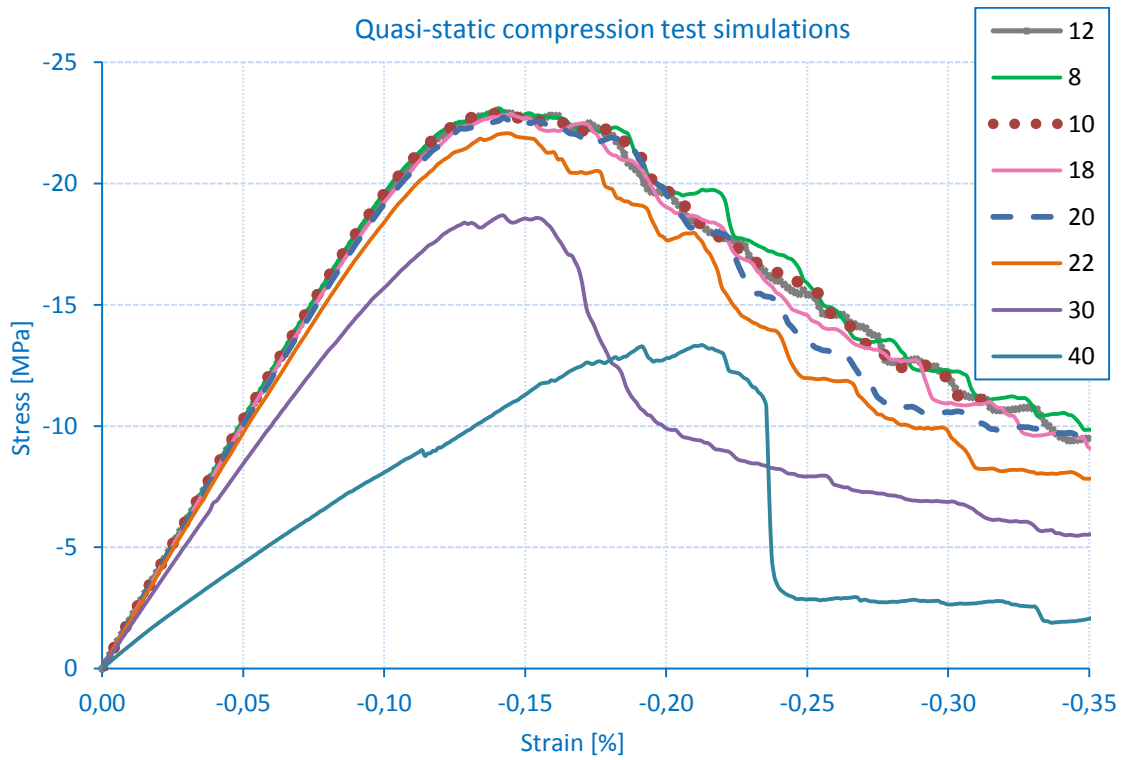


Figure 3.6: HEXA finite element size influence

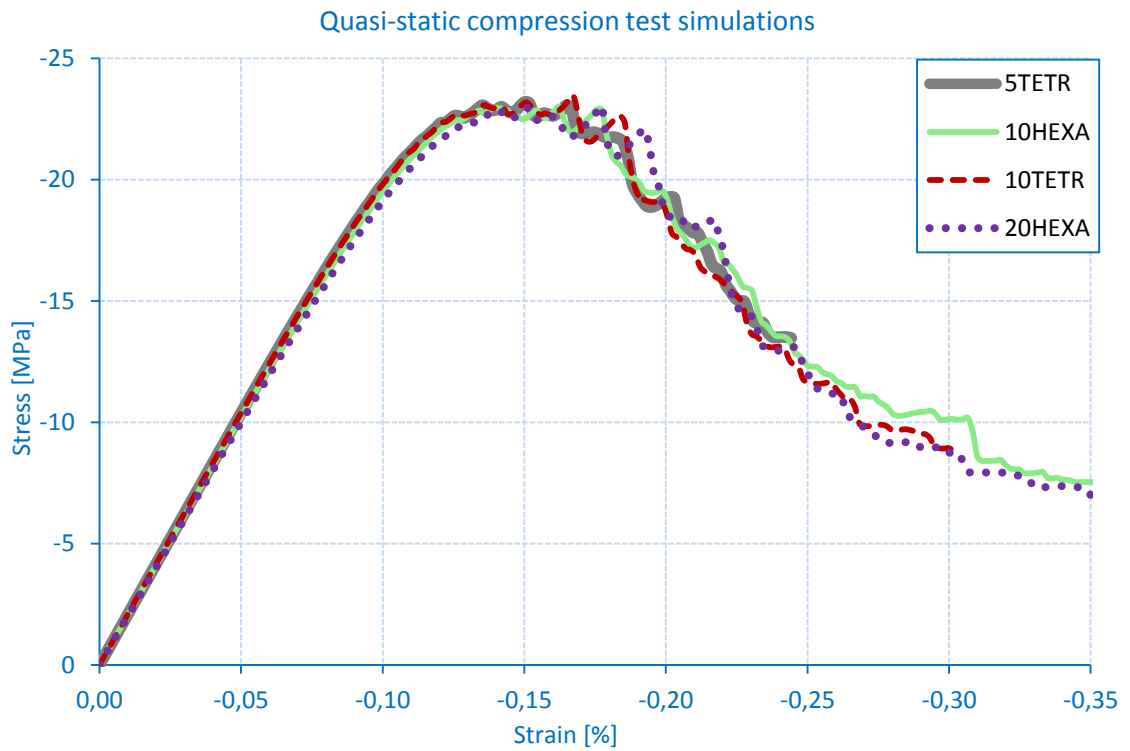


Figure 3.7: FE size and type influence

3.1.2 Mesh generation parameters

In this unity, we will prove that the parameters of our discrete element constitutive model are not mesh dependent only if all the meshes are created using the same procedure of mesh discretisation. For this reason, the mesh creation parameters need to be identified before the calibration of the model. We will study the influence of the mesh generation parameters not only on the macroscopic behaviour but also on the mesh characteristics. We are seeking of an isotropic and homogeneous mesh with the least possible amount of particles thus the computational cost remains rational.

Several assumptions need to be made for the creation of the discrete element mesh to ensure macroscopic homogeneity and isotropy. The mesh generation parameters are defined on the quasi-static compression test. Initially, the geometry of the specimen needs to be selected; a parallelepiped with dimensions is $0.07 \times 0.07 \times 0.14 \text{ m}^3$. In contrast, the experimental specimens are cylindrical however the first assumption is to use a parallelepiped mesh with the same slenderness of samples, for the sake of simplicity of postscript strains computations.

First, the packing method uses a tetrahedral mesh to generate an assembly of discrete elements; thus the volume of the specimen is discretised with tetrahedral finite elements. Then, the ratio $k_1 = \frac{R_{max}}{R_{min}}$ and FE tetrahedron edge length over the mean DE diameter $k_2 = \frac{FE_{edge}}{DE_{mean}}$ are selected. As has been shown by Potapov et al. [107] a mesh with four tetrahedral per short side, $k_1=3$ and $k_2 = 4$ produces a satisfying homogeneous and isotropic discrete element assembly. However, for the present study different meshes are created by varying all the parameters of the geometric mesh algorithm (number of FE per short side, k_1 , k_2 and iterations of densification phase). Table 3.3 presents six Table 3.3s in order to detect the influence of the mesh creation parameters on the assembly characteristics and the macroscopic behaviour of the sample.

A FE mesh with four tetrahedral per short side, $k_1 = 3$ and $k_2 = 4$ is employed for the four first meshes, since the set of these parameters offer the desired homogeneity and isotropy according to Potapov et al. [107]. Those four meshes differ in the number of iterations for the densification phase of the packing. The fifth mesh is selected to be similar to the second by increasing the ratio k_1 from three to five. Finally, the sixth mesh is entirely different from the rest, it represents a loose mesh like the one used by Rousseau [112] and all the parameters are selected based on her mesh. It should be mentioned that Rousseau generated her mesh with SDEC software that creates DE assemblies only for simple geometries. The last mesh was a good example to observe that a very loose mesh is not adequate to represent the local constitutive behaviour of the interactions.

3.1.2.1 Influence of mesh generation parameters on the mesh characteristics

k_1 : By increasing the ratio of the maximum over the minimum radius the compactness, the maximum radius of the DE mesh, the number of discrete elements and the coefficient of interaction range are increasing, while the minimum radius is decreasing.

k_2 : By increasing the number of discrete elements per finite element the number of discrete elements and the compactness is decreasing, whereas the size of the particles and the coefficient of interaction range are increasing. However, we noticed that when this ratio is equal to 4 is giving the densest mesh.

Number of iterations: By increasing the number of iterations, the number of discrete elements and the compactness of the DE mesh are increasing. Also, after the 3rd iteration (or 5th for big values of k_1 like 12) the compactness of the mesh does not change.

Mesh	FE number per side	k_1	k_2	Iterations	DE Total number	R_{max} (cm)	R_{min} (cm)	Compactness	λ
1	4	3	4	0	7096	0.36	0.12	0.503	1.4802
2	4	3	4	2	11018	0.36	0.12	0.588	1.3984
3	4	3	4	5	11540	0.36	0.12	0.595	1.3896
4	4	3	4	10	11547	0.36	0.12	0.594	1.3894
5	4	5	4	2	19025	0.4	0.08	0.615	1.4227
6	3	4.133	4.39	0	2145	0.53	0.13	0.459	1.5191

Table 3.3: Mesh generation parameters and assembly's characteristics

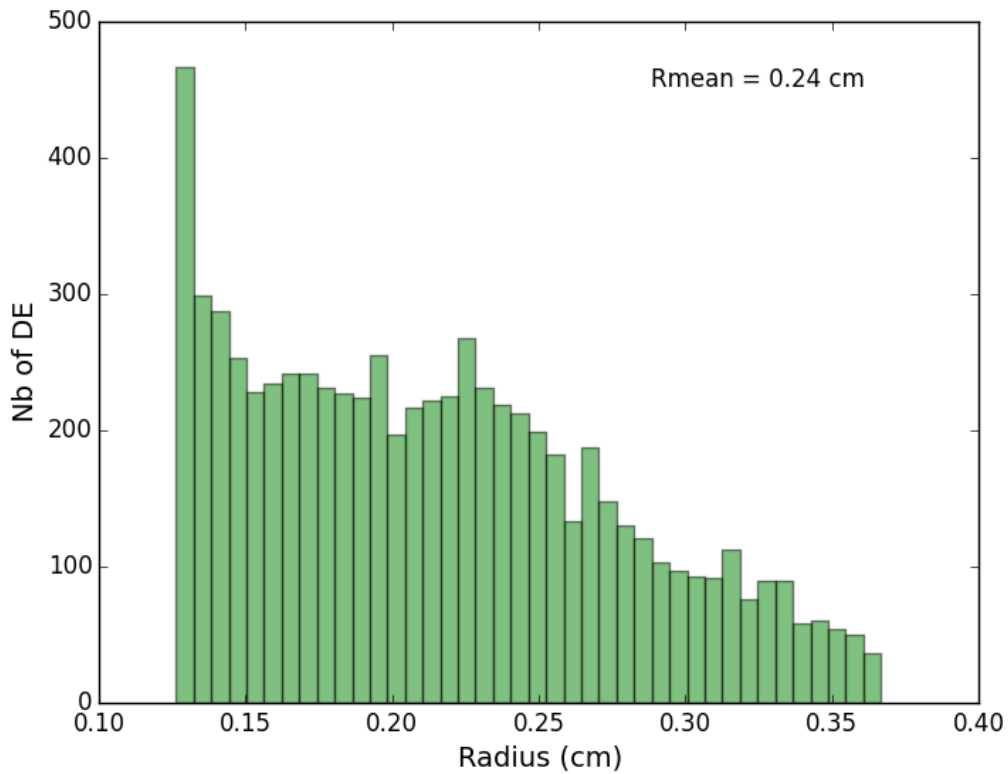


Figure 3.8: Mesh 1 histogram of radius distribution

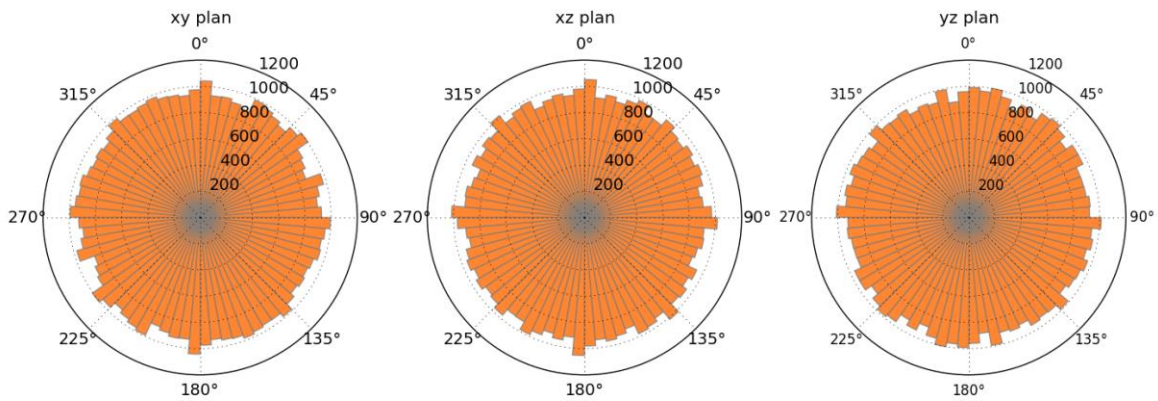


Figure 3.9: Mesh 1 orientation of interaction in the three planes

Figure 3.8 gives the histogram of the mesh 1 size distributionFigure 3.8;; this packing shows some irregularity in the middle with almost a plateau with around 200 elements for radius between 0.15 cm and 0.25 cm. The highest and lowest peaks of the figure appear at the maximum radius (470 elements) and the minimum radius (35 elements). Figure 3.9 shows the orientation of interactions in the three planesFigure 3.9; this mesh seems to be isotropic with approximately 800 – 900 links in every direction.

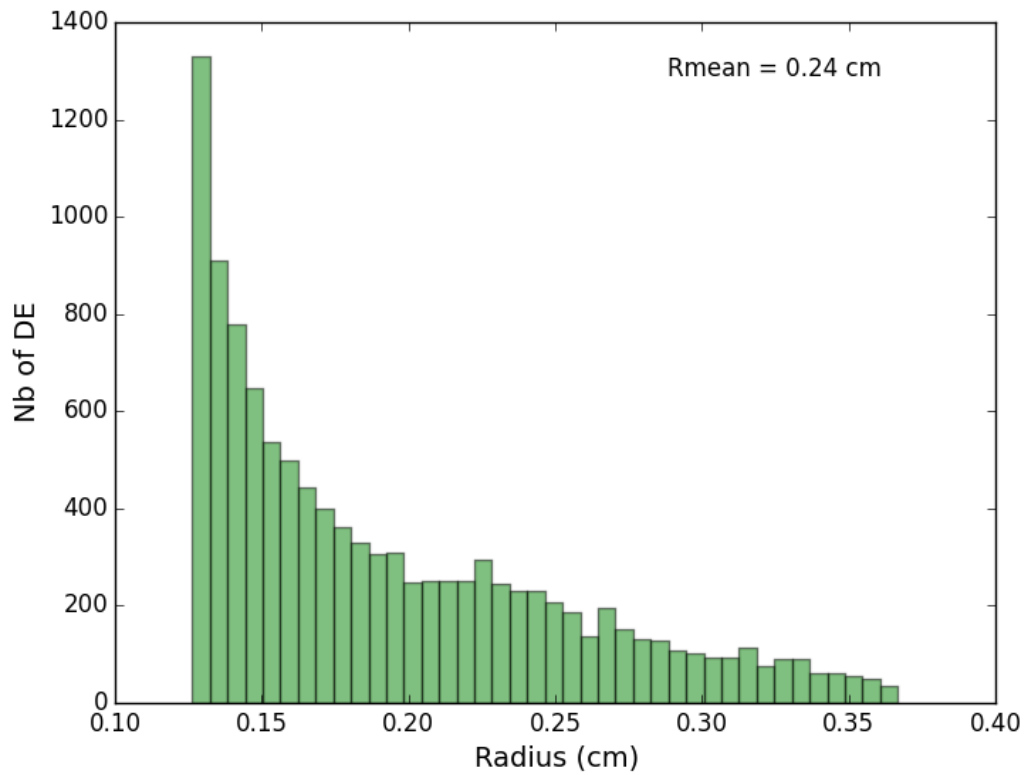


Figure 3.10: Mesh 2 histogram of radius distribution

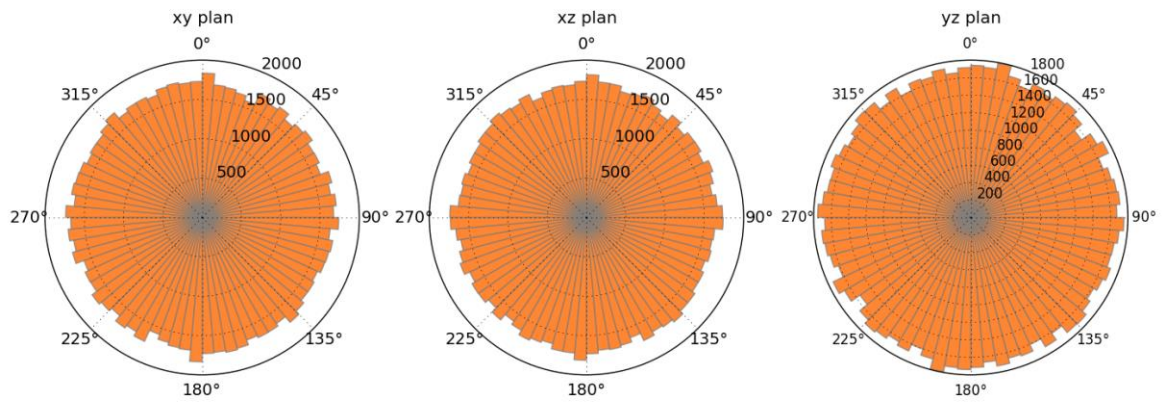


Figure 3.11: Mesh 2 orientation of interaction in the three planes

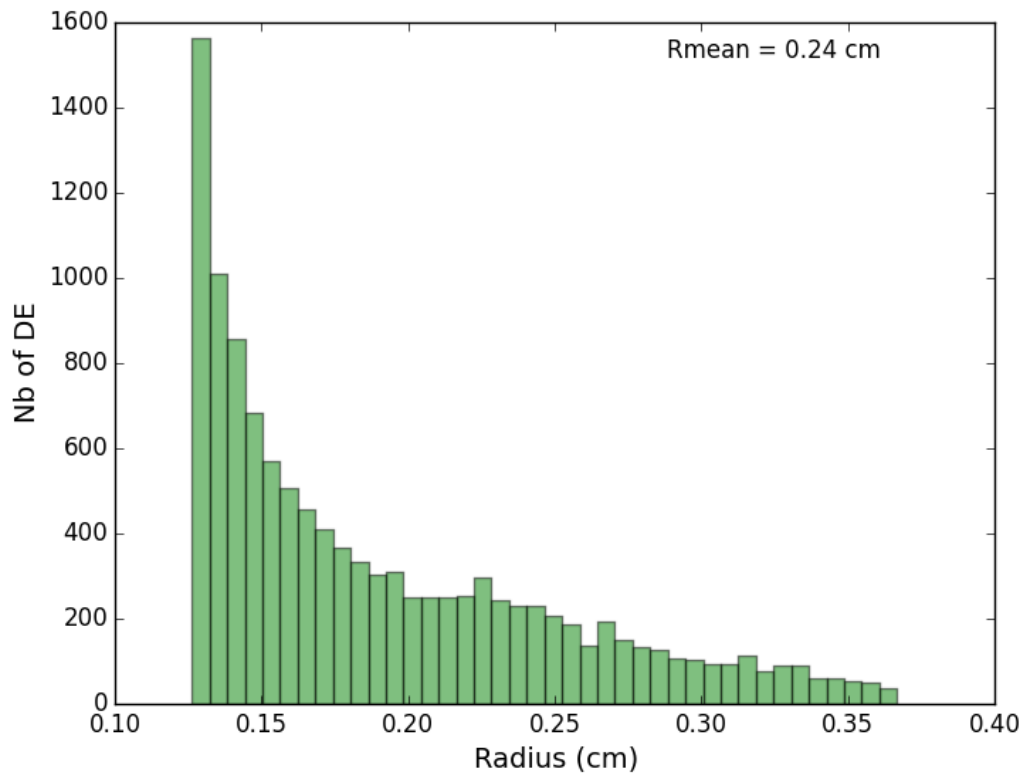


Figure 3.12: Mesh 3 histogram of radius distribution

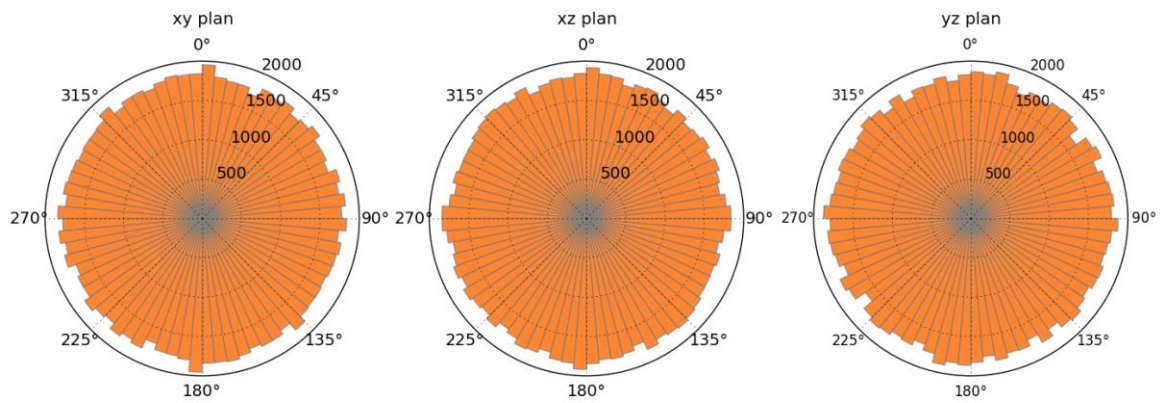


Figure 3.13: Mesh 3 orientation of interaction in the three planes

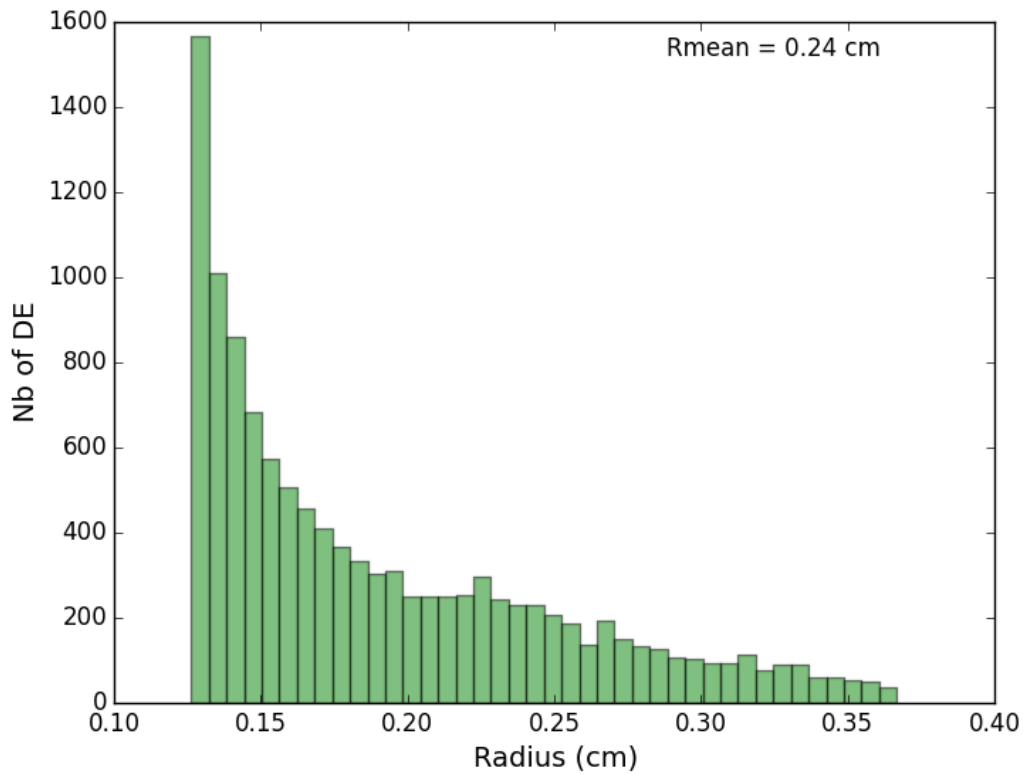


Figure 3.14: Mesh 4 histogram of radius distribution

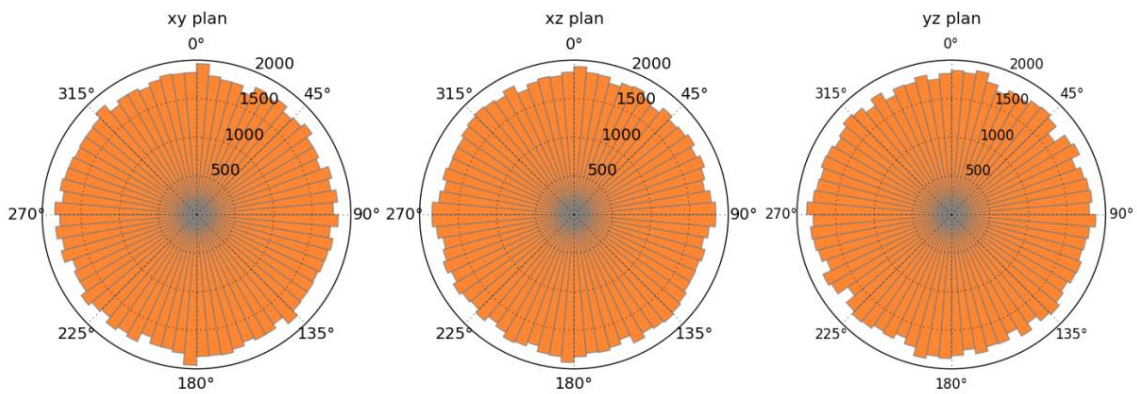


Figure 3.15: Mesh 4 orientation of interaction in the three planes

The histograms of sphere distribution of the mesh 2, mesh 3 and mesh 4 are illustrated in Figure 3.10, Figure 3.12 and Figure 3.14. As can be seen, those three meshes are quite similar with a regular degradation of the histogram distribution. Also, Table 3.3 demonstrates similar compactness for the three of them (0.59-0.6) and their coefficients λ are almost the same; although the total number of elements of the second mesh is lower than the total number of elements of the third and the fourth meshes, with a difference of 500 spheres. Mesh 3 and mesh 4 have almost the same amount of

particles. Figure 3.11, Figure 3.13 and Figure 3.15 display the interaction orientations, the three packing are isotropic. Mesh 2 appears approximately 1600 links in all the directions, while the links for mesh 3 and mesh 4 are increasing to nearly 1700. In contrast, mesh 1 has very few discrete elements 4000 less than the three other meshes and its number of links pre direction is almost half than these three other meshes. Thus mesh one seems to be weaker than mesh 2, mesh 3 and mesh 4. For this reason, zero iteration of densification should be avoided.

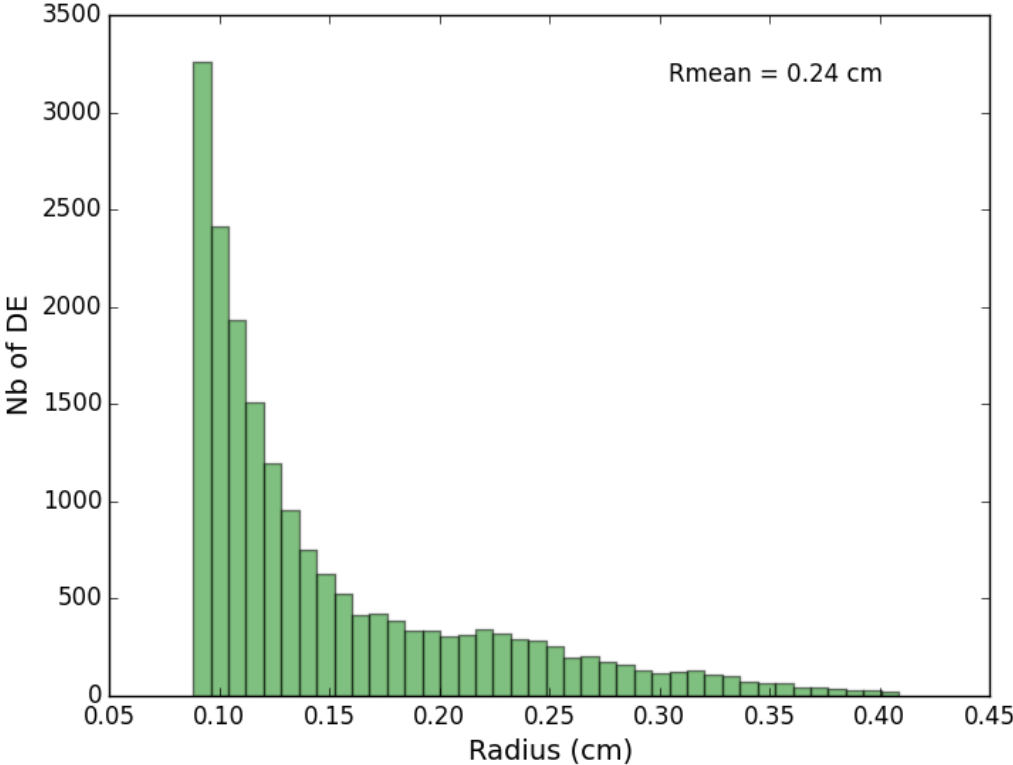


Figure 3.16: Mesh 5 histogram of radius distribution

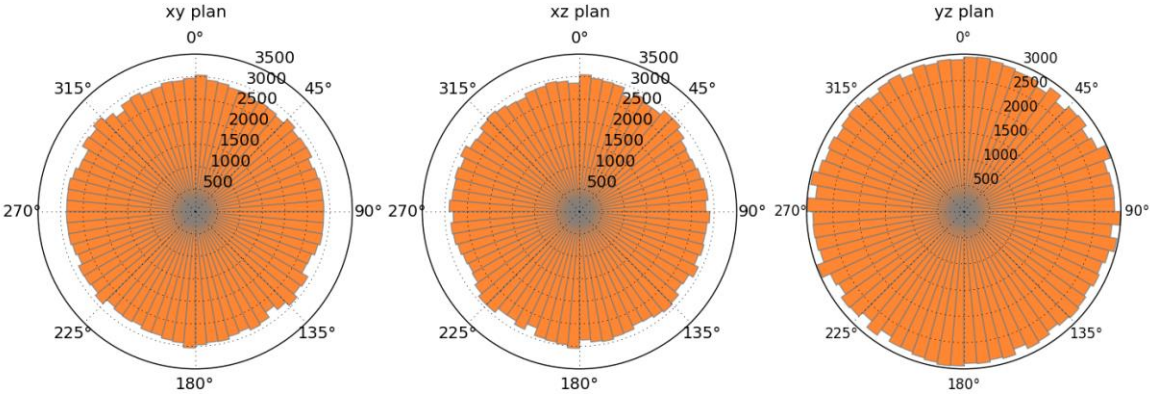


Figure 3.17: Mesh 5 orientation of interaction in the three planes

Mesh 5 has a regular sphere distribution but with a significant concentration of particles close to the higher radius and very few for the lower radius (Figure 3.16). It is the densest mesh and its interaction range coefficient is bigger than the meshes 2,3 and 4 because it contains quite smaller discrete elements. For this reason, mesh 5 seems to be the strongest one. Figure 3.17 plots its links orientation have a rise of thousand links (around 2500 – 3000).

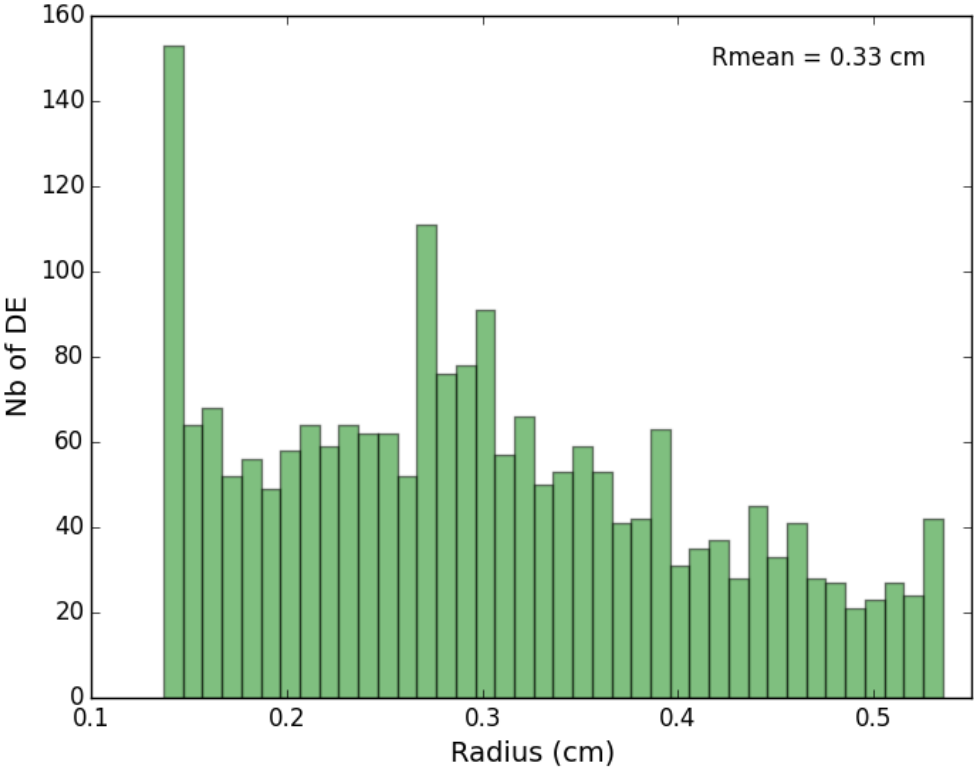


Figure 3.18: Mesh 6 histogram of radius distribution

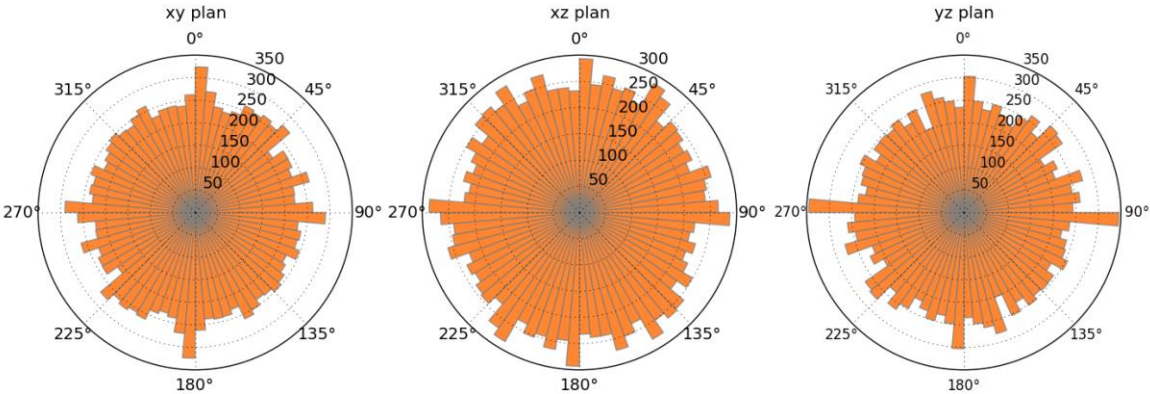


Figure 3.19: Mesh 6 orientation of interaction in the three planes

The sixth mesh has the most irregular distribution and it is not homogeneous (Figure 3.18). The total number of discrete elements decreases dramatically to 2145 and the interaction range becomes bigger with $\lambda = 1.52$; thus the link behaviour is not local anymore. Figure 3.19 gives the orientation of interactions from where it can be concluded that the mesh is not isotropic with higher links in privileged directions.

3.1.2.2 Influence of mesh generation parameters on the macroscopic behaviour of concrete

Figure 3.20 and Figure 3.21 compare the response of the six meshes under quasi-static compression and tension. As it was expected mesh 1 and mesh 6 are the weakest with lower Young's modulus and peak stress, while mesh 5 is the strongest and the other three meshes give quite similar stress-strain curves.

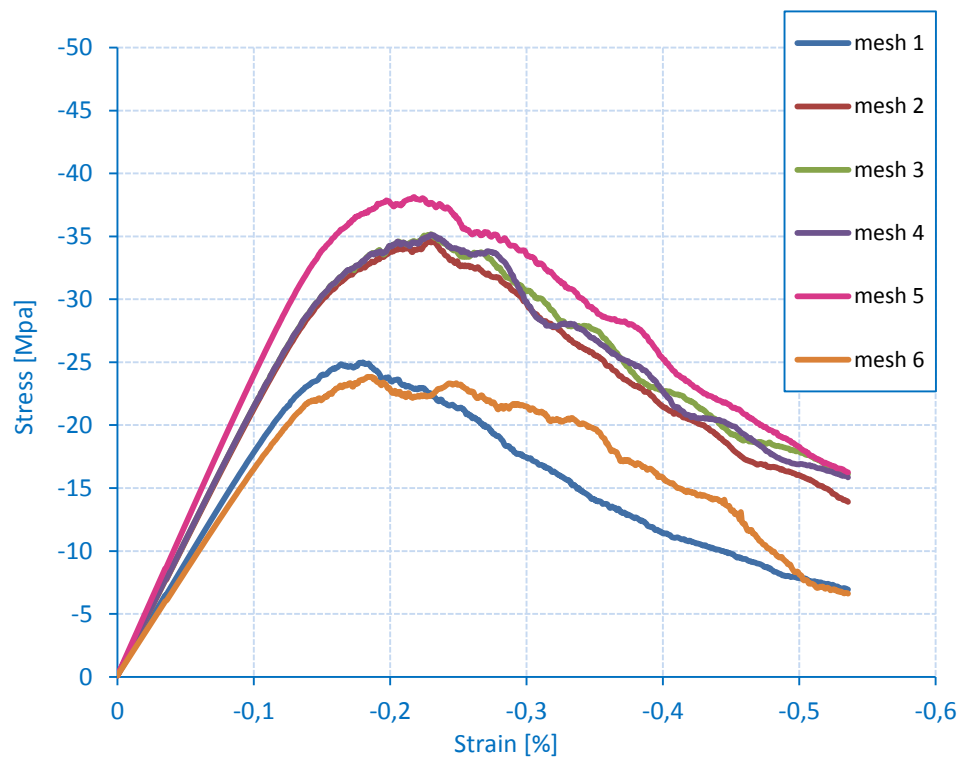


Figure 3.20: Simulations of quasi-static compression test

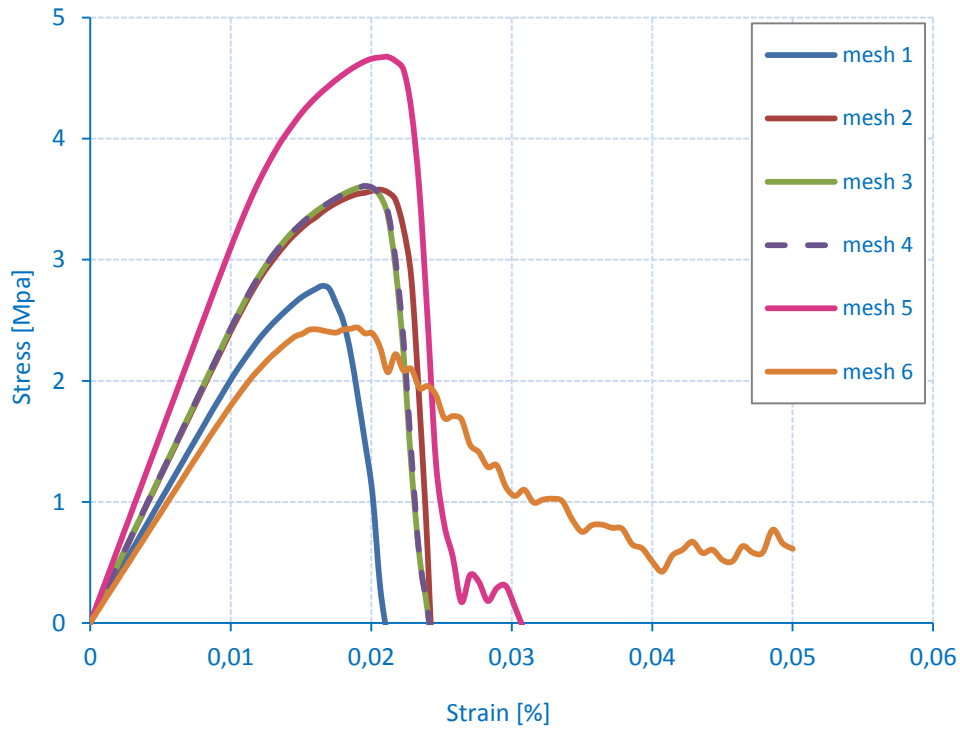


Figure 3.21: Simulations of quasi-static tensile test

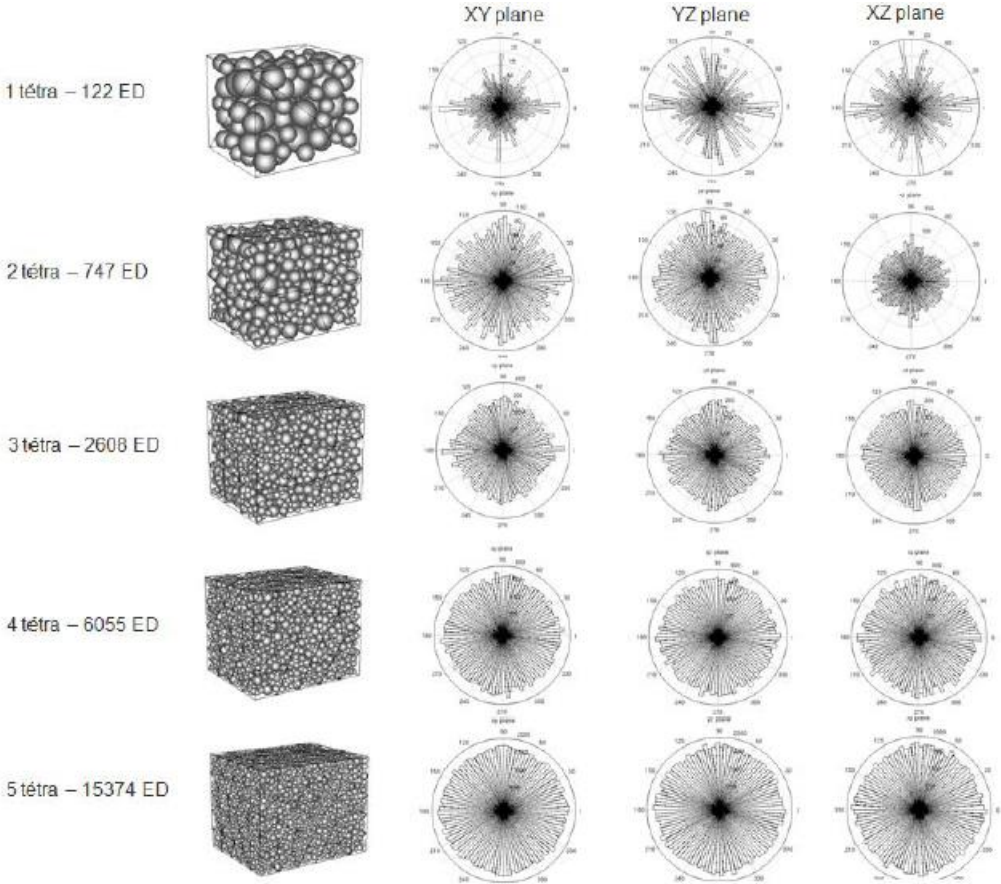
It is obvious that the packing parameters k_1 and k_2 affect the linear and non-linear macroscopic behaviour of concrete. The iteration number for the densification phase does not influence the macroscopic behaviour of concrete if it is higher than 2.

In addition, the compactness of the mesh affects its ductility in traction. For less than 0.5 compact meshes the tensile macroscopic behaviour appears to be very ductile. A possible explanation is that a loose mesh (like mesh six) contains very few particles with bigger distance between them. Thus to satisfy the average number of links per element to be at least 12, the radius of interaction needs to increase quite a lot. For this reason, this adjustment offers more ductility to the model since the constitutive law is not local anymore.

After the sensitivity study for the parameters of the geometric algorithm for the generation of polydisperse spatial packing, it was decided to use the set of parameters $k_1 = 3$, $k_2 = 4$ and four tetrahedral finite elements per short side for the creation of all the meshes. The iteration number for the densification phase was selected to be two since more iteration gives almost the same packing with a few more discrete elements. Additionally, with this choice, the computation time of the simulations is reduced and the meshes generation algorithm creates the mesh faster.

Moreover, Potapov et al. [107] evaluated the isotropy of DEM meshes by employing a parallelepiped sample with increasingly refined tetrahedral consisting between 1 and 9 tetrahedral per short side. For all the meshes were created DE packings with the parameters $k_1 = 3$, $k_2 = 4$. As can be seen on Figure 3.22, the increase of tetrahedral decreases the size of the discrete elements. The orientation of interactions shows that isotropy is established as the mesh becomes more refined. Also, for meshes with 4 tetrahedral and more the distribution of interactions uniform and those meshes considered to exhibit isotropic behaviour.

Then, Potapov et al. [107] determined the parameters for the linear response of the sample with the 4 tetrahedral. The same parameters were imposed to all the meshes for quasi-static compression simulation. After, they measured the Young’s modulus and Poisson’s ratio of all the meshes (Figure 3.23). From their results, we can conclude that the macroscopic linear behaviour (E, ν) for finer meshes is almost equivalent with a maximum error of 8%. Thus, our DEM model allows reusing the sale set of parameters for different discretisation, as long as they are produced with the same mesh generator parameters.



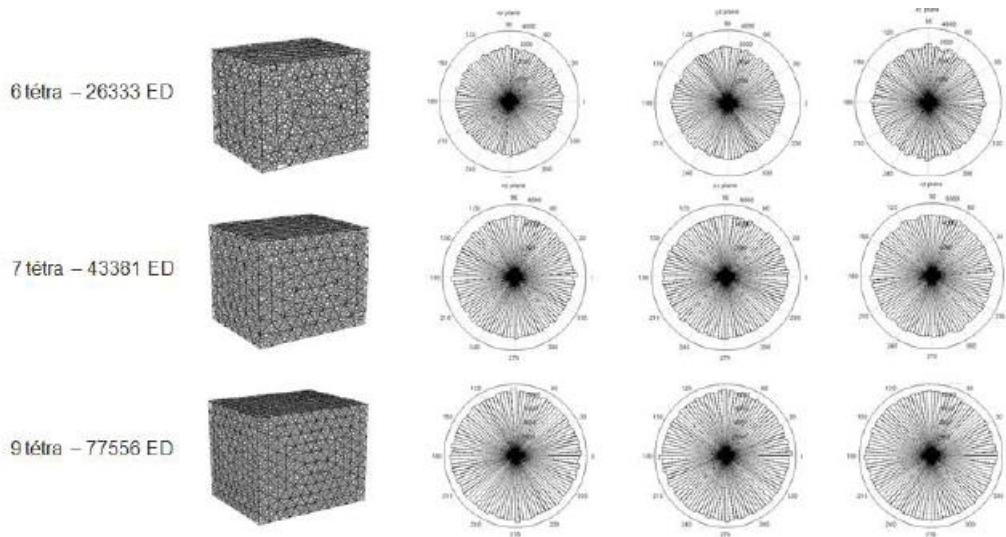


Figure 3.22: DE meshed and of orientation of interaction in the three planes (Potapov et al. [107])

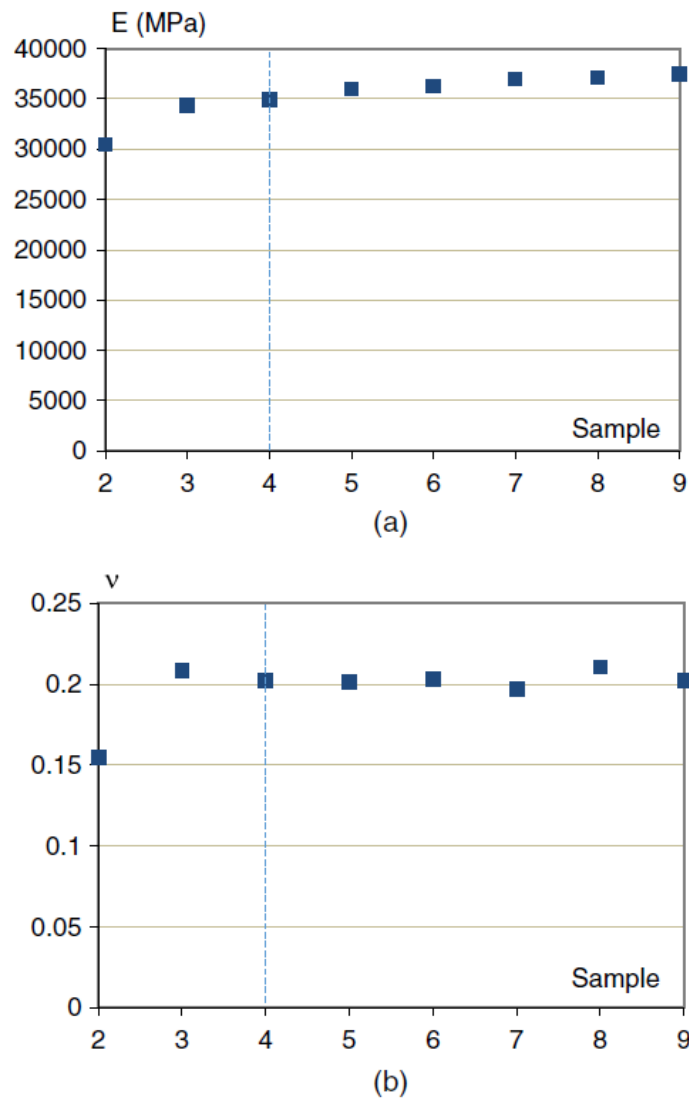


Figure 3.23: Reproducibility of (a) Young's Modulus and (b) Poisson's ratio values for various DE meshes (Potapov et al. [107])

3.2 Identification of the parameters for the concrete constitutive model

3.2.1 Mesh for quasi-static uniaxial tests

For the current study, the mesh for the quasi-static test simulations is selected to be parallelepiped with dimensions $0.07 \times 0.07 \times 0.14 \text{m}^3$. Then, a four tetrahedral finite element per short side is used to create the skeleton for the packing of geometrical algorithm Figure 3.24. Padder parameters $k_1 = 3$, $k_2 = 4$, and two iterations of densification are applied to obtain the discrete element mesh for the quasi-static simulations Figure 3.25. The mesh packing characteristics can be found in Table 3.3 (mesh 2), the histogram of size distribution is given in Figure 3.10 and the links' orientation in Figure 3.11. During the simulation, the two small faces of the specimen are in contact with two rigid plates, which apply the kinematic conditions. EUROPLEXUS is a fast dynamics software; thus it is necessary to verify the equilibrium state of the specimen. For this reason, we computed the forces on the two plates and we compared them with the kinematic energy and the potential energy; thus we chose a constant velocity of 5 mm/s to apply the kinematic condition. A friction coefficient of 0.5 is imposed at the interface zone between the loading plates and the concrete sample.

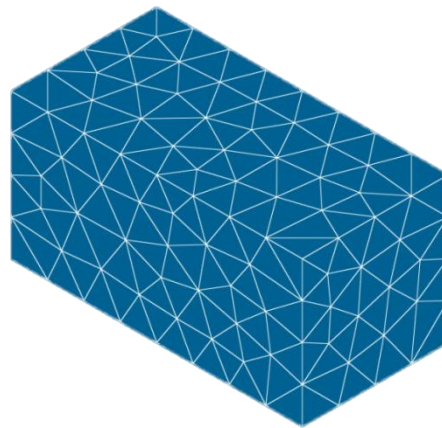


Figure 3.24: Four tetrahedral finite element discretisation of the quasi-static test mesh

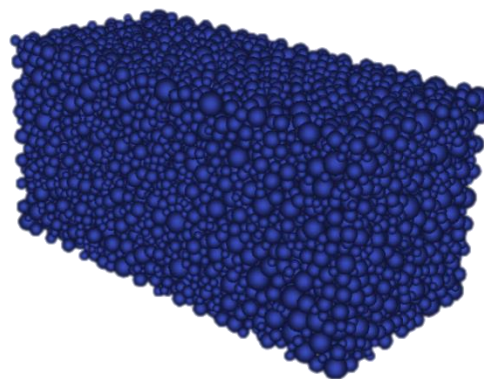


Figure 3.25: Mesh for quasi-static tests

3.2.1.1 Moment transfer law parameters

The parameters of moment transfer law (MTL) are the second choice that should be made at the beginning for a specific type of concrete to simplify the process.

The quasi-static compressive test is used, for the calibration of the MTL rolling stiffness coefficient β_r and plastic limit coefficient η . Those two parameters are identified with the help of a set of linear and not linear behaviour parameters but not the final one since those parameters need to calibrate after β_r and η are obtained. The quasi-static compressive test was conducted by Vu [136] in the 3S-R laboratory (University Grenoble Alpes). The experiment was performed on ordinary fully saturated concrete R30A7. Table 3.4 presents its composition and mechanical propertiesTable 3.4. The tensile mechanical properties were assumed due to lack of experimental data.

The two parameters were varied between the values 1,3 and 5 in order to evaluate their effect on the linear branch, the smoothness of the peak stress and the post-peak curve ductility. The results are grouped in five cases by keeping constant one of the two parameters and changing the other one. Figure 3.26, Figure 3.27 and Figure 3.28 illustrate the simulations for constant η equal to 1, 3 and 5 respectively, while Figure 3.29 and Figure 3.30 present the results for constant β_r equal to 1 and 5.

Concrete mix proportions	
Water	169 kg/m ³
Sand d _{max} 1.8 mm	838 kg/m ³
Aggregate d 0.5 – 8 mm	1007 kg/m ³
Cement CEM 52.5 N PM ES CP2 (Vicat)	263 kg/m ³
Characteristics	
Maximum size aggregate	8 mm
Concrete measured porosity	12%
Density	2390 kg/m ³
Mechanical properties	
Young's Modulus E	25 GPa

Poisson's ratio ν	0.16
Compressive strength σ_c	34 MPa
Tensile strength σ_T	3.6 MPa
ultimate strain ϵ_u	0.025%

Table 3.4: Composition and mechanical properties of R30A7 ordinary fully saturated concrete

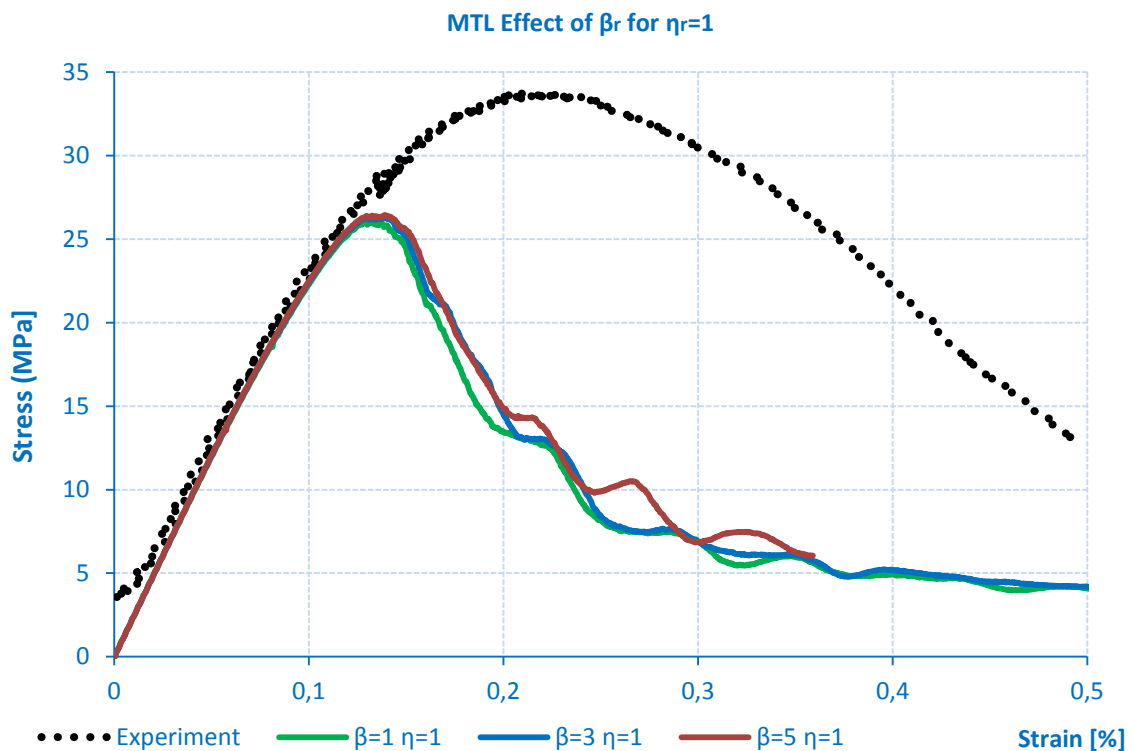


Figure 3.26: MTL effect of β_r for $\eta_r=1$

When the coefficient of the plastic limit η is equal to 1, the post-peak behaviour is always brittle and the width of the peak stress is very narrow. Also, the rolling stiffness coefficient β_r seems to have an insignificant influence on the results (Figure 3.26).

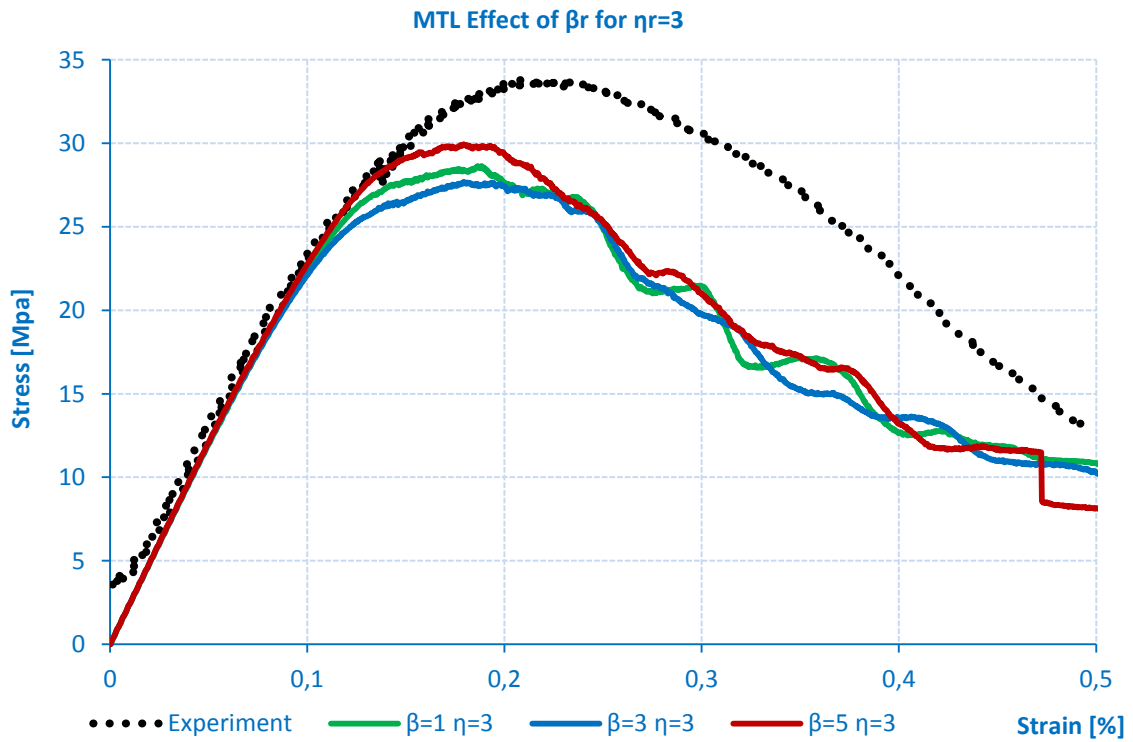


Figure 3.27: MTL effect of β_r for $\eta_r=3$

For η equal to 3, the post-peak behaviour is more ductile and the width of the peak stress becomes wide. In addition, the peak stress is increasing for higher values of β_r (Figure 3.27)

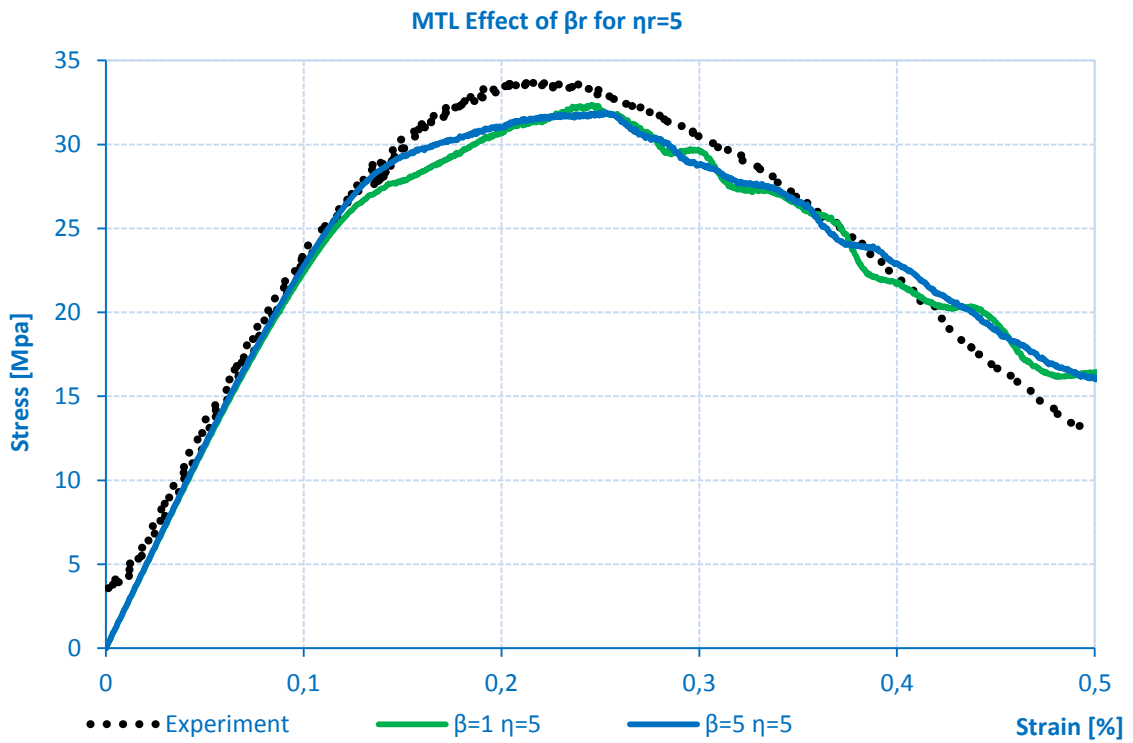


Figure 3.28: MTL effect of β_r for $\eta_r=5$

When η takes the value 5, the response becomes very ductile and the peak stress is increasing with a broad curvature. However, with the increase of β_r the peak stress is higher and smoother (Figure 3.28).

Comparing the resultant curves for β_r equal to 1 the peak stress and the ductility are increasing with the increase of η (Figure 3.29).

Figure 3.30 presents a similar response to Figure 3.29, where one can see that when β_r is increasing from one to five, the peak stress curvature is smoother.

For the previous simulations a preliminary set of quasi-static behaviour parameters was employed ($\alpha = 3.9$, $\beta = 3.75$, $\gamma = 5$, $C_0 = 3.5 \text{ MPa}$, $T = 3 \text{ MPa}$, $\xi = 3$, $\varphi_i = 30^\circ$ and $\varphi_c = 30^\circ$). The parameters for the Moment Transfer Law were computed to be $\beta_r = 5$ and $\eta = 5$. However, the identification of the rest parameters for the quasi-static constitutive behaviour requires to be improved.

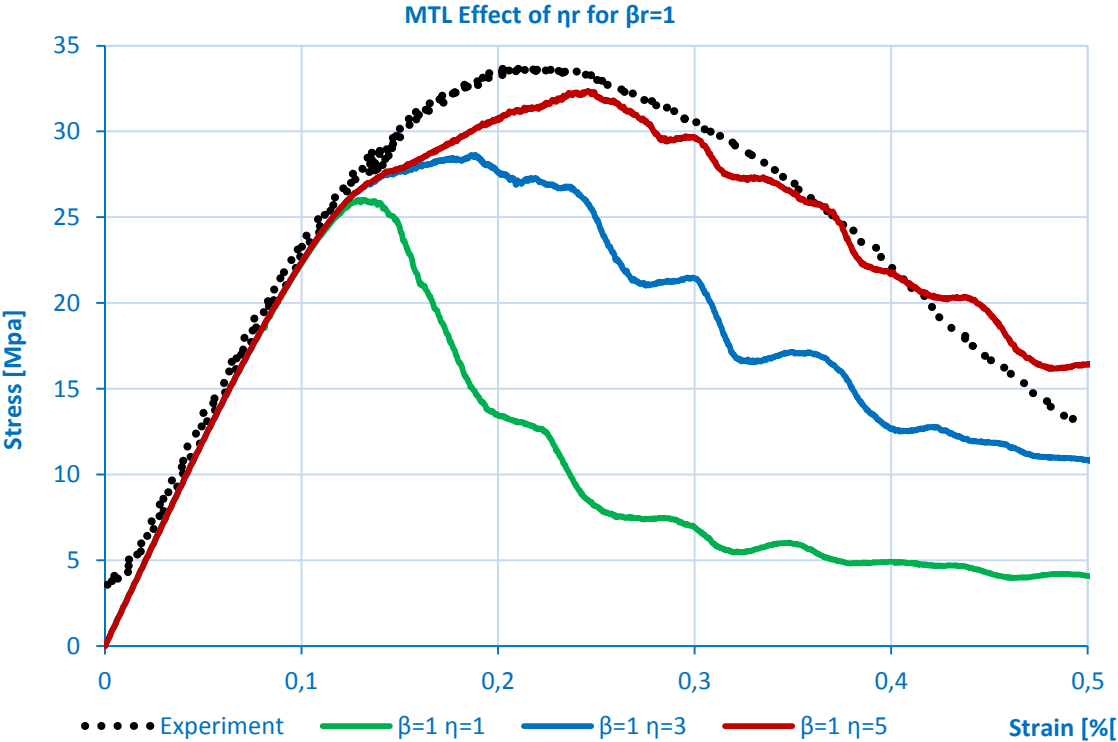


Figure 3.29: MTL effect of η_r for $\beta_r=1$

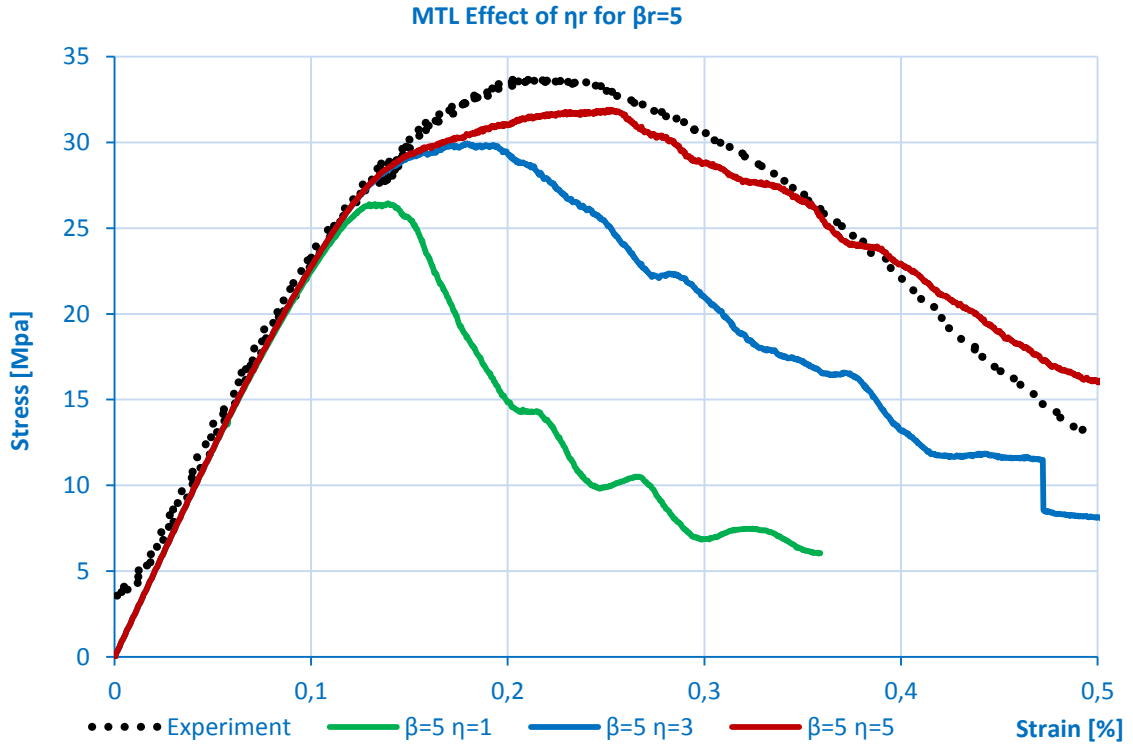


Figure 3.30: MTL effect of η_r for $\beta_r=5$

3.2.1.2 Linear-elastic behaviour parameters

The relations for the elastic behaviour of concrete were created to describe the local microscopic parameters K_N and K_S from the global macroscopic elasticity parameters, Young's modulus E , and Poisson's ratio ν . The global macroscopic parameters are the input values of the model whereas α , β and γ parameters need to be identified by mean of quasi-static compression and tension test on the linear branch. The equations (2.16) for concrete's elastic behaviour are originated from Voigt's hypothesis and the best-fit approximation of Liao model for regular assemblies and Donzé [36] modified them to account for disordered polydisperse assemblies. According to Huang [68] the ratio of Young's modulus E over E_0 is dependent on the ratio of the shear stiffness over the normal stiffness $\frac{K_S}{K_N}$ equation (2.30). E_0 derives from equation (2.16) when the ratio of stiffnesses is equal to one $\frac{K_S}{K_N} = 1$.

Firstly, the macroscopic parameters (E, ν) are selected from the experimental data of ordinary fully saturated concrete (R30A7). The mechanical properties (Table 3.4) of this type of concrete have been analytically identified in previous studies [51], [136]. Hence the input values of Young's modulus and Poisson's ratio are $E = 25 \text{ GPa}$, $\nu = 0.16$. Afterwards, we employ an iterative method, where the

ratio of the tangential stiffness over the normal stiffness $coef = \frac{K_S}{K_N}$ is varying between 0 and 1 with interval 0.1. To succeed that we modify the constitutive equation (2.31) such as:

$$K_S = K_N \text{ coef} \quad (b) \quad 0 \leq coef \leq 1$$

Thus, we launch eleven simulations for every value of the parameter α , while we keep $\beta = 1$ and $\gamma = 1$. Once the values for the Poisson ratio ν obtained from the simulations satisfy the calculated values from the constitutive equation (2.29) the parameter α is identified. Figure 3.31 illustrates the comparison between the values of the equation (2.29) and from the simulations with $\alpha = 3.9$.

The next step is to determine the value of the ratio β/γ by using the same iterative method. This time we keep $\alpha = 3.9$ and we launch the eleven simulation, one for every interval of coef and for every value of the ratio β/γ . This ratio is identified once the results from the simulations fit the dimensionless expression of Young's modulus E/E_0 (2.30). Figure 3.32 shows the comparison between equation (2.30) and the simulations with the ratio $\beta/\gamma = 0.75$.

The last step is to decouple the parameters β and γ and calibrate them to result in the Poisson's ratio and Young's Modulus equal to the input values. For this step, the initial equation (2.31) of the model is used without any modifications. To detect the values of the two last parameters we use as input data $\alpha = 3.9, \beta = 0.75\gamma$ and we vary γ in every simulation. The three values were found to be $\alpha = 3.9, \beta = 3.75$ and $\gamma = 5$ to satisfy the macroscopic parameters $E = 25 \text{ GPa}, \nu = 0.16$.

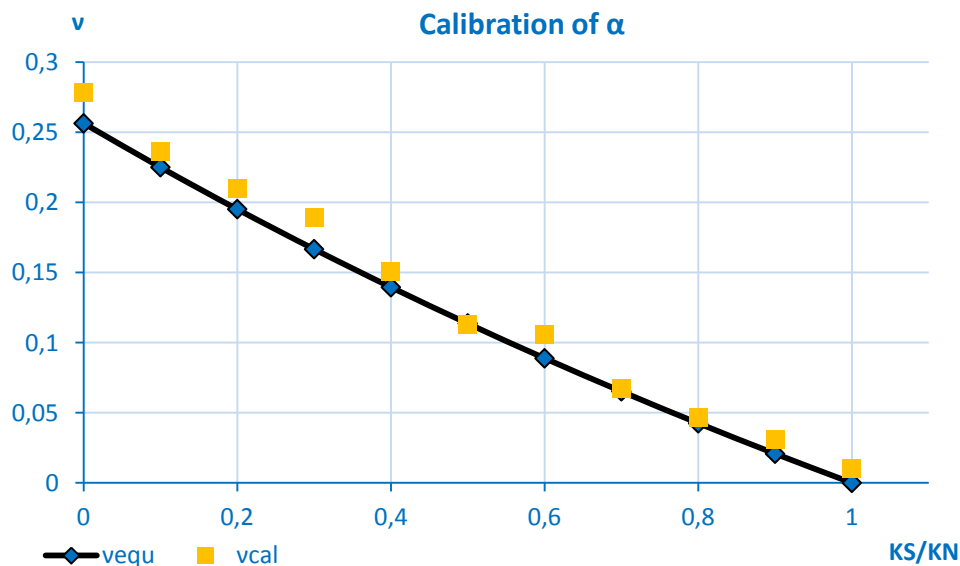


Figure 3.31: Calibration of coefficient α

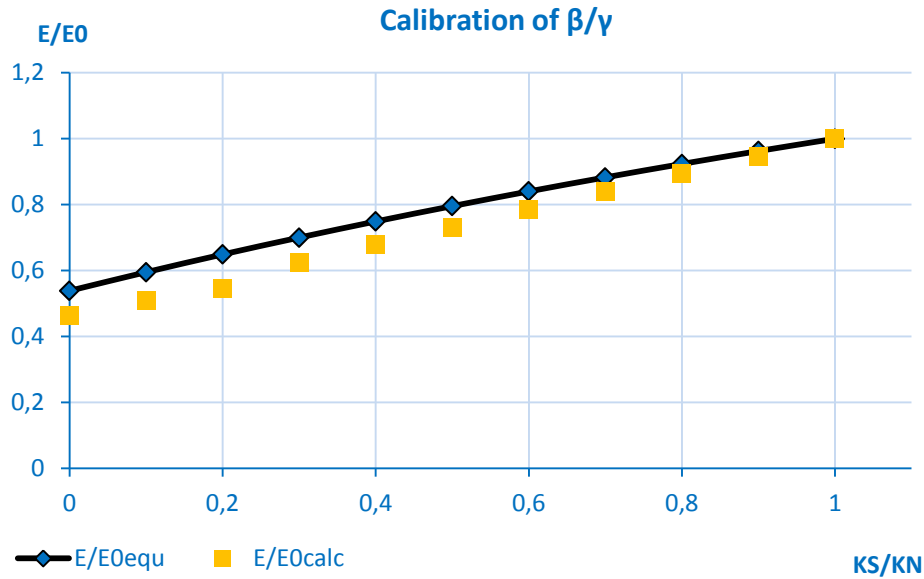


Figure 3.32: Calibration of the ratio β/γ

3.2.1.3 Non-linear elastic with damage behaviour parameters

The non-linear elastic with damage behaviour of concrete is characterised by a modified Mohr-Coulomb criterion Figure 2.12 with sliding function f_1 and a tensile rupture f_2 for cohesive links equation (2.44). The model of cohesive interactions consists from a friction angle φ_i , a cohesion stress C_0 , a local tensile cut off stress T and a softening factor ξ . Contact links follow a simple Mohr-Coulomb criterion with a contact angle φ_c equation (2.45).

A sensitivity study employed to study the influence of the non-linear behaviour parameters Figure 2.10 on the quasi-static macroscopic behaviour of concrete. Figure 3.33 and Figure 3.34 show the effect of the tensile cut off stress T which increases the peak stress and the broadness of the curvature after yield strength in both tension and compression. Also, it increases the ultimate strain of the tensile curve and offers more ductility to the compressive curve. Figure 3.35 and Figure 3.36 present the effect of the softening factor ξ , with a slight increase in peak stress in both tension and compression. This parameter has almost no effect on the ductility of the compressive curve. However, it grows the width of the tensile curve dramatically after the yielding stress until the peak stress and consequently, it increases so the ultimate tensile strain. As can be seen, different combinations of the parameters T and ξ result either the same ultimate strain Figure 3.37 or the same peak stress Figure 3.38. For this reason, those two parameters need to be chosen carefully in order to obtain the desirable macroscopic behaviour of concrete.

Cohesion stress C_0 (Figure 3.39), friction φ_i and contact φ_c angles (Figure 3.41) do not influence the tensile behaviour of concrete. Therefore, Cohesion stress C_0 affects the peak stress (Figure 3.40) and the two angles influence the values and the width of the peak stress and the response of the softening regime of the compressive curve (Figure 3.42). Thus, these three parameters need to be identified in order to reproduce the macroscopic compressive curve well.

After studying the influence of each parameter of the non-linear behaviour on quasi-static compression and tension we defined the procedure for the identification of the constitutive model parameters. The first step is to obtain the macroscopic tensile stress $\sigma_T = 3.6 \text{ MPa}$ and ultimate strain $\varepsilon_u = 0.025\%$ by identifying the microscopic tensile parameters T and ξ (Figure 3.43). The second step is the calibration cohesion stress C_0 , in order to satisfy the macroscopic compressive stress $\sigma_C = 34 \text{ MPa}$. The last step is the adjustment of the friction φ_i and contact φ_c angles to well reproduce the peak curvature and the post-peak regime of the compressive stress-strain response (Figure 3.44).

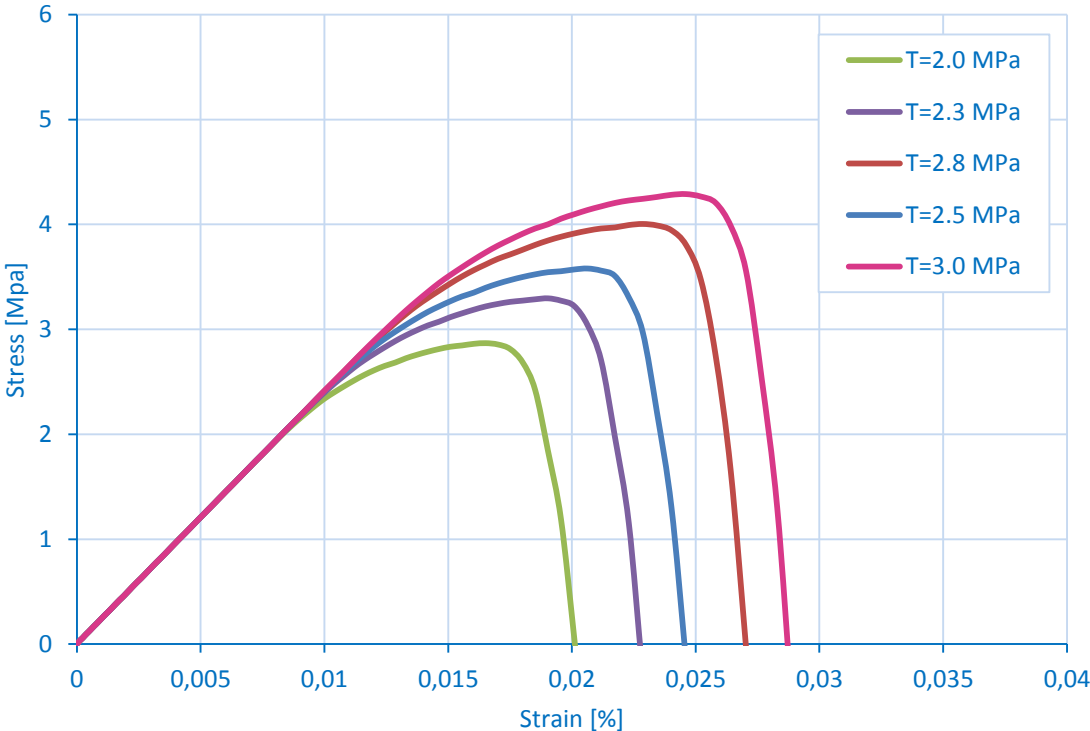


Figure 3.33: Effect of tensile cut of stress T on the tensile stress-strain curve

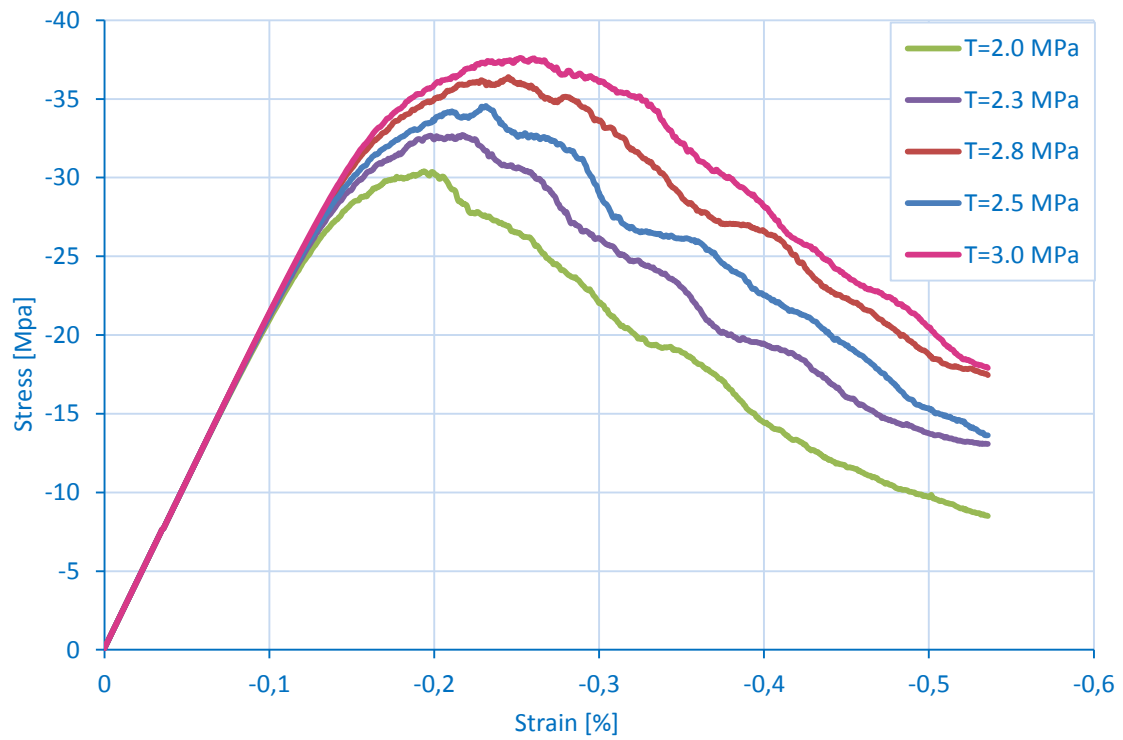


Figure 3.34: Effect of tensile cut of stress T on the compressive stress-strain curve

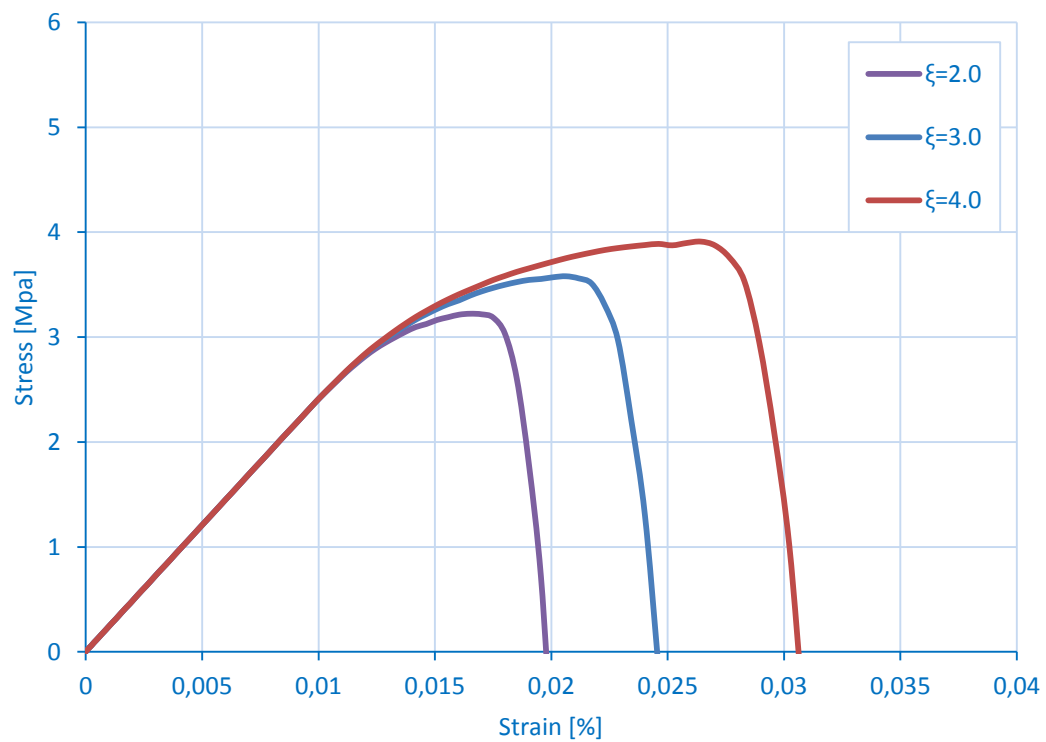


Figure 3.35: Effect of softening factor ξ on the tensile stress-strain curve

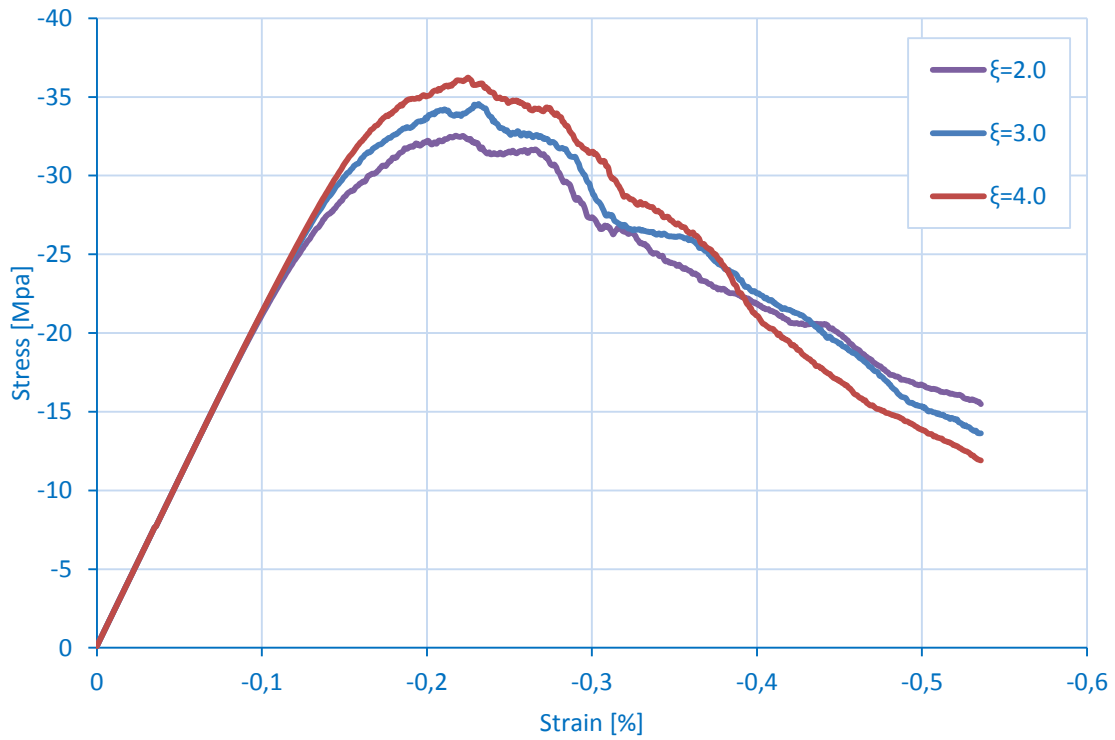


Figure 3.36: Effect of softening factor ξ on the compressive stress-strain curve

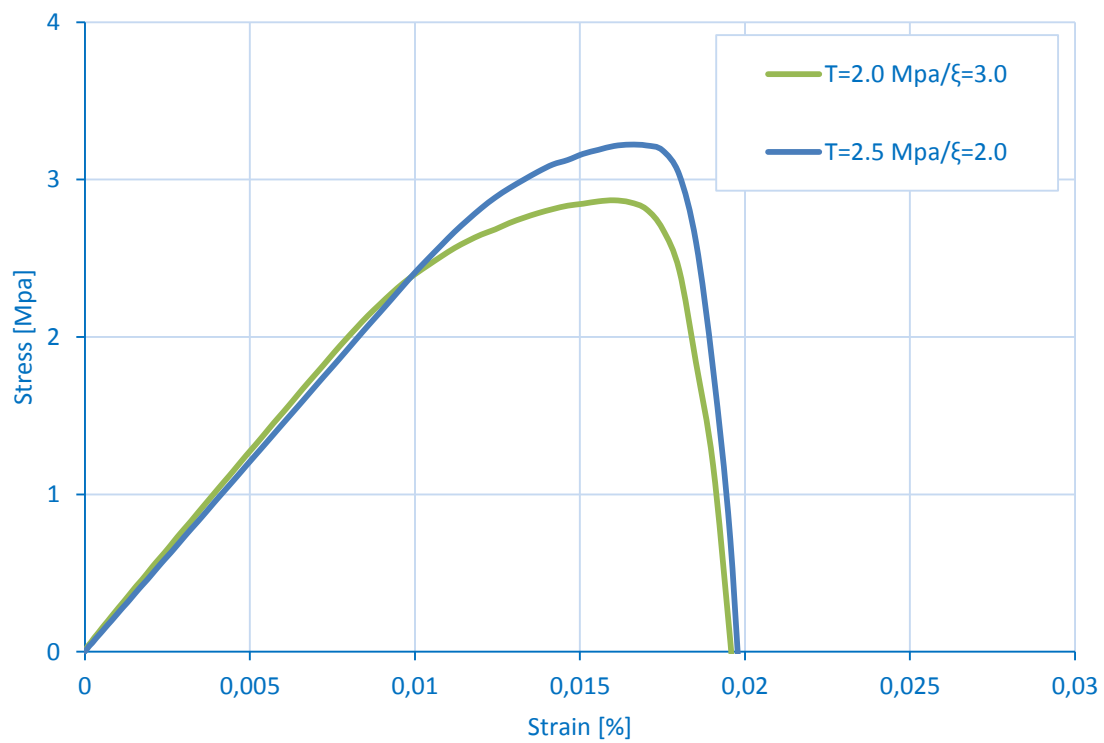


Figure 3.37: Effect of tensile cut of stress T and softening factor ξ on the tensile stress-strain curve

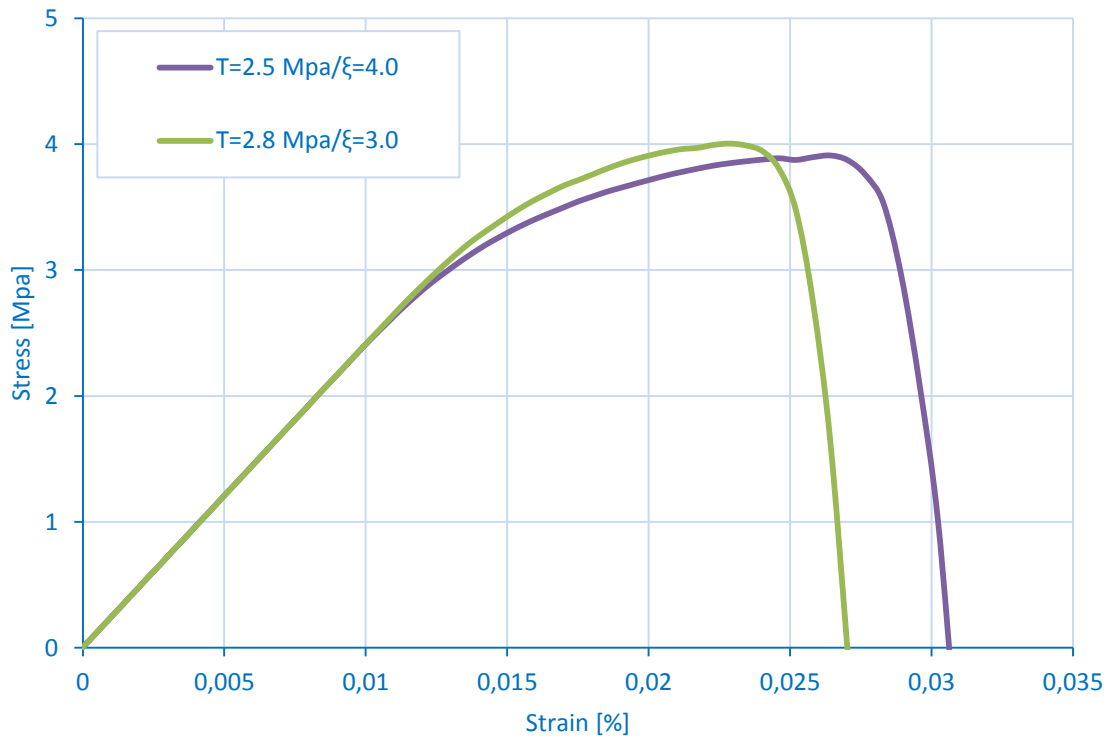


Figure 3.38: Effect of tensile cut of stress T and softening factor ξ on the tensile stress-strain curve

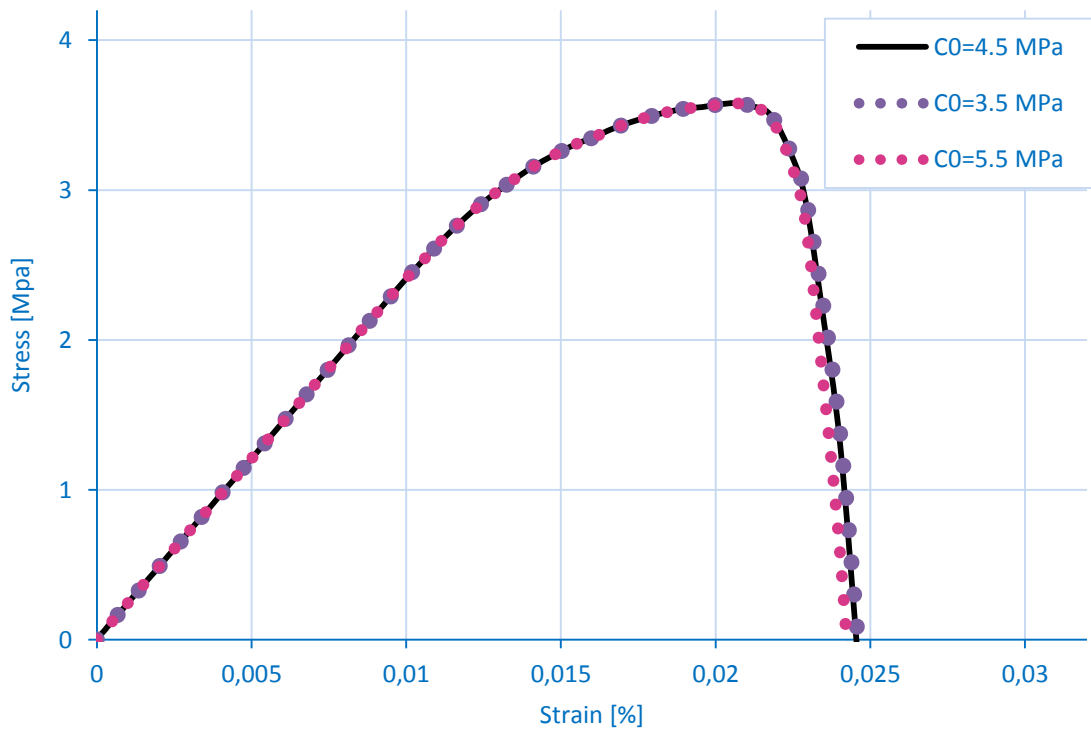


Figure 3.39: Effect cohesion stress C_0 on the tensile stress-strain curve

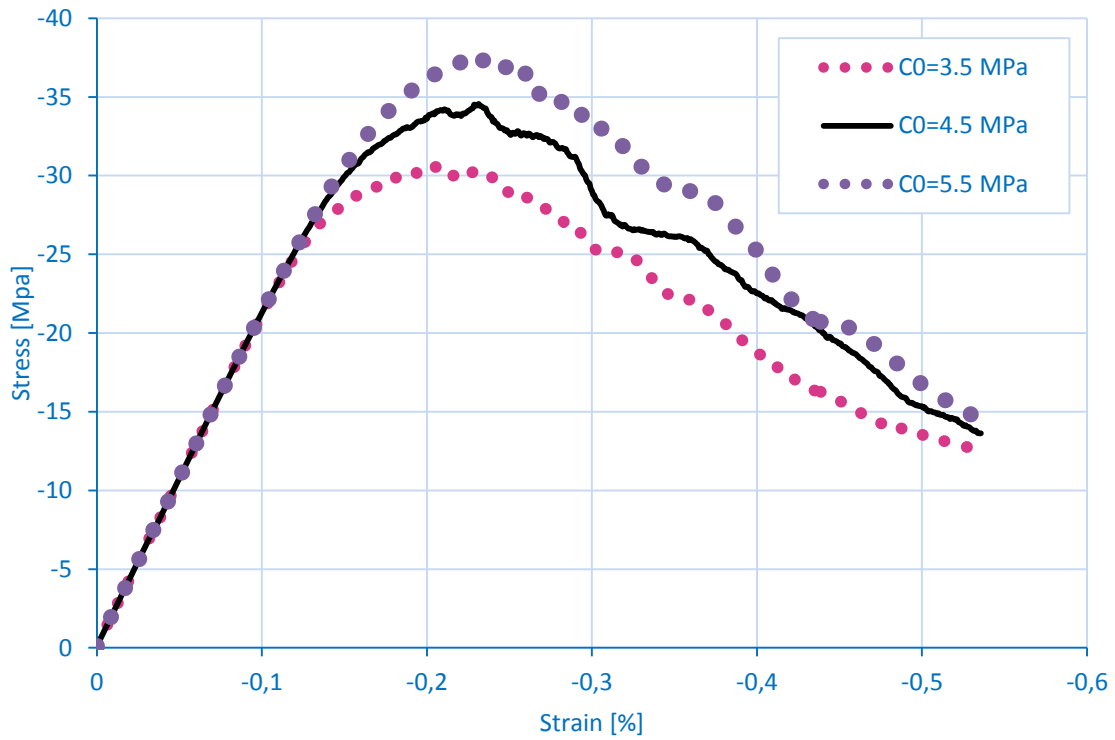


Figure 3.40: Effect cohesion stress C_0 on the compressive stress-strain curve

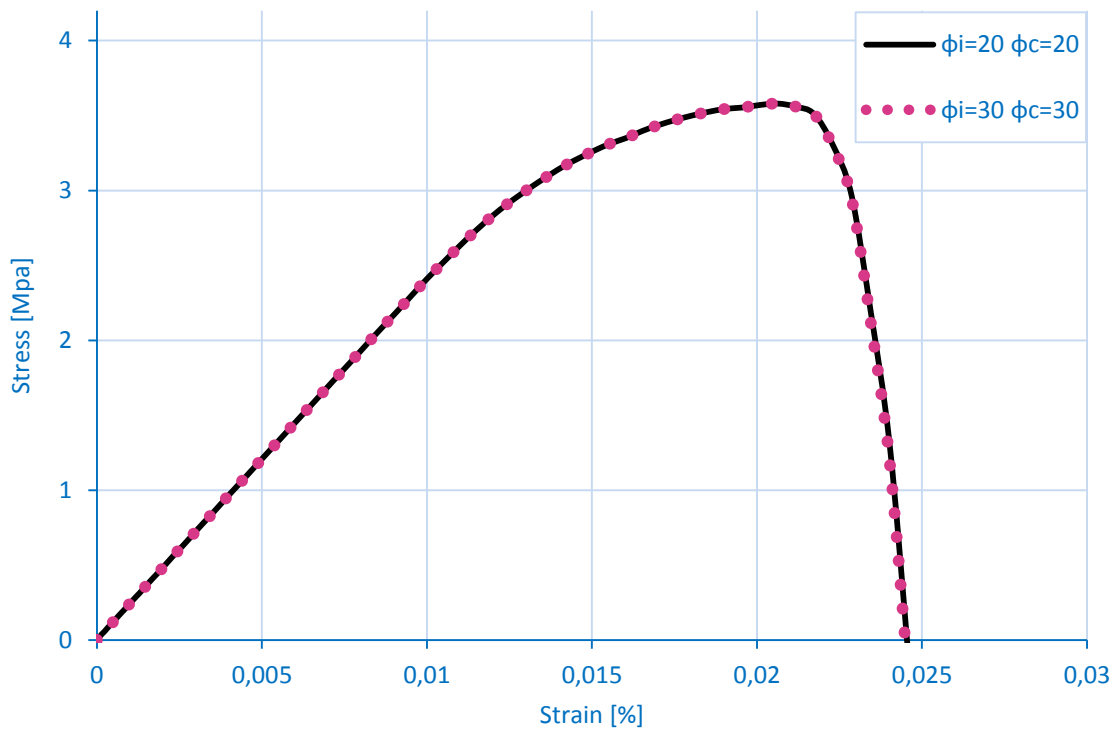


Figure 3.41: Effect of friction φ_i and contact φ_c angles on the tensile stress-strain curve

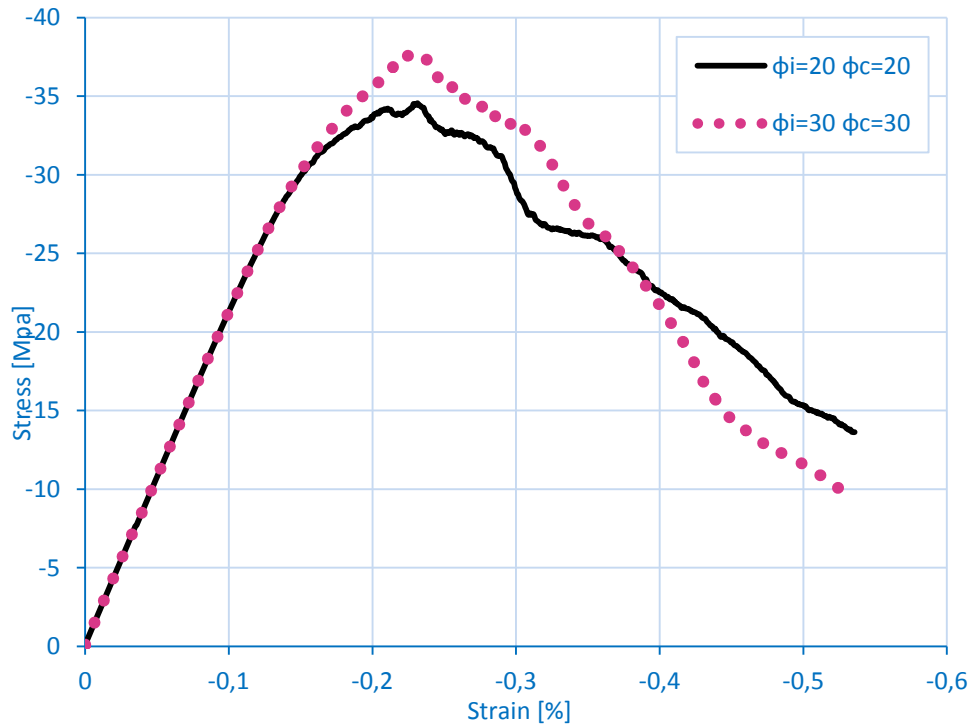


Figure 3.42: Effect of friction φ_i and contact φ_c angles on the compressive stress-strain curve

We identified the non-linear elastic with damage behaviour parameters as $C_0 = 4.5 \text{ MPa}$, $T = 2.5 \text{ MPa}$, $\xi = 3$, $\varphi_i = 20^\circ$ and $\varphi_c = 20^\circ$ by modelling quasi-static tests with macroscopic $\sigma_C = 34 \text{ MPa}$, $\sigma_T = 3.6 \text{ MPa}$ and $\varepsilon_u = 0.025\%$.

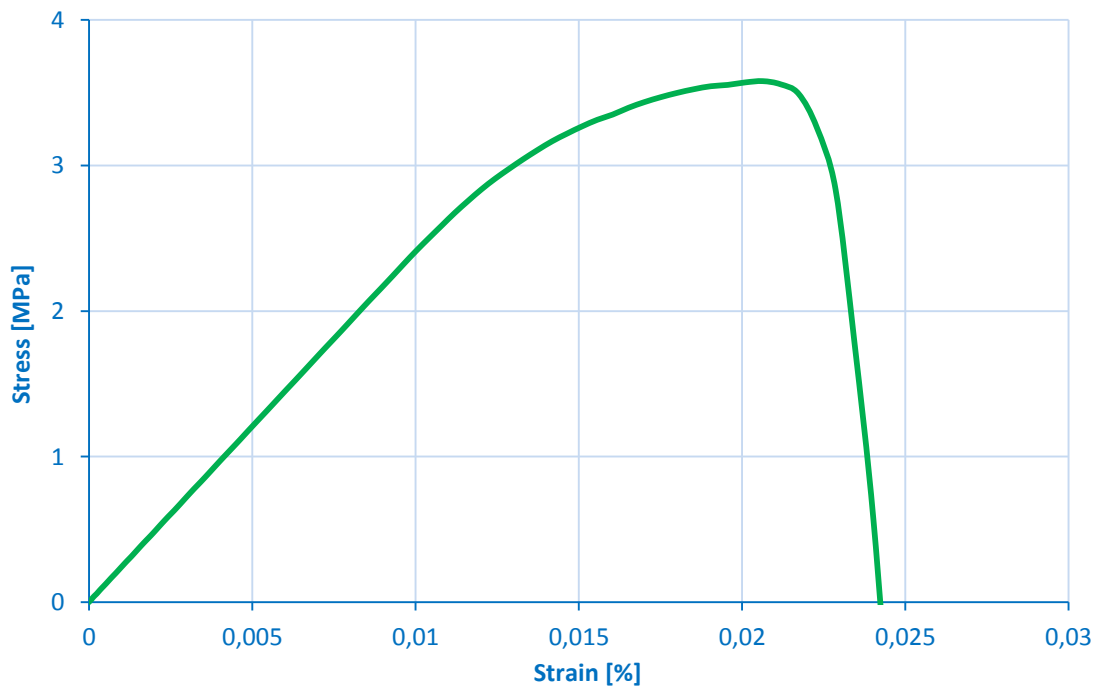


Figure 3.43: Quasi-static tension simulation

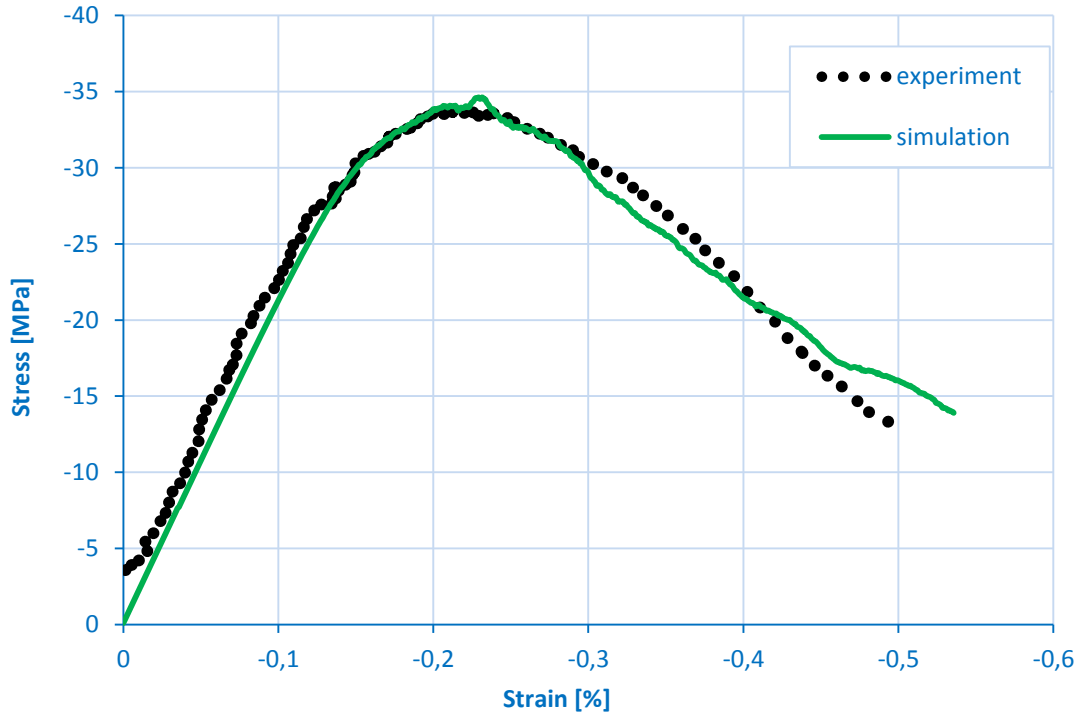


Figure 3.44: Quasi-static compression test and simulation

3.2.2 Mesh for high-confinement tests

We created the mesh for the high-confinement test by following the same steps with the mesh for the quasi-static uniaxial test. A cubical shape with dimensions $0.1 \times 0.1 \times 0.1 \text{ m}^3$ is discretised with four tetrahedral finite elements per side and the concrete discrete element packing is generated with Padder. Mesh parameters are kept the same $k_1 = 3$, $k_2 = 4$, and two iterations of densification, because of the dependency of the microscopic parameters on the packing. The polydisperse assemble consist of 4427 DE with a maximum radius of 0.55 cm, a minimum radius of 0.18 cm and with 0.592 compactness (Table 3.5). Its interaction range coefficient is calculated to be 1.402, in order to ensure an average of twelve links per DE. As can be seen from the size distribution Figure 3.46 and the orientation of all the links Figure 3.47, the mesh is homogeneous and isotropic. The specimen is placed in frictionless contact with six rigid elements one on every side which are applying the loading conditions Figure 3.45.

FE number per side	k_1	k_2	Iterations	DE Total number	R_{max} (cm)	R_{min} (cm)	Compactness	λ
4	3	4	2	4427	0.55	0.18	0.592	1.402

Table 3.5: DE diameters

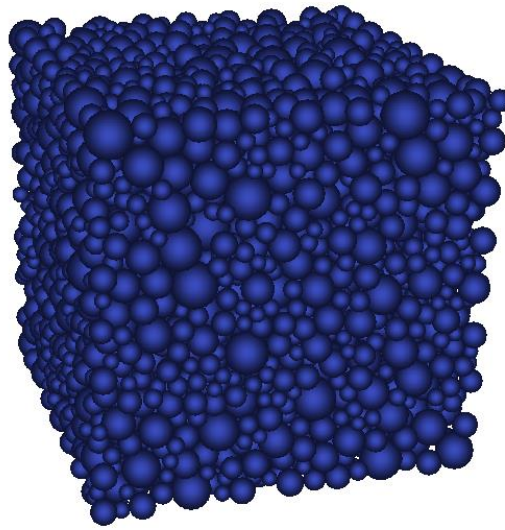


Figure 3.45: Compaction mesh

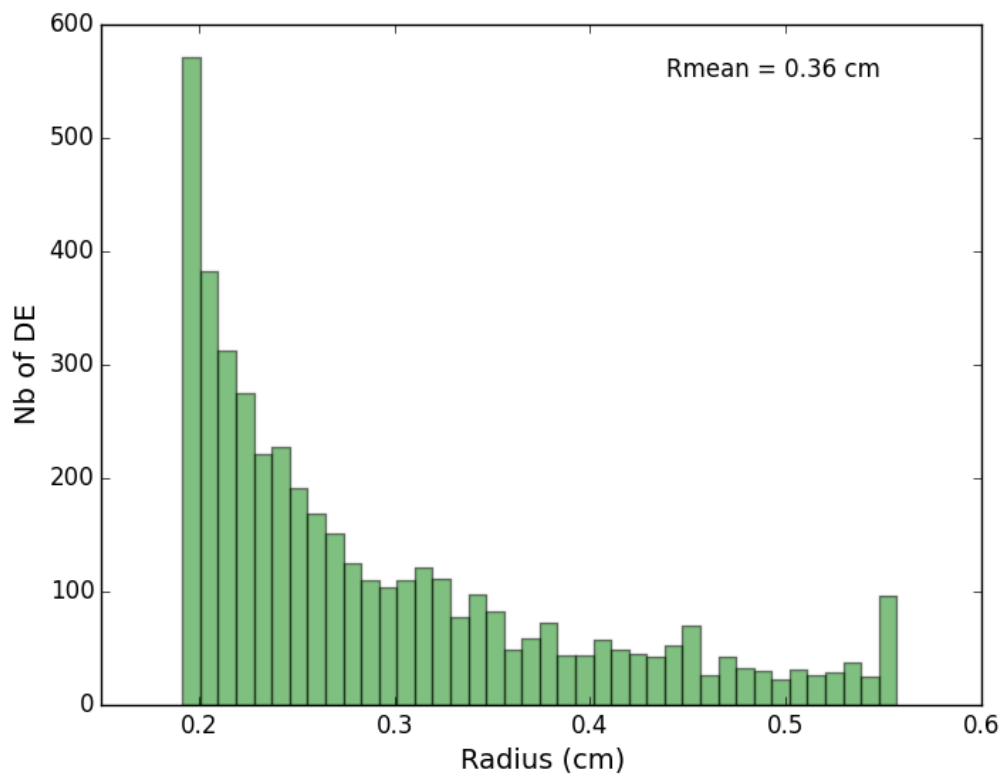


Figure 3.46: High-confinement mesh histogram of radius distribution

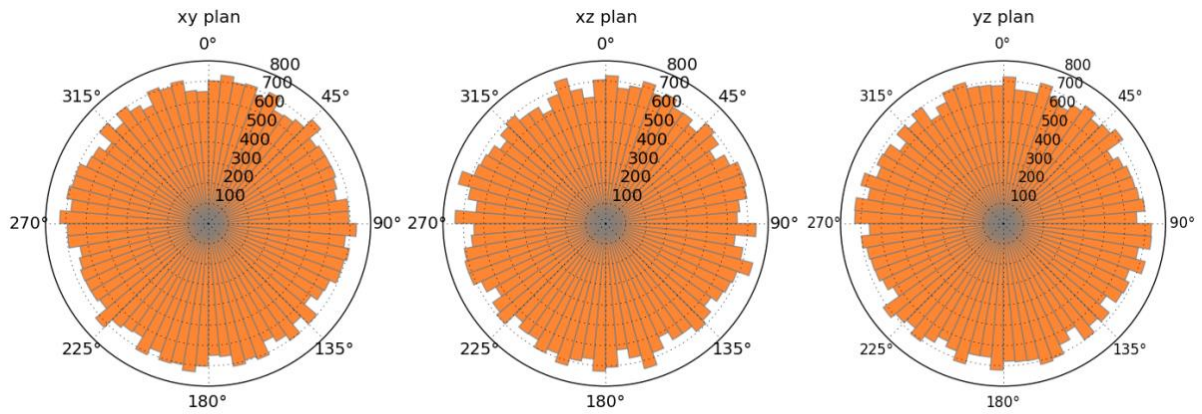


Figure 3.47: High-confinement mesh orientation of interaction in the three planes

3.2.2.1 Compaction Law parameters

The compressive non-linear plastic behaviour under high confining pressures is following the compaction phenomenon. A trilinear elasto-plastic-hardening model gives the microscopic constitutive behaviour (compaction law). The compaction law parameters are defined employing hydrostatic and oedometric tests obtained thanks to a triaxial device that allows performing triaxial compression tests on concrete with high confining pressure up to 650 MPa [52][53][88][137].

We launched several hydrostatic simulations in order to understand the influence of each parameter of compaction law on the macroscopic behaviour of our concrete model under high confining pressures. Figure 3.48 gives the effect of C_{cel} ; this parameter controls the elastic branch of the hydrostatic simulation by increasing its stiffness. Figure 3.49 compares the hydrostatic response after varying the parameter C_{cpl} . It is clear that this parameter defines the starting point of the hardening branch. Finally, the coefficient ξ_1 (Figure 3.50) influences the slope of the plastic regime while the coefficient ξ_2 (Figure 3.51) affects the stiffness of the hardening regime. The compaction law parameters are defined on a hydrostatic test and an oedometric test is used to verify their validity.

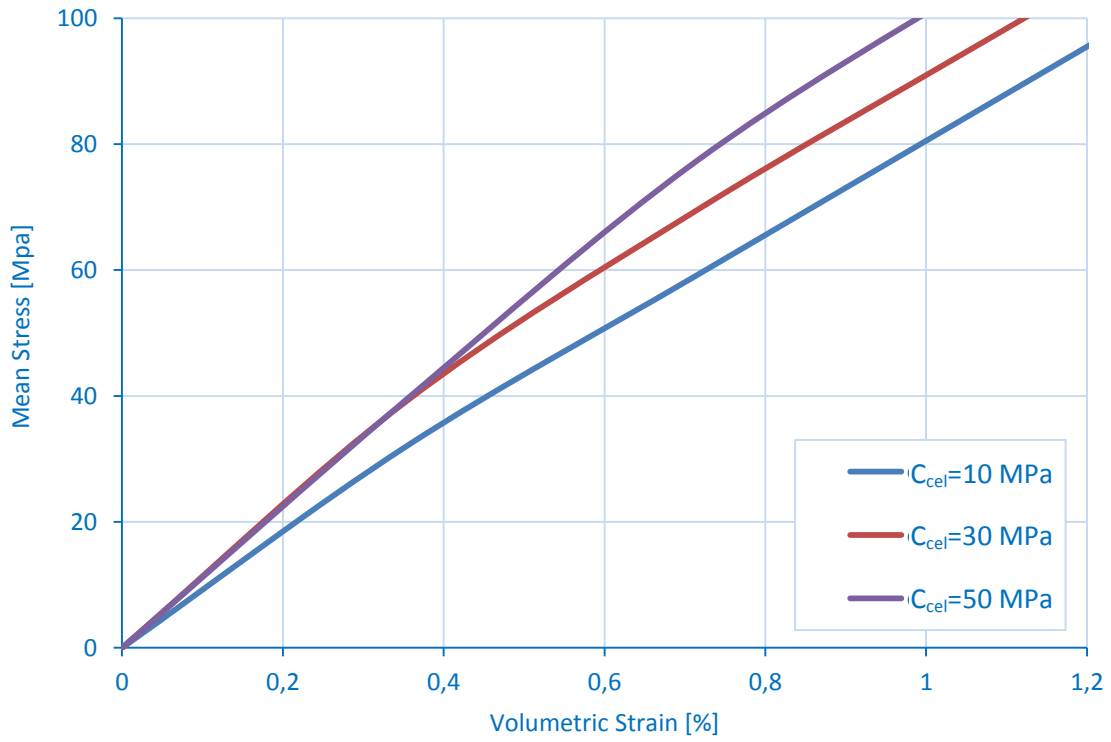


Figure 3.48: Effect of C_{cel} on the hydrostatic simulation

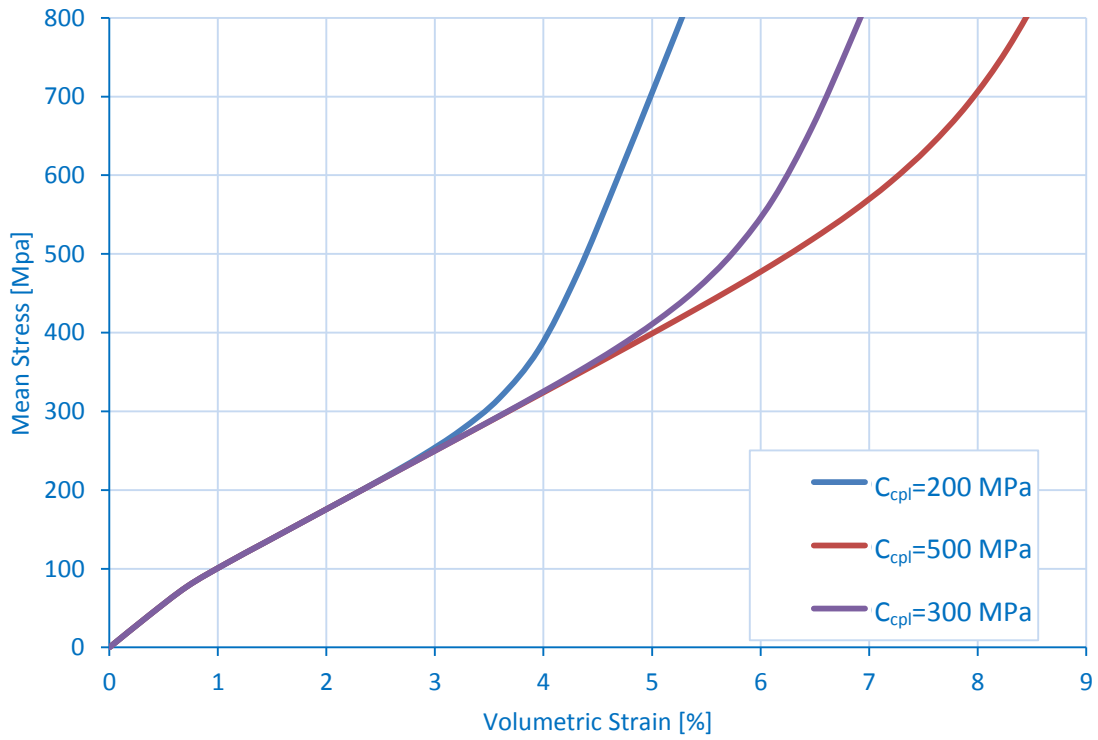


Figure 3.49 Effect of C_{cpl} on the hydrostatic simulation

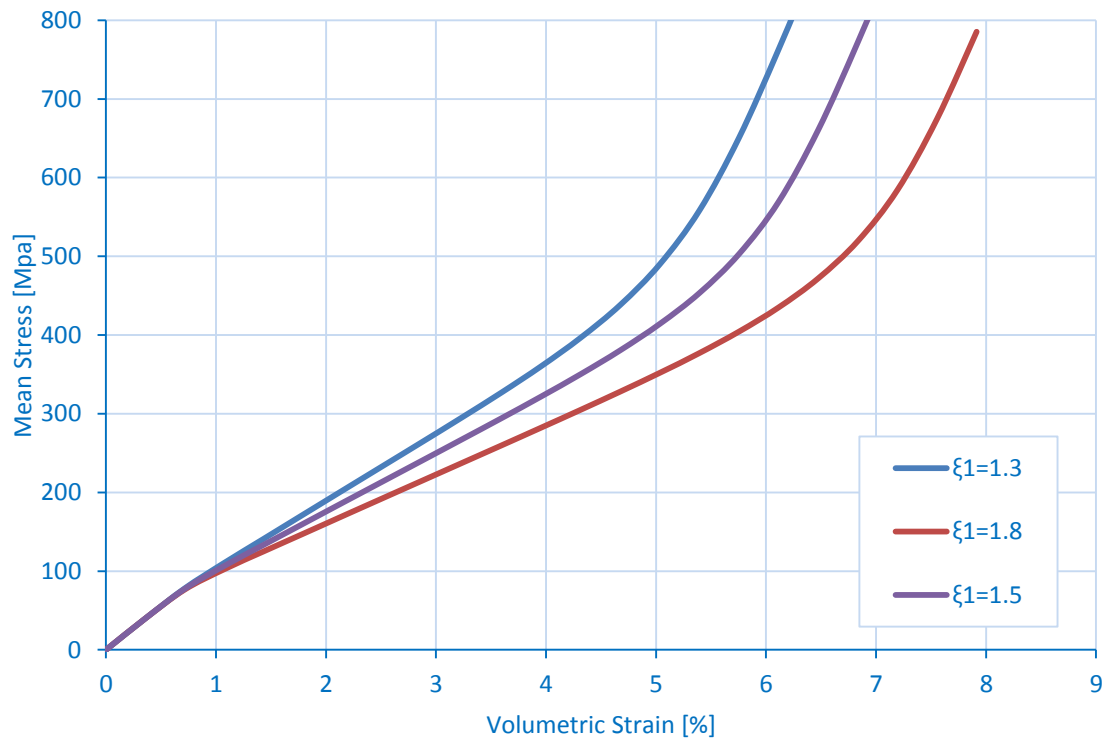


Figure 3.50: Effect of ξ_1 on the hydrostatic simulation

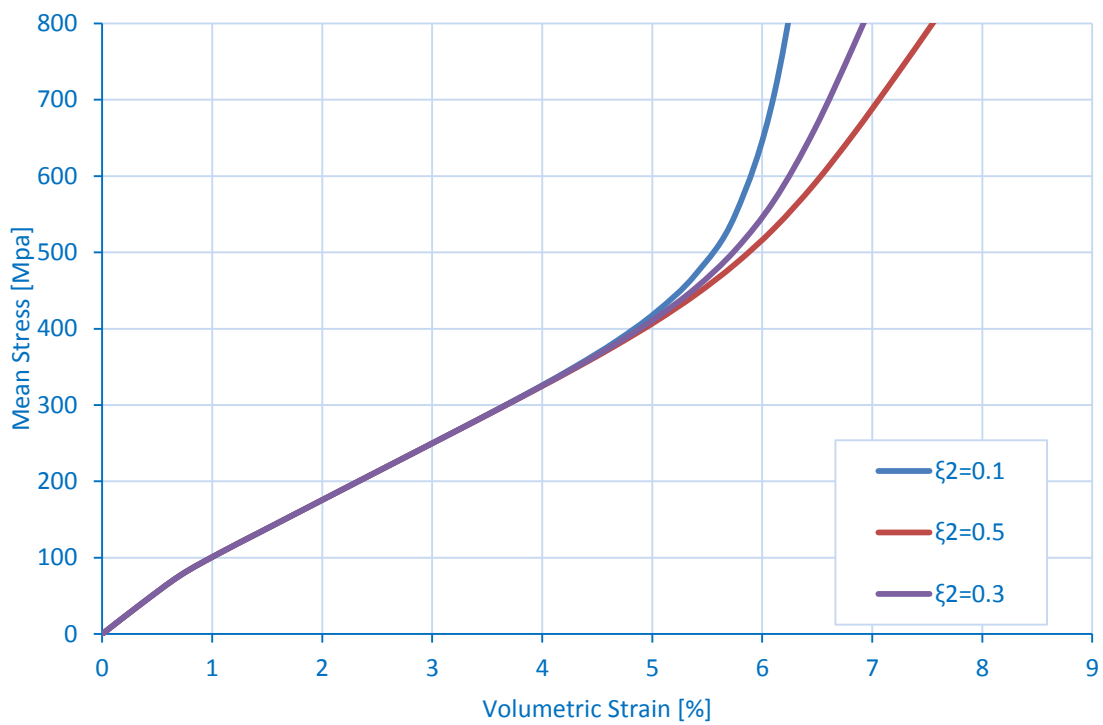


Figure 3.51: Effect of ξ_2 on the hydrostatic simulation

We calculated the local parameters for the high confining pressure model as $C_{cel} = 50 \text{ MPa}$, $C_{cpl} = 300 \text{ MPa}$, $\xi_1 = 1.5$ and $\xi_2 = 0.3$. The simulations of the hydrostatic and oedometric test are

plotted with the experimental results in Figure 3.53 and Figure 3.52. The experiments were conducted by Gabet [51] in the 3S-R laboratory (University Grenoble Alpes).

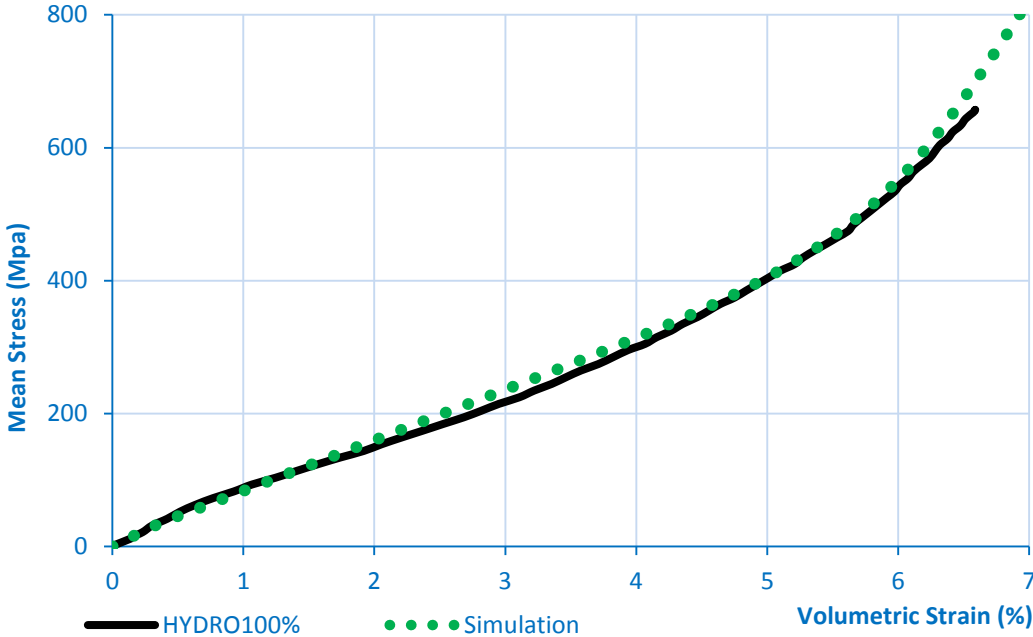


Figure 3.52: Hydrostatic test and simulation

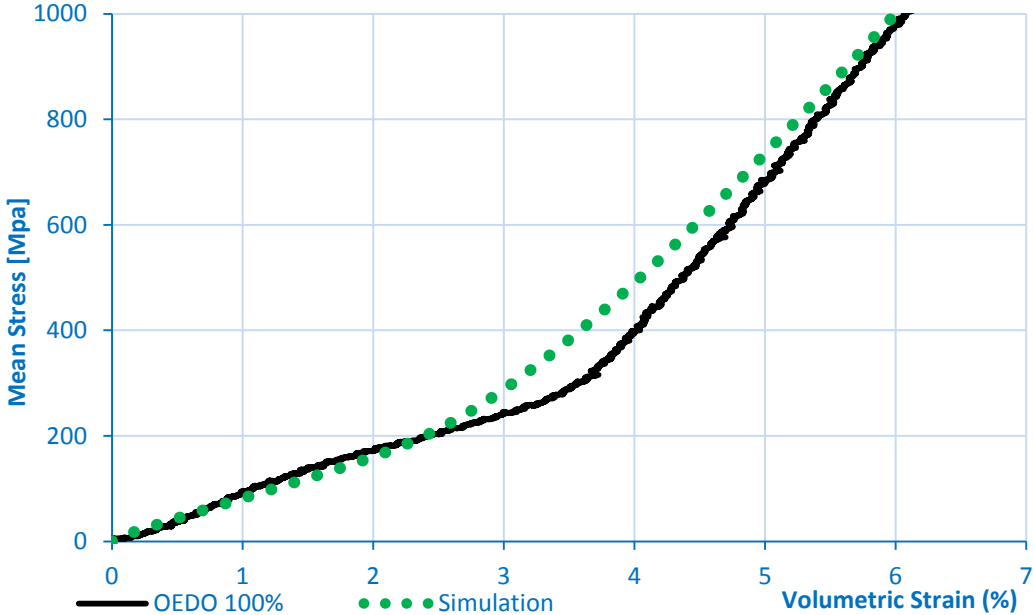


Figure 3.53: Oedometric test and simulation

3.2.3 Mesh for dynamic spalling test

Likewise, the mesh for the dynamic spalling test is created using the same procedure of the previous meshes. The specimen is cylindrical with diameter 46 mm and length 142 mm. It consists 18376 DE of 0.21 cm maximum radius, 0.07 cm minimum radius, compactness of 0.582 and an interaction range coefficient of 1.3965 (Table 3.5). Figure 3.54 shows the histogram of the size distribution and Figure 3.55 illustrates the discrete element mesh for the dynamic spalling Hopkinson bar test. The pulse is applied on directly on the front face of the sample and the rear face velocity is recorded to identify the dynamic increase factor law parameters.

FE number per side	k_1	k_2	Iterations	DE Total number	R_{max} (cm)	R_{min} (cm)	Compactness	λ
4	3	4	2	18376	0.21	0.07	0.582	1.3965

Table 3.6: DE diameters

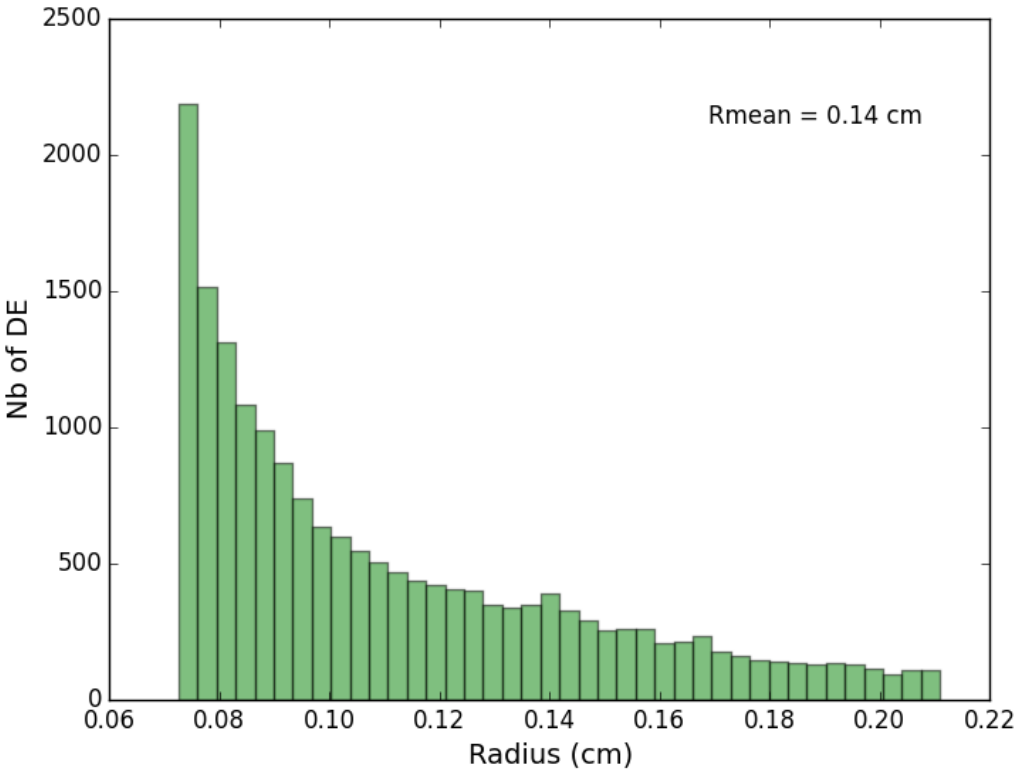


Figure 3.54: Spalling test mesh histogram of radius distribution

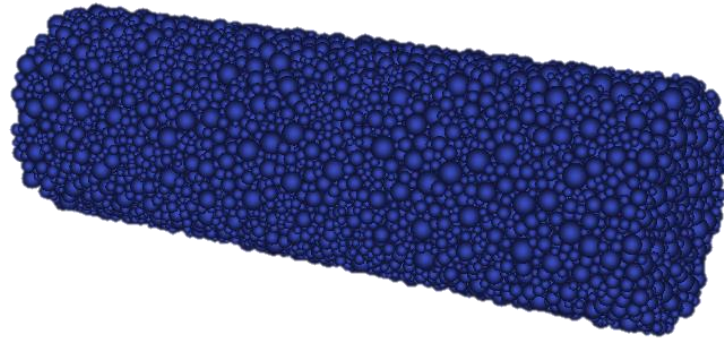


Figure 3.55: Compaction mesh

3.2.3.1 Strain rate dependency parameters

The strain rate dependency is inspired by the CEB formula [20] for the calculation of the macroscopic dynamic tensile strength as a function of strain rate, by defining a ratio DIF (Dynamic Increase Factor) of the dynamic tensile strength over the static tensile strength T_{dyn}/T_{st} . The local parameters: static strain rate ($\dot{\epsilon}_{st}$), moderate ($\dot{\epsilon}_m$) strain rates δ_1 and δ_2 were computed with the simulations of spalling tests [3]. The experiments launched during my master thesis in the laboratory 3S-R by the supervision of professor Pascal Forquin. The experimental rear face velocity of the spalling tests is reproduced with the parameters $\dot{\epsilon}_{st} = 10^{-6} \text{ s}^{-1}$, $\dot{\epsilon}_m = 1 \text{ s}^{-1}$, $\delta_1 = 0.0355$ and $\delta_2 = 0.333$.

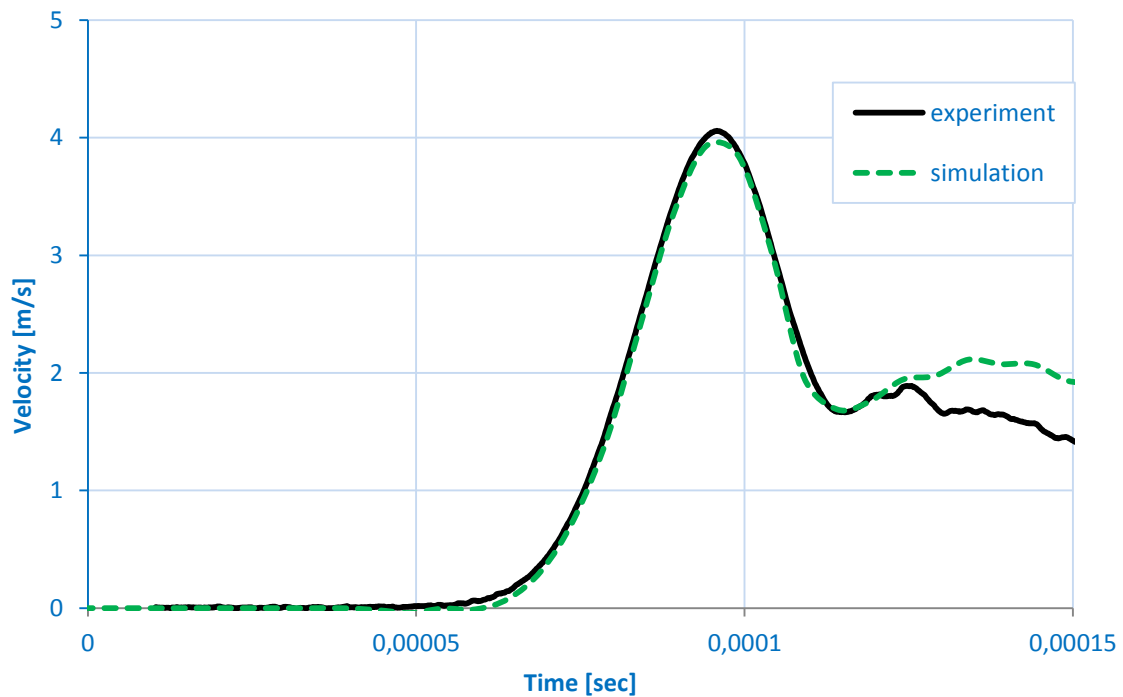


Figure 3.56: Spalling test and numerical simulation (impact velocity 4.28 m/s)

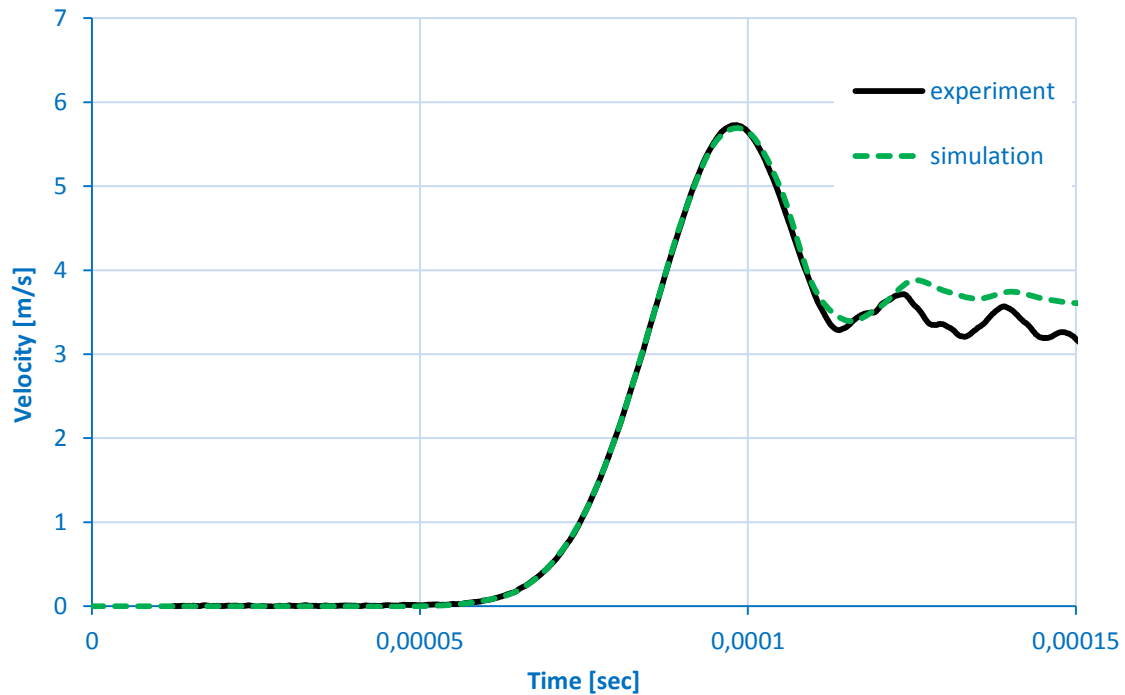


Figure 3.57: Spalling test and numerical simulation (impact velocity 5.85 m/s)

3.3 Conclusion

This chapter is separated into two units, the identification of the parameters for the mesh generation and the concrete constitutive model. The first unit gives the influence of the mesh generation parameters on both the mesh characteristics and the macroscopic behaviour of the concrete model. We demonstrated that the mesh parameters affect the density of the packing and the number of discrete elements. Also, they influence the behaviour of the constitutive model. Thus, we identified a set of mesh parameters to eliminate the dependency of our model to the assembly of the particles. We selected a packing that offers a homogeneous and isotropic mesh with the least possible amount of particles thus the computational cost remains rational. Furthermore, we defined a ratio between the FE size and the mean DE diameter, for proper contact between the two objects.

The second unit shows the influence of our constitutive model parameters on the macroscopic behaviour of concrete. These parameters were identified on fully saturated ordinary concrete. After comprehending the effect of each parameter, we established a procedure for their identification. We calibrated the linear and non-linear elastic model under low pressures with the help of quasi-static compressive and tensile test. Hydrostatic and oedometric test were used for compaction law parameters under high confining pressures. We calculated the parameters of the dynamic constitutive law on spalling Hopkinson bar test.

After defining all the parameters; our model is ready to simulate hard impacts on concrete and reinforced concrete target which is the primary objective of the current PhD study. Additionally, with the simulation of hard impact tests, we will validate the capability of the proposed discrete/finite element numerical approach to reproduce complex phenomena such as multi-cracking.

Chapter 4

Numerical simulations of impact experiments

The reliability of the proposed discrete element numerical model is validated with the simulation of hard impacts. The numerical results are compared with the experimental data to show the capability of our model to predict the damage modes of impacted concrete. First, we simulate the perforation and penetration test of CEA-Gramat [8],[106] to verify the ability of our model to produce the effects of hard impacts into concrete. They performed rigid impacts on confined concrete specimens. Then, the numerical calculation of Erzar's [40] edge-on impact on concrete tiles presents the evolution of damages in a two-dimensional configuration. Finally, the simulation of the drop-weight impact on a reinforced concrete beam from the University of Toronto [114] validates the capability of the steel-concrete bond [91] to model the response of reinforced concrete.

4.1 CEA impact experiments

A series of impact tests performed by CEA-Gramat [8], [106] with a gas launcher "DEIMOS" Figure 4.1. Rigid ogive-nosed steel projectiles with a nose radius to diameter ratio of 5.77, a 52.06 mm shank diameter, a 299.43 mm length and a 2.442 kg mass (Table 4.1) were used to hit the centre of unreinforced cylindrical concrete specimens. Acceleration recorder system embedded into the steel projectile (Figure 4.2) to measure axial deceleration during the experiment and to obtain both displacement and velocity by integration. The correct integration of the acceleration was validated by the comparison of the integrated and measured projectile velocities using a laser technique.



Figure 4.1: Gas launcher “DEIMOS”

Mass	Diameter	Length	Nose radius/Diameter	Length/Diameter
2.442 kg	52.06 mm	299.43 mm	5.77 mm	5.77 mm

Table 4.1: Projectile properties



Figure 4.2: Ogive-nosed steel projectile with its accelerometer

Targets were made of fully saturated unreinforced R30A7 ordinary concrete confined with a thin steel jacket. R30A7 concrete composition and mechanical properties are given in Table 3.4 which were widely investigated in previous studies [52], [53], [88], [137], [138]. The target diameter is 800 mm, while the thickness is 300 mm for the perforation test and 800 mm for the penetration test. The confined steel jacket has a 15 mm thickness and it is fixed to the concrete target. Furthermore, high-speed video cameras were used to observe the interaction between the projectile and the target. Figure 4.3 illustrates the recording of perforation test phases. One can observe the impact effects found in the literature [76]. Initially, spalling appears with the ejection of fragments from the proximal face of the target (0.6 -2.5 ms). At the same time, the penetration phase of the projectile

initiates with tunnelling into the target. In the end, the striker perforates the concrete specimen with scabbing on the distal face (4.4 -8 ms).

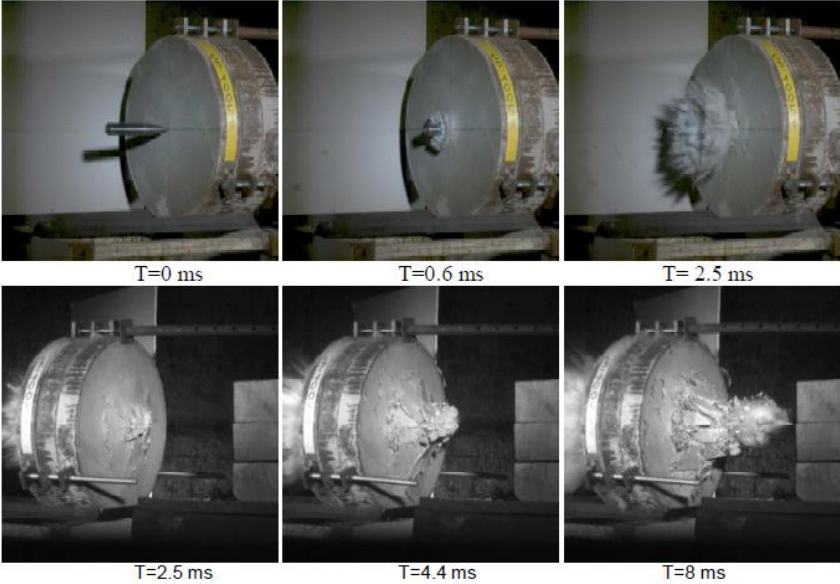


Figure 4.3: Perforation test phases

Three tests have been conducted with different striking velocities, one perforation test at 333m/s and two penetration tests at low velocity (LV, 227 m/s) and high velocity (HV, 347.4 m/s) Table 4.2. After the test, a topographic laser system was used to measure the crater dimension and the penetration depth.

Test	Perforation	Penetration (LV)	Penetration (HV)
Velocity	333 m/s	227 m/s	347.4 m/s
Thickness	300 mm	800 mm	800 mm

Table 4.2: CEA-Gramat impact test striking velocities

Figure 4.4, Figure 4.5, and Figure 4.6 show the damage on the concrete specimens after impact. The sample under perforation Figure 4.4 appears cratering on both faces with wider damage zone on the rear face than the front face. The perforation test samples are damaged with a cone cracking mode.

As expected the damage on the concrete target under HV penetration Figure 4.6 is higher than on the specimen under LV penetration Figure 4.5.



Figure 4.4: Target's front face (left) and rear face (right) after perforation test



Figure 4.5: Target's front face (left) and rear face (right) after penetration LV test



Figure 4.6: Target's front face (left) and rear face (right) after penetration HV test

4.1.1 Modelling of CEA impact experiments

The cylindrical concrete specimen model is with discrete elements, while tetrahedral finite elements are used for the steel confining jacket Figure 4.7 and the steel projectile Figure 4.8. The discretisation of this problem was very challenging because the projectile diameter (52.06 mm) is very small compared to the target diameter (300 mm). FE size cannot be bigger than 1 cm; otherwise, the discretisation is not providing the correct shape of the projectile. It is significant to keep the FE size bigger than the mean DE diameter ensuring proper creation of contacts between the two objects.

Table 4.3 gives the DE characteristics of the perforation and penetration of concrete specimens, which respect the condition for correct contact between FE and DE, Figure 4.9 and Figure 4.11 gives their histogram distributions Figure 4.9 Figure 4.11. Figure 4.10 illustrates the perforation test model while Figure 4.12 shows the penetration test model with a DE mesh for the concrete specimen confined with a FE steel jacket. The projectile is placed 7 cm above the middle of the concrete specimen. The steel elements are modelled with a linear elastic behaviour of $E = 210 \text{ GPa}$ and $\nu = 0.3$.

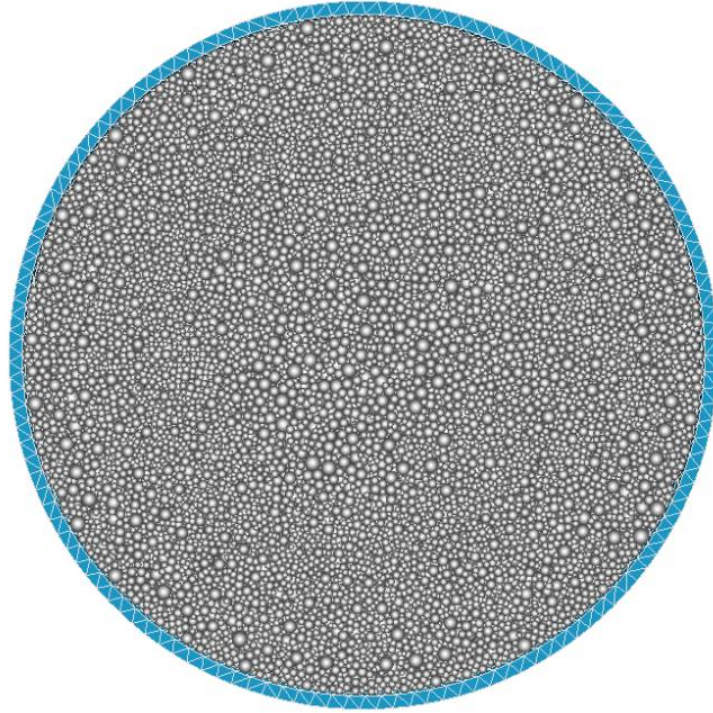


Figure 4.7: Discrete element model of concrete target with finite element model of confining steel jacket

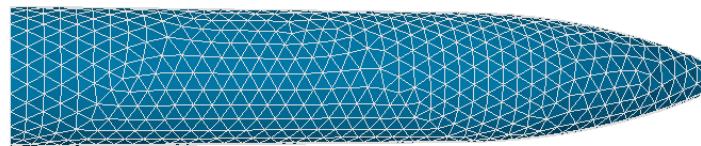


Figure 4.8: Steel projectile FEM model with tetrahedral

Mesh	DE Total number	D_{max} (cm)	D_{min} (cm)	D_{mean} (cm)	Compactness	λ
Perforation	141765	1.8	0.6	0.942	0.6086	1.3986
Penetration	336467	1.8768	0.6256	0.982	0.6154	1.402

Table 4.3: Perforation and penetration assembly characteristics

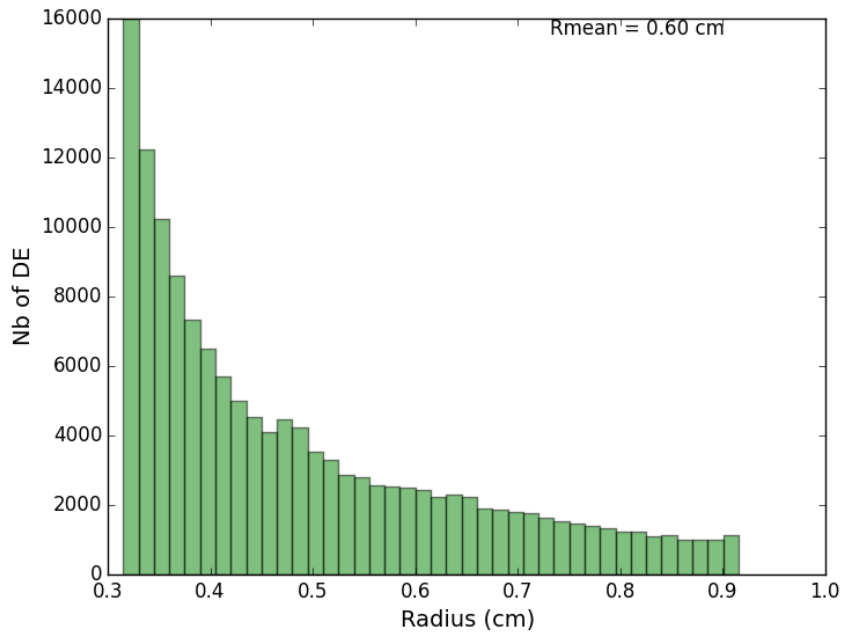


Figure 4.9: Perforation test mesh histogram of radius distribution

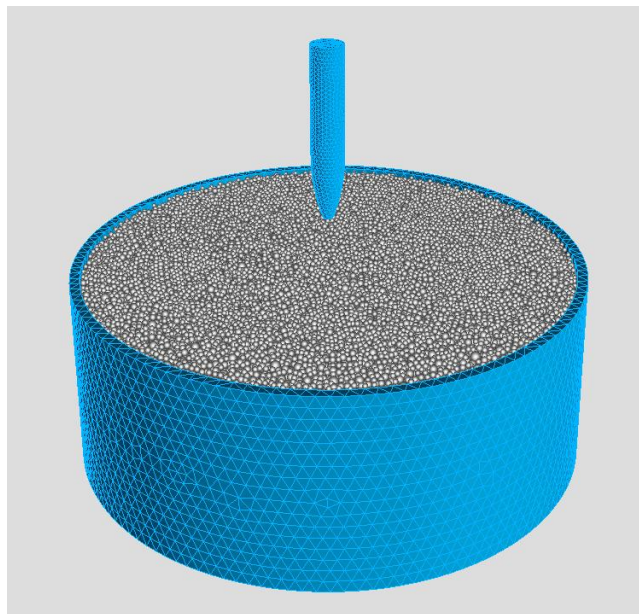


Figure 4.10: Perforation test model with DE concrete specimen (800mm diameter, 300mm height) confined with FE steel jacket and FE steel projectile (52.06 mm diameter, 299.43 mm length)

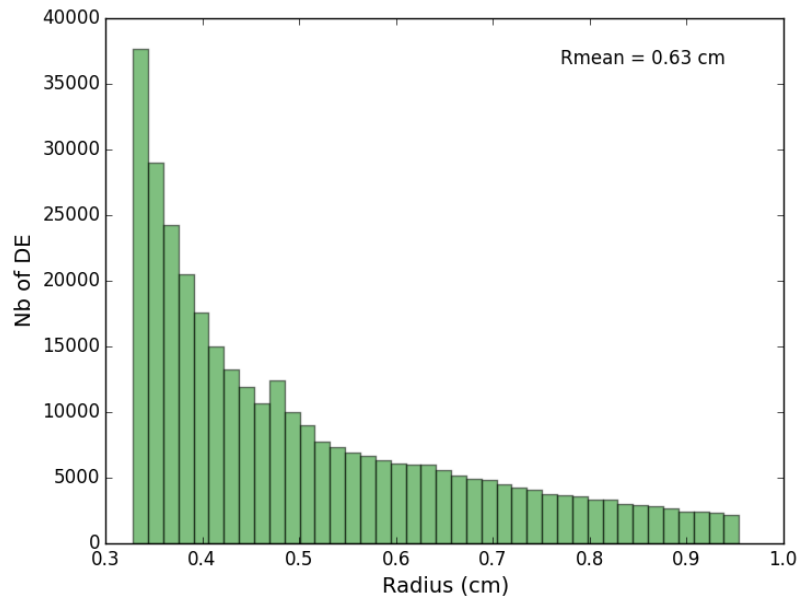


Figure 4.11: Penetration test mesh histogram of radius distribution

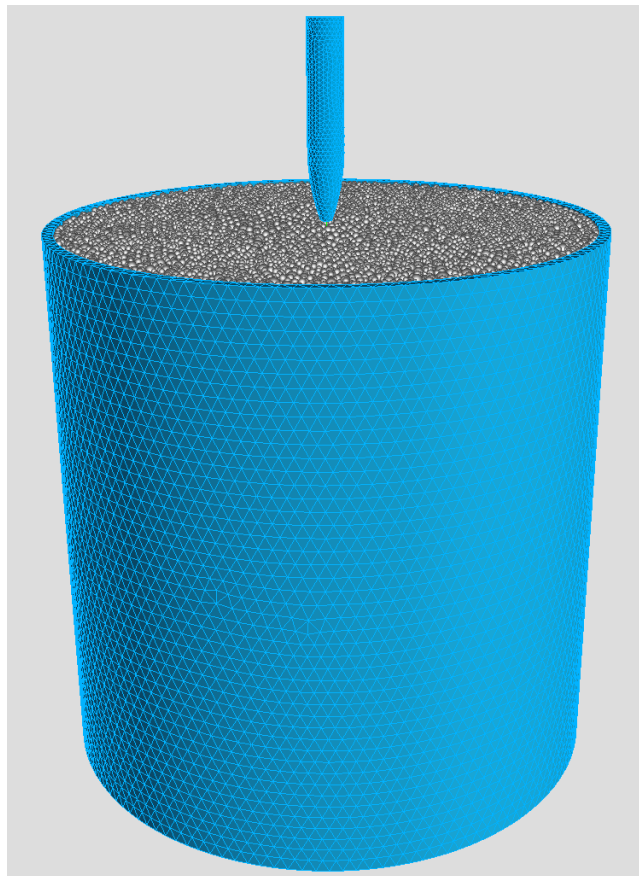
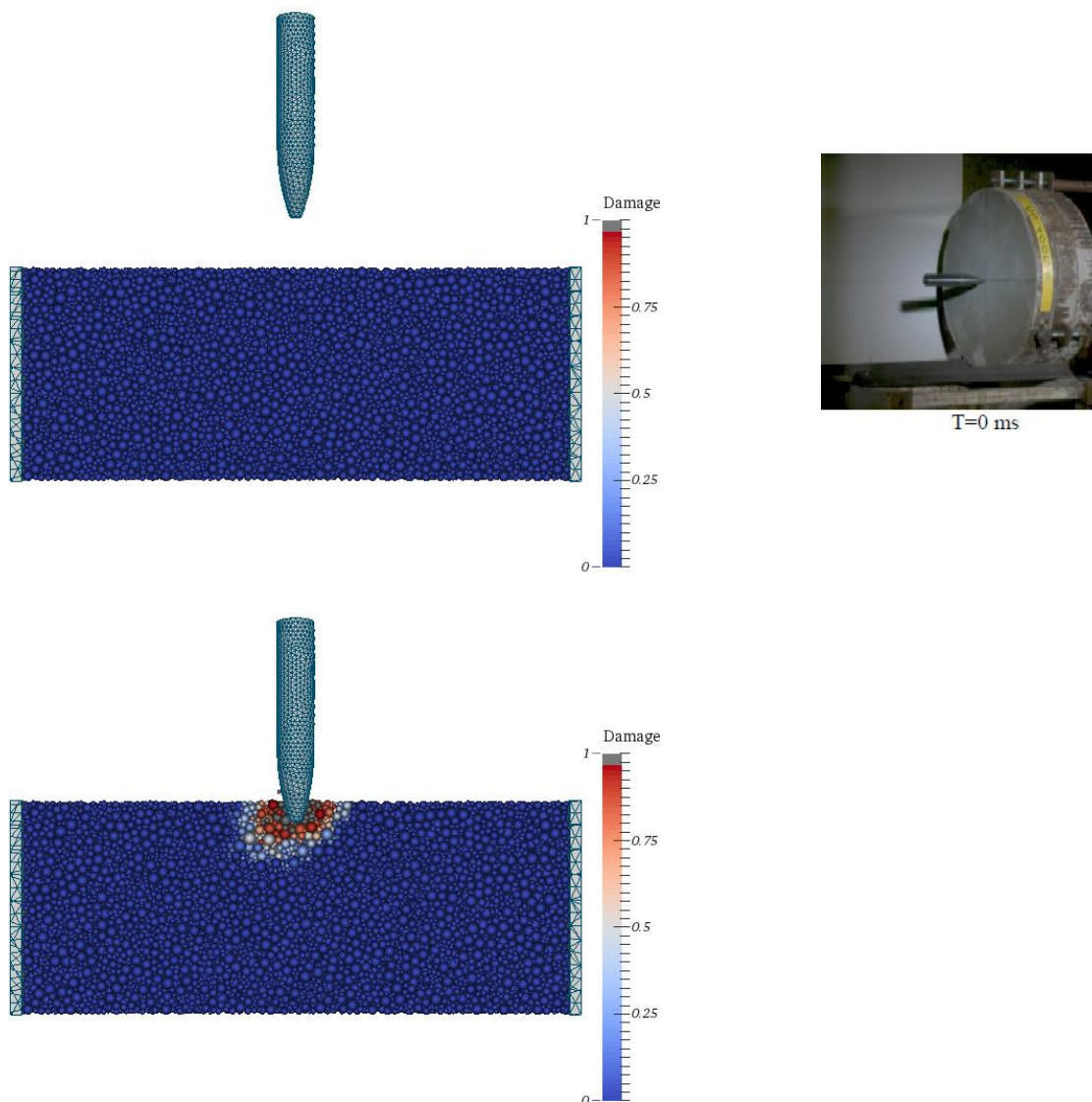
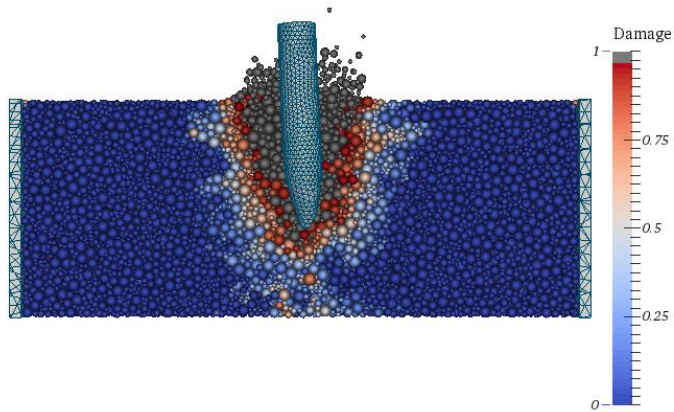


Figure 4.12: Penetration test model with DE concrete specimen (800mm diameter, 800mm height) confined with FE steel jacket and FE steel projectile (52.06 mm diameter, 299.43 mm length)

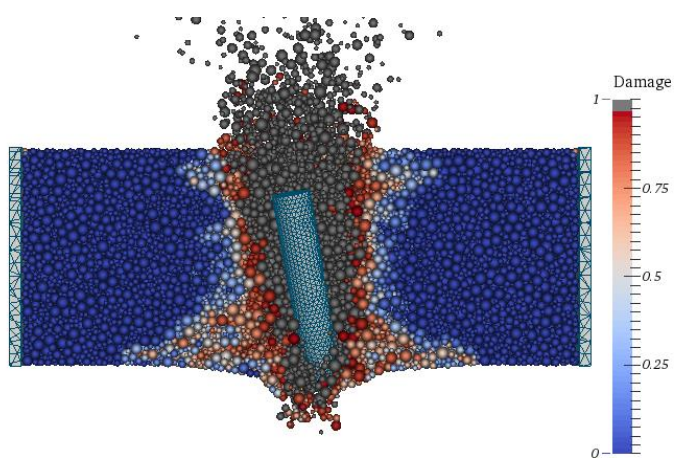
4.1.2 Numerical results

Figure 4.13 shows the evolution of damage during the simulation of the perforation test for six instants (left side) and pictures from the experiment Figure 4.3 (right side). The simulation represents all the damage modes of concrete under perforation from rigid projectiles sufficiently. We can see the initial cratering at 0.3 ms, the initiation of spalling at 0.6 ms following by the tunnelling due to penetration of the projectile. Then, scabbing appears at the rear face at 2.5 ms and finally, the projectile perforates the target.

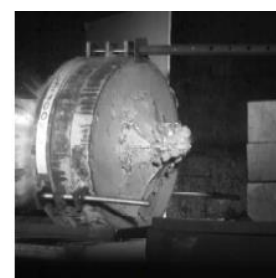
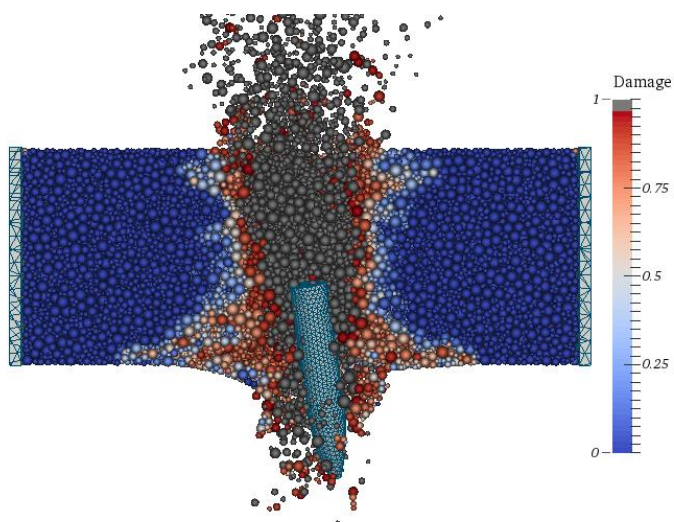




T=0.6 ms



T=2.5 ms



T=4.4 ms

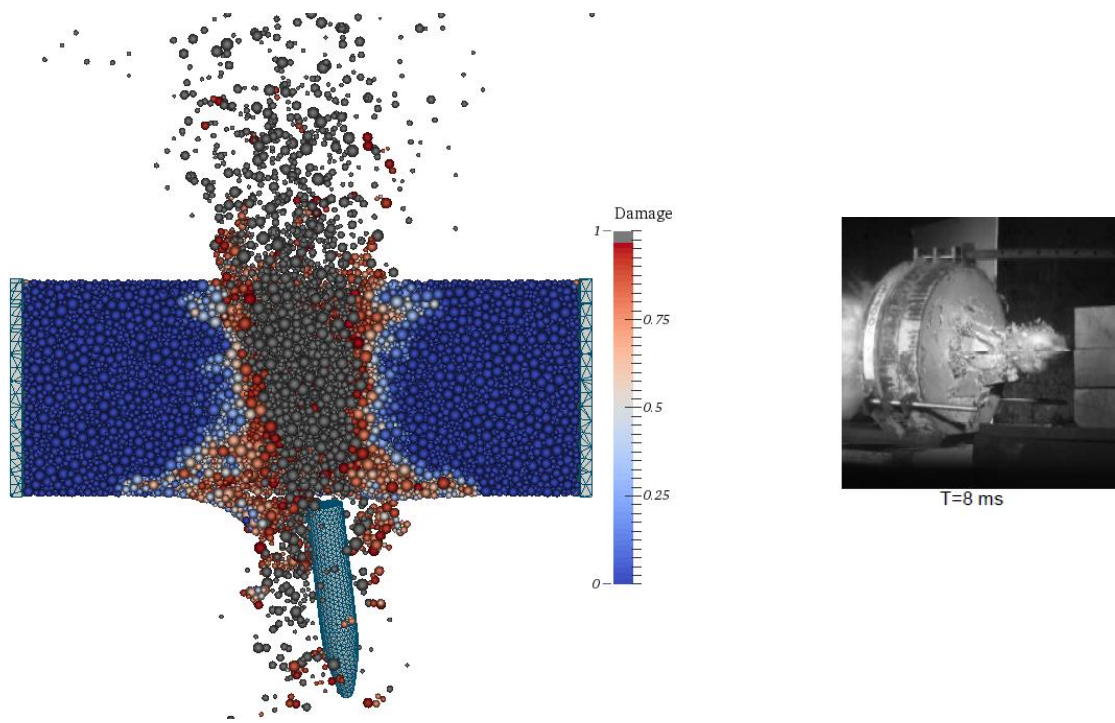


Figure 4.13: Perforation damage state of concrete at $t = 0, 0.3 \text{ ms}, 0.6 \text{ ms}, 2.5 \text{ ms}, 4.4 \text{ ms}$ and 8 ms (from top to bottom)

Figure 4.14 and Figure 4.15 plot the axial displacement and velocity of the perforation impact test, where black curves give the experimental results and blue the simulation. Experimental data perfectly match with numerical results.

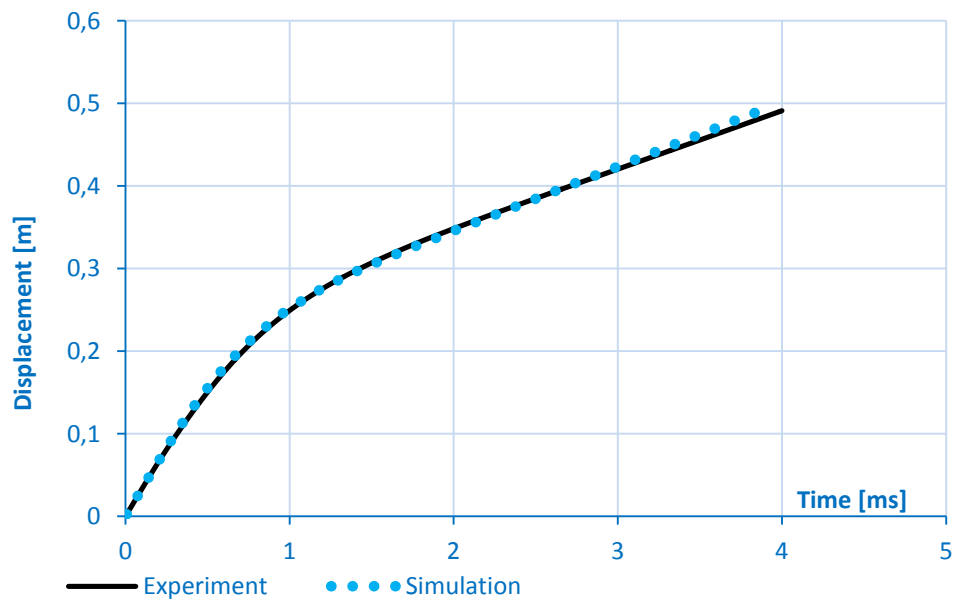


Figure 4.14: Perforation test, simulation and experiment, projectiles axial displacement

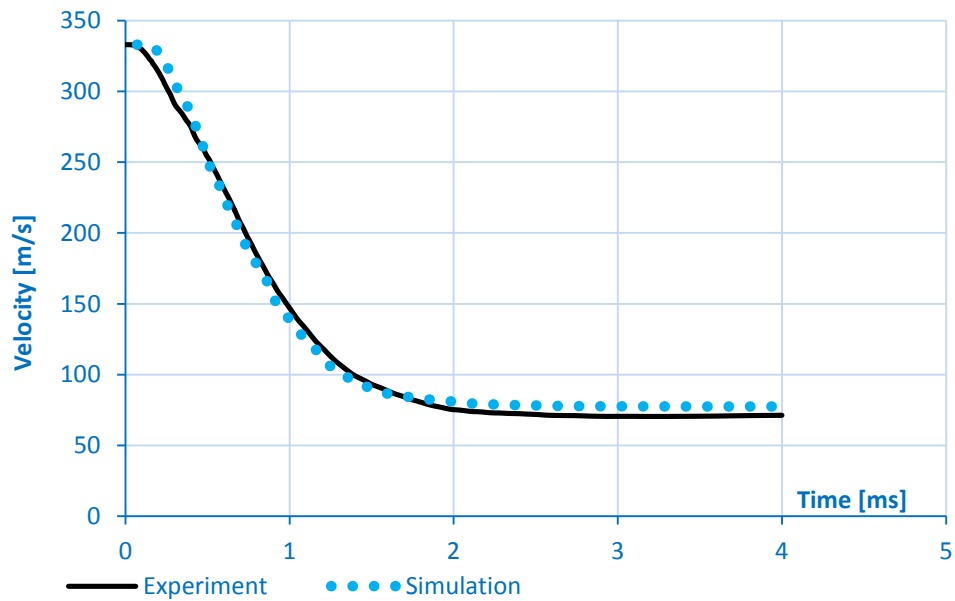


Figure 4.15: Perforation test, simulation and experiment, projectiles axial velocity (right)

Figure 4.16 presents the crack pattern observed after the perforation test (right side) and the damage state obtained from the numerical simulation (left side). The colours on the two figures are not related, the colour of the left side figure define damage for the DEs that are not blue while the colours of the right side figure show the ejected fragments of the concrete.

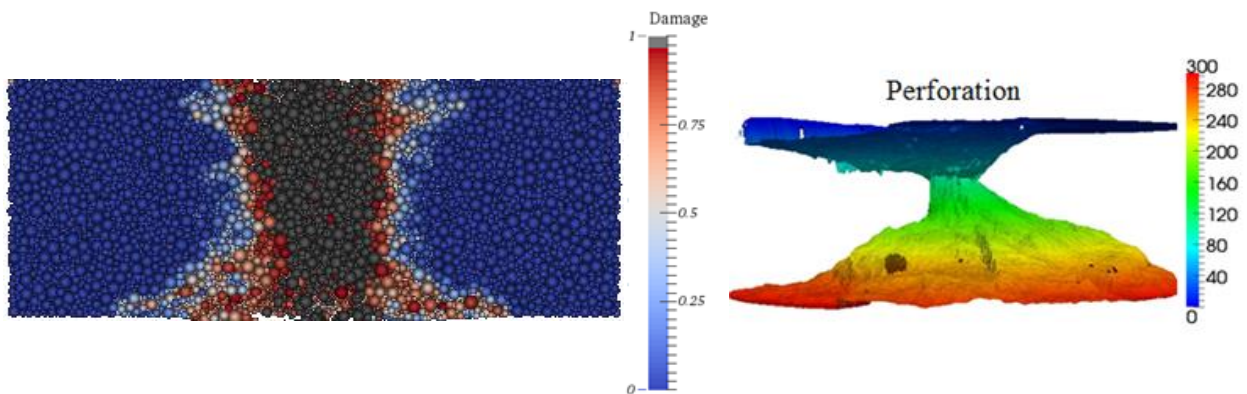
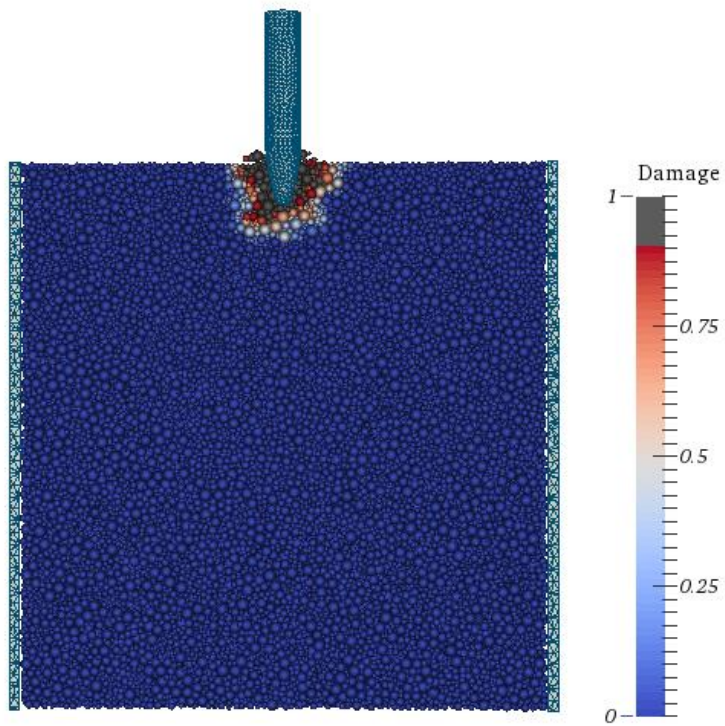
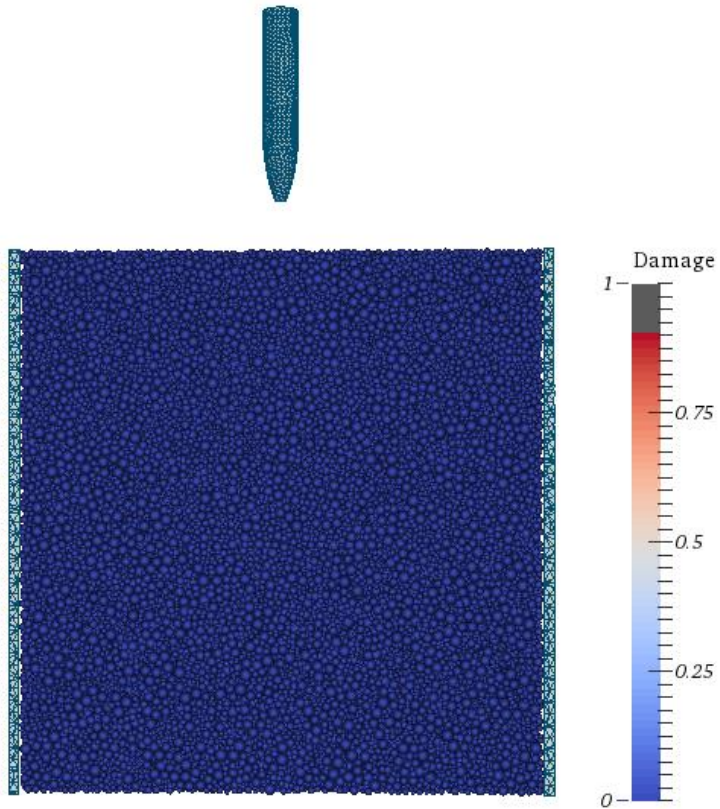


Figure 4.16: Perforation crack pattern, simulation (left) and experiment (right)

Figure 4.17 shows the crack propagation throughout the simulation of the LV penetration test for four moments. The target for the penetration test is thicker than the perforation test; thus the projectile does not perforate the specimen. The simulation produces all the impact effects into concrete with spalling and cratering on the front face by conical cracks at 0.6 ms and the penetration of the projectile creates a cylindrical hole with diameter very close to the projectile's diameter at 1.2-1.4 ms.



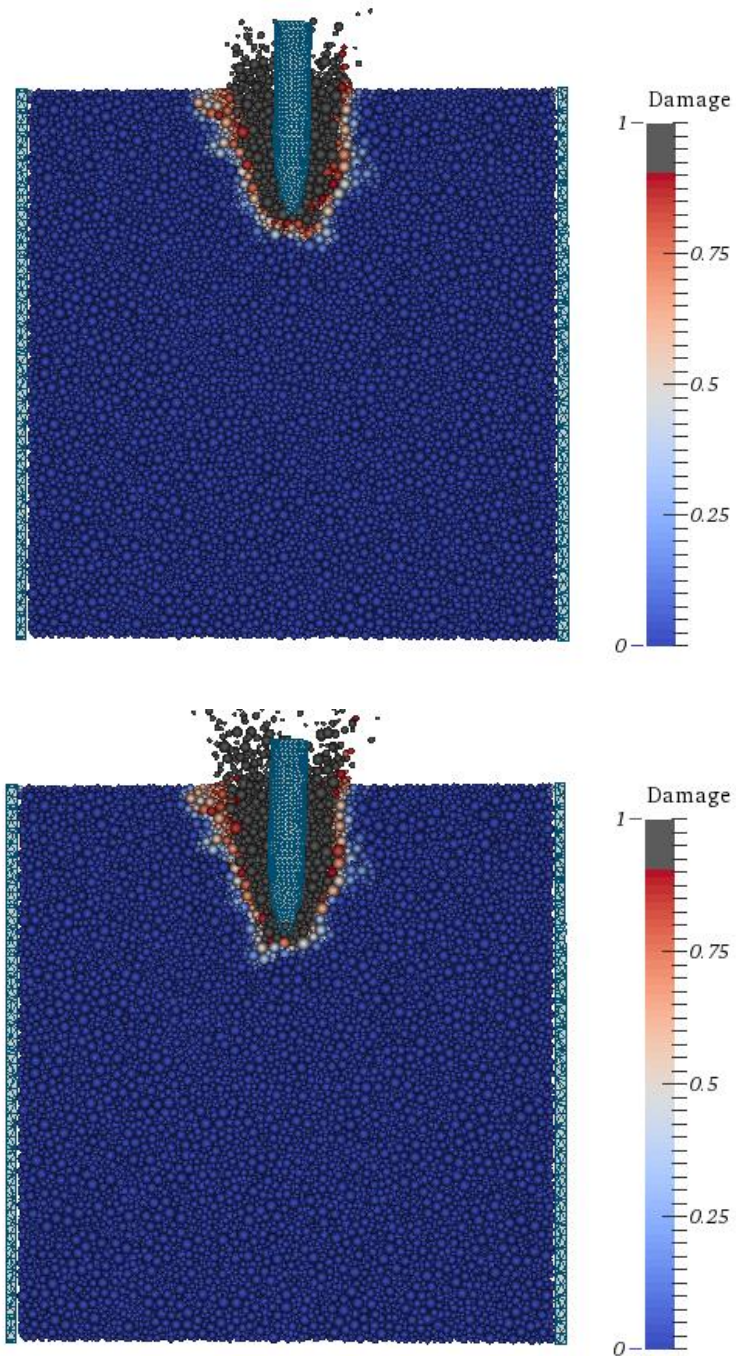


Figure 4.17: Penetration LV damage state of concrete at $t = 0, 0.6 \text{ ms}, 1.2 \text{ ms}$ and 1.4 ms (from top to bottom)

Figure 4.18 compare axial displacement of the projectile during the LV perforation between the experimental (black curve) and simulation (blue curve), while similarly Figure 4.19 gives its axial velocity.

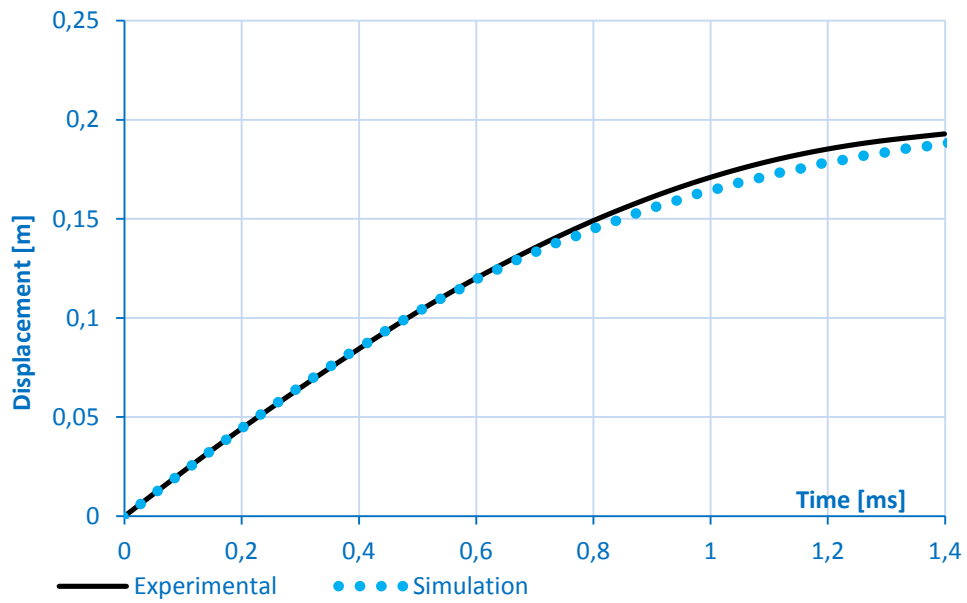


Figure 4.18: LV Penetration test, simulation and experiment, projectile axial displacement

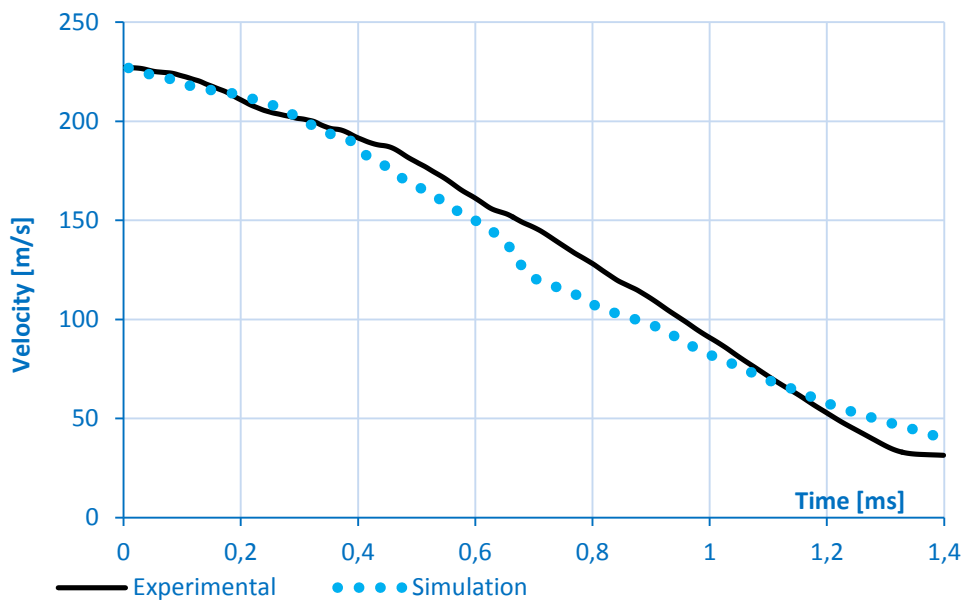


Figure 4.19: LV Penetration test, simulation and experiment, projectile axial velocity

Figure 4.20 (right side) shows LV penetration test damage in Figure 4.20 and the damage after the simulation (left side).

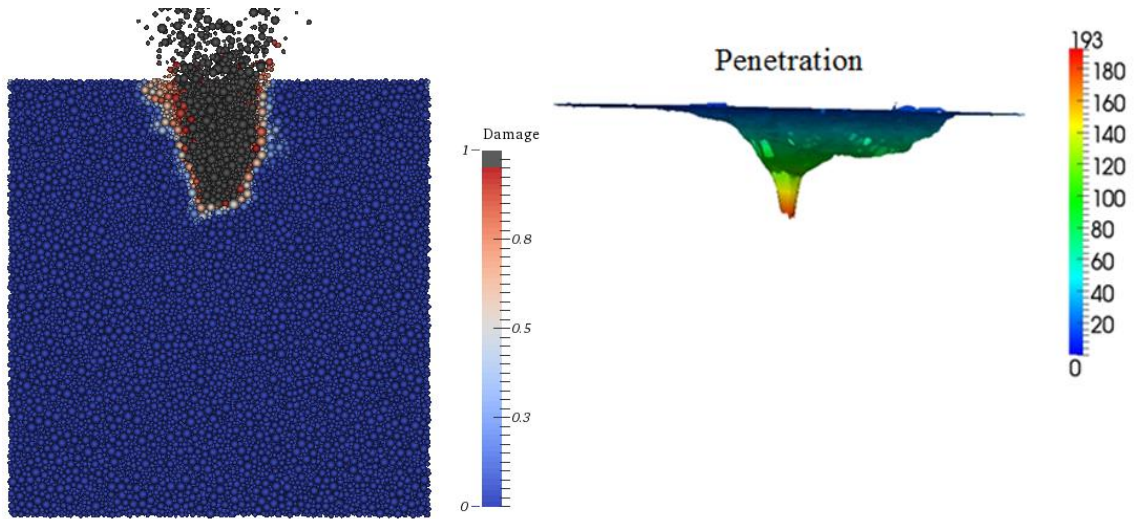
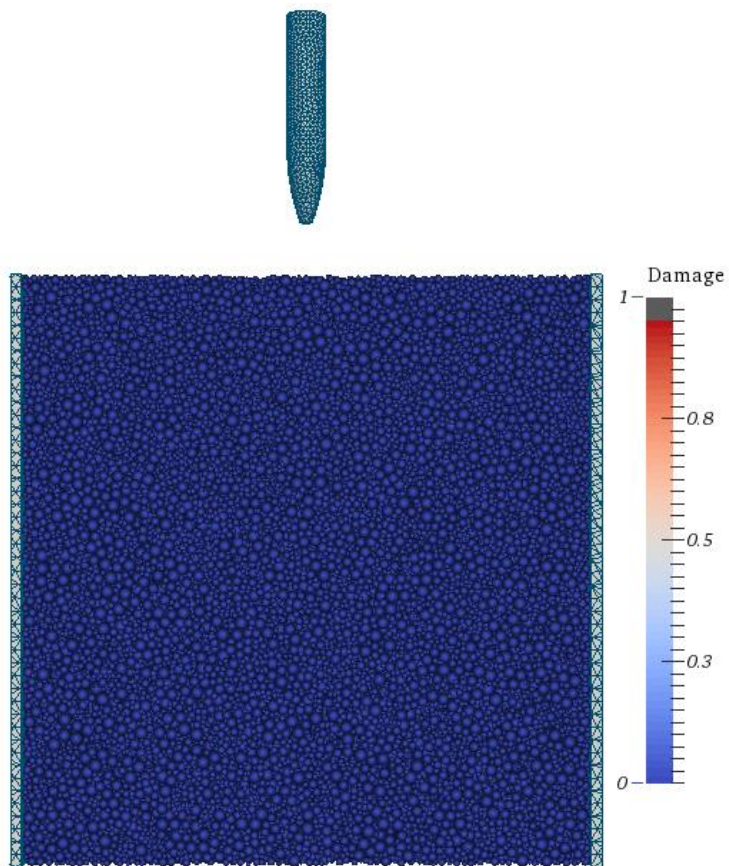
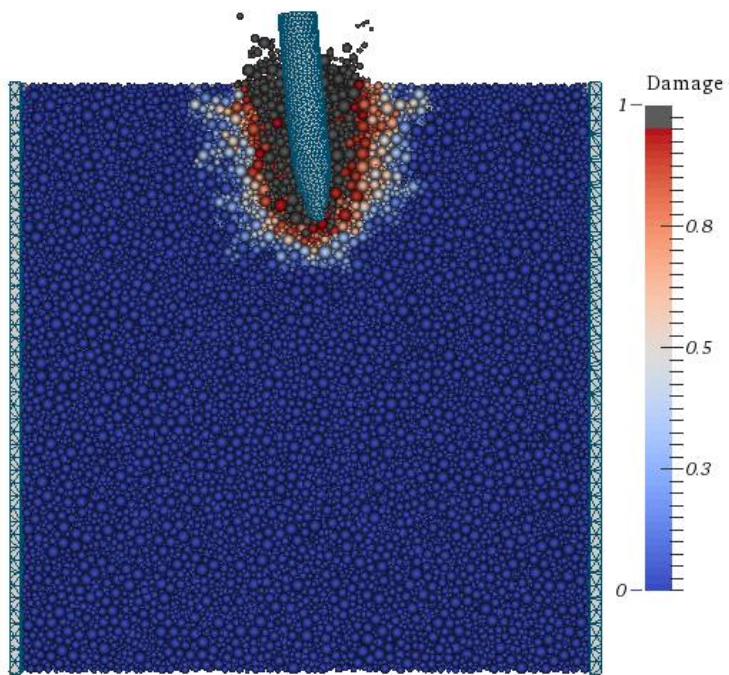
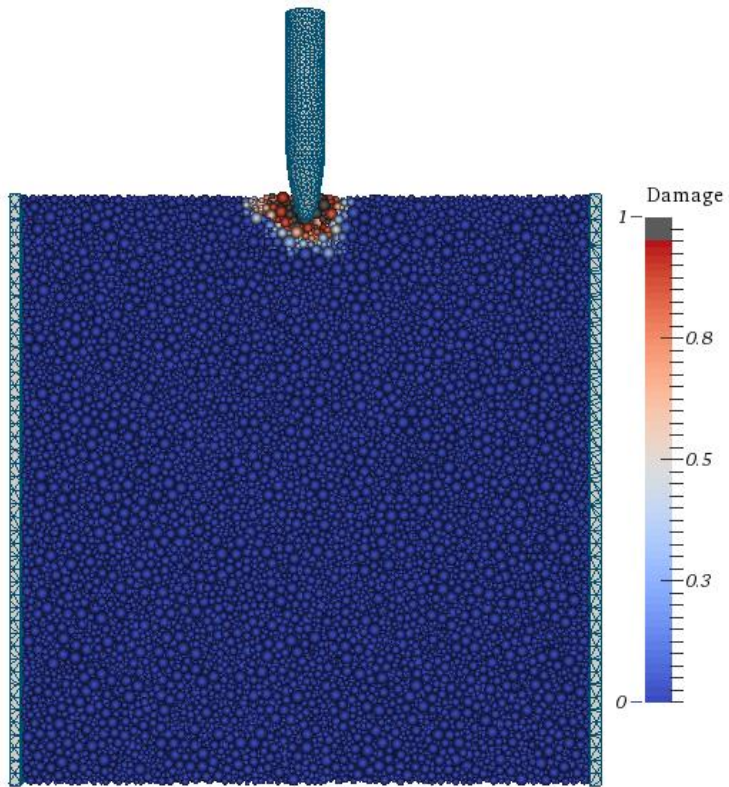


Figure 4.20: LV Penetration crack pattern, simulation (left) experiment (right)

Figure 4.21 shows the cracks during the simulation of the HV penetration test for four instants. Likewise, the LV impact test the same impact effects appear at the HV simulations (spalling with cratering and tunnelling through penetration). However, the penetration depth of the HV penetration test is bigger than the LV penetration, as expected.





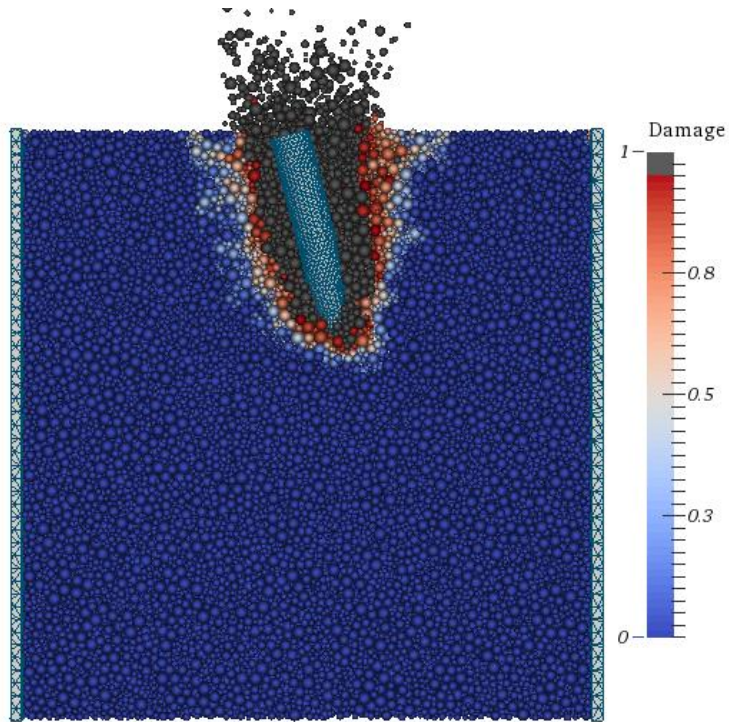


Figure 4.21: Penetration HV damage state of concrete at $t = 0, 0.4 \text{ ms}, 0.8 \text{ ms}$ and 1.4 ms (from top to bottom)

Figure 4.22 and Figure 4.23 illustrate the axial displacement and velocity of the projectile of the HV penetration test.

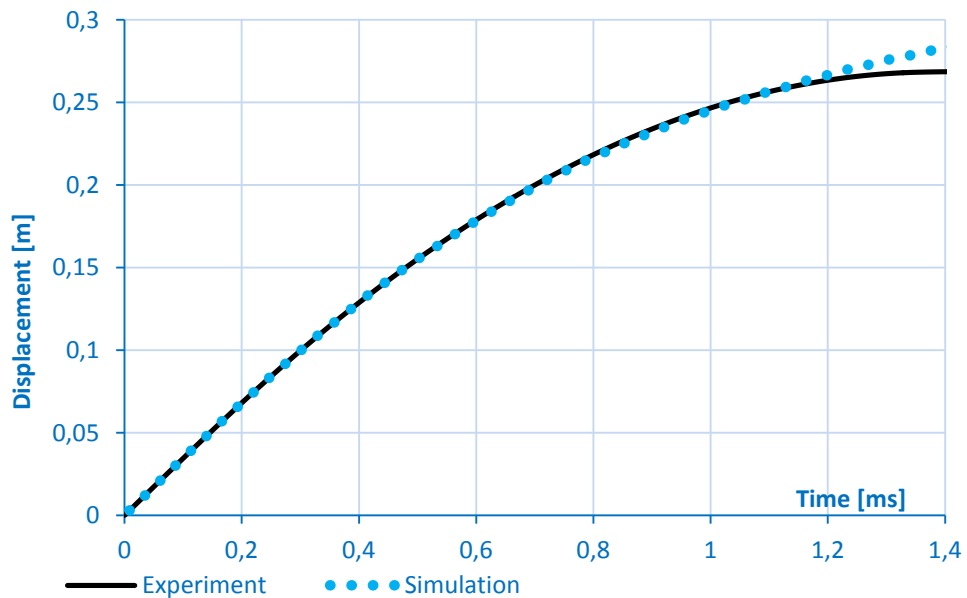


Figure 4.22: HV Penetration test, simulation and experiment, projectile axial displacement

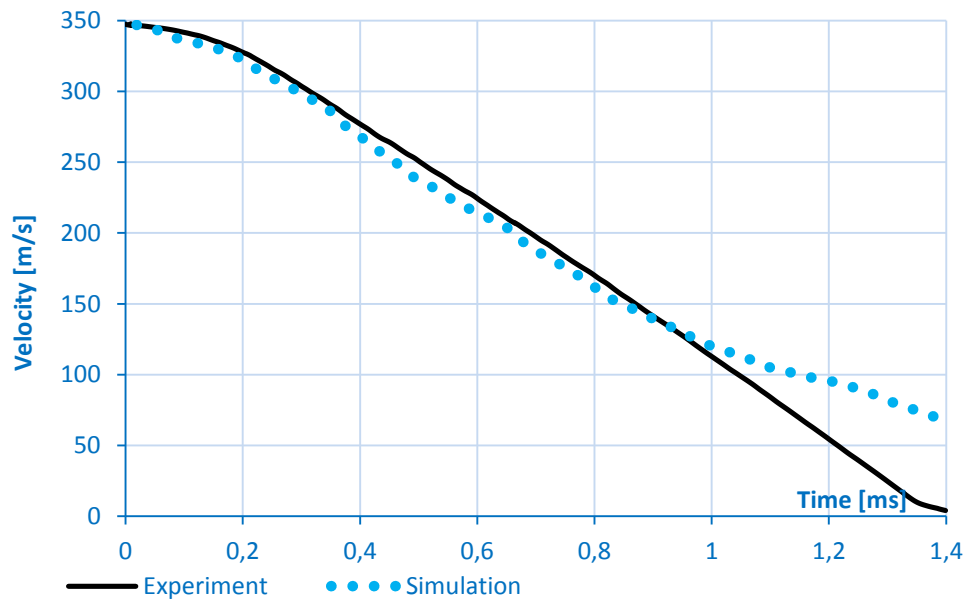


Figure 4.23: HV Penetration test, simulation and experiment, projectile axial velocity

Figure 4.24 shows the crack pattern after the HV penetration simulation (right side) and the experiment (left side).

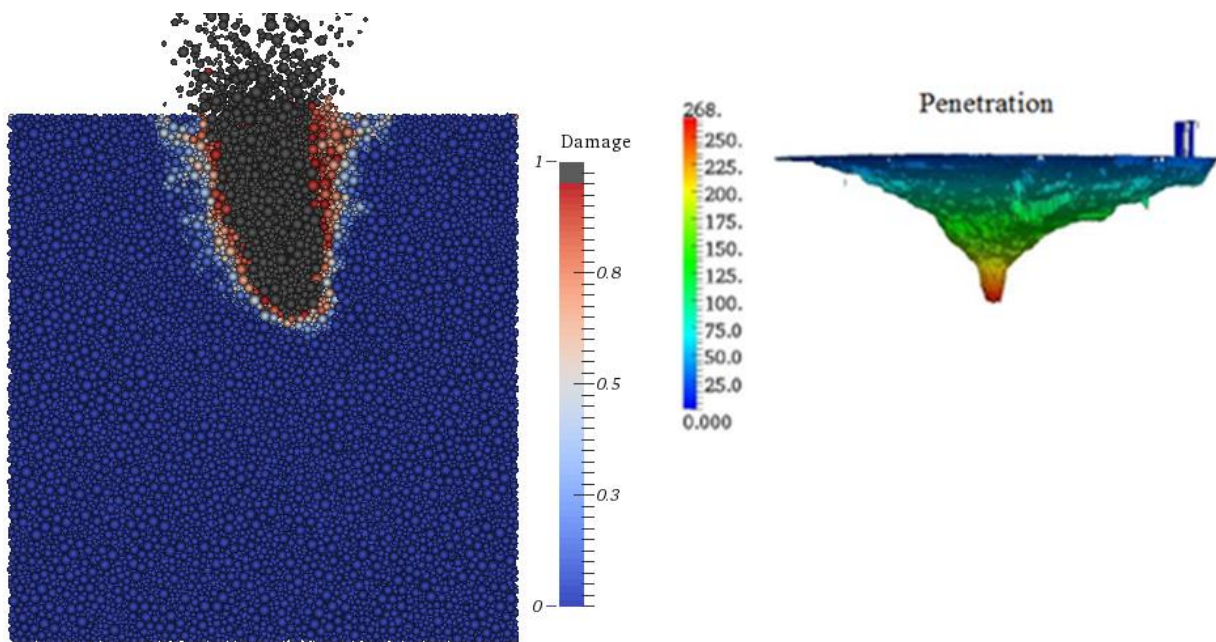


Figure 4.24: HV Penetration crack pattern, simulation (left) experiment (right)

The numerical results are in good accordance with the experimental ones. For the perforation test results thoroughly match with the simulation. However, a slight difference is observed on the curves of the penetration tests.

The damage for all experiments seems to be quite similarly produced by the DE model. The perforated specimen appears more significant diagonal cracks at the bottom than the top, like the experiment. It is evident that the phenomena observed experimentally, such as spalling on the front face with injection of fragments and tunnelling have successfully been generated through all the simulations. In addition, scabbing with diagonal cracking is presented on the rear face of the perforation specimen. Furthermore, a cratering damage mode observed in the penetration tests, which was also reproduced in numerical results. Finally, the simulations calibrated successfully bigger penetration depth for the HV impact than the LV impact.

4.2 Edge-on-impact test

The edge-on impact test (EOI) developed by the Ernst Mach Institute – Germany [66], [128] and Centre Technique d’Arcueil – France [46], [110], to study fragmentation of concrete at high strain-rates. The principle of this experiment is to visualise the evolution of damages by producing loading equivalent to that of a ballistic impact in a two-dimensional configuration.

This study is analysing the simulation of two edge-on impact test to verify the damage reliability of the current discrete element method. Erzar [40] performed the two edge-on impact experiments Figure 4.25 at the University of Metz. EOI test consists of a thin concrete tile (200 x 120 x 15 mm³) impacted by aluminium projectiles of 19.9 mm diameter Figure 4.25 and three rigid plates. Two of the plates constrain the vertical displacements of the top and bottom specimen faces, whereas a flexible vertical plate with fixed ends limits the horizontal displacement of the rear face of the tile. Concrete specimens are fully saturated unreinforced ordinary concrete R30A7 (Table 3.4). The projectiles have particular homothetic geometry and are made of aluminium Figure 4.26.

The first experiment EOI-Small is conducted by a small projectile (62.15 mm length) with 75.5 m/s impact velocity. The second experiment EOI-Big performed with a big (122.15 mm length) with 56 m/s impact velocity. Table 4.4 shows the characteristic of the projectiles for the EOI test.

Projectile	Mass	Diameter	Length	Velocity
Small	0.1304 kg	19.9 mm	62.15 mm	75.5 m/s
Large	0.27390 kg	19.9 mm	122.15 mm	56 m/s

Table 4.4: EOI tests projectile properties

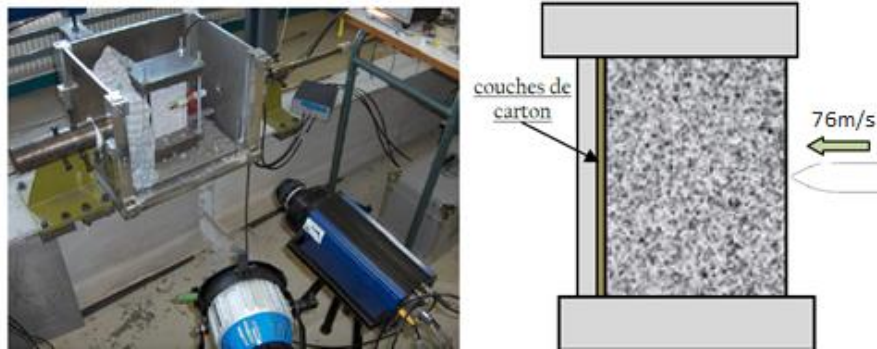


Figure 4.25: Edge-on impact setup

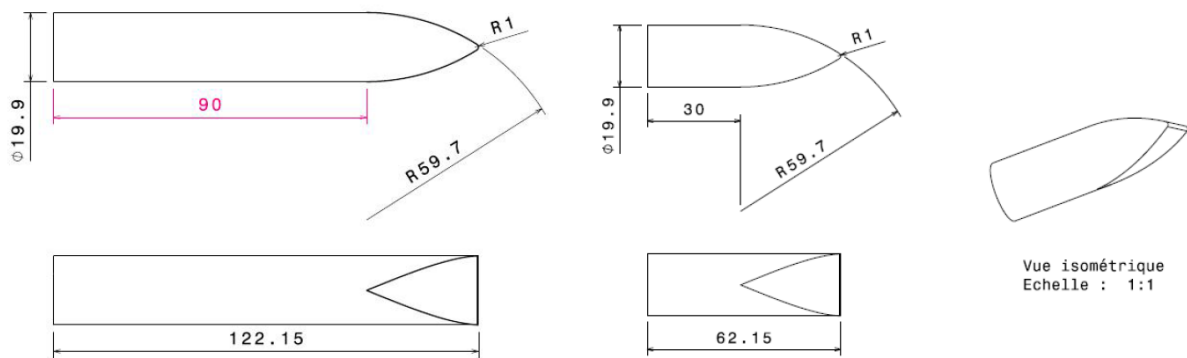


Figure 4.26: Ogive-nosed with homothetic geometry projectiles

4.2.1 Edge-on-impact modelling

The concrete tile model is with discrete elements and for the projectiles are used tetrahedral finite elements while the three rigid plates are made with hexahedral finite elements. The discretisation of the projectiles cannot be bigger than 0.39 cm, in order to describe their shapes correctly. Figure 4.27 shows the two sides of the finite element model for the small projectile and similarly Figure 4.29 for the big projectile. The aluminium projectiles are modelled with a linear elastic behaviour of $E = 70 \text{ GPa}$ and $\nu = 0.3$.

The creation of the discrete element mesh for the concrete specimen follows the same steps as for the previous mesh (quasi-static mesh, high-confinement mesh etc.). Table 4.5 provides the DE characteristics of the edge-on impact concrete specimen, which respect the condition for correct contact between FE and DE, and Figure 4.31 shows the histogram distribution Figure 4.31.

Figure 4.28 and Figure 4.30 present the edge-on impacts test models for small and big projectiles with FE, with a DE mesh for the concrete specimen surrounded by three FE rigid plates.

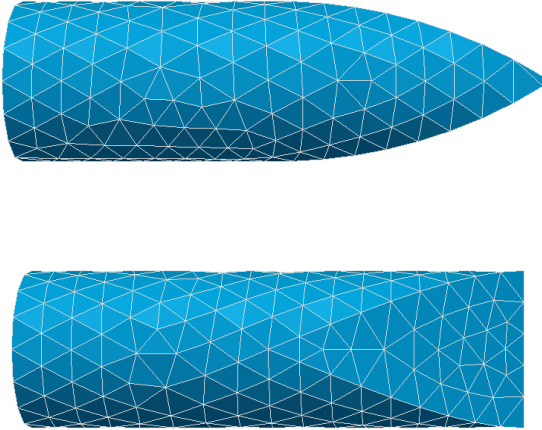


Figure 4.27: Finite element model of small projectile

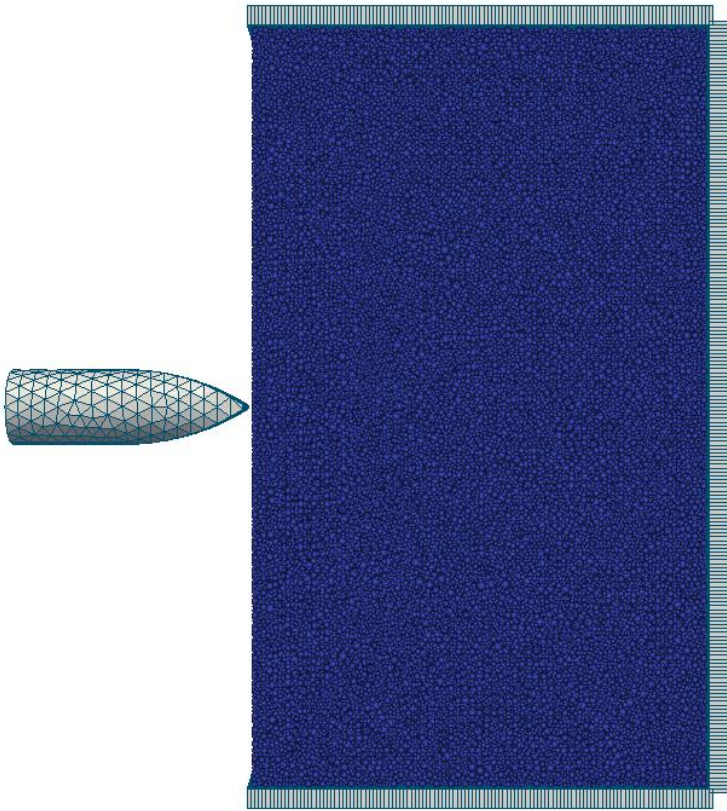


Figure 4.28: Edge-on impact test small projectile DEM/FEM model

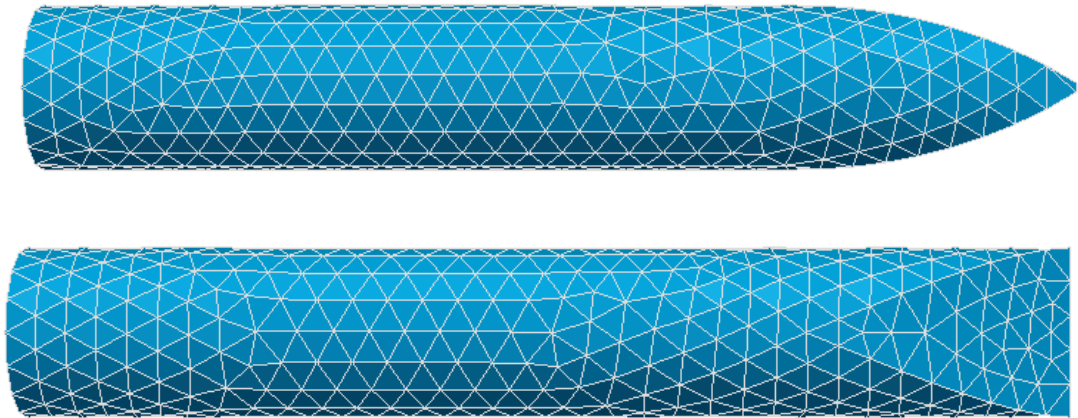


Figure 4.29: Finite element model of big projectile

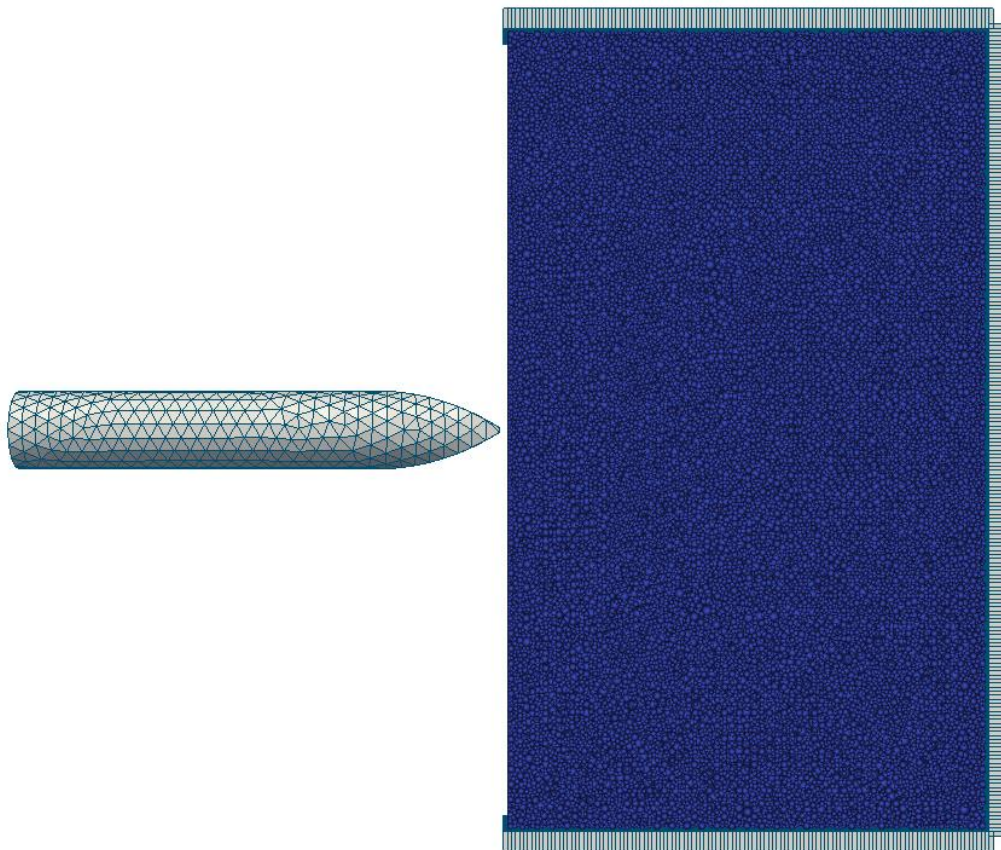


Figure 4.30: Edge-on impact test big projectile DEM/FEM model

DE Total number	D_{max} (cm)	D_{min} (cm)	D_{mean} (cm)	Compactness	λ
118209	0.28	0.933	0.136	0.6098	1.37

Table 4.5: Edge-on impact assembly characteristics

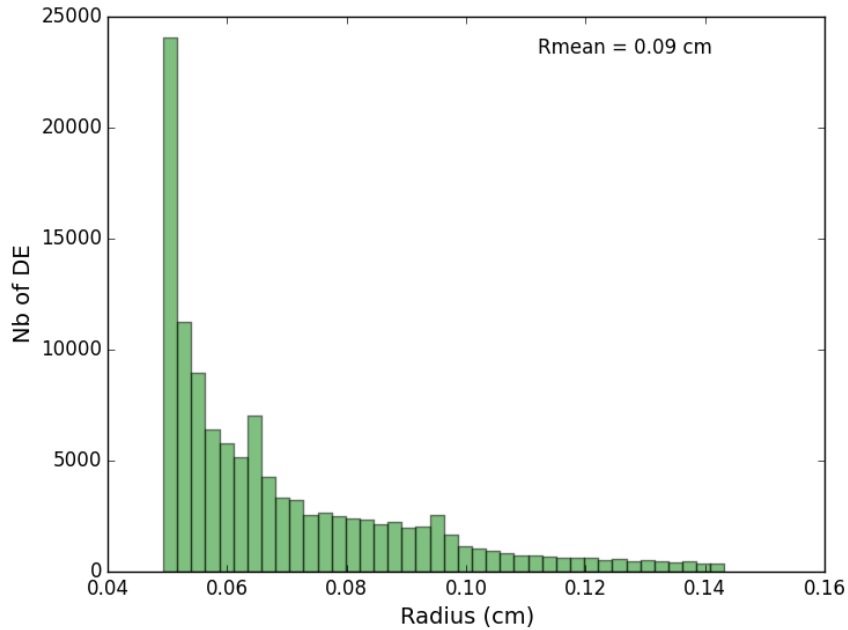


Figure 4.31: Edge-on impact mesh histogram of radius distribution

4.2.2 Numerical results

Figure 4.32 shows the final damage stage of the edge-on-impact experiment with the small projectile. Figure 4.33 presents the results from the numerical simulation which is in good agreement with the experiment, especially for the cratering damage mode. The calculated penetration depth of the projectile corresponds to the experimental one as can be seen in Figure 4.34.

Figure 4.35 presents the final cracks of the edge-on-impact test with the big projectile. Figure 4.36 corresponds to the numerical simulation which matches with the experimental damage mode. On Figure 4.37 can be seen that the penetration depth of the projectile from the simulation is in good agreement with the experimental measure.



Figure 4.32: EOI-Small final damage state (experiment)

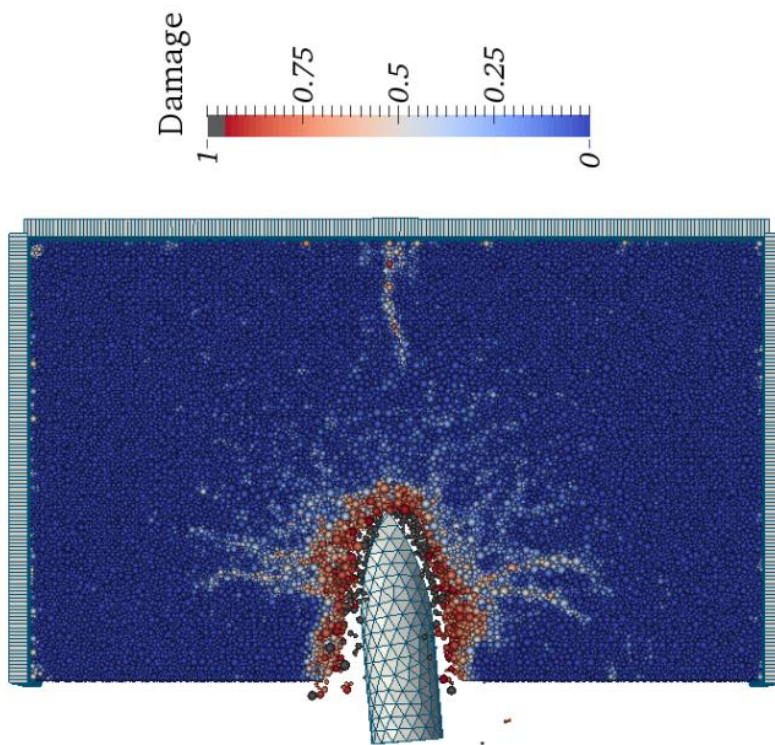


Figure 4.33: EOI-Small final damage state (simulation)

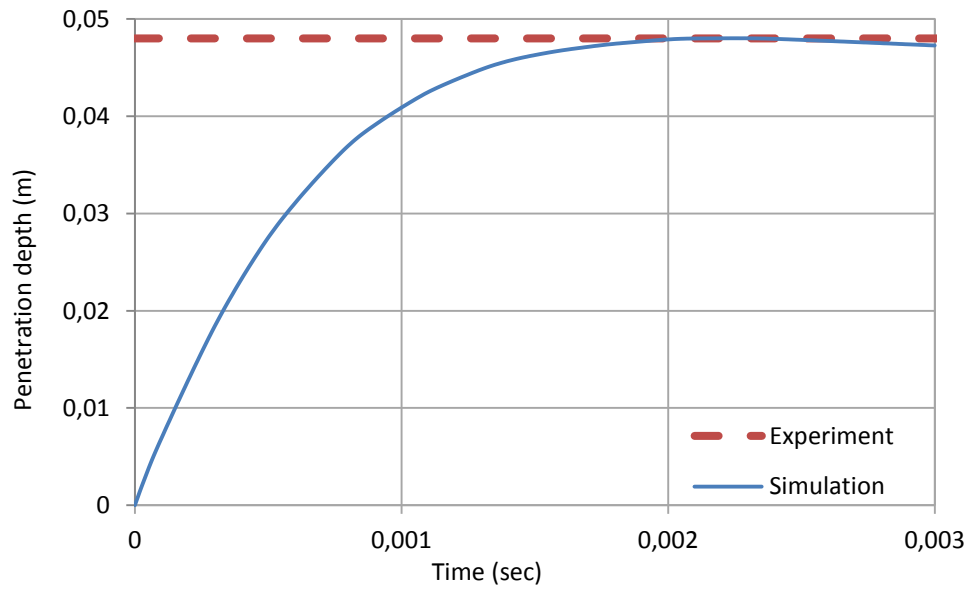


Figure 4.34: EOI-Small projectile's penetration depth



Figure 4.35: EOI-Big final damage state (experiment)

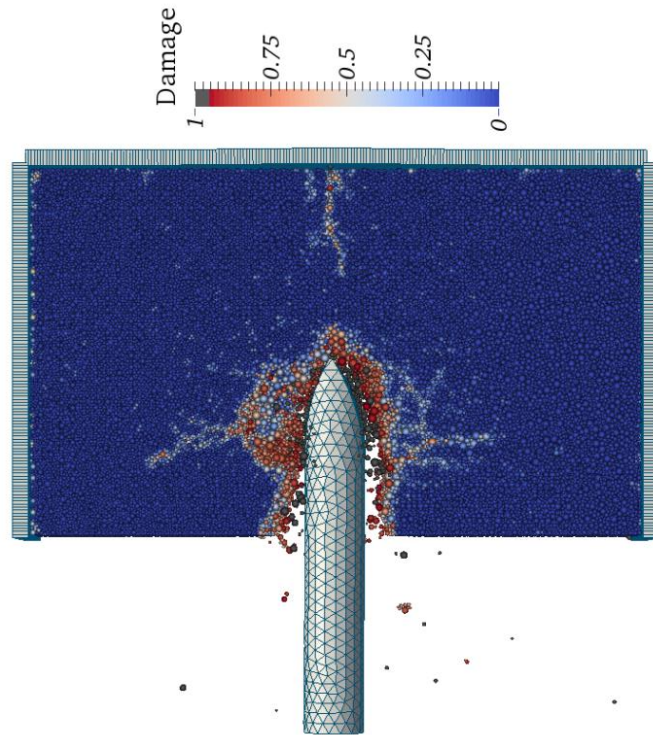


Figure 4.36: EOI-Big final damage state (simulation)

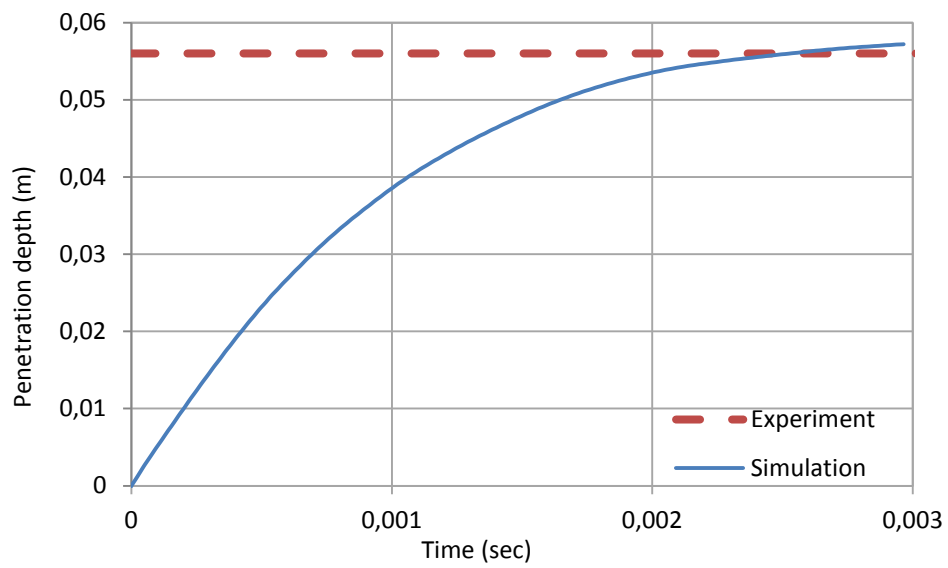


Figure 4.37: EOI-Big projectile's penetration depth

4.3 Drop-weight impact on a reinforced concrete beam

The SS0b test from an experimental program conducted in 2007 by the University of Toronto [114] is simulated to verify the capability of the new approach proposed by Masurel [91] to model reinforced concrete. These experiments aimed to produce experimental data for hard impacts by testing large reinforced beam specimens under free falling drop-weights Figure 4.38.



Figure 4.38: Specimen dimensions

The SS0b beam was doubly-reinforced with four longitudinal bars No. 30 having 30 mm diameter and 700 mm^2 cross section. The bars were placed symmetrically along the height in order to have the same resistance properties of the beam in positive and negative bending and they spanned the entire length of the beam. In the considered SS0b test no transverse reinforcement was used that maximised damage. The beam was simply supported as shown in Figure 4.38. However, to prevent uplift of the beam from the supports during the impact an arrangement with four No. 30 support bars was used holding the beam down. At the bottom end, these vertical bars were fitted to spherical bearings to enable free rotation, whereas at the top they were fixed to a structural steel section with a hinge allowing the beam to rotate freely at the supports.

The concrete used for the beam was an ordinary concrete with 10 mm aggregate size. During the casting of the beams several standard cylinder samples (150 mm in diameter and 300 mm in height) were created to determine the compressive strength of the concrete. The age of the beam specimens and the cylinders samples was more than one year at the time of impact testing. The compressive peak stress measured on the cylinders was 50.1 MPa and the strain at peak stress was 0.0023. The standard prisms (152 x 153 x 508 mm) were tested to determine the tensile coupon strength of the concrete. The direct tensile strength for 1 year dried specimen was estimated at 3.2 MPa (Table 4.6). Standard tensile tests were carried out to determine the properties of the steel reinforcement (Table 4.7).

Concrete mix proportions	
Characteristics	
Maximum size aggregate	10 mm
Density	2437 kg/m ³
Mechanical properties	
Young's Modulus E	35 GPa
Poisson's ratio ν	0.2
Compressive strength σ_c	50.1 MPa
Tensile strength σ_T	3.2 MPa

Table 4.6: Composition and mechanical properties ordinary concrete for drop-weight test

Density	Yield strain ($\times 10^{-3}$)	Yield stress	Ultimate strength	Modulus of elasticity
5.3 kg/m	2.38	464 MPa	630 MPa	195 GPa

Table 4.7: Steel mechanical properties

A heavy drop-weight of 600 kg was used for the testing. It was manufactured by filling a 300 mm square HSS (hollow structural steel) section with concrete and adding thick steel plates welded to the HSS section. The weight was hung on the crane by a nylon rope that was cut resulting in the fall of the weight on the specimen. Two I-shaped steel columns were used to guide the weight and ensure hitting the right point on the beam. A 30 mm clearance between the weight and the flanges of the columns excluded any friction during the fall. A 300 mm² steel plate of 50 mm thickness was placed on the beam at the impact point, to obtain a well-distributed impact force. The weight was dropped from a clear height of 3.26 m above the specimen resulting in an impact velocity of 8 m/s.

The drop-weight punched through and caused massive concrete spalling both at the top and the bottom of the beam (Figure 4.39).

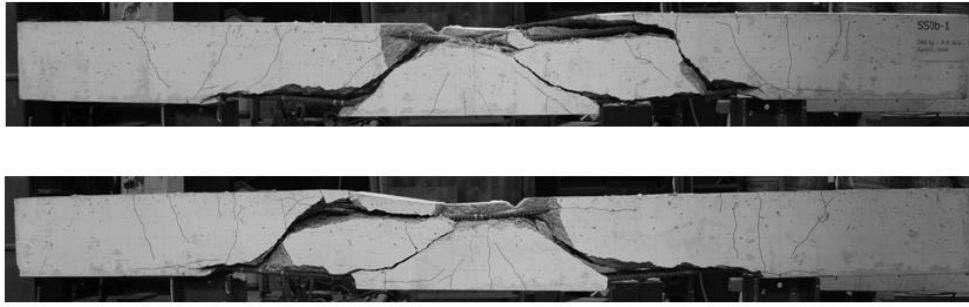


Figure 4.39: Final damage state of the front and back faces for SS0b test

The longitudinal reinforcing bars were exposed and severely bent. There were also signs of bond failure of the reinforcement bars at the supports. One notable result was the formation of a shear plug with major diagonal cracks starting at the top from the impact point and propagating downwards with an angle of approximately 45-degrees. Because SS0b test had no stirrups, the middle segment punched through with almost no visible bending deformations. In addition, several diagonal cracks parallel to the major shear-plug cracks also developed as well as some bending cracks at the mid-span and at the supports. Another diagonal crack developed alongside the shear plug starting from the supports and becoming horizontal close to the top before reaching the impact zone. As indicated in the test report, the flexural behaviour of the beam was minimal.

4.3.1 Modelling

A detailed numerical model is built to model the experimental setup (Figure 4.40). Standard FEM is used to model the longitudinal steel reinforcement, the upper and lower support plates, the anti-uplift bars, the impactor and a square steel plate inserted under the drop weight. The discrete element modelling is used for concrete Table 4.8. Unilateral contact conditions are prescribed everywhere between the discrete and finite elements of the model. Steel-concrete bond laws described by Masurel [91] are applied to describe the interaction between the concrete and the steel reinforcement. Gravity is taken into account for the whole discrete/finite element model.

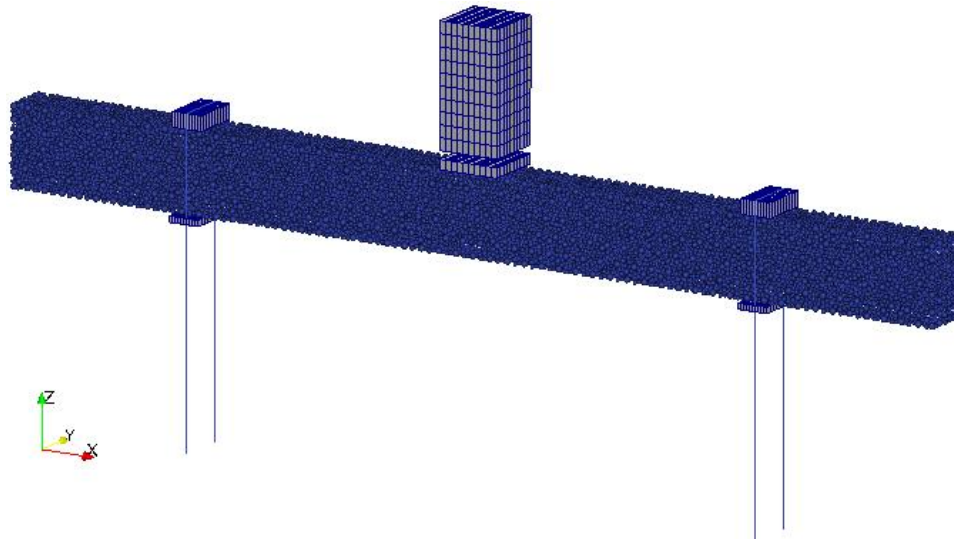


Figure 4.40: View of the DE/FE model

DE Total number	D_{max} (cm)	D_{min} (cm)	D_{mean} (cm)	Compactness	λ
0.0	2.82	0.94	1.357	0.6024	1.3969

Table 4.8: Drop-weigh assembly characteristics

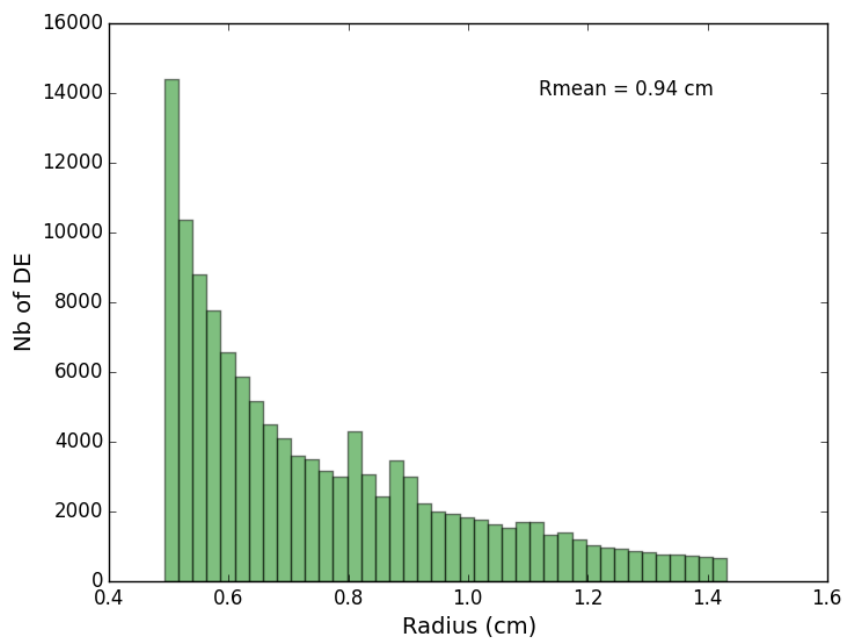


Figure 4.41: Drop-weigh mesh histogram of radius distribution

4.3.2 Calibration of parameters

Since the concrete for this experiment was different, we started from the calibration of the constitutive parameters, with a series of EUROPLEXUS calculations by changing the local parameters. Calibration in tension and compression is made on prism-type discrete element specimens.

Before simulating the SS0b test, we apply the set of parameters obtained by calibration to simulate the standard compression test on a cylinder and compare the numerical results with the measures realised in [114] on concrete cylinders. In this test, the cylinder is compressed very slowly by two rigid steel plates until its full ruin. We simulate this test by modelling frictional contact between the steel plates and the discrete element model of the cylinder. Figure 4.42 shows the damage state of the cylinder for different strain levels. As can be seen the concrete near the cylinder ends is not damaged because of friction constraint. A cone damage mode of the discrete element model is conforming to experimental observation.

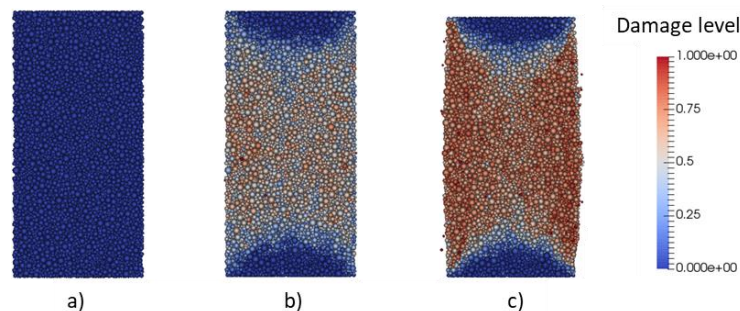


Figure 4.42: Damage state of the cylinder: a) initial state, b) for $\varepsilon=0.2\%$, c) for $\varepsilon=0.6\%$

Figure 4.43 shows the stress-strain curve obtained in this simulationFigure 4.43. Both the trend of the curve and the peak value are correctly reproduced.

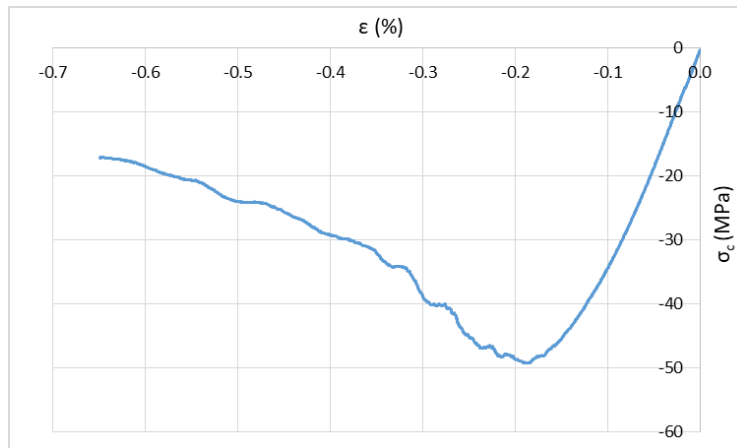
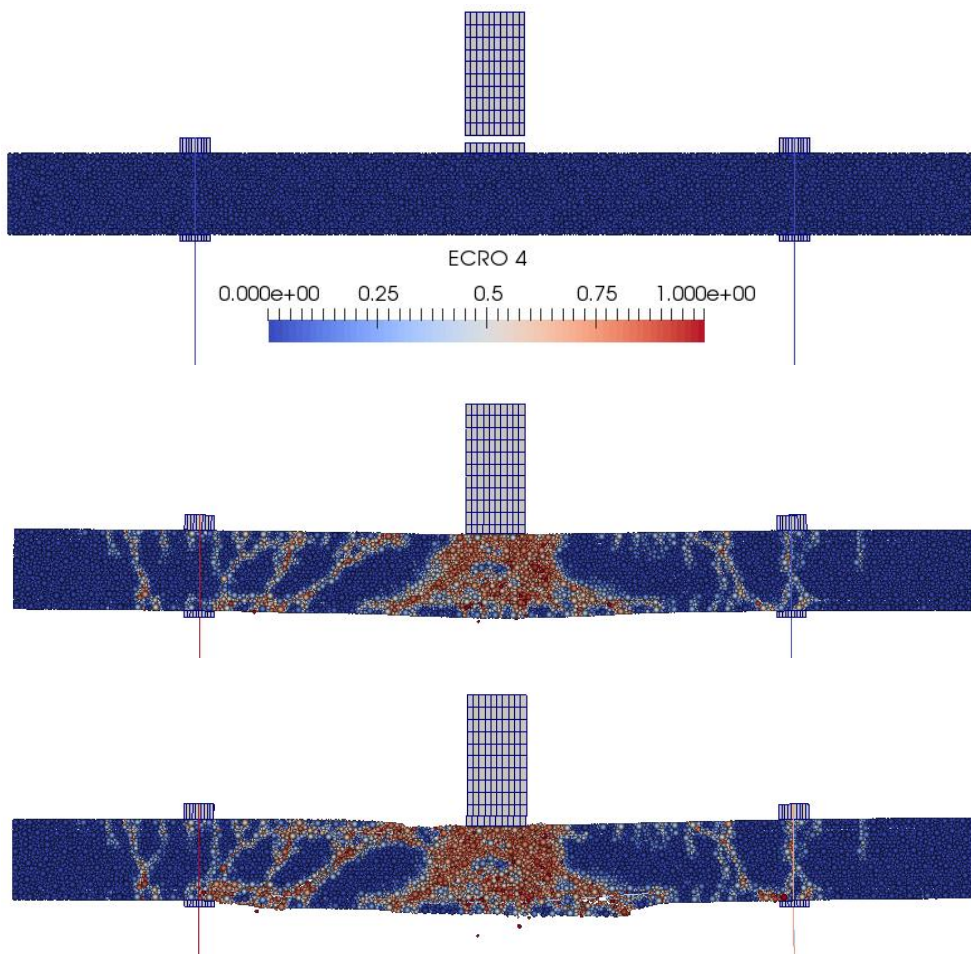


Figure 4.43: Stress-strain curve in the cylinder compression test simulation

4.3.3 Numerical results for SS0b test

Then, the drop-weight test was simulated and Figure 4.44 shows the evolution of damage of the RC beam for five consecutive time stations.



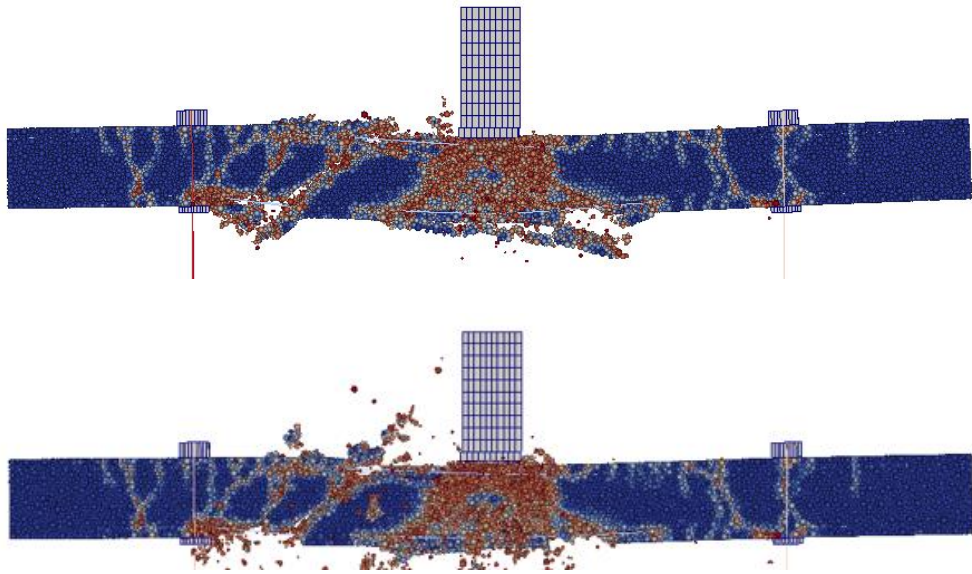


Figure 4.44: Damage state of concrete at $t = 0, 10 \text{ ms}, 20 \text{ ms}, 50 \text{ ms},$ and 200 ms (from top to bottom)

For the considered case the real material discontinuities can be seen when plotting the vertical displacement field (Figure 4.45). The basic colour changes reveal the presence of at least three oblique macro-cracks delimiting different material fragments. These are in good agreement with the macro-cracks observed in the experiment (Figure 4.39).

It is difficult to produce a fully static solution corresponding to the final state of the experiment, because this analysis used the explicit-type time integration algorithm. As can be seen in Figure 4.46, the beam has resisted to the first impact and not completely failed, but several oscillation periods are needed to completely dissipate the impact energy and obtain the final crack opening due to the drop-weight gravity action.

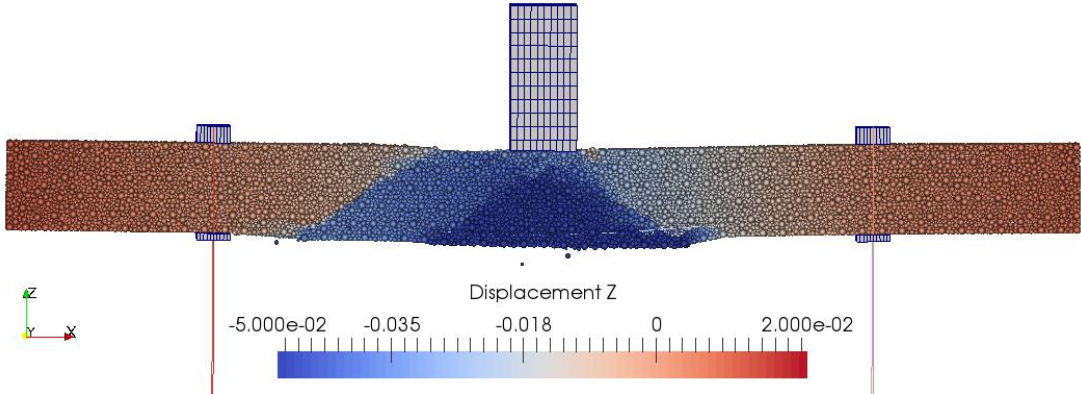


Figure 4.45: Vertical displacement U_z at 17 ms

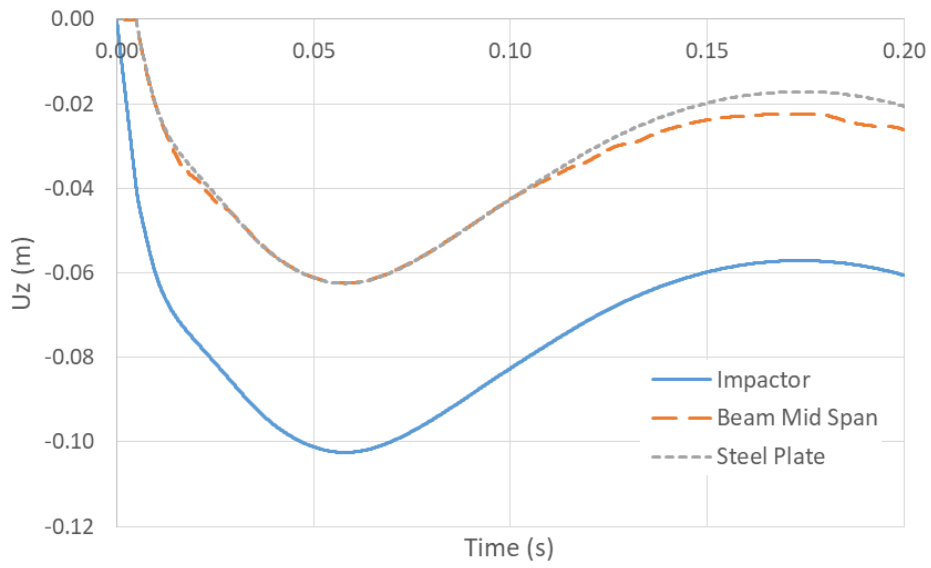


Figure 4.46: Vertical displacements versus time in the simulation

Analysis of the results obtained in the simulation of SS0b impact test shows that the main physical phenomena observed in the experiment are represented correctly by the mixed discrete/finite element model.

Conclusions and perspectives

Conclusions

This project is a collaboration between the laboratory 3S-R (University of Grenoble Alpes) and the research centre of EDF R&D (Paris-Saclay). It is following a series of previous studies on the discrete element methods, which were initialised in 2003 with the developments of Hentz in SDEC software. He extended the original discrete element method of Cundall and Strack by introducing the concept of cohesive interactions allowing to model cohesive materials such as concrete. Later, Frangin in 2006 developed FE/DE coupling for 3D elements. After, in 2009 Rousseau established in EUROPLEXUS the framework of a coupling FE/DE method with shell FE able to model the macro-cracking of a reinforced concrete structure under impacts. Masurel in 2015 developed a new finite element model for the reinforcement coupled with discrete elements. At the same time, in 2015 Omar improved the constitutive model for concrete to better control the brittle behaviour with the Moment Transfer Law and to treat the strain rate effects under dynamic loading.

The present study is aiming at the development of an original engineering tool, for the design of infrastructures protection systems under impacts. The purpose is to assimilate the previous developments and further implementation in EUROPLEXUS, for a reliable prediction of damage on reinforced concrete structures, subjected to severe loadings due to natural or manmade hazards such as an aircraft or missile impacts. Furthermore, the aim of our study is the implementation of constitutive compaction law, to properly account for the behaviour of concrete under high confining pressures. Thereby, we study the influence of both mesh creation and constitutive law parameters, in order to verify the proper modelling of concrete.

Firstly, a sensitivity study of the parameters for the mesh generation algorithm was employed, in order to investigate their influence on the macroscopic behaviour of concrete. We observed that it is not necessary to use more than two or three iterations for the densification phase of the mesh creation since the mesh properties do not vary a lot for a bigger number of iterations. The compactness of the mesh affects its ductility in traction. Less than 0.5 compact meshes are not acceptable because they result in ductile behaviour under tension. Loose meshes contain very few particles with bigger distances between them; thus the radius of interaction needs to be increased quite a lot. For this reason, this adjustment offers more ductility to the model since the constitutive law is not local anymore.

Secondly, we noticed that the model for the quasi-static mesh used in the previous studies was not reliable. They used a configuration by applying the loading directly to the discrete elements by blocking two layers of discrete elements laterally on the front and rear face of the specimen. This model leads in miscalculation of the local parameters since the roughness between the discrete elements of the specimen and discrete elements of loading zones induces additional friction in the system. Furthermore, the damage mode was not correct with the specimen deforming into a barrel shape due to Poisson's effect. Therefore, we model the loading zones with rigid elements to eliminate the undesired friction between loading zones and specimen. The new model of the quasi-static mesh has the ability to well represent the cone failure mode of the quasi-static compression test.

In EUROPLEXUS the shapes of rigid elements are limited to the basic (parallelepiped, cone, and cylinder). In this project, we simulated impact with complex geometry (ogive-nosed) projectiles; thus the impactors are modelled with finite elements. One of the most important parameters is the ratio between finite element sizes and discrete element sizes, that are in contact to ensure correct force transmission from one to the other. We study the influence of discretisation with the help of quasi-static simulation in compression by replacing the rigid elements loading zones with finite element plates. We concluded that the condition for proper contact between discrete-finite elements demands bigger finite element size than the mean discrete element diameter.

Afterwards, the local parameters of the constitutive model were calibrated by simulating the macroscopic behaviour of concrete on laboratory tests. It is important to note that the microscopic local parameters are mesh independent only if the mesh generation parameters are kept constant. The parameters are identified on fully saturated ordinary concrete. For the quasi-static behaviour the compressive test performed by Vu was used. In addition, for the high confined triaxial the on oedometric and the hydrostatic tests conducted by Gabet were simulated. The parameters of moment transfer law (MTL) are the second choice that should be made at the beginning for a certain type of concrete because it affects the overall macroscopic behaviour of concrete. All the experiments were performed in the laboratory 3S-R. The Moment Transfer Law parameters were defended on the quasi-static compressive simulation. We detected that the MTL parameters affect the smoothness of the peak stress and the ductility of the post-peak curve.

Moreover, this study proposed a modification of the initial dynamic increase factor constitutive law implemented in EUROPLEXUS initially by Omar. The modification gives a more realistic modelling of the fracture energy under dynamic loading by controlling the increase of the maximum distance limit

of the local interaction. The dynamic behaviour of concrete is calibrated on the spalling test launched during my master thesis in the laboratory 3S-R by the supervision of professor Pascal Forquin.

After calibrating the set of parameters for the constitutive model concrete hard impacts were simulated to validate the reliability of the proposed discrete element approach. Three different experimental campaigns were used. First a series of impact tests performed by CEA-Gramat, with confined cylindrical concrete specimens impacted by rigid ogive-nosed projectiles. We simulated one perforation test and two penetration test with three different impact velocities. Then, two edge-on impact test conducted by Erzar at the University of Metz with different projectile size and impact velocities were used to verify the ability of the model to represent the damage modes. Finally, the simulation of the drop-weight impact on a reinforced concrete beam test from the University of Toronto was simulated to study the capability of the new model of Masurel with finite elements for the reinforcement coupled with discrete elements for the concrete.

The numerical results are in good accordance with the experimental ones. For the perforation test results thoroughly match with the simulation. However, a slight difference is observed on the curves of the penetration tests. The damage for all experiments seems to be quite similarly produced by the discrete element model. The phenomenon observed experimentally, such as spalling on the front with an injection of fragment and tunnelling were generated successfully through all the simulations. In addition, scabbing with diagonal cracking is presented on the rear face of the perforation specimen. A cratering damage mode produced at the penetration simulations, with bigger penetration depth for the high-velocity impact than the low-velocity impact. The cratering failure mode was also successfully produced for the edge-on impact simulations. Furthermore, the drop-weight simulation was able to generate the oblique macro-cracks in good agreement with the experiment.

Perspectives

The current discrete element approach installed in EUROPLEXUS is already a powerful computational tool. It is capable of realising realistic simulation on reinforced concrete specimens under hard impacts. However, this method has the potential to extend into a fully operational tool, able to predict damages on reinforced concrete structures in a wide range of impacts. We can also indicate several tracks for future research.

Our model is now a complete and reliable numerical tool, capable of simulating impacts on concrete structures of good accordance with the multi-cracking observed experimentally. It is essential to

validate the new steel-concrete bond model on fragmentation tests with fracture of transverse and longitudinal steel, to develop an accomplished engineering tool. The adhesion laws of the steel-concrete tangential interaction need to be adjusted for different diameters of reinforcement and calibrated on pull-out tests.

Nevertheless, it will be fascinating to launch a simulation to study the response of an industrial-size concrete structure subjected to an aircraft or missile impact. The use of the FE/DE coupling approach developed by Rousseau is required for the simulation of a real-scale structure, in order to keep the computational cost reasonable. Frangin and Rousseau identified the coupling method only accounting for the elastic behaviour of DE and FE. For this reason, the FE/DE coupling model should be thoroughly studied and identified not only with the elastic behaviour; thus the size of the DE area can be reduced.

Bibliography

- [1] ACE. Fundamentals of protective structures. Report AT120 AT1207821, Army Corps of Engineers, Office of the Chief of Engineers, 1946.
- [2] Amirikian, A. (1950). Design of protective structures (A new concept of structural behavior) (No. NP-3726; NavDocks P-51). Bureau of Yards and Docks.
- [3] Antoniou, A. (2014). Contribution to the experimental analysis and numerical modelling of spalling technique into concrete specimens under dynamic tension. Master thesis, Université Joseph Fourier.
- [4] Arros, J., & Doumbalski, N. (2007). Analysis of aircraft impact to concrete structures. Nuclear engineering and design, 237(12-13), 1241-1249.
- [5] Belheine, N., Plassiard, J. P., Donzé, F. V., Darve, F., & Seridi, A. (2009). Numerical simulation of drained triaxial test using 3D discrete element modeling. Computers and Geotechnics, 36(1-2), 320-331.
- [6] Berriaud C., Dulac J., Sokolovsky A., Labrot R., Gueraud R., Avet-Flancard R., « Local behaviour of reinforced concrete walls under missile impact », Nuclear Engineering and Design, vol. 45, n°2, 1978, p. 457-469.
- [7] Berriaud, C. (1993). Perforation des enceintes en béton par un projectile dur – Rapport de synthèse. Rapport CEA/DMT/93-299.
- [8] Bian, H., Jia, Y., Shao, J., & Pontiroli, C. (2016). Numerical study of a concrete target under the penetration of rigid projectile using an elastoplastic damage model. Engineering Structures, 111, 525-537.
- [9] Bischoff, P. H., & Perry, S. H. (1991). Compressive behaviour of concrete at high strain rates. Materials and structures, 24(6), 425-450.
- [10] Beth RA. Penetration of projectiles in concrete. PPAB Interim Report No. 3, November 1941.
- [11] Borkovec, M., De Paris, W., & Peikert, R. (1994). The fractal dimension of the Apollonian sphere packing. Fractals, 2(04), 521-526.
- [12] Brace, W. F., & Jones, A. H. (1971). Comparison of uniaxial deformation in shock and static loading of three rocks. Journal of Geophysical Research, 76(20), 4913-4921.
- [13] Brara, A., & Klepaczko, J. R. (2006). Experimental characterization of concrete in dynamic tension. Mechanics of materials, 38(3), 253-267.

-
- [14] Bresler, B. (1975). Influence of high strain rate and cyclic loading of unconfined and confined concrete in compression. In Proc. of 2nd Canadian Conference on Earthquake Engineering, Hamilton, Ontario (pp. 1-13).
- [15] Burak, E., & Tuncan, A. Determination of frictional behavior between concrete and steel tube interaction. In Proceedings of the 7th European Conference on Steel and Composite Structures Eurosteel (pp. 521-522).
- [16] Buzaud, E., Cazaubon, C., & Chauvel, D. (2007). Assessment of empirical formulae for local response of concrete structures to hard projectile impact. In Concrete under severe conditions. Environment and loading.
- [17] Camborde, F. (1999). Modélisation du comportement dynamique du béton. Application aux problèmes d'impacts et d'explosions. THESE DE DOCTORAT PRESENTÉE A L'INSTITUT NATIONAL SUPERIEUR DES TECHNIQUES NUCLEAIRES (CEA)-DISCIPLINE: SCIENCE POUR L'INGENIEUR, SPECIALITE: GENIE MECANIQUE.
- [18] Chelapati, C. V., Kennedy, R. P., & Wall, I. B. (1972). Probabilistic assessment of aircraft hazard for nuclear power plants. Nuclear Engineering and Design, 19(2), 333-364.
- [19] Comité euro-international du béton. Plenary Session. (1988). Concrete structures under impact and impulsive loading: synthesis report. Comité euro-international du béton.
- [20] CEB-FIP model code 1990. Comité Euro-international du Béton. Ed. Thomas Telford (1993)
- [21] Chareyre, B. (2003). Modélisation du comportement d'ouvrages composites sol-géosynthétique par éléments discrets-application aux tranchées d'ancrage en tête de talus (Doctoral dissertation, PhD thesis at Grenoble University).
- [22] Chelapati, C. V., Kennedy, R. P., & Wall, I. B. (1972). Probabilistic assessment of aircraft hazard for nuclear power plants. Nuclear Engineering and Design, 19(2), 333-364.
- [23] Chen, X. W., & Li, Q. M. (2002). Deep penetration of a non-deformable projectile with different geometrical characteristics. International Journal of Impact Engineering, 27(6), 619-637.
- [24] Courant, R. (1994). Variational methods for the solution of problems of equilibrium and vibrations. Lecture Notes in Pure and Applied Mathematics, 1-1.
- [25] Cui, L., & O'Sullivan, C. (2003). Analysis of a triangulation based approach for specimen generation for discrete element simulations. Granular Matter, 5(3), 135-145.
- [26] Cundall, P. A. (1971). A computer model for simulating progressive, large-scale movement in blocky rock system. In Proceedings of the International Symposium on Rock Mechanics, 1971.
- [27] Cundall, P. A. (1988, June). Formulation of a three-dimensional distinct element model—Part I. A scheme to detect and represent contacts in a system composed of many polyhedral

-
- blocks. In *International Journal of Rock Mechanics and Mining Sciences & Geomechanics Abstracts* (Vol. 25, No. 3, pp. 107-116). Pergamon
- [28] Cundall, P. A. (1974). Rational Design of Tunnel Supports: A Computer Model for Rock Mass Behavior Using Interactive Graphics for the Input and Output of Geometrical Data. MINNESOTA UNIV MINNEAPOLIS DEPT OF CIVIL AND MINING ENGINEERING.
- [29] Cundall, P. A., & Strack, O. D. (1979). A discrete numerical model for granular assemblies. *geotechnique*, 29(1), 47-65.
- [30] Cundall, P. A., & Strack, O. D. L. (1978). BALL-A program to model granular media using the distinct element method. Technical note. Advanced Technology Group, Dames & Moore, London.
- [31] Cusatis, G., Pelessone, D., Mencarelli, A., & Baylot, J. T. (2007, January). Simulation of reinforced concrete structures under blast and penetration through lattice discrete particle modeling. In *ASME 2007 International Mechanical Engineering Congress and Exposition* (pp. 581-584). American Society of Mechanical Engineers.
- [32] Cusatis, G., Pelessone, D., & Mencarelli, A. (2011). Lattice discrete particle model (LDPM) for failure behavior of concrete. I: Theory. *Cement and Concrete Composites*, 33(9), 881-890.
- [33] Daudeville, L., & Malécot, Y. (2011). Concrete structures under impact. *European Journal of Environmental and Civil Engineering*, 15(sup1), 101-140.
- [34] Delaunay, B. (1934). Sur la sphere vide. *Izv. Akad. Nauk SSSR, Otdelenie Matematicheskii i Estestvennyka Nauk*, 7(793-800), 1-2.
- [35] Donzé, F. V., Richefeu, V., & Magnier, S. A. (2009). Advances in discrete element method applied to soil, rock and concrete mechanics. *Electronic Journal of Geotechnical Engineering*, 8(1), 44.
- [36] Donzé, F. V., Magnier, S. A., Daudeville, L., Mariotti, C., & Davenne, L. (1999). Study of the behavior of concrete at high strain rate compressions by a discrete element method. *ASCE J. of Eng. Mech*, 125(10), 1154-1163.
- [37] Dulac, J., & Giraud, J. P. (1981). Impact testing of reinforced concrete slabs. In *Structural mechanics in reactor technology*. Vol. J (b).
- [38] Eibl, J. (1987, September). Soft and hard impact. In *Proceedings of the First International Conference on Concrete for Hazard Protection*, Edinburgh.
- [39] Emeriault, F., Cambou, B., & Mahboubi, A. (1996). Homogenization for granular materials: non reversible behaviour. *Mechanics of Cohesive-frictional Materials: An International Journal on Experiments, Modelling and Computation of Materials and Structures*, 1(2), 199-218.

-
- [40] Erzar, B. (2010). Ecaillage, craterisation et comportement en traction dynamique de betons sous impact: approches experimentales et modelisation (Doctoral dissertation, Université de Metz).
- [41] Erzar, B., & Forquin, P. (2011). Experiments and mesoscopic modelling of dynamic testing of concrete. *Mechanics of Materials*, 43(9), 505-527.
- [42] Erzar, B., & Forquin, P. (2014). Analysis and modelling of the cohesion strength of concrete at high strain-rates. *International Journal of Solids and Structures*, 51(14), 2559-2574.
- [43] EUROPLEXUS User's manual - A computer program for the finite element simulation of fluid-structure systems under transient dynamic loading. <http://europlexus.jrc.ec.europa.eu>. Accessed: 2017-09-18.
- [44] Fang, Q., & Wu, H. (2017). Concrete structures under projectile impact. In *Concrete Structures Under Projectile Impact* (pp. 497-558). Springer, Singapore.
- [45] Fiquet, G., & Dacquet, S. (1977). Study of the perforation of reinforced concrete slabs by rigid missiles—experimental study, part II. *Nuclear Engineering and Design*, 41(1), 103-120.
- [46] Forquin, P. (2003). Endommagement et fissuration de matériaux fragiles sous impact balistique: rôle de la microstructure. (Doctoral dissertation, Ecole Normale Supérieure de Cachan, France).
- [47] Forquin, P., Arias, A., & Zaera, R. (2007). An experimental method of measuring the confined compression strength of geomaterials. *International Journal of Solids and Structures*, 44(13), 4291-4317.
- [48] Forrestal, M. J., Altman, B. S., Cargile, J. D., & Hanchak, S. J. (1994). An empirical equation for penetration depth of ogive-nose projectiles into concrete targets. *International Journal of Impact Engineering*, 15(4), 395-405.
- [49] Frangin, E., Marin, P., & Daudeville, L. (2006, March). Coupled finite/discrete element method to analyze localized impact on reinforced concrete structure. In *Computational Modelling of Concrete Structures, EURO-C*.
- [50] Fullard, K., Baum, M. R., & Barr, P. (1991). The assessment of impact on nuclear power plant structures in the United Kingdom. *Nuclear engineering and Design*, 130(2), 113-120.
- [51] Gabet, T. (2006). Comportement triaxial du béton sous fortes contraintes: Influence du trajet de chargement (Doctoral dissertation, Université Joseph-Fourier-Grenoble I).
- [52] Gabet, T., Malécot, Y., & Daudeville, L. (2008). Triaxial behaviour of concrete under high stresses: Influence of the loading path on compaction and limit states. *Cement and Concrete Research*, 38(3), 403-412.

-
- [53] Gabet, T., Vu, X. H., Malecot, Y., & Daudeville, L. (2006, August). A new experimental technique for the analysis of concrete under high triaxial loading. In *Journal de Physique IV (Proceedings)* (Vol. 134, pp. 635-640). EDP sciences.
- [54] Gingold, R. A., & Monaghan, J. J. (1977). Smoothed particle hydrodynamics: theory and application to non-spherical stars. *Monthly notices of the royal astronomical society*, 181(3), 375-389.
- [55] Gopalaratnam, V. S., & Shah, S. P. (1984). INSTRUMENTED IMPACT TESTING OF BRITTLE MATERIALS. In *Unknown Host Publication Title*. ASCE.
- [56] Gueraud, R., & Sokolovsky, A. (1977). Study of the perforation of reinforced concrete slabs by rigid missiles. *Nuclear Engineering and Design*, 41(1), 91-102.
- [57] Guirgis, S., & Guirguis, E. (2009). An energy approach study of the penetration of concrete by rigid missiles. *Nuclear Engineering and Design*, 239(4), 819-829.
- [58] Hamilton, S. W. R. (1834). *On a general method in dynamics* (p. 247). Richard Taylor.
- [59] Hamouine, A., & Lorrain, M. (1995). Etude de la résistance à l'arrachement de barres enrobées dans du béton de hautes performances. *Materials and Structures*, 28(10), 569-574.
- [60] Haldar, A., & Hamieh, H. A. (1984). Local effect of solid missiles on concrete structures. *Journal of Structural Engineering*, 110(5), 948-960.
- [61] Hart, R., Cundall, P. A., & Lemos, J. (1988, June). Formulation of a three-dimensional distinct element model—Part II. Mechanical calculations for motion and interaction of a system composed of many polyhedral blocks. In *International Journal of Rock Mechanics and Mining Sciences & Geomechanics Abstracts* (Vol. 25, No. 3, pp. 117-125). Pergamon.
- [62] Hentz, S., Donzé, F. V., & Daudeville, L. (2004). Discrete element modelling of concrete submitted to dynamic loading at high strain rates. *Computers & structures*, 82(29-30), 2509-2524.
- [63] Hentz, S., Daudeville, L., & Donzé, F. V. (2004). Identification and validation of a discrete element model for concrete. *Journal of engineering mechanics*, 130(6), 709-719.
- [64] Hentz, S. (2003). *Modélisation d'une structure en béton armé soumise à un choc par la méthode des éléments discrets sphériques*. (Doctoral dissertation, Université Grenoble Alpes).
- [65] Hopkinson, B. *Collective scientific papers*. Cambridge University Press, 1921
- [66] Hornemann U. et al. (1984) Report E4, Ernst Mach Institute, Germany
- [67] Hrennikoff, A. (1941). Solution of problems of elasticity by the framework method. *J. appl. Mech.*
- [68] Huang, H. (1999). *Discrete element modeling of tool-rock interaction*. University of Minnesota.

-
- [69] Huang, X. C., Yan, Y. X., Zhong, W. Z., Chen, Y. Z., & Zhu, J. S. (2011). A Numerical Method for Penetration into Concrete Target Using SPH-Lagrange Coupling Method. In *Advanced Materials Research* (Vol. 163, pp. 1217-1221). Trans Tech Publications.
- [70] Iwashita, K., & Oda, M. (1998). Rolling resistance at contacts in simulation of shear band development by DEM. *Journal of engineering mechanics*, 124(3), 285-292.
- [71] Jerier, J. F., Imbault, D., Donze, F. V., & Doremus, P. (2009). A geometric algorithm based on tetrahedral meshes to generate a dense polydisperse sphere packing. *Granular Matter*, 11(1), 43-52.
- [72] Jonas, W., Meschkat, R., Riech, H., & Rüdiger, E. (1979). Experimental investigations to determine the kinetic ultimate bearing capacity of reinforced concrete slabs subject to deformable missiles. In *Structural mechanics in reactor technology. Transactions. Vol. J.*
- [73] Jonas, W., Rüdiger, E., Gries, M., Riech, H., & Rützel, H. (1982). Kinetische grenztragfähigkeit von stahlbetonplatten. *Rapport technique RS*, 162.
- [74] Jonas, W., Rüdiger, E., Gries, M., Riech, H., & Rützel, H. (1982). Kinetische Grenztragfähigkeit von Stahlbetonplatten, RS 165, Schlussbericht (Rapport final). IV. Technischer Bericht, Hochtief AG.
- [75] Jones, S. E., & Rule, W. K. (2000). On the optimal nose geometry for a rigid penetrator, including the effects of pressure-dependent friction. *International Journal of Impact Engineering*, 24(4), 403-415.
- [76] Kennedy, R. P. (1976). A review of procedures for the analysis and design of concrete structures to resist missile impact effects. *Nuclear Engineering and Design*, 37(2), 183-203.
- [77] Kœchlin, P. (2007). *Modèle de comportement membrane-flexion et critère de perforation pour l'analyse de structures minces en béton armé sous choc mou. These de doctorat, Ecole Polytechnique.*
- [78] Kœchlin, P., & Potapov, S. (2009). Classification of soft and hard impacts—Application to aircraft crash. *Nuclear Engineering and Design*, 239(4), 613-618.
- [79] Kojima, I. (1991). An experimental study on local behavior of reinforced concrete slabs to missile impact. *Nuclear Engineering and Design*, 130(2), 121-132.
- [80] Kolsky, H. (1949). An investigation of the mechanical properties of materials at very high rates of loading. *Proceedings of the physical society. Section B*, 62(11), 676.
- [81] Li, Q. M., Lu, Y. B., & Meng, H. (2009). Further investigation on the dynamic compressive strength enhancement of concrete-like materials based on split Hopkinson pressure bar tests. Part II: numerical simulations. *International Journal of Impact Engineering*, 36(12), 1335-1345.

-
- [82] Li, Q. M., & Meng, H. (2003). About the dynamic strength enhancement of concrete-like materials in a split Hopkinson pressure bar test. *International Journal of solids and structures*, 40(2), 343-360.
- [83] Li, Q. M., Reid, S. R., Wen, H. M., & Telford, A. R. (2005). Local impact effects of hard missiles on concrete targets. *International Journal of impact engineering*, 32(1-4), 224-284.
- [84] Liao, C. L., Chang, T. P., Young, D. H., & Chang, C. S. (1997). Stress-strain relationship for granular materials based on the hypothesis of best fit. *International Journal of Solids and Structures*, 34(31-32), 4087-4100.
- [85] Lucy, L. B. (1977). A numerical approach to the testing of the fission hypothesis. *The astronomical journal*, 82, 1013-1024.
- [86] Magnier, S. A., & Donzé, F. V. (1997). Discrete Element Project. Rapport n°2, Université du Québec.
- [87] Magnier, S. A., & Donzé, F. V. (1998). Numerical simulations of impacts using a discrete element method. *Mechanics of Cohesive-frictional Materials: An International Journal on Experiments, Modelling and Computation of Materials and Structures*, 3(3), 257-276.
- [88] Malecot, Y., Daudeville, L., Dupray, F., Poinard, C., & Buzaud, E. (2010). Strength and damage of concrete under high triaxial loading. *European Journal of Environmental and Civil Engineering*, 14(6-7), 777-803.
- [89] Malvar, L. J., & Crawford, J. E. (1998). *Dynamic increase factors for concrete*. Naval Facilities Engineering Service Center Port hueneme CA.
- [90] Mang, H. A., Lackner, R., Meschke, G., & Mosler, J. (2003). Computational modeling of concrete structures (Vol. 3, pp. 541-606).
- [91] Masurel, A. (2015). Modélisation mixte éléments discrets/éléments finis de la dégradation de structures en béton armé sous impact sévère (Doctoral dissertation, Université Grenoble Alpes).
- [92] Mazars, J. (1984). Application de la mécanique de l'endommagement au comportement non linéaire et à la rupture du béton de structure. THESE DE DOCTEUR ES SCIENCES PRESENTÉE A L'UNIVERSITÉ PIERRE ET MARIE CURIE-PARIS 6.
- [93] McVay, M. K. (1988). Spall damage of concrete structures, Technical Report SL88-22.
- [94] Minerals commodity summary – cement – 2007. US United States Geological Survey. 1 June 2007. Archived from the original on 13 December 2007. Retrieved 16 January 2008.
- [95] Moës, N., Dolbow, J., & Belytschko, T. (1999). A finite element method for crack growth without remeshing. *International journal for numerical methods in engineering*, 46(1), 131-150.

-
- [96] Munjiza, A., Owen, D. R. J., & Bicanic, N. (1995). A combined finite-discrete element method in transient dynamics of fracturing solids. *Engineering computations*, 12(2), 145-174.
- [97] Nachtsheim, W., & Stangenberg, F. (1981). Impact of deformable missiles on reinforced concrete plates-comparisational calculations of Meppen tests. In *Structural mechanics in reactor technology*. Vol. J (b).
- [98] Nachtsheim, W., & Stangenberg, F. (1983). Interpretation of results of Meppen slab tests—comparison with parametric investigations. *Nuclear engineering and design*, 75(2), 283-290.
- [99] O'Connor, R. M. (1996). A distributed discrete element modeling environment: algorithms, implementation and applications (Doctoral dissertation, Massachusetts Institute of Technology).
- [100] Oda, M., Konishi, J., & Nemat-Nasser, S. (1982). Experimental micromechanical evaluation of strength of granular materials: effects of particle rolling. *Mechanics of materials*, 1(4), 269-283.
- [101] Ohno, T., Uchida, T., Matsumoto, N., & Takahashi, Y. (1992). Local damage of reinforced concrete slabs by impact of deformable projectiles. *Nuclear Engineering and Design*, 138(1), 45-52.
- [102] Omar, A., Marin, P., Potapov, S., & Daudeville, L. (2013). 3D discrete element modeling of concrete: Study of the rolling resistance effects on the macroscopic constitutive behavior,. XII International conference on Computational Plasticity-Fundamentals and Applications (Proceedings). COMPLAS XII Barcelona.
- [103] Omar, A. (2015). Développement et validation d'un modèle aux éléments discrets de comportement du béton sous chargement dynamique (Doctoral dissertation, Université Grenoble Alpes).
- [104] Plassiard, J. P. (2007). Modélisation par la méthode des éléments discrets d'impacts de blocs rocheux sur structures de protection type merlons (Doctoral dissertation, Université Joseph Fourier (Grenoble)).
- [105] Polanco-Loria, M., Hopperstad, O. S., Børvik, T., & Berstad, T. (2008). Numerical predictions of ballistic limits for concrete slabs using a modified version of the HJC concrete model. *International Journal of Impact Engineering*, 35(5), 290-303.
- [106] Pontiroli, C., Erzar, B., & Buzaud, E. (2014). Concrete behaviour under ballistic impacts: effects of materials parameters to penetration resistance and modeling with PRM model. *Comput Model Concr Struct Proc EURO-C*, 2, 685-693.

-
- [107] Potapov, S., Masurel, A., Marin, P., & Daudeville, L. (2016). Mixed DEM/FEM Modeling of Advanced Damage in Reinforced Concrete Structures. *Journal of Engineering Mechanics*, 143(2), 04016110.
- [108] Reddy, J. N. (2006). *Theory and analysis of elastic plates and shells*. CRC press.
- [109] Riera, J. D. (1968). On the stress analysis of structures subjected to aircraft impact forces. *Nuclear Engineering and Design*, 8(4), 415-426.
- [110] Riou P. et al. (1998) *Int. J. Impact Eng.*, 21 : 225 – 235.
- [111] Rousseau, J., Frangin, E., Marin, P., & Daudeville, L. (2008). Damage prediction in the vicinity of an impact on a concrete structure: a combined FEM/DEM approach. *Computers and Concrete*, 5(4), 343-358.
- [112] Rousseau, J. (2009). *Modélisation numérique du comportement dynamique de structures sous impact sévère avec un couplage éléments discrets/éléments finis (Doctoral dissertation, Université Joseph-Fourier-Grenoble I)*.
- [113] Rüdiger, E., & Riech, H. (1983). Experimental and theoretical investigations on the impact of deformable missiles onto reinforced concrete slabs. In *Transactions of the 7. International conference on structural mechanics in reactor technology*. Vol. J.
- [114] Saatci, S., *Behaviour and modelling of reinforced concrete structures subjected to impact loads*, Ph. D. Thesis, University of Toronto, 2007.
- [115] SALOME, Computer software, <http://www.salome-platform.org>
- [116] Samuely, F. J., & Hamann, C. W. (1939). *Civil protection*. Architectural Press.
- [117] Sawamoto, Y., Tsubota, H., Kasai, Y., Koshika, N., & Morikawa, H. (1998). Analytical studies on local damage to reinforced concrete structures under impact loading by discrete element method. *Nuclear engineering and design*, 179(2), 157-177.
- [118] Schmidt, M. J., Cazacu, O., and Green, M. L. (2009). Experimental and theoretical investigation of the high-pressure behavior of concrete. *International Journal for Numerical and Analytical Methods in Geomechanics*, 33:1–23.
- [119] Schöberl, J. (1997). NETGEN An advancing front 2D/3D-mesh generator based on abstract rules. *Computing and visualization in science*, 1(1), 41-52.
- [120] Schuler, H., Mayrhofer, C., & Thoma, K. (2006). Spall experiments for the measurement of the tensile strength and fracture energy of concrete at high strain rates. *International Journal of Impact Engineering*, 32(10), 1635-1650.
- [121] Sfer, D., Carol, I., Gettu, R., and Etse, G. (2002). Study of the Behavior of Concrete under Triaxial Compression. *Journal of Engineering Mechanics*, 128(2):156–163.
- [122] SherePadder++, Computer software, <https://subversion.assembla.com/svn/spherepadder/>

-
- [123] Shi, G. H. (1992). Discontinuous deformation analysis: a new numerical model for the statics and dynamics of deformable block structures. *Engineering computations*, 9(2), 157-168.
- [124] Shiu, W., Donzé, F. V., & Daudeville, L. (2008). Penetration prediction of missiles with different nose shapes by the discrete element numerical approach. *Computers & Structures*, 86(21-22), 2079-2086.
- [125] Smoljanović, H., Živaljić, N., & Nikolić, Ž. (2013). A combined finite-discrete element analysis of dry stone masonry structures. *Engineering structures*, 52, 89-100.
- [126] Sokolovsky, A., Gueraud, R., Dulac, J., & Labrot, R. (1977). Local behavior of reinforced concrete walls under missile impact (No. CEA-CONF--4062). CEA Centre d'Etudes Nucleaires de Saclay.
- [127] Strack, O. D. L., & Cundall, P. A. (1978). The distinct element method as a tool for research in granular media. Department of Civil and Mineral Engineering, University of Minnesota.
- [128] Strassburger E., Senf H. (1994) Report 3/94, Ernst Mach Institute, Germany.
- [129] Sugano, T., H. Tsubota, Y. Kasai, N. Koshika, S. Orui, W. A. Von Riesemann, D. C. Bickel, and M. B. Parks. (1993). Full-scale aircraft impact test for evaluation of impact force. *Nuclear Engineering and Design*, 140(3), 373-385.
- [130] Sugano, T., Tsubota, H., Kasai, Y., Koshika, N., Itoh, C., Shirai, K. Von Riesemann, W.A., Bickel, D.C., Parks, M.B. (1993). Local damage to reinforced concrete structures caused by impact of aircraft engine missiles Part 2. Evaluation of test results. *Nuclear Engineering and design*, 140(3), 407-423.
- [131] Sugano, T., Tsubota, H., Kasai, Y., Koshika, N., Ohnuma, H., Von Riesemann, W.A., Bickel, D.C., Parks, M.B. (1993). Local damage to reinforced concrete structures caused by impact of aircraft engine missiles Part 1. Test program, method and results. *Nuclear Engineering and Design*, 140(3), 387-405.
- [132] TAKEDA, J. I. (1959). A Loading Apparatus for High Speed Testing of Building Materials and Structures. In Proc. of the 2nd Japan Congress on Testing Materials, 1959.
- [133] Torre-Casanova, A. (2012). *Prise en compte de la liaison acier-béton pour le calcul de structures industrielles* (Doctoral dissertation, École normale supérieure de Cachan-ENS Cachan).
- [134] Toutlemonde F (1994) Ph.D. thesis: Résistance au choc des structures en béton : du comportement du matériau au calcul des ouvrages. LCPC, Paris
- [135] Tran, V. T. (2011). *Structures en béton soumises à des chargements mécaniques extrêmes: Modélisation de la réponse locale par la méthode des éléments discrets* (Doctoral dissertation, Grenoble).

-
- [136] Vu, X. H. (2007). Caractérisation expérimentale du béton sous fort confinement: influences du degré de saturation et du rapport eau/ciment (Doctoral dissertation, Université Joseph-Fourier-Grenoble I).
- [137] Vu, X. H., Malecot, Y., & Daudeville, L. (2009). Strain measurements on porous concrete samples for triaxial compression and extension tests under very high confinement. *The Journal of Strain Analysis for Engineering Design*, 44(8), 633-657.
- [138] Vu, X. H., Malecot, Y., Daudeville, L., & Buzaud, E. (2009). Experimental analysis of concrete behavior under high confinement: Effect of the saturation ratio. *International Journal of Solids and Structures*, 46(5), 1105-1120.
- [139] Walter, T. A., & Wolde-Tinsae, A. M. (1984). Turbine missile perforation of reinforced concrete. *Journal of Structural Engineering*, 110(10), 2439-2455.
- [140] Watstein, D. (1953, April). Effect of straining rate on the compressive strength and elastic properties of concrete. In *Journal Proceedings* (Vol. 49, No. 4, pp. 729-744).
- [141] Warren, T. L., Fossum, A. F., and Frew, D. J. (2004). Penetration into low-strength (23 MPa) concrete : target characterization and simulations. 30:477–503.
- [142] Weerheijm, J. (1992). Concrete under impact tensile loading and lateral compression (Doctoral dissertation, TU Delft, Delft University of Technology).
- [143] Weerheijm J., Doormaal A. Tensile failure of concrete at high loading rates.
- [144] Xu, J., Li, Y., Chen, X., Yan, Y., Ge, D., Zhu, M., & Liu, B. (2010). Characteristics of windshield cracking upon low-speed impact: numerical simulation based on the extended finite element method. *Computational Materials Science*, 48(3), 582-588.
- [145] Zaidi, A. M., Latif, Q. B., Rahman, I. A., & Ismail, M. Y. (2010). Development of empirical prediction formula for penetration of ogive nose hard missile into concrete targets. *American Journal of Applied Sciences*, 7(5), 711.
- [146] Zhang, M., Wu, H. J., Li, Q. M., & Huang, F. L. (2009). Further investigation on the dynamic compressive strength enhancement of concrete-like materials based on split Hopkinson pressure bar tests. Part I: Experiments. *International journal of impact engineering*, 36(12), 1327-1334.
- [147] Zhou, X. Q., & Hao, H. (2008). Modelling of compressive behaviour of concrete-like materials at high strain rate. *International Journal of Solids and Structures*, 45(17), 4648-4661.
- [148] Zielinski AJ (1982) Ph.D. thesis: fracture of concrete and mortar under uniaxial impact tensile loading. Delft University of Technology.
- [149] Zienkiewicz, O. C., and Y. K. Cheung. "The finite element in structural and continuum mechanics." McGraw-Mill Puolishing Company Limited 1967 年 (1967).
-

[150] Zukas J.A., 1992, "Penetration and perforation of solids, Impact Dynamics", Krieger Publishing Company.